ORGANOCATALYZED ATOM TRANSFER RADICAL POLYMERIZATION: DEVELOPMENT, CATALYST DESIGN, AND MECHANISTIC INVESTIGATION

by

JORDAN CORINNE THERIOT

B.S., California Institute of Technology, 2012

A thesis submitted to the

Faculty of the Graduate School of the

University of Colorado in partial fulfillment

of the requirement for the degree of

Doctor of Philosophy

Department of Chemistry and Biochemistry

2018

This thesis entitled:
Organocatalyzed Atom Transfer Radical Polymerization:
Development, Catalyst Design, and Mechanistic Investigation
written by Jordan Corinne Theriot
has been approved for the Department of Chemistry and Biochemistry

_____
Adjunct Prof. Garret Miyake

_____
Prof. Margaret Tolbert

Date _____

The final copy of this thesis has been examined by the signatories, and we find that both the content and the form meet acceptable presentation standards of scholarly work in the above mentioned discipline.

Theriot, Jordan Corinne (Ph.D., Chemistry)

Organocatalyzed Atom Transfer Radical Polymerization: Development, Catalyst Design, and Mechanistic Investigation

Thesis directed by Assistant Professor Garret M. Miyake

Atom transfer radical polymerization (ATRP) is one of the most powerful and most-used methodologies for the synthesis of precision polymeric materials with high levels of control over polymer molecular weight and chain-end functionality. ATRP is typically mediated by a metal catalyst, which has long been considered a limitation of the methodology due to the potential for metal contamination in the final product. This work describes the discovery and development of *N*,*N*-diaryl dihydrophenazines as a class of organic molecules capable of serving as photoredox catalysts for what has been named organocatalyzed ATRP, or O-ATRP. An investigation into the physical properties responsible for these catalysts' ability to achieve polymerization results on par with traditional metal catalysts uncovers the importance of intramolecular charge transfer in the photoexcited state. These charge transfer states are further shown to allow a catalyst to perform O-ATRP in solvents with a wide range of polarities. Synthesis of bench-stable radical cation salts of phenazine catalysts enables a reverse-initiation study of O-ATRP and substantiates the radical cation bromide of the catalyst as the species responsible for deactivation. Radical addition to catalyst is identified as a potential termination pathway in O-ATRP. It is found

that the use of substituted catalysts effectively blocks this termination pathway, resulting in increased initiator efficiency. Finally, phenazine photocatalysis is extended beyond O-ATRP to another type of controlled radical polymerization, photoinduced electron transfer reversible addition-fragmentation chain transfer polymerization (PET-RAFT), which allows for polymer synthesis through sequential PET-RAFT / O-ATRP and demonstrates the ability of these catalysts to produce transformative results throughout polymer chemistry.

ACKNOWLEDGEMENTS

I would like to thank my thesis committee – Prof. Garret Miyake, Prof. Maggie Tolbert, Prof. Doug Gin, Prof. Sandeep Sharma, and Prof. Charles Musgrave – for their guidance throughout the assembly and defense of this dissertation.

Many thanks to my fellow members of the Miyake Lab. It would be impossible to overstate the contributions of the group as a whole to both my research and my graduate experience. I would also like to thank the members of the Damrauer Lab and Boyer Lab for their warmth and camaraderie.

I would like to express my sincere gratitude to Sarah Lincoln, who worked with me side-by-side as an undergraduate researcher for the past three years. Thank you for your dedication to this project and to me.

This work was funded in part by a National Science Foundation Graduate Research Fellowship. I would also like to thank the NSF for awarding me an additional funding opportunity in the form of a Graduate Research Opportunities Worldwide award. This GROW award was used to sponsor a semester at the University of New South Wales in Sydney, Australia which resulted in the work featured in Chapter 5.

Finally, my sincere thanks to my family and friends, in particular my husband Ariel Hernandez, for your continuous support and encouragement throughout graduate school.

Contributor Attributions

Chapter 2

Contributions to this work were made by Dr. Chern-Hooi Lim, Dr. Haishen Yang, and Matthew Ryan. Chern is primarily responsible for the content of Section 2.4 and Figures 15 and 16. Chern also made contributions to Table 5. Matt is primarily responsible for the content of Section 2.5, Figure 17, Table 2, and the synthesis of PCs 5 and 6. Matt also made contributions to Tables 3 and 4. Haishen made contributions to chemical synthesis.

Chapter 3

Section 3.2 contains content adapted from a manuscript written by Dr. Chern-Hooi Lim. Chern and Matthew Ryan contributed to the creation of Figure 34. Steven Sartor is acknowledged for enlightening discussion. Section 3.3 contains content adapted from a manuscript written by Matthew Ryan. Matt contributed to data collection and preparation of Figure 39 and Tables 6 and 7. Section 3.5 contains contributions by Steven Sartor in the form of assistance with data analysis for Table 9. Section 3.6 is adapted from a manuscript co-authored by myself, Dr. Chern-Hooi Lim, and Blaine McCarthy. Both Blaine and Chern made major contributions to writing. Chern is also responsible for assembling Table 10.

Chapter 4

Sarah Lincoln made substantial contributions to data collection and analysis. Steven Fatur is acknowledged for assistance with electrochemical experiments, including data collection for Figures 51, 52, and 53. Crystal structure data was collected by Brian Newell of Colorado State University.

Chapter 5

This work was performed at the University of New South Wales under the direction of Prof. Cyrille Boyer. Prof. Jason Xu and Chenyu Wu are acknowledged for enlightening discussion and guidance.

This dissertation was copyedited by Dr. Kelsey Weigel.

CONTENTS

CHAPTER

TABLES

Table

FIGURES

Figure

CHAPTER 1

INTRODUCTION

1.1 Controlled Radical Polymerizations

Synthetic polymers are undeniably one of the most important classes of materials to ever be produced. Free radical polymerization is a widely-used technique for the production of synthetic polymers due to its low cost, simple reaction engineering, and inherent tolerance to a variety of functional groups.[1] As a consequence of its mechanism, however, polymers produced by free radical polymerization typically have a broad molecular weight distribution and poorly-defined chain end-groups. Because many polymer properties are dependent on molecular weight, it can be difficult to predict or control the structural properties of polymers with a broad molecular weight distribution. Additionally, a lack of defined chain end-groups restricts the use of free radical polymerization in the synthesis of higher-order polymeric structures, such as block copolymers.

In response to these limitations on the use of free radical polymerization, researchers have developed controlled radical polymerizations, or CRPs.[2] CRPs are based on the understanding that the propagating species in a free radical polymerization, a carbon-centered radical, is highly reactive. This reactivity results in a number of termination pathways which produce "dead" chains no longer capable of propagation, while other chains continue to grow. If the concentration of radicals is kept low, however, bimolecular

termination reactions are minimized. With limited termination pathways available, all polymer chains will continue to grow at a uniform rate until the monomer is consumed. As a result, the product polymer has a narrow molecular weight distribution, commonly quantified by the dispersity, $Đ$. The chain ends remain well-defined, and the addition of more monomer induces continued uniform growth of polymer chains. These attributes of CRPs have enabled the creation of some of the most advanced materials known today.[3]

CRPs are capable of producing such results because they operate on the principle of reversible-deactivation. The propagating radical can be switched between a dormant state, during which it is not available for reactions, and an active state, during which it is free to propagate. The many types of CRPs can be differentiated depending on the nature of the reversible-deactivation equilibrium. Some categories of CRP include nitroxide-mediated polymerization (NMP), in which the reversible-deactivation equilibrium lies between a nitroxide radical and an alkoxyamine[4,5]; reversible addition-fragmentation chain transfer (RAFT) polymerization, in which reversible-deactivation is based on chain transfer mediated by a thiocarbonylthio compound[6,7]; and atom transfer radical polymerization (ATRP), which is the primary focus of this work.

1.2 Atom Transfer Radical Polymerization

Among the many CRPs that have been developed, ATRP is the most widely used, due to its broad applicability and synthetic versatility.[8–10] In traditional ATRP, reversible-deactivation is commonly mediated by a copper catalyst, though several other transition metals have been used (Figure 1). In the activation step, a Cu^{I} catalyst reduces the alkyl halide initiator (typically an alkyl bromide), yielding a Cu^{II}-Br complex and a carbon-

centered radical which is free to react with monomer, propagating the polymerization. In the deactivation step, the Cu^{II} complex oxidizes the radical, placing the halogen atom back on the polymer chain and re-forming the Cu^{I} catalyst. Provided this equilibrium between active radical and dormant alkyl halide lies far enough in the direction of deactivation, the concentration of radicals is kept low and the polymerization is controlled.

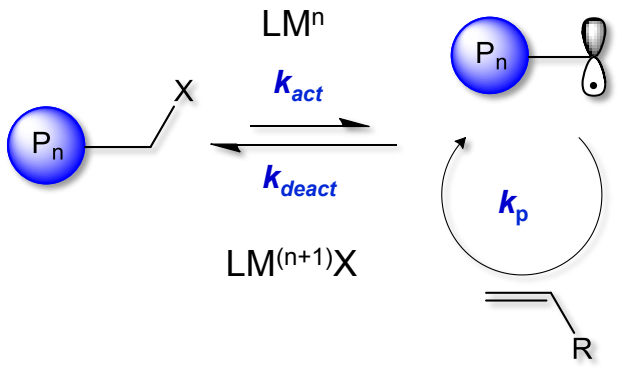

Figure 1. General mechanism of ATRP.

Research on ATRP has exploded in the past few decades, leading to dozens of variations on the above-described system.[11–13] Use of advanced ligands and other additives has increased the speed of the reactions and allowed the amount of catalyst needed to drop to low-ppm levels.[14,15] However, ATRP still relies on a transition metal catalyst which is notoriously challenging to remove from the product polymer. As a result, polymers produced using ATRP may have difficulty being employed in certain electronic or biomedical applications, and ATRP is yet to establish itself on a broad scale as an industrially-relevant methodology. Therefore, significant motivation exists to develop a variant of ATRP which requires no transition metal catalyst at all.[16] Recently, reversible chain-transfer[17] and reversible complexation[18,19] variants of ATRP that can use organic catalysts were reported.

However, these methodologies require the use of alkyl iodide initiators and are not effective with the alkyl bromides commonly employed in ATRP. A highly desirable CRP would match the performance, feasibility, and robustness of traditional ATRP while employing an organic catalyst under mild conditions. We have termed this concept organocatalyzed atom transfer radical polymerization, or O-ATRP.

1.3 Photoredox Catalysis and ATRP

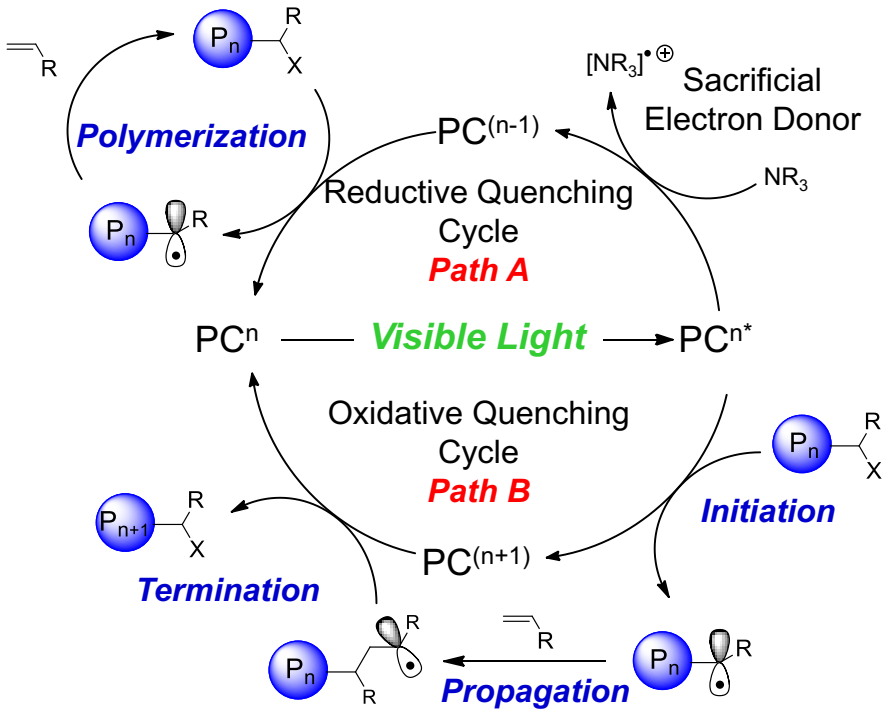

Figure 2. Mechanistic pathways for photoredox-mediated ATRP.

Photoredox catalysis offers an appealing option for envisioning a process in which an organic molecule could mediate the ATRP equilibrium. Photoredox catalysis employs light energy to excite a molecule which then participates in electron transfer reactions. Figure 2

shows the two pathways by which ATRP can be effected by a photoredox catalyst. In the reductive quenching pathway, the excited photocatalyst behaves as an electron acceptor. In the oxidative quenching pathway, the excited photocatalyst behaves as an electron donor. While photoredox-catalyzed polymerization systems that operate *via* reductive quenching have been developed[20,21], the reductive quenching pathway requires a sacrificial electron donor which can result in undesirable side reactions.[22] Therefore, it is most desirable to identify a suitable organic catalyst which can operate *via* an oxidative quenching cycle.

Photoredox catalysis which operates *via* the oxidative quenching pathway has been applied to ATRP, albeit using a transiton metal photocatalyst (PC). In the presence of a visible light source, *fac*-[Ir(ppy_3)], a common transition metal-based photoredox catalyst, has successfully catalyzed the ATRP of methacrylates[23,24] and acrylates[25] *via* an oxidative quenching cycle. One of the reasons *fac*-[Ir(ppy_3)] is successful as a photoredox ATRP catalyst is because it has been measured to possess a reduction potential of -1.73 V in its excited state. This reducing power enables it to efficiently participate in the initiation step, reduction of the alkyl bromide initiator to produce the oxidized catalyst, a halide anion, and a carbon-centered radical (Figure 2). The search for an organic catalyst capable of mediating O-ATRP began with a similar concept: the best candidate would be a visible-light absorbing organic dye with a low reduction potential in the photoexcited state.

1.4 Overview of Thesis Chapters

Chapter 2 of this thesis describes the foundational work of identification of such a catalyst suitable for O-ATRP. In this chapter, *N*,*N*-diaryl dihydrophenazines are established as the first class of visible-light absorbing organic PCs capable of producing O-ATRP results

on par with those of traditional ATRP. **Chapter 3** presents an investigation of the physical properties responsible for the superior performance of *N*,*N*-diaryl dihydrophenazines as O-ATRP catalysts, with an emphasis on the discovery of the crucial role intramolecular charge transfer plays in O-ATRP. The chapter is concluded with a perspective discussion of catalyst design principles for O-ATRP. **Chapter 4** moves into mechanistic studies of O-ATRP, aided by the synthesis of bench-stable radical cation bromide salts of phenazine catalysts. These radical cations are established as the species responsible for deactivation in O-ATRP, and radical addition to catalyst is identified as a termination pathway in O-ATRP. **Chapter 5** expands phenazine photoredox catalysis beyond O-ATRP to another photocontrolled CRP, PET-RAFT. The advantage of having one catalyst capable of mediating two types of polymerizations is demonstrated with a sequential PET-RAFT / O-ATRP copolymerization. **Chapter 6** offers summarizing and concluding remarks, as well as a discussion of future challenges for the field of O-ATRP.

CHAPTER 2

DEVELOPMENT OF O-ATRP*

2.1 Introduction

Our lab group's interest in the field of O-ATRP began in 2013 with the discovery that perylene, a polycyclic aromatic hydrocarbon dye, could serve as a visible-light organic photocatalyst (PC) for the reduction of alkyl bromides with visible light in order to catalyze the polymerization of methacrylates and styrene *via* an oxidative quenching pathway.[26,27] Support that this polymerization proceeds through an ATRP mechanism comes from its ability to produce both homopolymers and block copolymers, as well as direct chain-end analysis using MALDI-TOF and ^{1}H NMR. It also displays the characteristic kinetics of a CRP, which are first-order with respect to monomer concentration and have linear M_n growth with respect to conversion. The photocontrol aspect of the O-ATRP mechanism also means that the polymerization can be stopped and re-started simply by turning on and off the light source, allowing for both spatial and temporal control of the polymerization. Finally, the polymerization has been shown to proceed using natural sunlight as the light source. This foundational work showed much promise, however, the level of control over the polymerization (evidenced by low dispersity, *Đ,* and high initiator efficiency, *I**) was not up

* This chapter is extracted from Theriot, J. C. *et al. Science* **2016**, *352* (6289), 1082-1086. See *Contributor Attributions* for additional information.

to the standards set forth by copper-catalyzed ATRP. Around the same time, phenyl phenothiazine derivatives were also proven effective as PCs for the O-ATRP of methacrylates and acrylonitrile, but they required irradiation by UV light and left much room for improvement in terms of generating polymers with higher MWs and lower $Đ$ coupled with increased I^*.[28,29]

2.2 N,N-Diaryl Dihydrophenazine Photocatalysts

In order to identify suitable candidates for the next generation of PCs for O-ATRP, we returned to our proposed mechanism of photoredox O-ATRP (Figure 3C), which posits reversible electron transfer (ET) from the photoexcited PC to reversibly activate an alkyl bromide initiator (Figure 3C). In addition to the requirement that the excited triplet state $^3PC^*$ possess a sufficiently strong excited-state reduction potential (E^{0*}) to reduce the initiator, a delicate interplay must be balanced between the stability of the radical cation $^2PC^{\bullet+}$ and its oxidation potential relative to the propagating radical to efficiently deactivate the propagating polymer and yield a controlled radical polymerization.

Computationally directed discovery inspired us to focus on 5,10-diphenyl-5,10-dihydrophenazines as a potential class of PCs for O-ATRP (Fig. 3B). Interestingly, the phenazine core is shared by several biologically relevant molecules that serve as redox-active antibiotics[30,31], while synthetic derivatives have drawn interest in organic photovoltaics[32–34] and organic ferromagnets.[35,36] We hypothesized that an appropriate union between E^{0*} and the stability of the radical cation $PC^{\bullet+}$ resulting from ET to the initiator would be required for the production of polymers with controlled MW and low $Đ$. As such, we investigated electron donating (OMe, **1**), neutral (H, **2**), and withdrawing (CF_3, **3** and CN, **4**) moieties on the *N*-phenyl substituents.

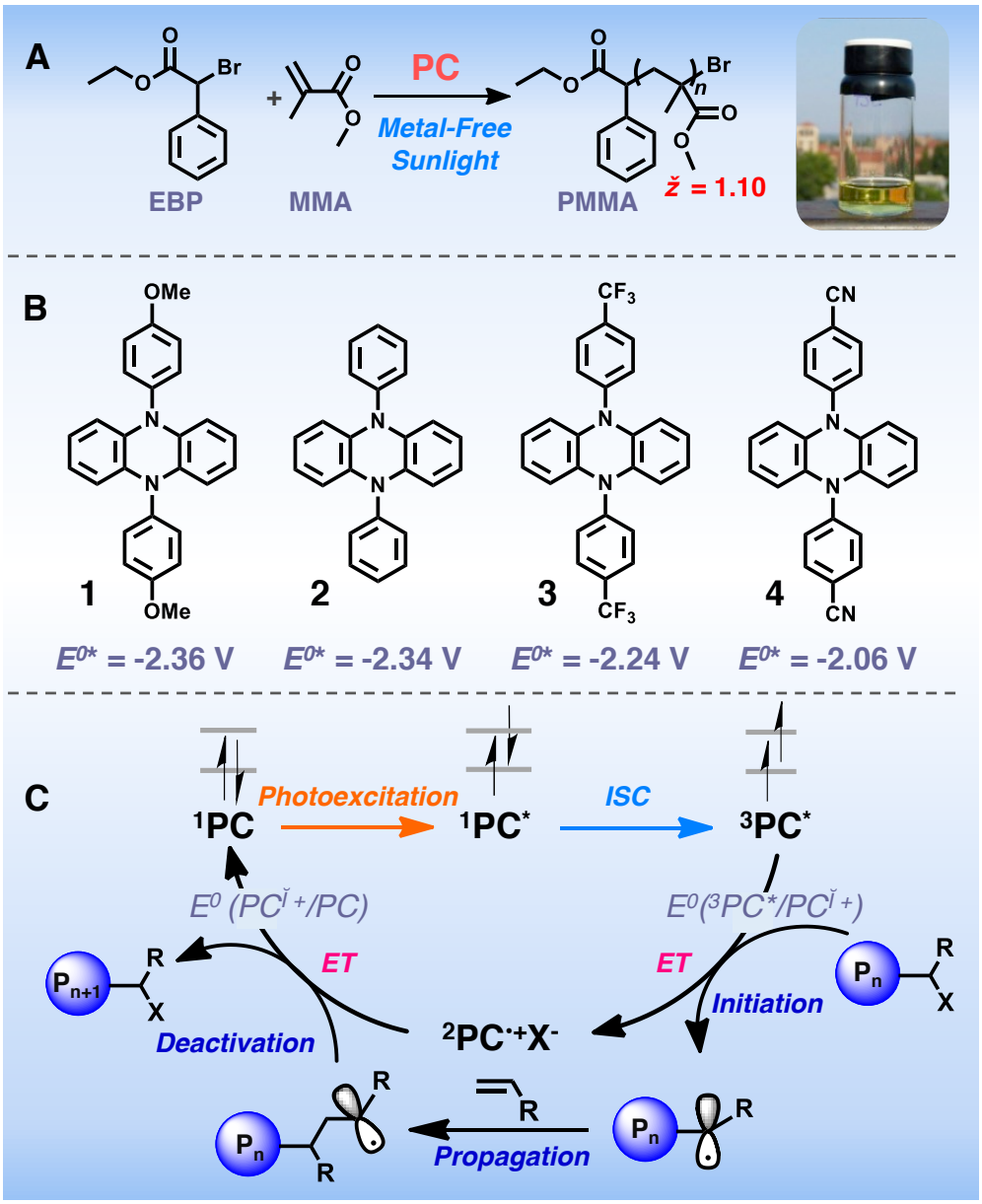

Figure 3. Photoredox catalyst development for O-ATRP. **A.** Polymerization of methyl methacrylate to well-defined polymers using photoredox O-ATRP driven by sunlight. **B.** Structures of the diphenyl dihydrophenazine PCs **1**-**4** used in this study. **C.** A proposed mechanism for ATRP mediated by a PC *via* photoexcitation to $^{1}PC^{*}$, intersystem crossing to the triplet state $^{3}PC^{*}$, ET to form the radical cation doublet $^{2}PC^{\bullet+}$ and back ET to regenerate PC and reversibly terminate polymerization.

Density Functional Theory (DFT) was used to calculate the reduction potentials of the triplet excited state PCs, initiator, and propagating radicals (Fig. 3B). We found that **2**

possesses a triplet excited-state reduction potential of $E^0(PC^{\bullet+}/{}^3PC^*)$ = -2.34 V *vs*. SCE. Functionalization of the phenyl substituents with an electron donating group OMe (**1**) strengthened the E^{0*} to -2.36 V, while introduction of CF^3 or CN electron-withdrawing groups (EWGs) weakened the E^{0*} to -2.24 V and -2.06 V for **3** and **4**, respectively, all of which is corroborated by the measured values within experimental error (Table 5). The triplet excited states of these PCs are all strongly reducing with respect to 1e- transfer to the ethyl α-bromophenylacetate (EBP) initiator; we calculated that $E^0(EBP/EBP^{-\bullet})$ = -0.74 V *vs*. SCE for an adiabatic ET, consistent with our cyclic voltammetry results, which show that the onset of EBP reduction occurs at ~ -0.8 V *vs.* SCE. Impressively, these phenazine derivatives are significantly more reducing than commonly used metal PCs[37], including polypyridyl iridium complexes (E^{0*} as negative as -1.73 V *vs*. SCE) that have been used in photomediated ATRP.[23,25] Iridium PCs are expensive, challenging to remove from the product, and have only been demonstrated to produce polymers with *Đ* as low as 1.19.

The remarkable reducing power of these dihydrophenazine based PCs arises from a distinct combination of their high triplet state energies (~2.2 – 2.4 eV) and the formation of relatively stable radical cations [$E^0(PC^{\bullet+}/PC)$ = ~ -0.1 to -0.2 V] upon their oxidation. These radical cations are also sufficiently oxidizing to deactivate the propagating chains. We computed E^0s for propagating radicals with n monomer repeat unit(s) bound to ethyl phenylacetate (EPA) of $E^0([EPA\text{-}MMA_n]/[EPA\text{-}MMA^n]^{\bullet-})$ = -0.74, -0.86, and -0.71 V for n = 0, 1 and 2, respectively. These E^0s are sufficiently negative with respect to oxidization by the radical cations to drive rapid radical deactivation and regeneration of the PC to complete the photocatalytic cycle.

*2.3 O-ATRP Using PCs **1**-**4***

An initial series of target PCs (**1**-**4**) were synthesized in two steps from commercial reagents in good yields (see Section 2.7). Under otherwise identical conditions, all of the PCs were tested in the polymerization of methyl methacrylate (MMA), using EBP as the initiator, and white LEDs for irradiation in dimethylacetamide (Table 1, run 1 and Table 3, runs S1 to S3). All four PCs proved effective in polymerization after 8 hours of irradiation, with the PCs bearing EWGs exhibiting the best catalytic performance. PC **3** proved superior in producing polymers with a combination of not only the lowest dispersity ($Đ$ = 1.17), but also the highest initiator efficiency (I^* = 65.9 %) (Table 1, run 1). Using methyl α-bromoisobutyrate as the initiator was also efficient, but did not achieve the same level of control of the polymerization achieved with EBP (Table 3, run S5). Additionally, polymerization could be driven by sunlight to produce poly (methyl methacrylate) (PMMA) with a low dispersity of $Đ$ = 1.10 (run 2 and Figure 4). Control polymerizations revealed no polymerization occurred in the absence of any single component (i.e. light, PC, or initiator), or in the presence of oxygen or TEMPO, (supporting a radical polymerization mechanism).

Table 1. Results for the Organocatalyzed Atom Transfer Radical Polymerization of Methyl Methacrylate Catalyzed by **3** Using White LEDs or Sunlight[a].

Run No.	[MMA]:[EBP]:[**3**]	Time (h)	Conv. (%)	M_w (kDa)	$Đ$ (M_w/M_n)	I^* ($M_{n(theo)}/M_{n(exp)}$)
1	[1000]:[10]:[1]	8	98.4	17.9	1.17	65.9
2[a]	[1000]:[10]:[1]	7	33.8	7.54	1.10	52.9
3	[1000]:[20]:[1]	8	78.9	7.12	1.18	69.5
4	[1000]:[15]:[1]	8	67.8	8.74	1.18	64.3
5	[1000]:[5]:[1]	8	86.9	37.3	1.26	59.6
6	[1000]:[2]:[1]	8	95.2	85.5	1.54	86.3
7	[5000]:[10]:[1]	8	74.7	77.4	1.32	64.2
8	[2500]:[10]:[1]	8	96.3	61.3	1.31	52.0
9	[750]:[10]:[1]	6.5	53.2	7.75	1.30	71.1
10	[500]:[10]:[1]	6.5	64.0	4.83	1.12	79.9

Ratios given in table 1 are based on 1 mL of MMA for runs 1 – 6, 2.5 mL of MMA for runs 7 and 8, 0.75 mL MMA for run 9, and 0.5 mL MMA for run 10. The amount of DMA used was 1 mL, except for run 7 (3.5 mL), run 8 (2.5 mL), run 9 (1.25 mL), and run 10 (1.5 mL). See below for additional information on run 2.

Figure 4. Photograph of Run 2 from Table 1, which was performed in sunlight.

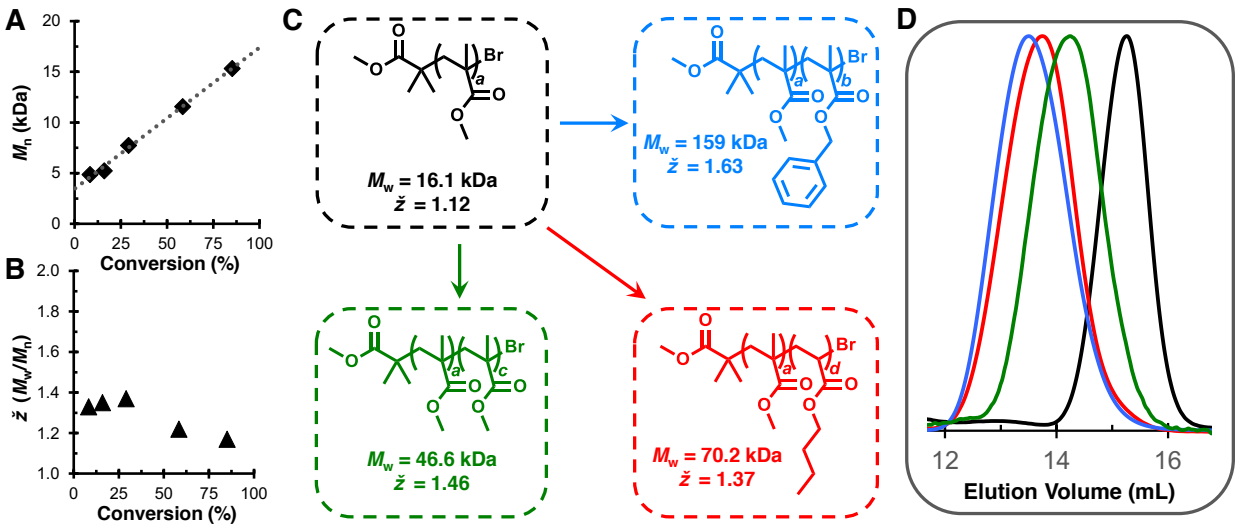

Figure 5. Polymerization results using PC **3. (A)** Plot of molecular weight as a function of monomer conversion and **(B)** Plot of dispersity as a function of monomer conversion for the polymerization of MMA mediated by **3**. **(C)** Chain-extension from a PMMA macro-initiator (black) to produce block copolymers with MMA (green), benzyl methacrylate (blue), and butyl acrylate (red). **(D)** GPC traces of each polymer depicted in **C** (color coded).

Time-point aliquots were taken during polymerization to monitor the MW and $Đ$ progression as a function of monomer conversion (Figures 5A and B). The control provided by **3** was evidenced by the linear increase in polymer MW and low $Đ$ throughout the course of polymerization. However, the y-intercept of the M_n *vs.* conversion plot was 3.46 kDa, suggesting an uncontrolled chain-growth period with addition of ~32 MMA equivalents during the onset of polymerization before precise control was attained; whereas, an ideal polymerization would have a y-intercept equal to the mass of the initiator (MW of EBP = 243 Da).

We next examined the effect of adjusting the initiator ratio relative to monomer and PC (runs 3 – 6 and Figure 6A). The M_w of the resulting PMMA could be modulated from 7.12 to 85.5 kDa. High EBP ratios resulted in controlled polymerizations and low dispersities ($Đ$ = 1.26 – 1.17), and despite the moderate loss of precise control over the polymerization at

low EBP ratios ($Đ$ = 1.54), high MW polymer was produced with high initiator efficiency (M_w = 85.5 kDa, I^* = 86.3 %). Alternatively, adjusting the monomer ratio relative to EBP and PC regulated polymer MW while also maintaining low $Đ$ (runs 7 – 10 and Figure 6B).

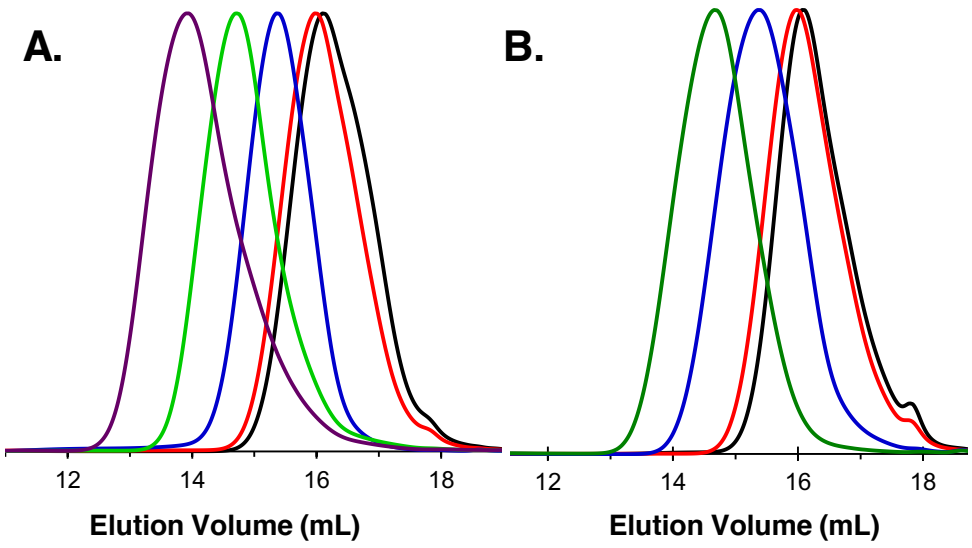

Figure 6. (A) GPC trace of runs 6 (purple), 5 (green), 1 (blue), 4 (red), and 3 (black), Table 1. **(B)** GPC trace of runs 10 (green), 9 (blue), 8 (red), and 7 (black), Table 1.

One of the greatest strengths of traditional ATRP is its capacity to synthesize advanced polymeric architectures, including block copolymers. The reversible-deactivation mechanism enforced in ATRP repeatedly reinstalls the Br chain-end group onto the polymer and thus, isolated polymers can be used to reinitiate polymerization. A combination of NMR spectroscopy (Figure 7) and MALDI-TOF MS were used to confirm the expected EBP derived polymer chain-end groups for a polymer produced through the proposed photoredox O-ATRP mechanism (Figure 8). Additionally, to further support the posited O-ATRP mechanism, a series of block polymerizations were performed to probe the Br chain-end group fidelity.

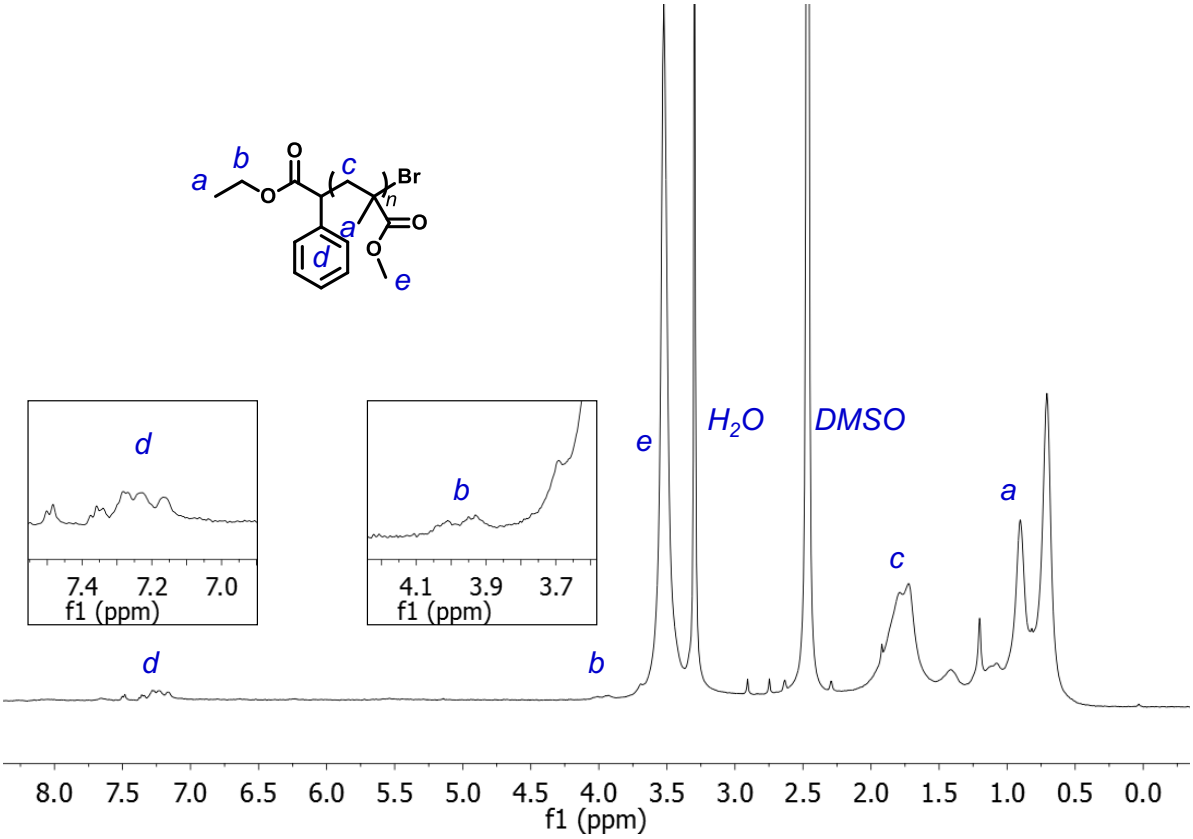

Figure 7. ^{1}H NMR spectrum of isolated poly(methyl methacrylate) (DMSO-d_6).

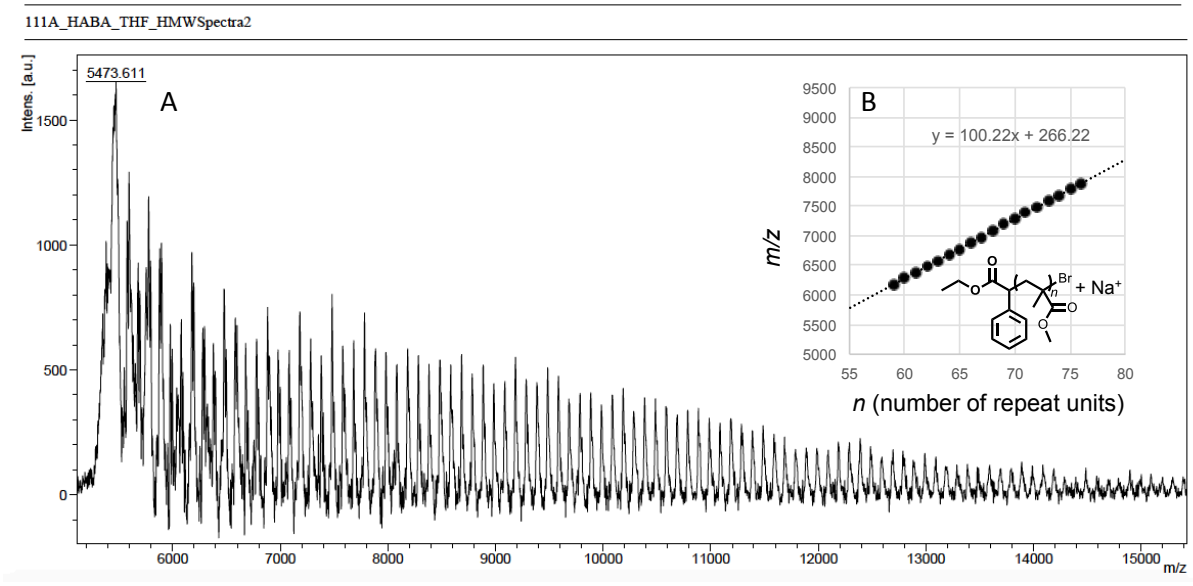

Figure 8. **(A)** MALDI-TOF mass spectrum of a PMMA sample. **(B)** Plot of m/z vs number of MMA repeat units revealing a slope equal to the mass of MMA and a y-intercept equal to the mass of the EBP chain-end group plus Na.

First, after initial polymerization of MMA proceeded for 12 h, additional MMA was added to the reaction mixture. Gel permeation chromatography (GPC) analysis revealed that the MW of the resulting polymer quantitatively increased (Figure 9). Second, after polymerization of MMA was allowed to proceed for 8 h, the reaction mixture was placed in the dark for 8 h and subsequently additional MMA (Figures 9 and 10), benzyl methacrylate (BMA) (Figures 11 and 12), or butyl acrylate (BA) was added (Figures 13 and 14). No polymerization took place during the dark period, while the subsequent addition of monomer and further illumination resulted in continued and controlled polymer chain growth. Third, an isolated polymer was reintroduced to a solution of monomer and catalysts and exposed to light to ascertain whether it would serve as a macro-initiator for the synthesis of block polymers. This chain-extension proved successful with MMA, BMA, and BA (Figures 5C and 5D). The chain-extension polymerization from an isolated polymer produced from this polymerization method firmly supports the conclusion that this methodology proceeds through the O-ATRP mechanism, while all of these experiments revealed base-line resolved peaks in the GPC traces, demonstrating high chain-end group fidelity.

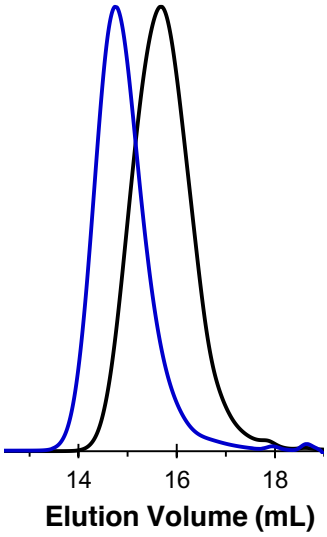

Figure 9. GPC trace showing the results of the synthesis of PMMA-b-PMMA. The polymer produced after 12 hours (black) and the polymer produced after additional monomer and 6 hours of irradiation (blue).

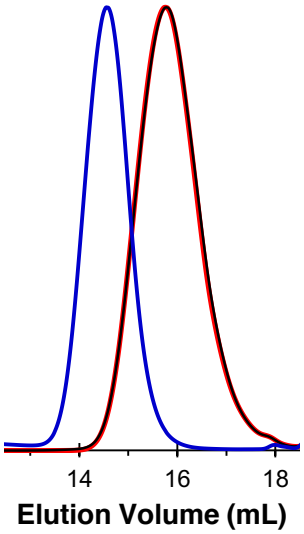

Figure 10. GPC trace showing the results of the synthesis of PMMA-*b*-PMMA with a dark resting period. The polymer produced after 8 hours (red), the polymer produced after the dark period (black), and the polymer produced after additional monomer and irradiation 8 hours of (blue).

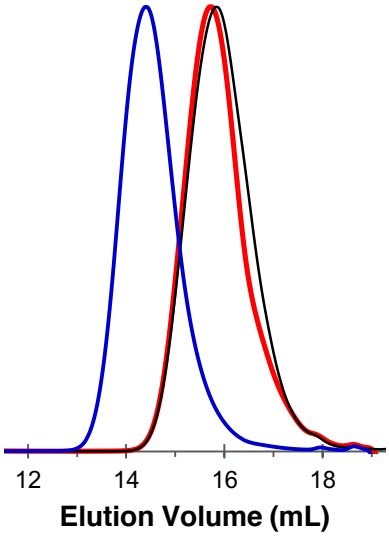

Figure 11. GPC trace showing the results of the synthesis of PMMA-*b*-PBA with a dark resting period. The polymer produced after 8 hours (red), the polymer produced after the dark period (black), and the polymer produced after additional monomer and 8 hours of irradiation (blue).

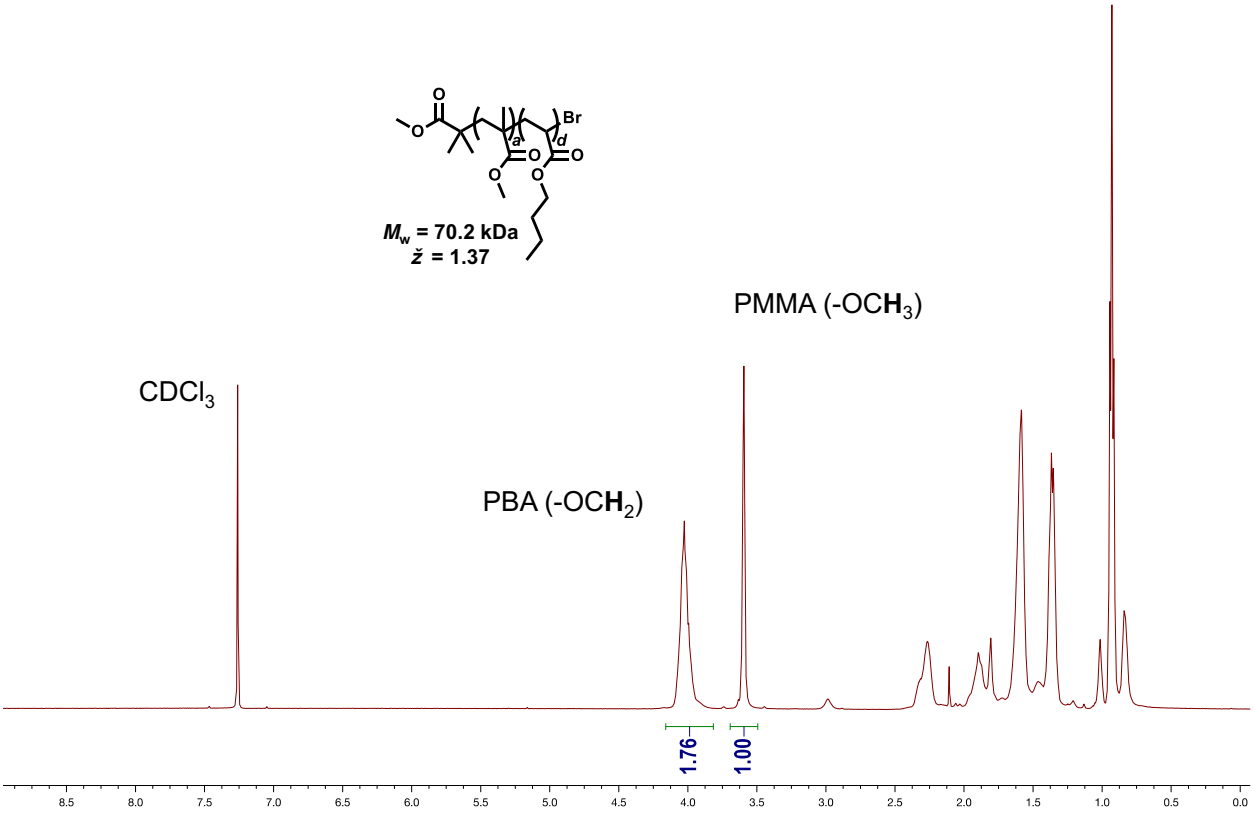

Figure 12. ^{1}H NMR of PMMA-*b*-PBA (CDCl$_3$).

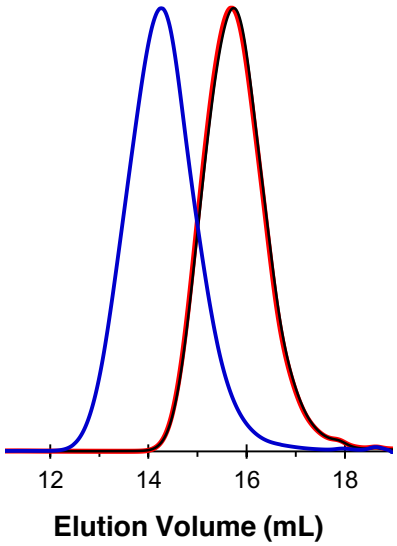

Figure 13. GPC trace showing the results of the synthesis of PMMA-*b*-PBnMA with a dark resting period. The polymer produced after 8 hours (red), the polymer produced after the dark period (black), and the polymer produced after additional monomer 8 hours of irradiation (blue).

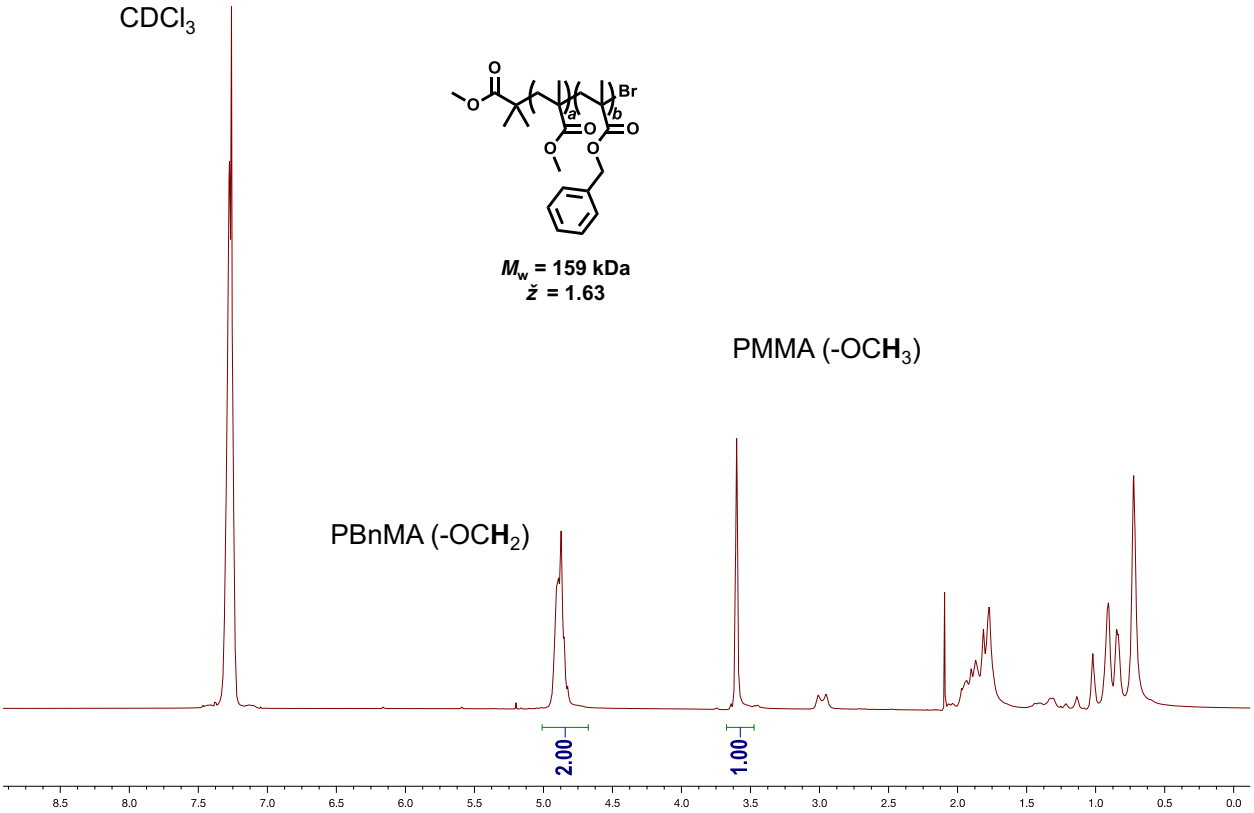

Figure 14. ^{1}H NMR of PMMA-*b*-PBnMA ($CDCl_3$).

2.4 Frontier Molecular Orbital Analysis

DFT calculations were performed to gain insight into the differences in the performances of the PCs, all of which possess similar $E^0(PC^{\bullet+}/{}^3PC^*)$s and $E^0(PC^{+\bullet}/PC)$s that are sufficiently reducing and oxidizing, respectively, to drive the photocatalytic cycle of Figure 3C. As such, we reasoned that the superior performances of **4** and, in particular, **3** must be qualitatively different from that of **1** and **2** and result from a more complex effect.

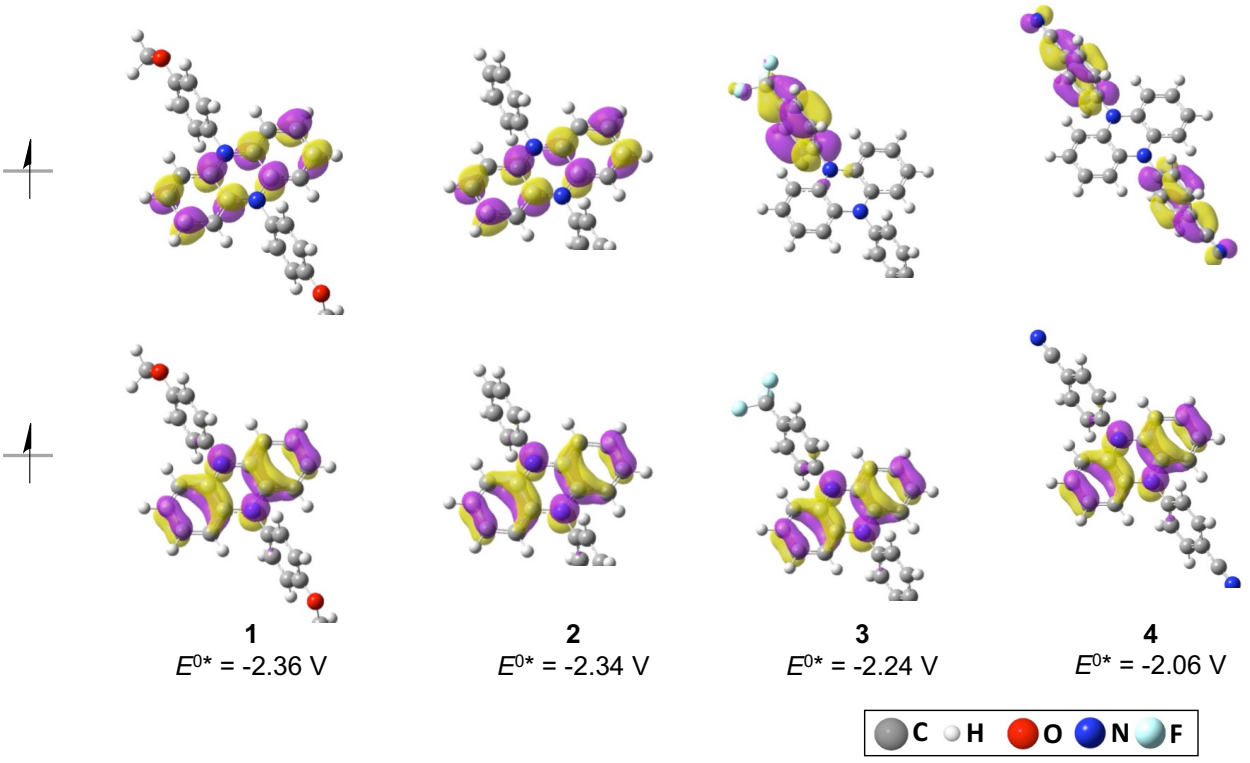

Figure 15. Calculated triplet state ($^3PC^*$) frontier orbitals and excited-state reduction potentials E^{0*} of diphenyl dihydrophenazine PCs **1**-**4**. Top figures show the higher-lying singly occupied molecular orbital (SOMO) and bottom figures the low-lying SOMO. Phenyl functionalization with electron withdrawing groups (CF_3 and CN) localizes the high-lying SOMO on the phenyl.

Inspection of the triplet state ($^3PC^*$) frontier orbitals reveals qualitative differences in these PCs (Figure 15). The low-lying singly occupied molecular orbitals (SOMO) of all the PCs are similar, with the electron localized over the phenazine π system. For PCs **1** (OMe) and **2**

(H), the high-lying SOMO is also localized on the phenazine rings; in contrast, for **3** (CF_3) and **4** (CN) the high-lying SOMO, occupied by the reducing e^-, resides on the phenyl ring(s). We contend that the CF_3 and CN EWGs of **3** and **4** stabilize their π^* orbitals localized on the phenyl rings relative to the phenazine localized π^* orbital that is the high-lying SOMO of **1** and **2**. This reorders the energies of the π^* orbitals such that a π^* orbital localized on the phenyls becomes the high-lying SOMO of **3** and **4**, although the low-lying SOMO localized on the phenazine moiety remains singly occupied. Thus, **3** and **4** differ qualitatively from **1** and **2** in that their two triplet electrons reside on either the phenazine or the phenyl substituent and are thus spatially separated.

Furthermore, a comparison of **3** to **4** elucidates another important distinction. For **3**, the high-lying SOMO is localized on one of the phenyl rings, while in **4** the reducing e^- is delocalized over both phenyl rings. Surprisingly, calculations revealed one of the C-F bonds of the CF_3 functionalized phenyl bearing the high-lying SOMO of **3**, is lengthened from 1.35 Å to 1.40 Å, indicating partial localization of electron density on the C-F antibond. This symmetry-breaking effect in the triplet state of **3** creates a more localized, higher electron density of the reducing electron of **3** relative to **4** while also maintaining the spatial separation between the two SOMO electrons that preserves the reducing potential of the triplet.

*2.5 O-ATRP Using PCs **5** and **6***

With the above observations in mind, we attempted to discover even more efficient PCs to mediate O-ATRP using computational chemistry to design diaryl dihydrophenazines that possess sufficiently strong E^{0*}s and spatially separated excited state SOMOs with the higher energy SOMO localized over only one of the aromatic substituents off the

dihydrophenazine core. Using these principles, we designed and synthesized 2-napthyl (**5**) and 1-napthyl (**6**) derivatives, with strong E^{0*}s of -2.20 and -2.12 V, respectively, and SOMOs with the targeted desirable geometric features (Figure 16). Using EBP as the initiator, both PCs proved successful in the polymerization of MMA (Table 3, runs S8 and S9). Although **5** produced PMMA with an impressively low $Đ$ of 1.03 (M_w = 9.35 kDa, I^* = 46.1 %) – rivaling metal ATRP catalysts – **6** produced PMMA with a slightly higher I^* (47.5 %), faster polymerization rates, and similarly low $Đ$ of 1.08 (M_w = 12.3 kDa). The plot of M_n *vs.* monomer conversion exhibits a y-intercept of 850 Da, demonstrating the attainment of control over polymerization after the addition of only ~6 MMA units correspondingly much more efficient control in the O-ATRP mediated by **6** than achieved with **3** (Figure 17A). Thus, we investigated **6** in more detail as the PC in the polymerization of MMA.

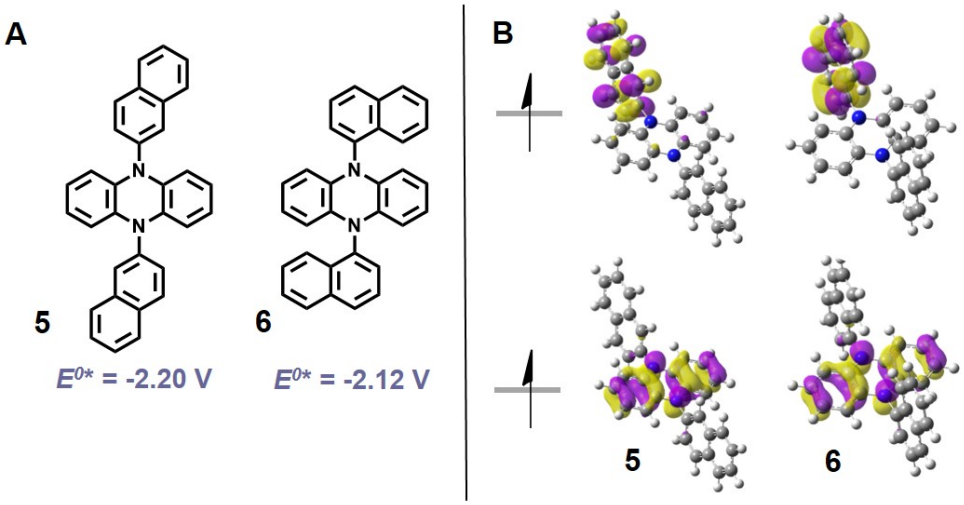

Figure 16. Computationally directed discovery of PCs **5** and **6**. **(A)** Structures of **5** and **6** and the calculated E^{0*}. **(B)** Triplet state frontier orbitals of **5** and **6** showing the higher-lying SOMO and bottom figures the low-lying SOMO.

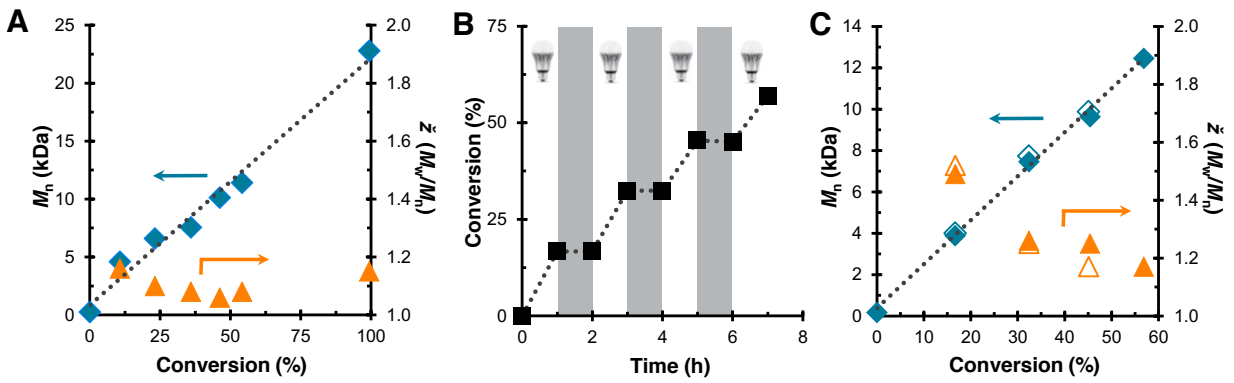

Figure 17. Results for the polymerization of MMA using PC **6**. **A**. Plot of M_n and $Đ$ *vs.* monomer conversion for the polymerization of MMA under continuous irradiation. **B.** Plot of monomer conversion *vs.* time, and **C.** Plot of M_n and $Đ$ (filled symbols from after irradiation and empty symbols from after dark period) *vs.* monomer conversion using **6** as the PC during pulsed light irradiation with white LEDs. See Section 2.7 for experimental details.

Table 2. Results for the Organocatalyzed Atom Transfer Radical Polymerization of Methyl Methacrylate Catalyzed by **6** Using White LEDs.

Run No.	[MMA]:[MBP]:[**6**]	Time (h)	Conv. (%)	M_w (kDa)	$Đ$ (M_w/M_n)	I^* ($M_{n(theo)}/M_{n(exp)}$)
11	[1000]:[10]:[1]	8	71.7	10.6	1.28	88.1
12	[1000]:[20]:[1]	8	73.1	5.24	1.29	94.5
13	[1000]:[15]:[1]	8	70.8	7.52	1.36	88.5
14	[5000]:[10]:[1]	8	69.5	46.9	1.32	98.7
15	[2500]:[10]:[1]	8	64.5	21.9	1.34	99.3
16	[750]:[10]:[1]	8	69.0	6.93	1.23	94.7
17	[500]:[10]:[1]	8	76.4	5.74	1.39	95.7

Ratios are based on 1 mL of MMA for runs 11 – 15, 5 mL of MMA for run 16, 2.5 mL of MMA for run 17, 0.75 mL of MMA for run 18, and 0.5 mL of MMA for run 19. The amount of DMA used was 2 mL, except for runs 16 and 17 (5 mL), and run 19 (1 mL).

A survey of initiators commonly employed in traditional metal-catalyzed ATRP in conjunction with **6** (Table 2, run 11 and Table 3, runs S9 – S12) revealed that methyl 2-bromopropionate (MBP) provided the best overall results for the polymerization of MMA (M_w = 10.6 kDa; $Đ$ = 1.28; I^* = 88.1 %). Furthermore, temporal control was realized by employing a pulsed-irradiation sequence (Figures 17B and 17C). Polymerization was only

observed during irradiation, paused during dark periods, and the MW steadily increased with continued irradiation while producing a polymer with a low $Đ$ of 1.17. Efficient control over the polymerization by **6** is highlighted by the consistently high I^* achieved over broad reaction conditions to produce polymers with tunable MWs through varying initiator (Runs 11 – 14) or monomer (Runs 15 – 17) ratios.

We envision that this O-ATRP catalyst platform will expand the application scope for polymers beyond those synthesized by metal-catalyzed ATRP, while their impressively strong reducing power presents great promise for their application toward other challenging chemical transformations. We also anticipate that the governing principles that afford these organic photocatalysts with their desirable properties will be exploited through computational design to discover additional photochemical platforms with capacities for a variety of applications.

2.6 Supplemental Polymerization Results

Table 3. Supplemental polymerization data, including information for PCs **1**, **2**, **4**, and **5**, and an initiator screen for PCs **3** and **6**.

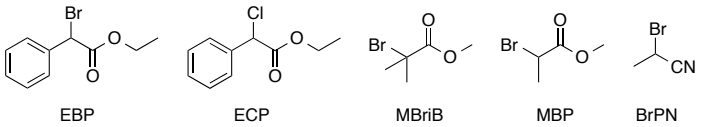

Run No.	PC	Initiator	DMA	Time (h)	Conv. (%)	M_w	M_n	Đ (M_n/M_w)	I^*
S1	**1**	EBP	1 mL	8	69.6	36.3	24.7	1.47	29.2
S2	**2**	EBP	1 mL	8	85.9	18.4	11.9	1.55	74.5
S3	**4**	EBP	1 mL	8	73.5	21.4	16.1	1.33	47.2
S4	**4**	EBP	1 mL	7	36.7	9.63	7.47	1.29	52.5
S5	**3**	MBriB	1 mL	8	94.0	18.8	15.0	1.25	63.5
S6	**3**	MBP	1 mL	8	86.0	9.80	7.37	1.33	118
S7	**3**	EClP	1 mL	4	96.0	21.9	8.62	2.54	111
S8	**5**	EBP	1 mL	5	39.4	9.35	9.08	1.03	46.1
S9	**6**	EBP	1 mL	5	54.1	12.3	11.4	1.08	47.5
S10	**6**	BrPN	2 mL	8	73.3	15.8	12.8	1.24	58.1
S11	**6**	EClP	2 mL	8	93.7	24.3	18.0	1.35	53.2
S12	**6**	MBriB	2 mL	8	90.2	14.4	10.7	1.35	85.9

Polymerizations were performed according to the above general polymerization procedure using 9.35 mmol (1000 eq.) monomer, 9.35 µmol (1 eq.) catalyst, and 93.5 µmol initiator.

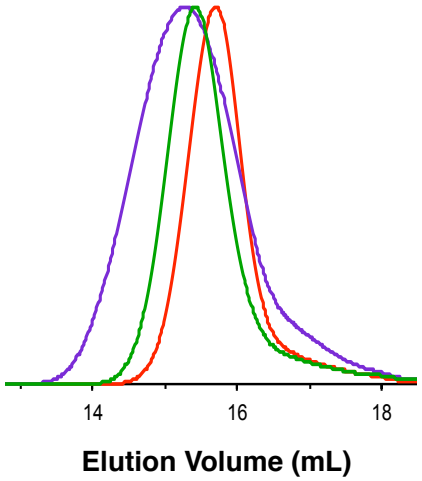

Figure 18. GPC traces of runs S10 (red), S11 (purple), and S12 (green).

Table 4. Monomer scope of catalysts **3** and **6**.

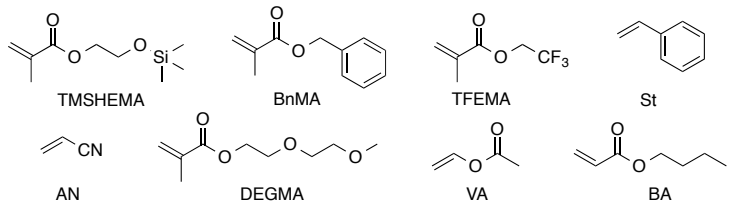

Run No.	PC	Monomer	Initiator	Conv. (%)	M_w	M_n	Đ (M_n/M_w)	I^*
S13	3	TMSHEMA	EBP	83.3	25.3	20.0	1.26	85.5
S14	3	TFEMA	EBP	77.4	58.2	54.7	1.06	24.2
S15	3	DEGMA	EBP	94.7	30.1	21.3	1.41	84.6
S16	3	BA	EBP	98.5	26.6	16.4	1.62	60.0
S17	3	St	EBP	0.0	n/a	n/a	n/a	n/a
S18	3	VA	EBP	0.0	n/a	n/a	n/a	n/a
S19	3	AN	EBP	71.3	40.3*	23.7*	1.70	15.6
S20	6	TMSHEMA	MBP	90.8	18.7	16.0	1.17	116
S21	6	TFEMA	MBP	79.4	53.9	32.9	1.64	41.3
S22	6	DEGMA	MBP	92.6	22.8	18.4	1.24	96.0
S23	6	BA	MBP	99.9	30.1	21.2	1.42	60.3
S24	6	BnMA	MBP	96.6	53.4	43.1	1.24	79.0

Polymerizations were performed according to the above general polymerization procedure using 9.35 mmol (1000 eq.) monomer, 9.35 μmol (1 eq.) catalyst, 93.5 μmol initiator, and 1.00 mL DMA. *Determined using PMMA standards.

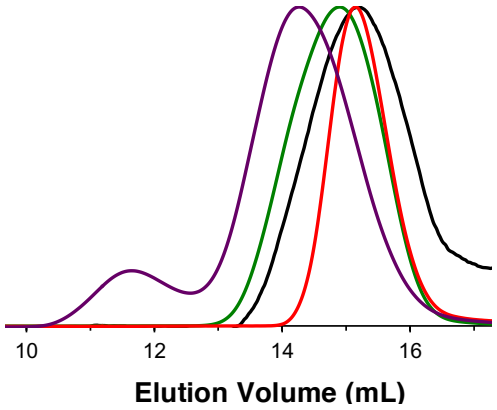

Figure 19. GPC traces of runs S13 (blue), S14 (red), S15 (purple), and S16 (orange).

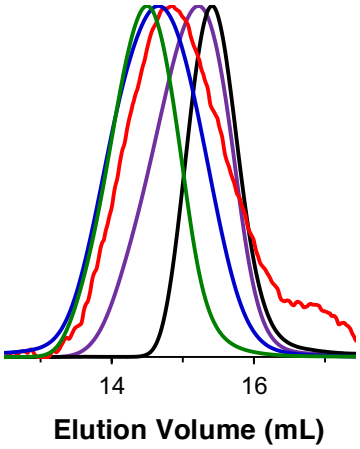

Figure 20. GPC traces of runs S20 (blue), S21 (red), S22 (purple), S23 (orange), and S24 (green).

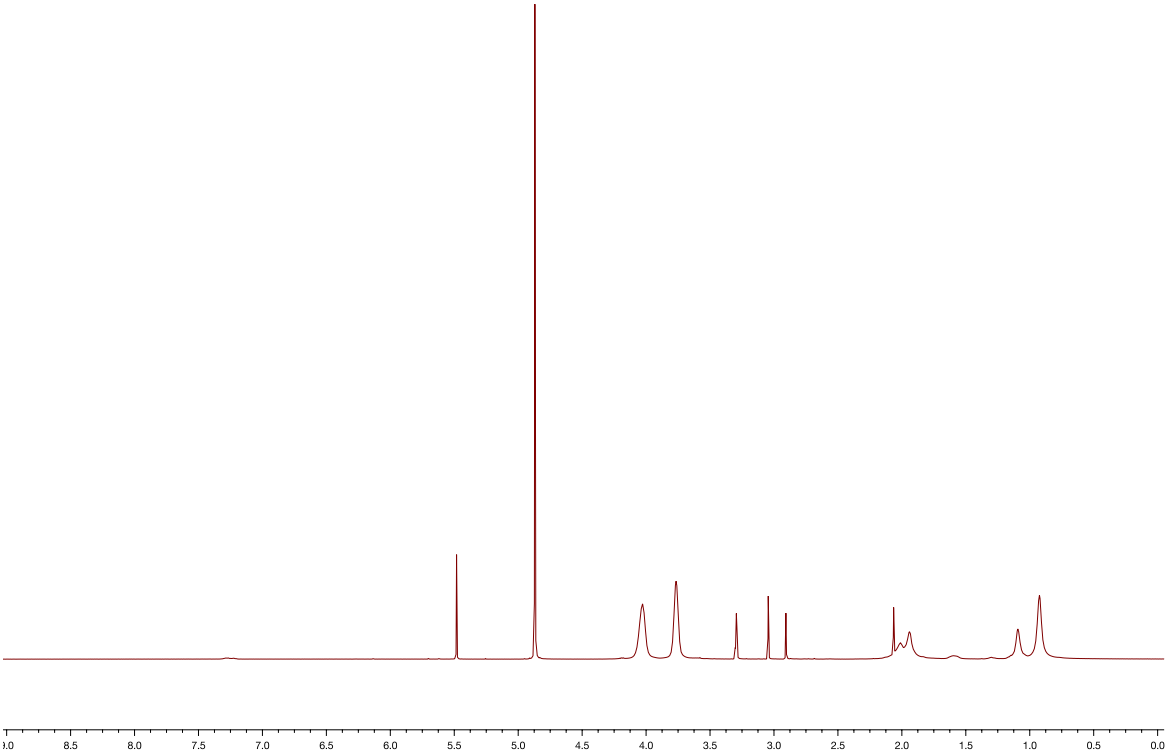

Figure 21. ^{1}H NMR spectrum of isolated poly(TMS-HEMA) made using **3** as the catalyst. It was found that the isolation method (described in the above general procedures section) resulted in loss of the TMS groups to give poly(HEMA), whereas the TMS groups remained intact in the ^{1}H NMR of the aliquot used to determine the values found in Table 4.

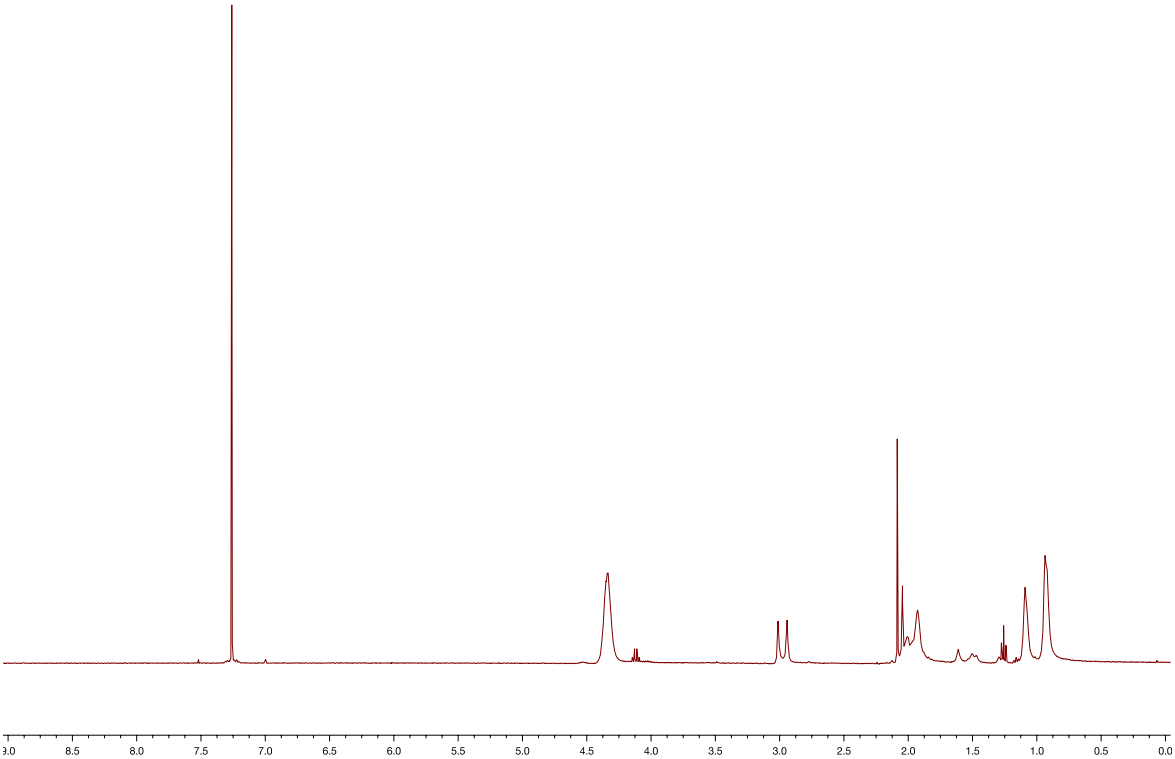

Figure 22. ^{1}H NMR spectrum of isolated poly(TFEMA) made using **3** as the catalyst.

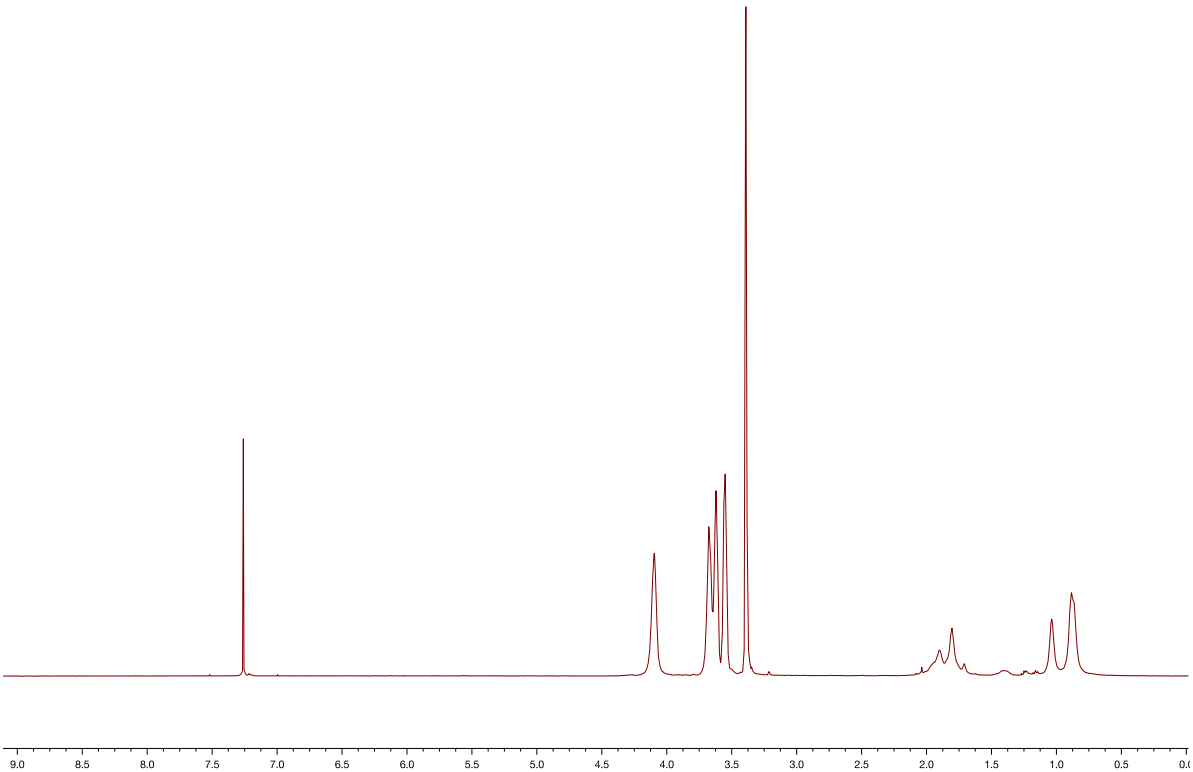

Figure 23. ^{1}H NMR spectrum of isolated poly(DEGMA) made using **3** as the catalyst.

2.7 Supporting Information

2.7.1 General Methods

All reagents were purchased from Sigma-Aldrich. Those chemicals used in polymerizations, including methyl methacrylate (MMA), benzyl methacrylate (BnMA), n-butyl acrylate (BA), styrene (St), trimethylsilylhydroxyethyl methacrylate (TMSHEMA), 2,2,2-trifluoroethyl methacrylate (TFEMA), di(ethylene glycol) methacrylate (DEGMA), vinyl acetate (VA), acrylonitrile (AN), ethyl α-bromophenylacetate (EBP), ethyl α-chlorophenylacetate (EClP), methyl α-bromoisobutyrate (MBriB), methyl bromopropionate (MBP), 2-bromopropionitrile (BrPN), dimethylformamide (DMF), and dimethylacetamide (DMA) were purified by vacuum distillation followed by three freeze-pump-thaw cycles and stored under a nitrogen atmosphere before use. 2-Dicyclohexylphosphino-2,6-diisopropoxybiphenyl (RuPhos) and Chloro-(2-Dicyclohexylphosphino-2,6-diisopropoxy-1,1-biphenyl) [2-(2-aminoethyl)phenyl] palladium(II) - methyl-t-butyl ether adduct (RuPhos precatalyst) were stored under nitrogen atmosphere. All other reagents were used as received. The visible light source was a 16-inch strip of double-density white LEDs, purchased from Creative Lighting Solutions (item no. CL-FRS1210-5M-12V-WH), wrapped inside a 400 mL beaker (Figure 24).

^{1}H, ^{13}C, and ^{19}F NMR spectroscopy were performed in a Varian INOVA 300 MHz, 400 MHz, or 500 MHz spectrometer, as specified. Chemical shifts are referenced to the internal solvent resonance and reported as parts-per-million relative to tetramethylsilane. Analysis of polymer molecular weights was performed *via* gel permeation chromatography (GPC) coupled with multi-angle light scattering (MALS), using an Agilent HPLC fitted with one guard column and two PLgel 5 μm MIXED-C gel permeation columns, a Wyatt Technology

TrEX differential refractometer, and a Wyatt Technology miniDAWN TREOS light scattering detector, using THF as the eluent at a flow rate of 1.0 mL/min. Ultraviolet-visible spectroscopy was performed on an Agilent spectrophotometer using DMF as the solvent. Emission spectroscopy was performed on a SLM 8000C spectrofluorimeter using DMF as the solvent. Samples were sparged with argon for 15 minutes prior to analysis. Cyclic voltammetry was performed with a CH Instruments electrochemical analyzer with a $Ag/AgNO_3$ (0.01 M in MeCN) reference electrode using MeCN as the solvent. Samples were sparged with argon for 5 minutes prior to analysis. ESI mass spectrometry analysis was performed at the University of Colorado Boulder mass spectrometry facility on a Waters Synapt G2 HDMS Qtof using acetonitrile as the solvent. MALDI-TOF mass spectrometry analysis was performed at the Colorado State University mass spectrometry facility on a Bruker Microflex-LRF mass spectrometer in positive ion, reflector mode using THF as the solvent.

For computational details, see Theriot, J. C. *et al. Science* **2016**, *352* (6289), 1082-1086.

2.7.2 Polymerization Procedures

General Polymerization Procedure[27]

A 20 mL vial was charged with a small stirbar and catalyst and transferred into a nitrogen-atmosphere glovebox. Solvent, monomer, and initiator were then added sequentially via pipette. The vial was then sealed, placed inside a beaker illuminated by white LED light, and stirred (Figure 24). To analyze the progress of a polymerization at a given time point, a 0.1 mL aliquot of the reaction media was removed *via* syringe and injected into a vial containing 0.7 mL $CDCl_3$ with 250 ppm butylated hydroxytoluene (BHT). This aliquot was

then analyzed by ^{1}H NMR for conversion, dried under reduced pressure, and then re-dissolved in THF for analysis of M_w and M_n by gel permeation chromatography coupled with multi-angle light scattering.

Figure 24. Photograph of the general reaction setup for polymerizations using LED irradiation.

Procedure for Polymerization Performed in Sunlight

A 20 mL vial was charged with a small stirbar and catalyst (9.35 μmol, 1.00 eq.) and transferred into a nitrogen-atmosphere glovebox. DMA (1.00 mL), MMA (1.00 mL, 9.35 mmol, 1000 eq.) and EBP (16.4 μL, 93.5 μmol, 10.0 eq.) were added sequentially *via* pipette. The vial was then removed from the glovebox, sealed with electrical tape, and placed on the roof of the University Memorial Center at the University of Colorado, Boulder from 9 AM to 4 PM on August 20th, 2015 (Figure 4).

Isolation

For copolymers specified as isolated, isolation was performed by pouring the reaction mixture into a 50-fold excess of CH_3OH, causing the polymer to precipitate. After 1 hour of stirring, the precipitate was collected *via* vacuum filtration and dried under reduced

pressure. NMR analysis of poly(DEGMA) and poly(TFEMA) was performed by pouring their respective reaction mixtures into 50 mL water, stirring for 1 hour, and collecting the precipitate *via* vacuum filtration. NMR analysis of poly(TMSHEMA) was performed by pouring the reaction mixture into 50 mL CH_2Cl_2, stirring for 1 hour, and collecting the precipitate *via* vacuum filtration.

Analysis by ^1H NMR

MMA (4.00 mL, 37.4 mmol, 250 eq.), EBP (262 μL, 1.50 mmol, 10 eq.), and **3** (10.4 mg, 0.025 mmol, 1 eq.) were dissolved in 6.00 mL DMA and reacted according to the above general polymerization procedure for 3.5 hours. At this time, the reaction was removed from the glovebox, poured into 200 mL of a mixture of 50% methanol and 50% water and stirred overnight. The resulting precipitate was then isolated by vacuum filtration and washed with excess methanol. The polymer was then re-dissolved in a minimal amount of THF and again poured into 200 mL of a mixture of 50% methanol and 50% water and stirred overnight. The product was again collected by vacuum filtration and dried under reduced pressure to reveal a white powder (M_w = 8.83 kDa, $Đ$ = 1.17).

Analysis by MALDI-TOF

MMA (1.00 mL, 9.35 mmol, 1000 eq.), EBP (16.4 μL, 93.5 μmol, 10 eq.), and **3** (4.4 mg, 9.35 μmol, 1 eq.) were dissolved in 1.00 mL DMA and reacted according to the above general polymerization procedure for 8 hours. At this time, the reaction was removed from the glovebox, poured into 50 mL methanol and stirred for 1 hour. The resulting precipitate was then isolated by vacuum filtration and washed with excess methanol. The polymer was

then re-dissolved in a minimal amount of THF and the above precipitation and isolation process repeated twice to reveal a white powder (M_w = 10.26 kDa, $Đ$ = 1.22).

Synthesis of PMMA Macroinitiator

MMA (3.00 mL, 28.1 mmol, 1000 eq.), methyl α-bromoisobutyrate (54.5 μL, 0.42 mmol, 15 eq.), and **3** (13.2 mg, 0.03 mmol, 1 eq.) were dissolved in 3.00 mL DMA and reacted according to the above general polymerization procedure for 5 hours. At this time, the reaction was removed from the glovebox, poured into 100 mL of methanol, stirred for approximately 1 hour, and the product polymer was then isolated by vacuum filtration and washed with excess methanol. The polymer was then re-dissolved in a minimal amount of THF and the process repeated a total of three times to ensure complete removal of any unreacted monomer, initiator, or catalyst (M_w = 16.1 kDa, $Đ$ = 1.12).

Synthesis of PMMA-b-PMMA

MMA (1.00 mL, 9.35 mmol, 1000 eq.), EBP (16.4 μL, 93.5 μmol, 10 eq.), and **3** (4.4 mg, 9.35 μmol, 1 eq.) were dissolved in 1.00 mL DMA and reacted according to the above general polymerization procedure for 12 hours. At this time, an aliquot was taken for analysis (conv. = 76.2%, M_w = 14.3 kDa, $Đ$ = 1.21) and an additional 1.00 mL MMA and 1.00 mL DMA were added to the reaction mixture. After an additional 6 h, the resulting polymer was isolated according to the above general polymerization procedure and analyzed (isol. yield = 72%, %, M_w = 40.7 kDa, $Đ$ = 1.16).

Synthesis of PMMA-b-PMMA with a dark resting period

MMA (1.00 mL, 9.35 mmol, 1000 eq.), EBP (16.4 µL, 93.5 µmol, 10.0 eq.), and **3** (4.4 mg, 9.35 µmol, 1.00 eq.) were dissolved in 1.00 mL DMA and reacted according to the above general polymerization procedure for 8 h. At this time, an aliquot was taken for analysis (conv. = 61.2%, M_w = 12.0 kDa, $Đ$ = 1.25). The reaction was then covered and left in the dark for 8 h. At this time, an aliquot was taken for analysis (conv. = 61.0%, M_w = 12.0 kDa, $Đ$ = 1.26) and an additional 1.00 mL MMA and 1.00 mL DMA were added to the reaction mixture and irradiated. After 8 h, the resulting polymer was isolated according to the above general polymerization procedure and analyzed (isol. yield = 70%, M_w = 40.7 kDa, $Đ$ = 1.16).

Synthesis of PMMA-b-PMMA from isolated macroinitiator

PMMA macroinitiator (*vide supra*) (100 mg, 6.25 µmol, 10.0 eq.), MMA (200 µL, 1.88 mmol, 3000 eq.), and **3** (0.3 mg, 0.63 µmol, 1.0 eq.) were dissolved in 2.00 mL DMA and reacted according to the above general polymerization procedure for 8 h. The resulting polymer was isolated according to the above general polymerization procedure and analyzed (isol. yield = 62%, M_w = 46.6 kDa, $Đ$ = 1.46).

Synthesis of PMMA-b-PBA with a dark resting period

MMA (1.00 mL, 9.35 mmol, 1000 eq.), EBP (16.4 µL, 93.5 µmol, 10.0 eq.), and **3** (4.4 mg, 9.35 µmol, 1.00 eq.) were dissolved in 1.00 mL DMA and reacted according to the above general polymerization procedure for 8 h. At this time, an aliquot was taken for analysis (conv. = 72.0%, M_w = 13.7 kDa, $Đ$ = 1.24). The reaction was then covered and left in the dark for 8 h. At this time, an aliquot was taken for analysis (conv. = 71.4%, M_w = 13.3 kDa, $Đ$ =

1.32) and an additional 1.30 mL BA and 1.00 mL DMA were added to the reaction mixture. After 8 h, the resulting polymer was isolated according to the above general polymerization procedure and analyzed (isol. yield = 27%, M_w = 84.5 kDa, $Đ$ = 1.33).

Synthesis of PMMA-b-PBA from isolated macroinitiator

PMMA macroinitiator (*vide supra*) (100 mg, 6.25 μmol, 10.0 eq.), BA (448 μL, 3.13 mmol, 5000 eq.), and 3 (0.3 mg, 0.63 μmol, 1.00 eq.) were dissolved in 2.00 mL DMA and reacted according to the above general polymerization procedure for 8 h. The resulting polymer was isolated according to the general polymerization procedure described above and analyzed (isol. yield = 47%, M_w = 70.2 kDa, $Đ$ = 1.37).

Synthesis of PMMA-b-PBnMA with a dark resting period

MMA (1.00 mL, 9.35 mmol, 1000 eq.), EBP (16.4 μL, 93.5 μmol, 10.0 eq.), and **3** (4.4 mg, 9.35 μmol, 1.00 eq.) were dissolved in 1.00 mL DMA and reacted according to the above general polymerization procedure for 8 h. At this time, an aliquot was taken for analysis (conv. = 66.0%, M_w = 11.2 kDa, $Đ$ = 1.34). The reaction was then covered and left in the dark for 8 h. At this time, an aliquot was taken for analysis (conv. = 66.0%, M_w = 11.1 kDa, $Đ$ = 1.34) and an additional 1.50 mL BnMA and 1.00 mL DMA were added to the reaction mixture. After 8 h, the resulting polymer was isolated according to the above general polymerization procedure and analyzed (isol. yield = 69%, M_w = 62.5 kDa, $Đ$ = 1.32).

Synthesis of PMMA-b-PBnMA from isolated macroinitiator

PMMA macroinitiator (*vide supra*) (100 mg, 6.25 μmol, 10.0 eq.), BnMA (529 μL, 3.13 mmol, 5000 eq.), and 3 (0.3 mg, 0.63 μmol, 1.00 eq.) were dissolved in 2.00 mL DMA and reacted according to the above general polymerization procedure for 8 h. The resulting polymer was isolated according to the above general polymerization procedure and analyzed (isol. yield = 79%, M_w = 158.8 kDa, $Đ$ = 1.63).

2.7.3 Catalyst Synthesis

5,10-dihydrophenazine

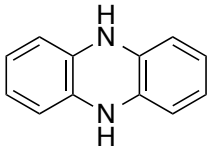

5,10-dihydrophenazine was synthesized according to a modified literature procedure.[35] A 500 mL round bottom flask was charged with a mixture of H_2O (200 mL), EtOH (50 mL), and a stir bar. The mixture was sparged with nitrogen for 30 minutes and then phenazine (2.00 g, 11.1 mmol, 1.00 eq.) and $Na_2S_2O_4$ (23.3 g, 111 mmol, 10.0 eq.) were then added. This mixture was subsequently heated at reflux under nitrogen atmosphere for 3h. After cooling to RT, the product was isolated as a precipitate via cannula filtration, washed with excess deoxygenated H_2O, and dried under reduced pressure to yield a light green powder (1.35 g, 7.42 mmol, 67%). The product was stored under nitrogen until further use.

*5,10-di(4-methoxyphenyl)-5,10-dihydrophenazine (**1**)*

1 was synthesized using a modified literature procedure.[29] An oven-dried vacuum tube was charged with 5,10-dihydrophenazine (1.00 g, 5.50 mmol, 1.00 eq.), NaOtBu (2.11 g, 22.00 mmol, 4.00 eq.), RuPhos (103 mg, 0.22 mmol, 0.04 eq.), RuPhos precatalyst (180 mg, 0.22 mmol, 0.04 eq.), 4-bromoanisole (4.05 g, 22.0 mmol, 4.00 eq), and 8.00 mL dioxane. This flask was sealed under nitrogen and heated at 110 °C for 10 h. After cooling to room temperature, 200 mL CH_2Cl_2 was added to the reaction mixture and this was extracted three times with 200 mL H_2O. The organic layer was dried with $MgSO_4$, filtered, and the volatiles were removed under reduced pressure to reveal a brown solid. Purification by column chromatography (1:3 mixture of CH_2Cl_2 and hexanes) afforded the product **1** as a light yellow solid (1.00 g, 2.53 mmol, 46%). ^{1}H NMR (C_6D_6, 500 MHz): δ 7.11 – 7.02 (m, 4H), 6.78 – 6.67 (m, 4H), 6.33 (dd, J = 5.9, 3.4 Hz, 4H), 5.89 (dd, J = 5.8, 3.5 Hz, 4H), 3.23 (s, 6H). ^{13}C NMR (C_6D_6, 100 MHz): δ 54.53, 112.60, 116.33, 120.94, 127.52, 132.18, 137.24, 159.05. HRMS (ESI): calc'd for M+ $C_{26}H_{22}N_2O_2$, 394.1681; found 394.1675. UV/Vis: λ_{max} 373 nm.

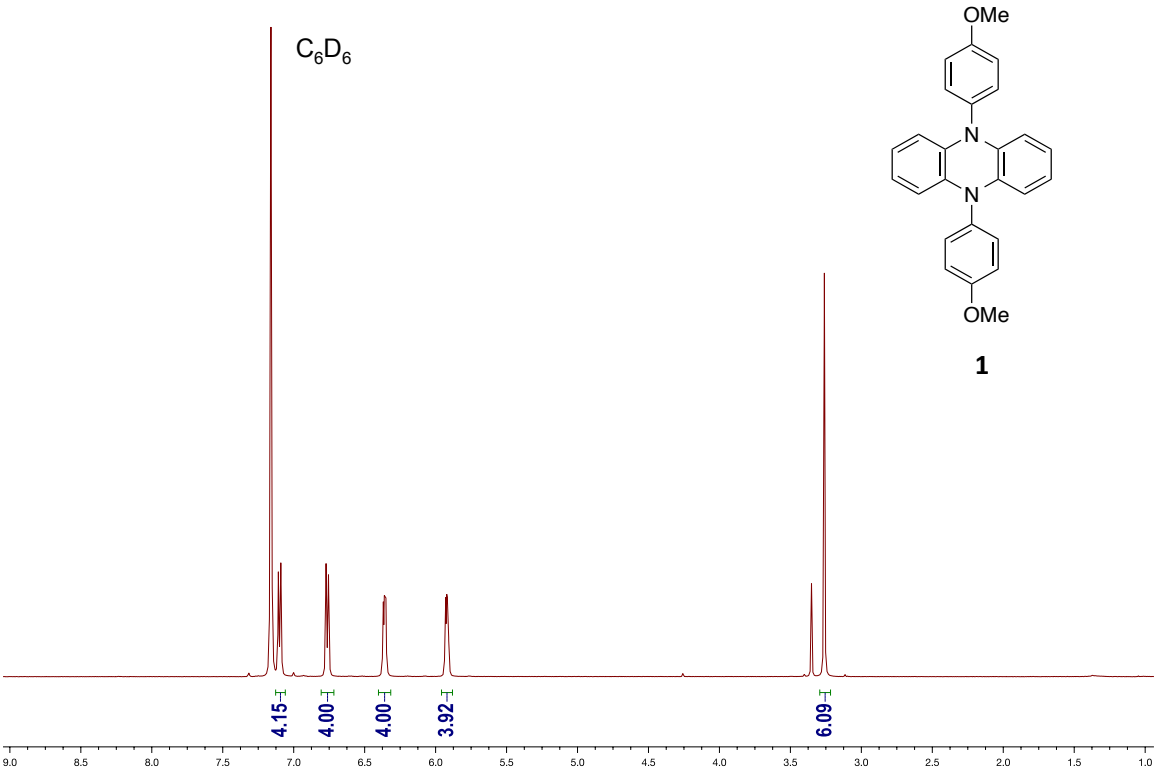

Figure 25. ^{1}H NMR spectrum of **1**.

*5,10-diphenyl-5,10-dihydrophenazine (**2**)*

2 was synthesized using a modified literature procedure.[29] An oven-dried vacuum tube was charged with 5,10-dihydrophenazine (1.00 g, 5.50 mmol, 1.00 eq.), NaOtBu (2.11 g, 22.00 mmol, 4.00 eq.), RuPhos (103 mg, 0.22 mmol, 0.04 eq.), RuPhos precatalyst (180 mg, 0.22 mmol, 0.04 eq.), iodobenzene (4.49 g, 22.0 mmol, 4.00 eq), and 8.00 mL dioxane. This flask was sealed under nitrogen and heated at 110 °C for 10 h. After cooling to room temperature, 200 mL CH_2Cl_2 was added to the reaction mixture and this was extracted three times with 200 mL H_2O. The organic layer was dried with $MgSO_4$, filtered, and the volatiles were removed under reduced pressure to reveal a red-brown solid. Purification by column chromatography (1:3 mixture of CH_2Cl_2 and hexanes) afforded the product **2** as a light yellow

solid (1.27 g, 3.80 mmol, 69%). Further purification by layering a solution of the product in CH_2Cl_2 with hexanes gave 2 as yellow needles. ^1H NMR (C_6D_6, 400 MHz): δ 7.16 (could not be resolved from NMR solvent peak), 7.07 – 7.00 (m, 2H), 6.31 – 6.25 (m, 4H), 5.85 – 5.79 (m, 4H). ^{13}C NMR (C_6D_6, 100 MHz): δ 112.69, 121.03, 127.69, 131.03, 131.22, 136.75, 140.38. HRMS (ESI): calc'd for M+ $C_{24}H_{18}N_2$, 334.1470; found 334.1482. UV/Vis: λ_{max} 370 nm.

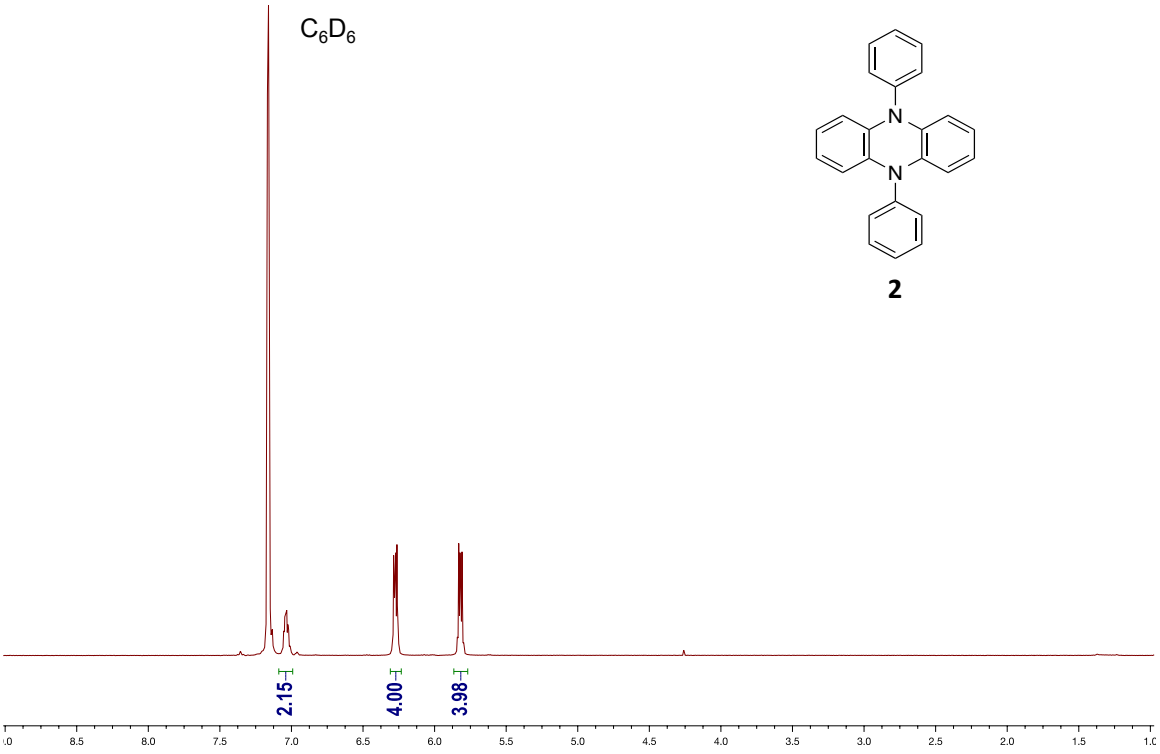

Figure 26. ^1H NMR spectrum of **2**.

*5,10-di(4-trifluoromethylphenyl)-5,10-dihydrophenazine (**3**)*

3 was synthesized using a modified literature procedure.[29] An oven-dried vacuum tube was charged with 5,10-dihydrophenazine (1.01 mg, 5.55 mmol, 1.00 eq.), NaOtBu (2.13 g, 22.22 mmol, 4.00 eq.), RuPhos (102 mg, 0.22 mmol, 0.04 eq.), RuPhos precatalyst (180 mg, 0.22 mmol, 0.04 eq.), 4-bromobenzotrifluoride (5.00 g, 22.22 mmol, 4.00 eq), and 8.00 mL

dioxane. This flask was sealed under nitrogen and heated at 110 °C for 10 h. After cooling to room temperature, 200 mL CH_2Cl_2 and 200 mL H_2O was added to the reaction flask, causing the product to precipitate. Filtration and washing with CH_2Cl_2 afforded **3** as a light yellow powder (1.65 g, 3.52 mmol, 63%). Further purification by layering a solution of the product in CH_2Cl_2 with hexanes gave **3** as light yellow needles. ^{1}H NMR (C_6D_6, 400 MHz) δ 7.25 (d, J = 8.1 Hz, 4H), 6.90 (d, J = 8.0 Hz, 4H), 6.36 – 6.30 (m, 4H), 5.69 - 5.63 (m, 4H). ^{13}C NMR (C_6D_6, 100 MHz): δ 113.26, 121.65, 128.17,127.52, 128.21, 131.32, 135.91, 143.54. ^{19}F NMR (C_6D_6, 376 MHz): δ -62.23. HRMS (ESI): calc'd for M+ $C_{26}H_{16}F_6N_2$, 470.1218; found 470.1216. UV/Vis: λ_{max} 367 nm.

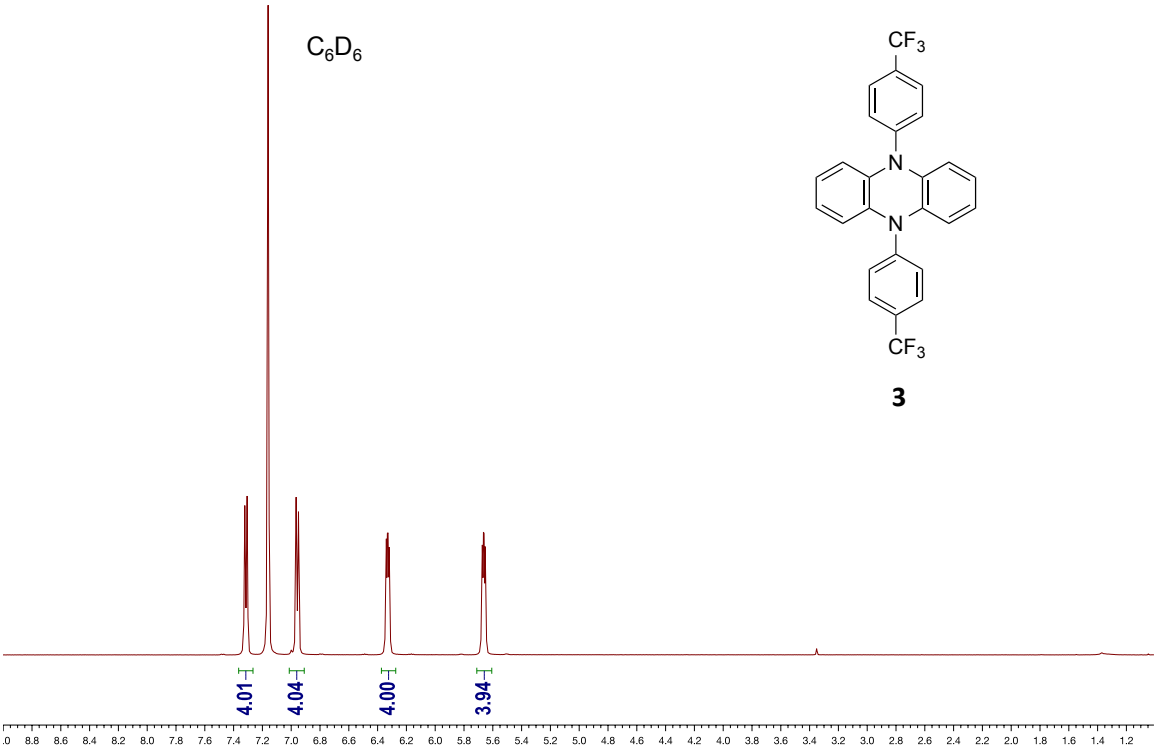

Figure 27. ^{1}H NMR spectrum of **3**.

*5,10-di(4-cyanophenyl)-5,10-dihydrophenazine (**4**)*

4 was synthesized using a modified literature procedure.[29] An oven-dried vacuum tube was charged with 5,10-dihydrophenazine (500 mg, 2.75 mmol, 1.00 eq.), NaOtBu (1.06 g, 11.00 mmol, 4.00 eq.), RuPhos (51 mg, 0.11 mmol, 0.04 eq.), RuPhos precatalyst(90 mg, 0.11 mmol, 0.04 eq.), 4-bromobenzonitrile (2.00 g, 11.0 mmol, 4.00 eq), and 3.00 mL dioxane. This flask was sealed under nitrogen and heated at 110 °C for 10 h. After cooling to room temperature, 200 mL CH_2Cl_2 was added to the reaction mixture and this was extracted three times with 200 mL H_2O. The organic layer was dried with $MgSO_4$, filtered, and the volatiles were removed under reduced pressure to reveal a brown solid. Purification by column chromatography (1:1 mixture of CH_2Cl_2 and hexanes) produced the product **4** as a brown powder (718 mg, 1.87 mmol, 68%). Further purification by layering a solution of the product in CH_2Cl_2 with hexanes gave **4** as dark gold needles. ^{1}H NMR (C_6D_6, 400 MHz) δ 6.98 – 6.89 (m, 4H), 6.73 – 6.64 (m, 4H), 6.42 - 6.36 (m, 4H), 5.72 - 5.66 (m, 4H). ^{13}C NMR (C_6D_6, 100 MHz): δ 111.56, 114.16, 117.82, 121.96, 130.35, 134.52, 135.69, 144.12. HRMS (ESI): calc'd for M+ $C_{26}H_{16}N_4$, 384.1375; found 384.1370. UV/Vis: λ_{max} 322 nm.

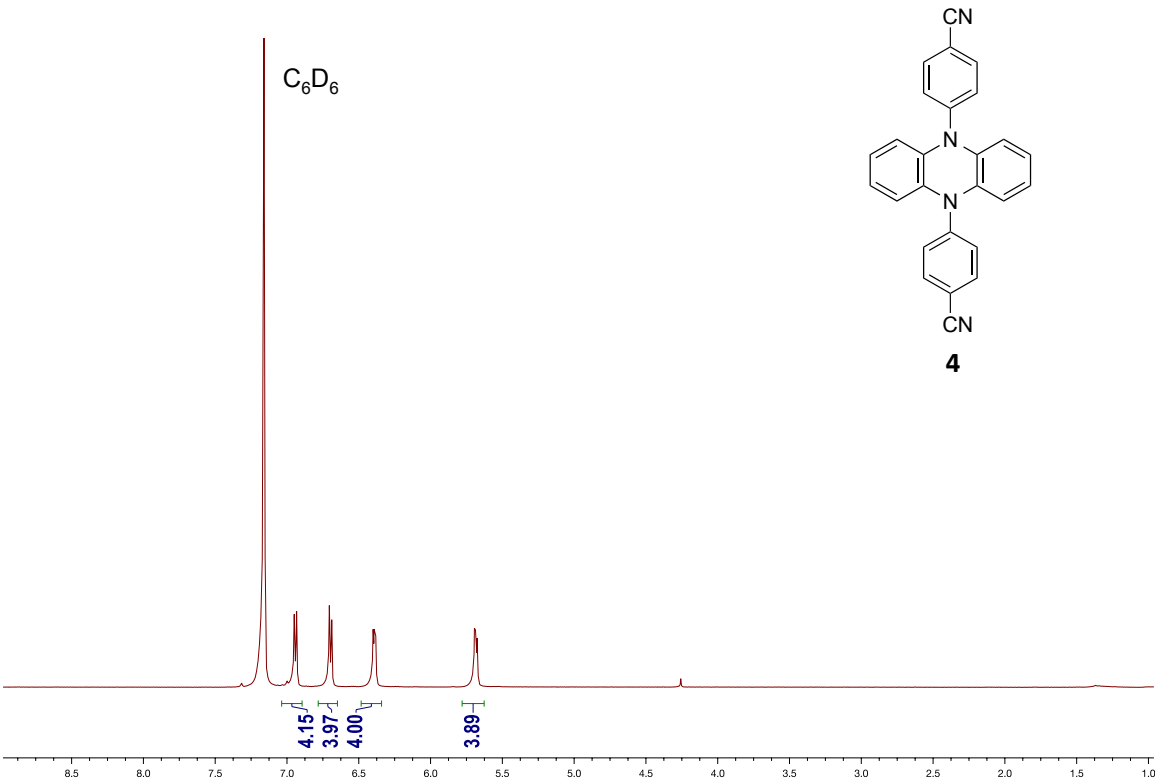

Figure 28. ^{1}H NMR spectrum of **4**.

*5,10-di(2-naphthyl)-5,10-dihydrophenazine (**5**)*

See Theriot, J. C. *et al. Science* **2016**, *352* (6289), 1082-1086.

*5,10-di(1-naphthyl)-5,10-dihydrophenazine (**6**)*

See Theriot, J. C. *et al. Science* **2016**, *352* (6289), 1082-1086.

2.7.4 Photophysical Characterization of Catalysts

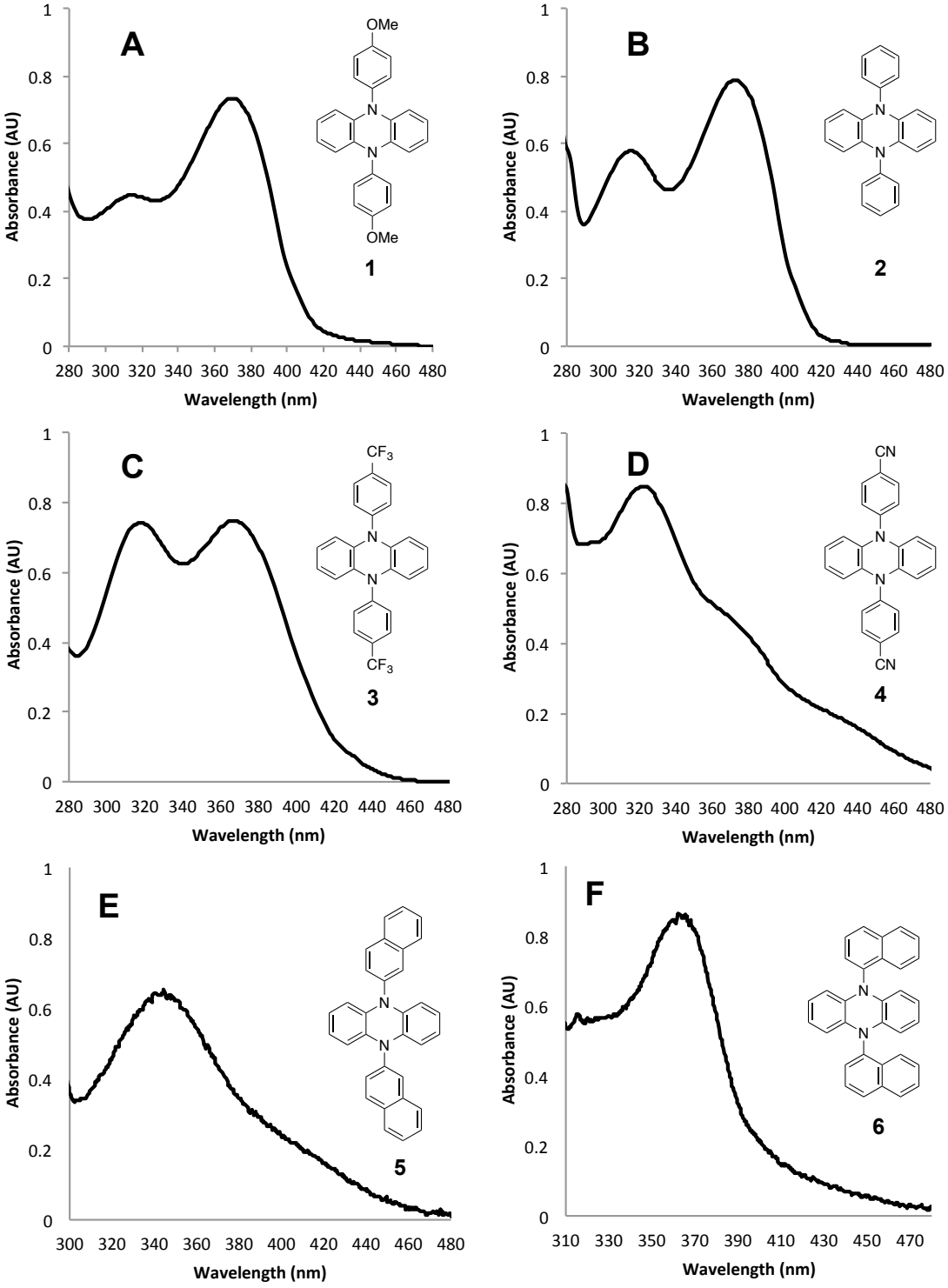

Figure 29. UV-Vis spectra of catalysts **1** (A), **2** (B), **3** (C), **4** (D), **5** (E), and **6** (F) at 0.15 mM in DMF.

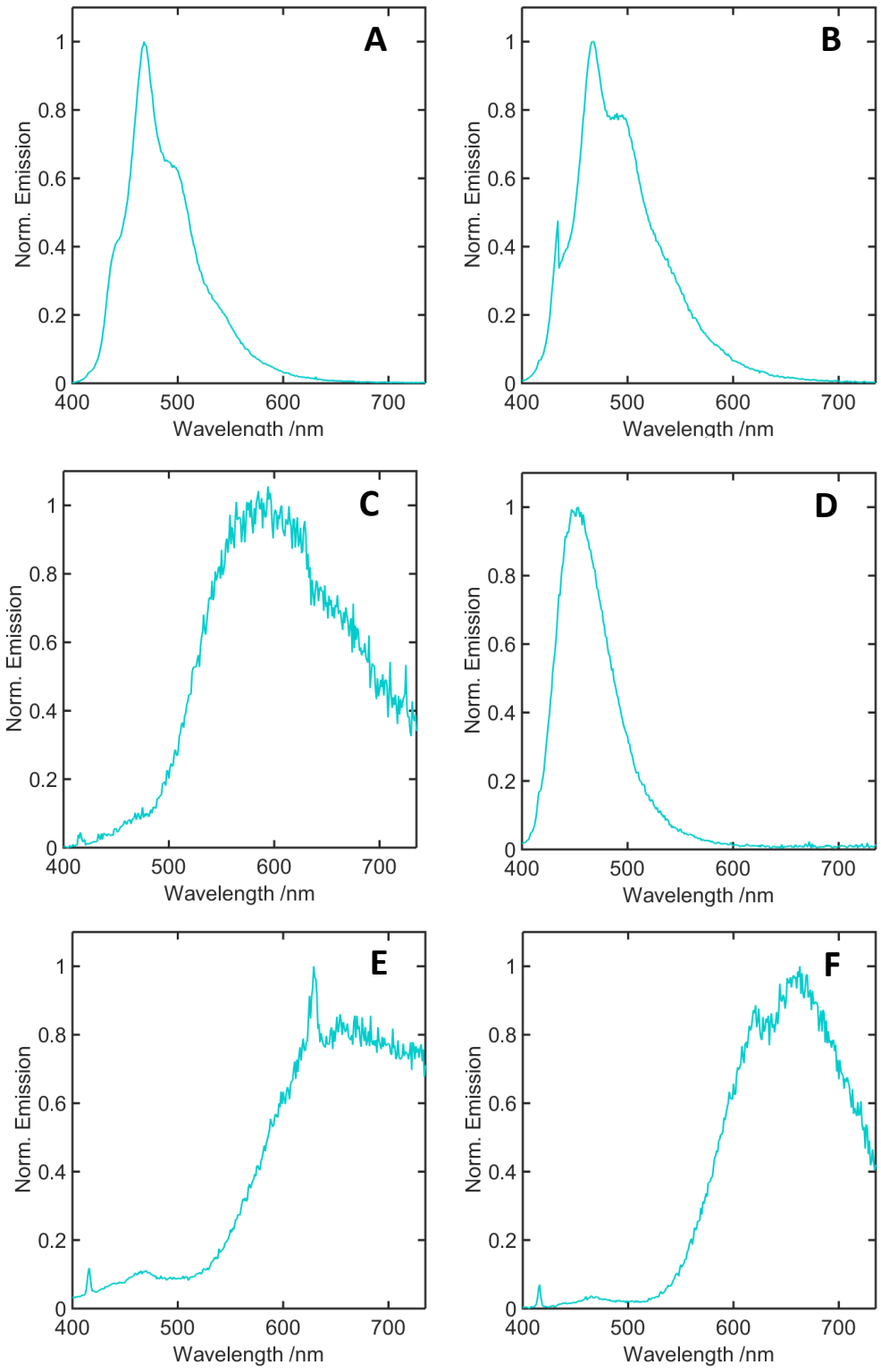

Figure 30. Emission spectra of catalysts **1** (A), **2** (B), **3** (C), **4** (D), **5** (E), and **6** (F) in DMF.

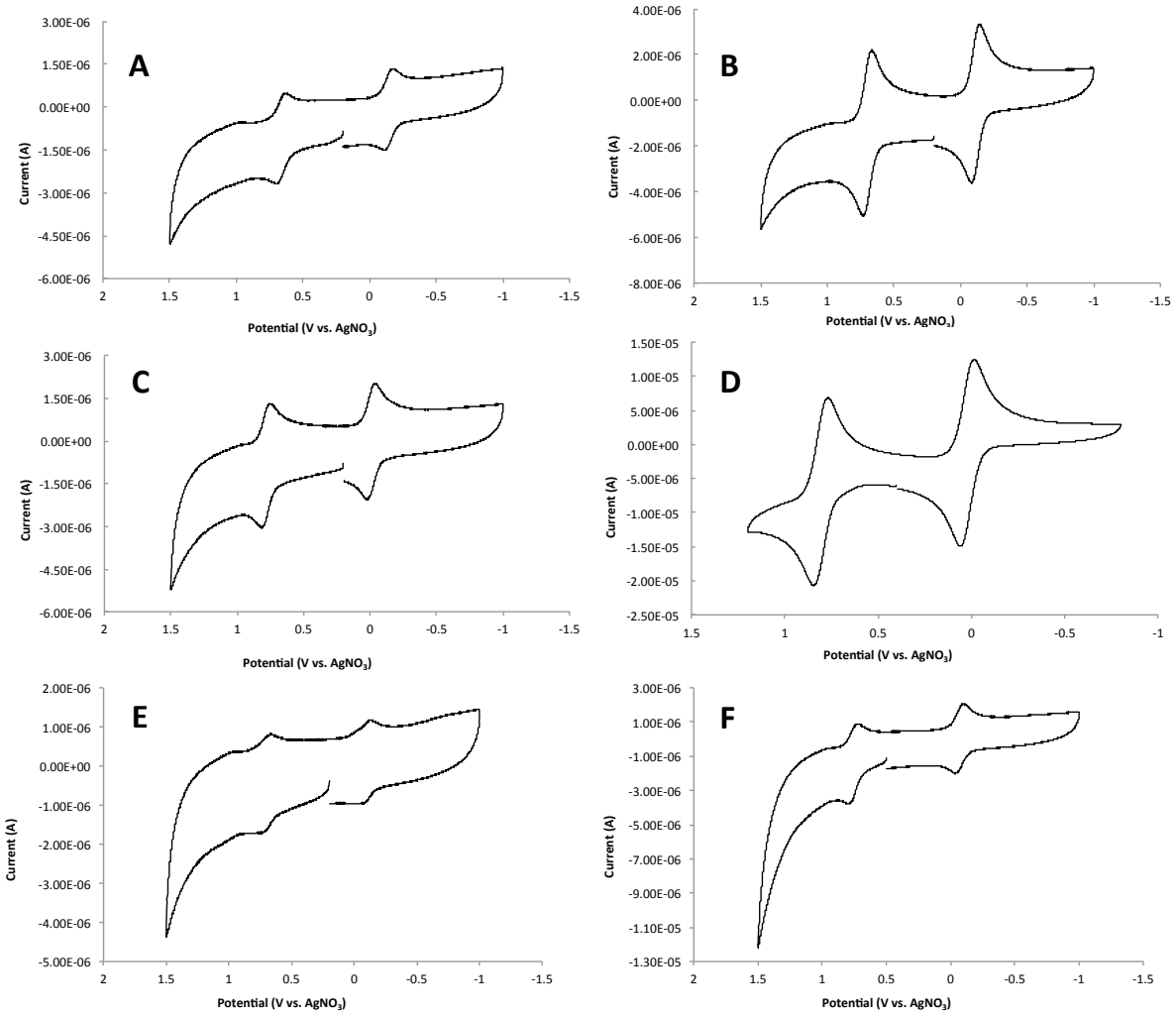

Figure 31. Cyclic voltammograms (*vs.* $Ag/AgNO_3$) of catalysts **1** (A), **2** (B), **3** (C), **4** (D), **5** (E), and **6** (F) in MeCN.

Table 5. Calculation of excited state reduction potentials of photocatalysts **1** – **6**.

PC	abs λ_{max} (nm)	$\varepsilon_{\lambda max}$ [α]	em λ_{max} (nm)	E(em λ_{max}) (V)	$E_{1/2}$ [β]	E* (*calc'd*) [β]	E*+ (*theo.*) [β]
1	373	5200	467	2.66	0.16	-2.50	-2.36
2	370	4900	467	2.66	0.19	-2.47	-2.34
3	367	4700	594	2.09	0.29	-1.80	-2.24
4	322	5600	453	2.74	0.32	-2.42	-2.06
5	340	6300	654	1.90	0.19	-1.71	-2.20
6	366	5500	663	1.87	0.23	-1.64	-2.12

[α] L/mol*cm [β] V *vs.* SCE

CHAPTER 3

CATALYST DESIGN FOR O-ATRP

3.1 Introduction[†]

Following the introduction of *N*,*N*-diaryl dihydrophenazines as PCs for O-ATRP, there existed great motivation to learn more about this class of catalysts, especially with respect to rational catalyst design for O-ATRP. Of particular interest was the observation that although all of the PCs tested in Chapter 2 possessed very strong excited state reduction potentials and stable radical cations, that alone could not determine if a particular dihydrophenazine would be a good candidate for an O-ATRP PC. It was in fact the observation of spatially-separated SOMOs in the photoexcited state which was the strongest indicator of PC performance. This observation made it clear that in order to continue to improve PC design for O-ATRP, it would be necessary to gain additional understanding about PC behavior within the O-ATRP catalytic cycle.

Figure 3C depicts the proposed mechanism of O-ATRP. The cycle begins with photoexcitation of a ground state PC into a singlet excited state (^{1}PC*) by absorption of UV or visible light. After photoexcitation, ^{1}PC* can react from the singlet manifold or undergo intersystem crossing (ISC) to form a triplet excited state (3PC*). ^{1}PC* is more reducing than

[†] This section is extracted from Theriot, J.C. *et al. Macromol. Rapid Commun*. **2017**, 1700040. See *Contributor Attributions* for additional information.

^{3}PC* but shorter-lived (lifetime, τ, typically in the nanoseconds), whereas ^{3}PC* is often much longer-lived (τ often in the microseconds) and are usually invoked as the reactive excited state species participating in photoredox reactions.[38] Potentially, both ^{1}PC* and ^{3}PC* could participate in the activation step, a reduction of the alkyl halide bond of a polymer chain to liberate a carbon-centered radical capable of propagation. Ideally, the polymer chains are extended by a minimal number of monomer units before being deactivated by the radical cation form of the PC ($PC^{\bullet+}$) to minimize termination reactions. Deactivation returns the polymer chain to a dormant state and the PC to a ground state, completing the photoredox-mediated O-ATRP cycle.

By considering each step involved in the O-ATRP mechanism, the chemical and photophysical properties that are important for PC performance can be determined. First, photoexcitation can be performed with a variety of wavelengths of light. However, photoexcitation using UV light can lead to side reactions which complicate the synthesis of well-defined polymers.[39] It is preferable, then, for a PC to absorb in the visible, ideally possessing a wavelength of maximum absorbance (λ_{max}) in the visible region with a high molar extinction coefficient (ε). After photoexcitation, the PC should efficiently cross over to the triplet excited state, indicated by a high rate of intersystem crossing (ISC). The PC must possess a sufficiently long excited state lifetime (τ) and be sufficiently reducing in the excited state to execute the electron transfer reaction required for polymer activation, approximately - 0.8 V *vs*. SCE for the alkyl bromides commonly employed in ATRP.[40]

The thermodynamic feasibility of activation and deactivation can be evaluated from the excited state reduction potential of PC* [$E^{0*} = E^0(PC^{\bullet+}/PC^*)$] and oxidation potential of $PC^{\bullet+}$ [$E^0_{ox} = E^0(PC^{\bullet+}/PC)$]. Of the PC parameters discussed so far, the requirement of a strong

E^0* is arguably the most stringent and greatly narrows the field of potential candidates.[41] Although more remains to be learned about the precise mechanism of deactivation, it has been proposed that a termolecular reaction involving $PC^{\bullet+}$, X^-, and the propagating radical species is the most favorable pathway for deactivation.[42] However, in another study, it was argued that the termolecular pathway is most likely entropically improbable given the low concentrations of the species involved. Instead, it was suggested that ion pairing between $PC^{\bullet+}$and X^- to form a $PC^{\bullet+}X^-$ complex reduces deactivation to a more feasible bimolecular reaction, and indeed the ion complexation strength between $PC^{\bullet+}$ and X^- was shown to be an important factor in polymerization outcomes.[43]

Analysis of the mechanism leads to a list of the chemical and photophysical properties that should be considered in the design of a PC for O-ATRP. It should not be a surprise that this list bears a striking resemblance to a similar list proposed for metal photoredox catalysts.[38] However, this list has some modifications to address the specific needs of photoredox-mediated O-ATRP.

1. Strong visible light absorption (λ_{max} close to visible and high ε)
2. High rate of ISC / high triplet QY
3. Sufficiently long τ for ET to occur
4. $E^0(PC^{\bullet+}/PC^*) < -0.8$ V *vs*. SCE
5. Stable $PC^{\bullet+}$ with $E^0(PC^{\bullet+}/PC) > -0.8$ V *vs*. SCE

This chapter will address different aspects of PC design for O-ATRP, including both those which appear in this list (that is, those that arise in a straightforward manner from the mechanism) and those which do not (and instead were empirically determined to improve polymerization outcomes), such as intramolecular charge transfer. The chapter ends with a

perspective-style summary of what has been learned so far about catalyst design within the now rapidly-expanding field of O-ATRP.

3.2 Intramolecular Charge Transfer and Solvatochromism[‡]

In Chapter 2, it was demonstrated that *N,N*-diaryl dihydrophenazines possessing computationally-predicted singly occupied molecular orbitals (SOMOs) which are spatially separated (i.e. with the lower-energy SOMO on the core of the molecule and the higher-energy SOMO on the *N*-aryl substituent) gave superior performance as PCs for O-ATRP.[40] This phenomenon was also observed for similar *N*-aryl phenoxazines PCs.[44] These spatially-separated SOMOs represent intramolecular charge transfer (CT).

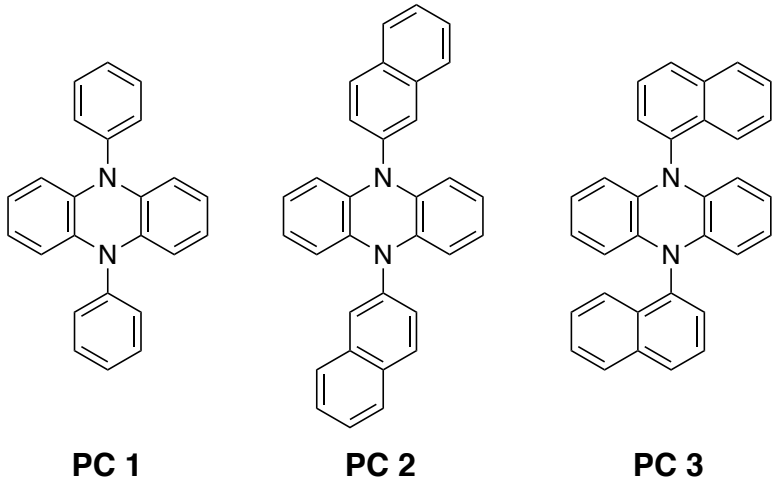

Figure 32. Structure of PCs **1** – **3** used in the study of intramolecular CT and solvatochromism.

Evidence for the existence of CT can be found in the absorption and emission spectra of PCs **1** – **3** (Figures 32 and 33). For PC **1**, which does not display intramolecular CT, the

[‡] Portions of this section have been adapted from Lim, C.-H. *et al. J. Am. Chem. Soc.* **2016**, *139* (1), 348-355. See *Contributor Attributions* for additional information.

Stokes shift (the difference in energies between absorption and emission resulting from vibrational relaxation) is 98 nm. Conversely, PCs **2** and **3** display much larger Stokes shifts, 311 nm for PC **2** and 301 nm for PC **3**. This difference is a result of a LUMO of much lower energy for PCs **2** and **3**. PCs **2** and **3** also display a broad and featureless emission spectrum (compared to the narrow emission spectrum of PC 1), another sign of a CT excited state.

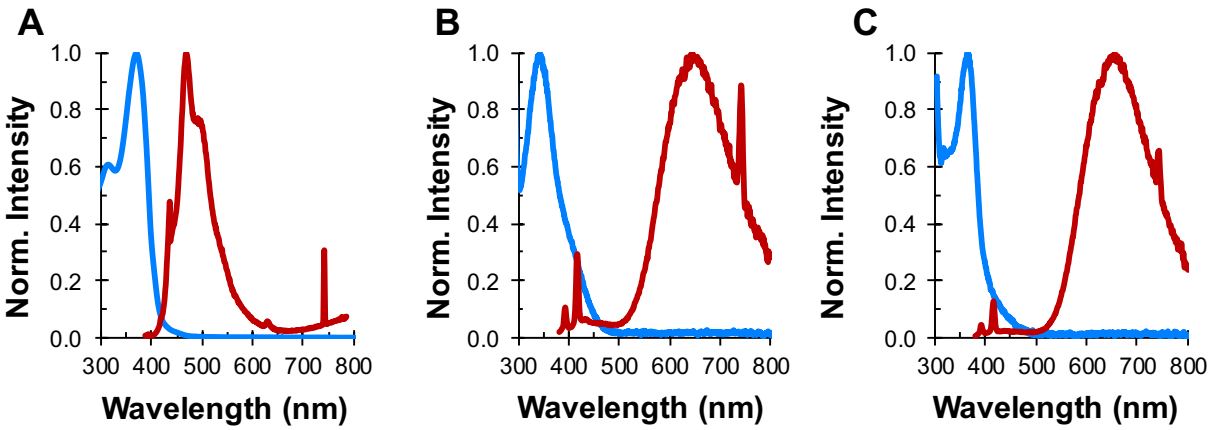

Figure 33. Overlaid absorption (blue) and emission (red) spectra of PCs **1** (A), **2** (B) and **3** (C) in DMAc.

Because CT states are highly polar, we reasoned that solvent polarity would have a differential effect on the emission profiles of the two types of PCs. Increased solvent polarity should stabilize the LUMO for PCs 2 and 3, resulting in red-shifted emission. However, a change in solvent polarity should have little effect on the LUMO of PC 1, and therefore there should be no change in the wavelength of emission. To test this, we measured the emission spectra of PCs 1 – **3** in solvents of varying polarity (Figure 34). While no change was seen in the emission wavelength of PC **1**, it was found that PCs 2 and 3 are highly solvatochromic, another hallmark of intramolecular CT.

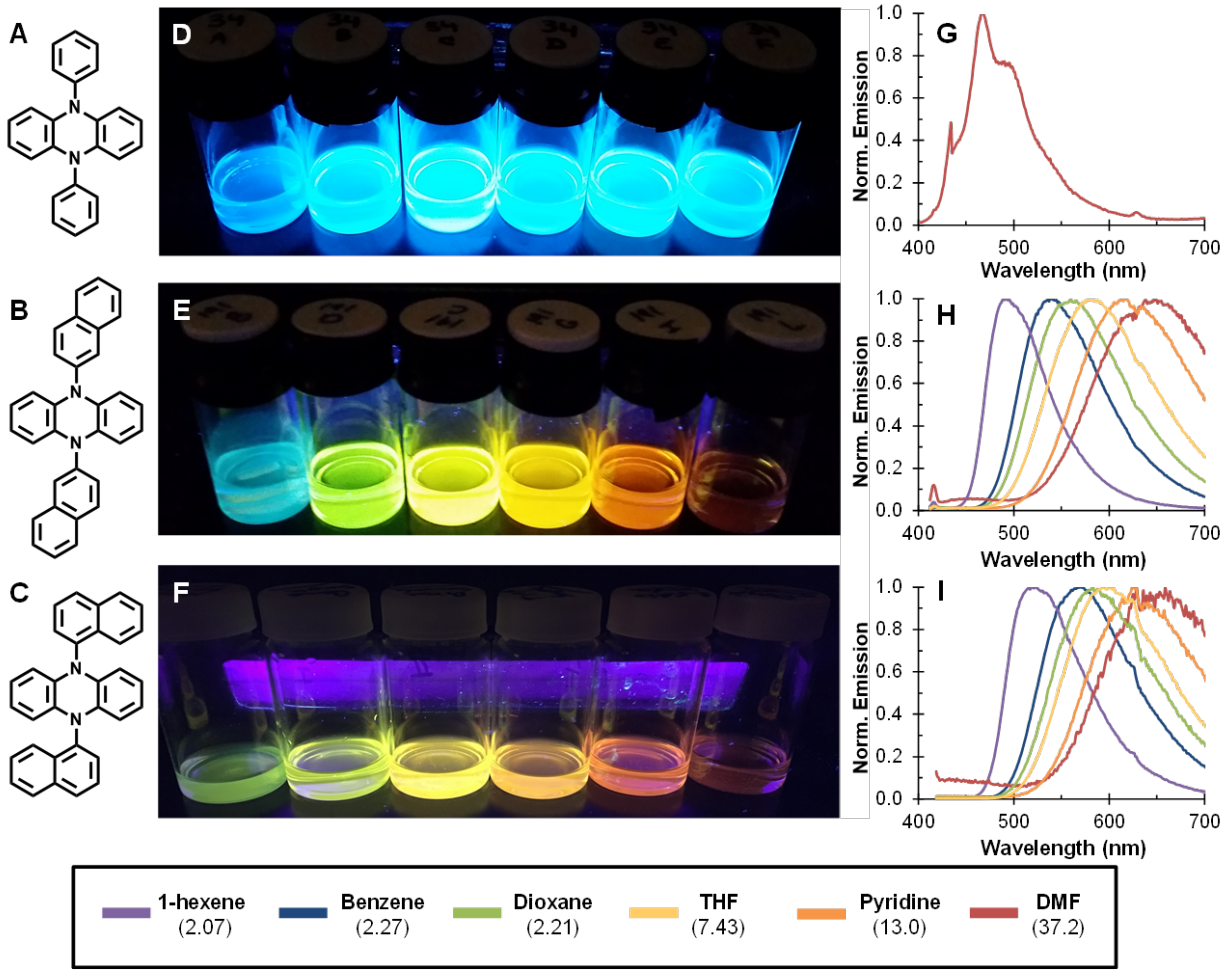

Figure 34. Structures of diaryl dihydrophenazines with LE (**A**) or CT (**B** and **C**) natures. Photographs of solutions of the diaryl dihydrophenazines upon excitation with 365 nm light (**D**, **E**, and **F**) and their emission spectra (**G**, **H**, and **I**) in solvents with varying polarity. For **D** - **F**, the order of solvents from left to right (dielectric constant, ε): 1-hexene (ε = 2.07), benzene (ε = 2.27), dioxane (ε = 2.21), THF (ε = 7.43), pyridine (ε = 13.0), and DMF (ε = 37.2).

The sensitivity of the maximum wavelength of emission to changes in solvent polarity can be related to the change in dipole moment between the ground and excited state using the Lippert equation[45]:

$$\Delta v = \frac{2}{hc}\frac{\Delta\mu^2}{a^3}\Delta f + c$$

where Δv is the observed Stokes shift in a given solvent, h is Planck's constant, c is the speed of light, $\Delta\mu$ is the change in dipole upon excitation, a is the radius of the solvent sphere surrounding the molecule, Δf is the solvent orientation polarizability, a value derived from both the solvent's dielectric constant and refractive index, and c is a constant. A plot of Δv versus Δf, referred to as a Lippert-Mataga plot, gives a slope from which $\Delta\mu$ can be extracted (Figures 40 and 41). To estimate a, a spherical approximation, where a equals half the length of the molecule, was used for **3**. An ellipsoidal approximation, where a equals 0.4 times the length of the molecule, was used for the more elongated **2**. This gave a value for $\Delta\mu$ of 16.0 D for **3** and 22.1 D for **2**, which is in good agreement with the computationally-derived values of 17.2 D and 20.8 D, respectively.

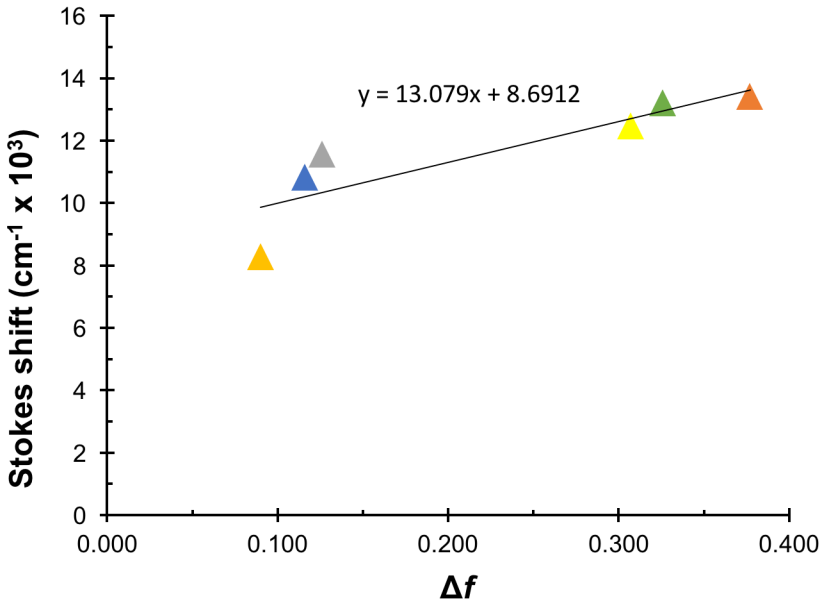

Figure 35. The Lippert-Mataga plot for PC **2**, where the stokes shift (Δv) is plotted as a function of solvent orientation polarizability (Δf) for 1-hexene (orange), benzene (blue), dioxane (gray), THF (yellow), pyridine (green), and DMF (red).

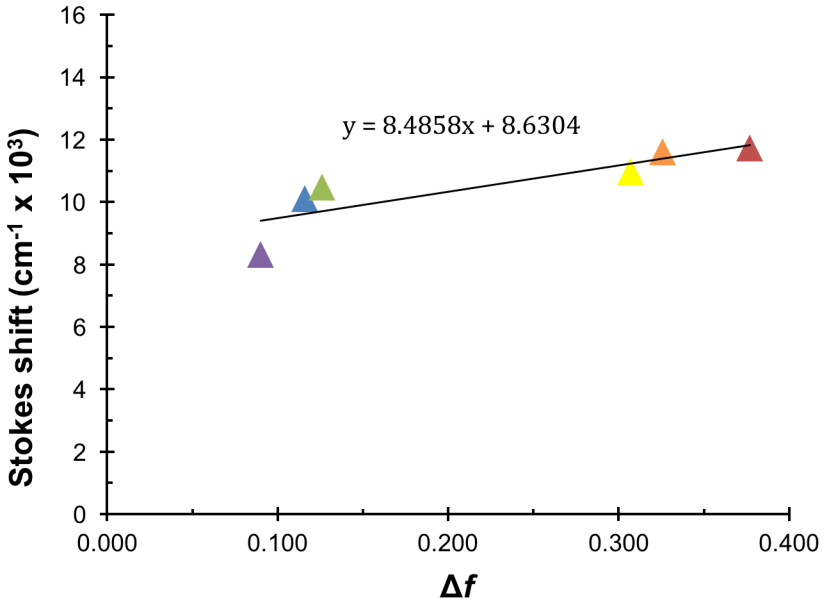

Figure 36. The Lippert-Mataga plot for PC **3**, where the stokes shift ($\Delta\nu$) is plotted as a function of solvent orientation polarizability (Δf) for 1-hexene (purple), benzene (blue), dioxane (green), THF (yellow), pyridine (orange), and DMF (red).

3.3 Solvent Effects on O-ATRP[§]

3.3.1 Study of Solvent Effects

With the identification of intramolecular CT as a crucial component of the success of *N,N*-diaryl dihydrophenazine PCs, and the observation of their strong solvatochromic behavior, the question arose of the potential impact of solvent polarity on O-ATRP. PCs **1** – **9** (Figure 37) were synthesized. Examination of their absorption and emission profiles (Figure 38) allowed for the identification of PCs **1** – **4** as non-CT and of PCs **5** – **9** as displaying CT. First, all 9 PCs were tested in the polymerization of MMA in a single solvent, DMAc (Table 6). PCs **1** – **4**, the non-CT PCs, all give significantly higher $Đ$ than CT PCs **5** – **9**. These results solidify our assertion that access to intramolecular CT is required for efficient O-ATRP.

[§] Data presented in this section also appears in Ryan, M.D. *et al. J. Polym. Sci. A* **2017**, *55* (18), 3017-3027. See *Contributor Attributions* for additional information.

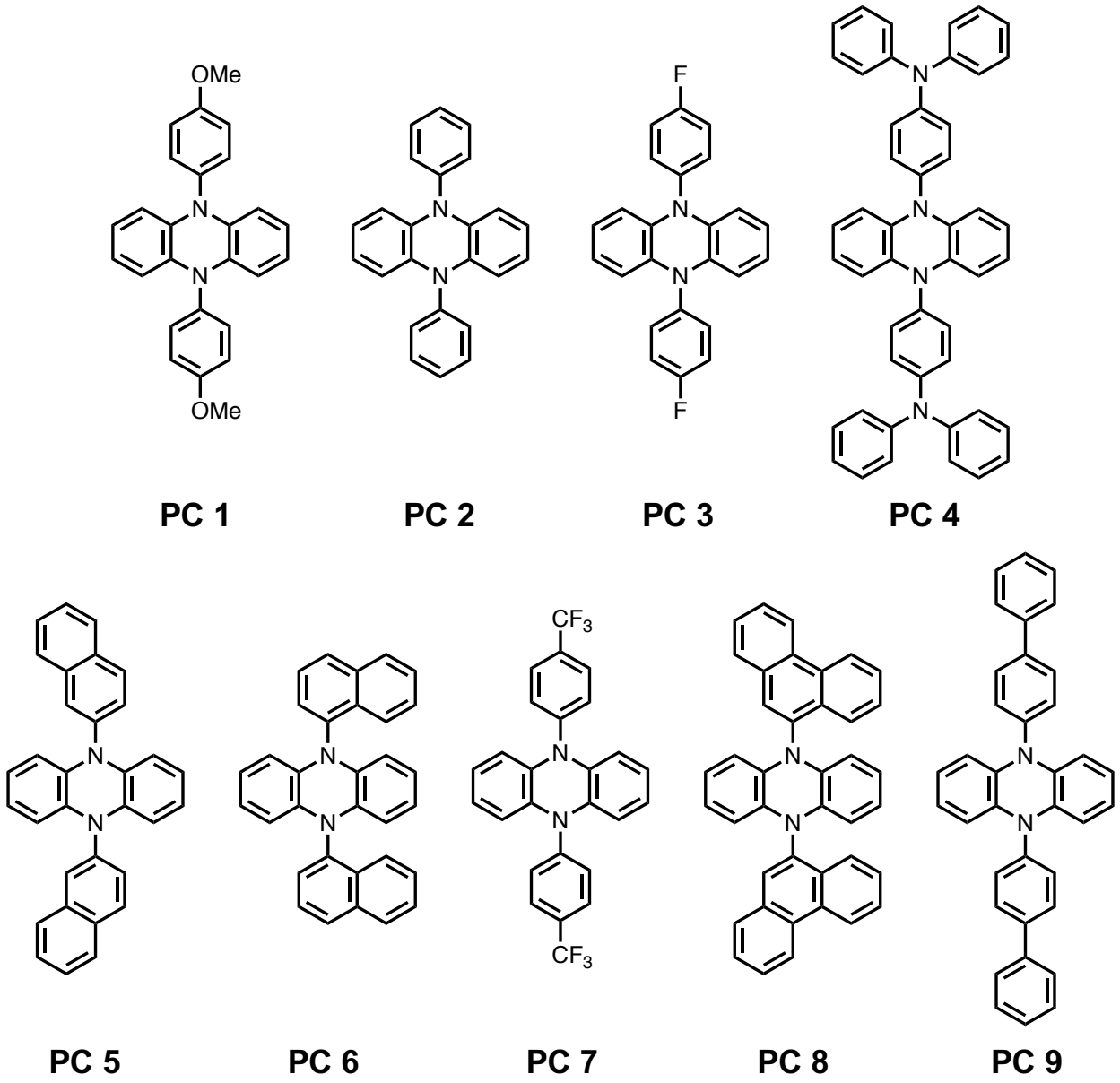

Figure 37. The PCs used in this study of solvent effects on O-ATRP.

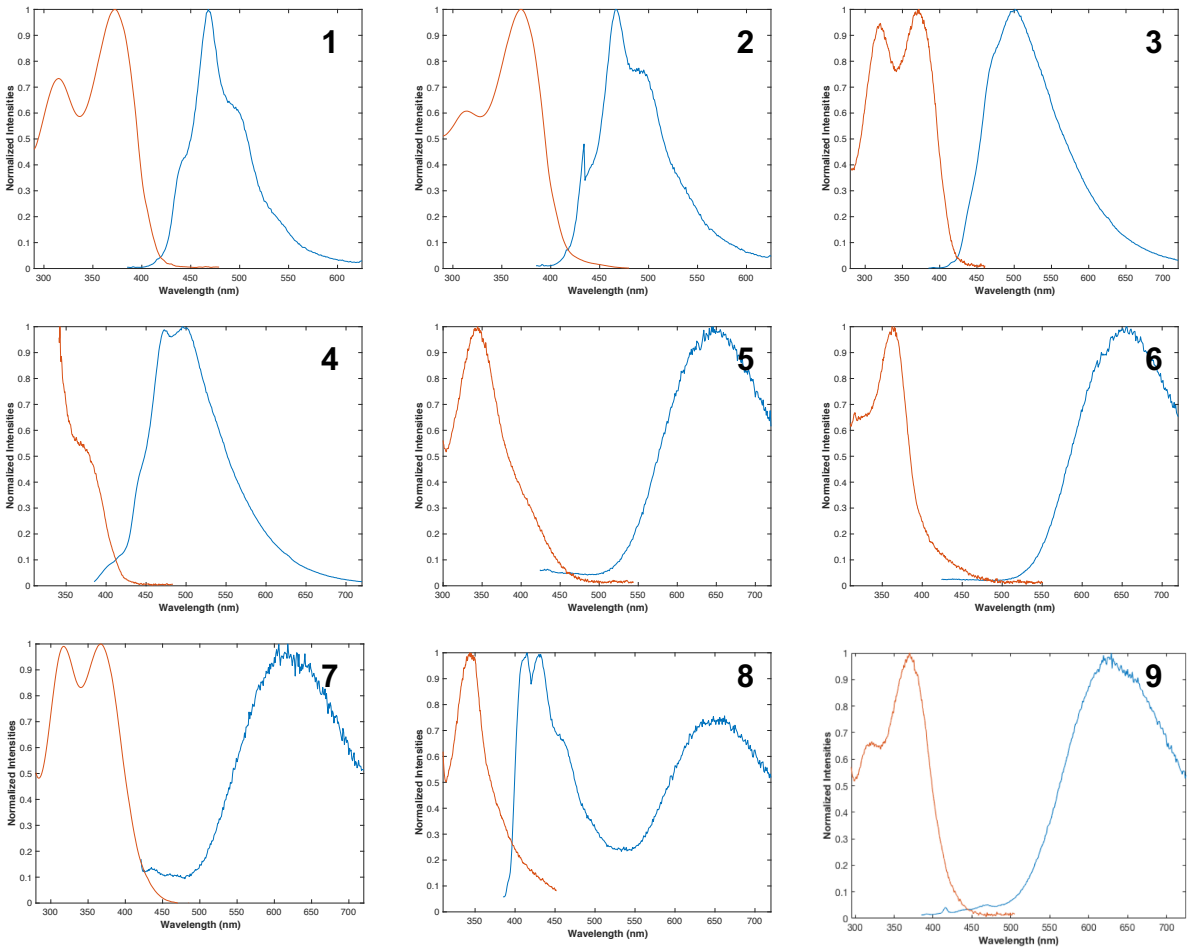

Figure 38. Overlaid UV-Vis (red) and emission (blue) spectra of photocatalysts **1-9.**

Table 6. Polymerization Results for the O-ATRP of MMA in DMAc Using PCs **1** – **9**.[a]

Trial	PC	Conv. (%)[b]	M_n (kDa)[c]	M_W (kDa)[c]	$Đ$ (M_W/ M_n)[c]	I^* (%)[d]
1	1	69.6	24.7	36.3	1.57	29.2
2	2	85.9	11.9	18.4	1.55	74.5
3	3	77.5	16.4	27.4	1.67	48.7
4	4	82.3	18.9	32.6	1.72	44.7
5	5	87.1	22.6	26.4	1.17	39.7
6	6	93.1	13.3	14.5	1.09	71.9
7	7	98.4	15.3	17.9	1.17	65.9
8	8	59.0	7.48	9.27	1.24	80.8
9	9	90.0	13.0	15.8	1.22	71.0

[a]Polymerizations were performed with 1.00 mL MMA (9.35 mmol, 1000 eq), 16.4 µL EBP (93.5 µmol, 10 eq), 3.12-6.26 mg of PC (9.35 µmol, 1 eq), 1.00 mL DMA, and irradiated by white LEDs for 8 h. Polymerization stoichiometry: [MMA]:[EBP]:[PC] 1000:10:1. [b]% Conversion measured by ^{1}H NMR. [c]Measured using GPC-MALS. [d]Initiator efficiency (I^*) calculated from theo. M_n/exp. M_n.

The O-ATRP behavior of all 9 PCs was then tested for the polymerization of MMA in 5 additional solvents of varying lower polarities (Figure 39). It was found that, with the exception of THF, non-CT PCs do not generally perform well in any of these lower-polarity solvents. CT PCs, on the other hand, gave robust O-ATRP results in all solvents tested. In general, $Đ$ was lower for polymers produced in all of the tested solvents compared to $Đ$ measured in DMAc. Given that EtoAc is considered to be a "green" solvent, it was chosen as the solvent for further optimization. When optimized for initiator and time, EtoAc gives excellent O-ATRP results for all of the CT PCs (Table 7). This work points to the power of intramolecular CT as a tool for manipulation of PC behavior by modulation of solvent polarity, resulting in improved O-ATRP outcomes.

Photocatalyst	**Hexanes** $E_T(30)$ = 31.0 (kcal mol^{-1})	**Benzene** $E_T(30)$ = 34.3 (kcal mol^{-1})	**Dioxane** $E_T(30)$ = 36.0 (kcal mol^{-1})	**Tetrahydrofuran** $E_T(30)$ = 37.4 (kcal mol^{-1})	**Ethyl Acetate** $E_T(30)$ = 38.1 (kcal mol^{-1})
	non-Charge Transfer				
1 μ = 3.27	Conv < 10 %	Conv < 10 %	Conv < 10 %	Conv: 34.5 % M_n: 7.61 M_W: 10.1 *I**: 46.4 % *Đ*: 1.32	Conv < 10 %
2 μ = 0.00	Conv < 10 %	Conv < 10 %	Conv < 10 %	Conv: 38.3 % M_n: 7.68 M_W: 9.49 *I**: 51.1 % *Đ*: 1.24	Conv < 10 %
3 μ = 0.00	Conv: 16.0 % M_n: 14.2 M_W: 21.1 *I**: 13.0 % *Đ*: 1.49	Conv: 13.0 % M_n: 5.8 M_W: 8.4 *I**: 26.7 % *Đ*: 1.45	Conv: 13.4 % M_n: 8.32 M_W: 9.23 *I**: 16.4 % *Đ*: 1.11	Conv: 33.2 % M_n: 5.31 M_W: 7.15 *I**: 64.0 % *Đ*: 1.35	Conv < 10 %
4 μ = 0.33	Conv < 10 %	Conv < 10 %	Conv < 10 %	Conv: 32.2 % M_n: 6.13 M_W: 7.85 *I**: 53.8 % *Đ*: 1.28	Conv < 10 %
	Charge Transfer				
5 μ = 21.03	Conv < 10 %	Conv: 39.4 % M_n: 8.88 M_W: 9.32 *I**: 47.1 % *Đ*: 1.05	Conv: 30.8 % M_n: 6.58 M_W: 7.39 *I**: 47.9 % *Đ*: 1.12	Conv: 62.6 % M_n: 8.10 M_W: 8.90 *I**: 79.2 % *Đ*: 1.10	Conv: 18.9 % M_n: 6.49 M_W: 9.09 *I**: 29.8 % *Đ*: 1.40
6 μ = 18.11	Conv: 15.8 % M_n: 5.28 M_W: 7.69 *I**: 30.7 % *Đ*: 1.46	Conv: 42.3 % M_n: 8.34 M_W: 8.73 *I**: 52.0 % *Đ*: 1.05	Conv: 39.4 % M_n: 8.87 M_W: 9.43 *I**: 45.5 % *Đ*: 1.06	Conv: 67.8 % M_n: 11.4 M_W: 11.9 *I**: 60.9 % *Đ*: 1.04	Conv: 25.5 % M_n: 6.30 M_W: 6.60 *I**: 41.5 % *Đ*: 1.05
7 μ = 19.93	Conv: 17.0 % M_n: 4.30 M_W: 4.77 *I**: 40.5 % *Đ*: 1.11	Conv: 41.0 % M_n: 7.85 M_W: 8.40 *I**: 53.5 % *Đ*: 1.07	Conv: 26.4 % M_n: 6.09 M_W: 6.79 *I**: 44.4 % *Đ*: 1.11	Conv: 87.0 % M_n: 12.7 M_W: 14.4 *I**: 70.2 % *Đ*: 1.13	Conv: 26.5 % M_n: 5.81 M_W: 6.25 *I**: 49.8 % *Đ*: 1.08
8 μ = 19.77	Conv: 61.4 % M_n: 8.90 M_W: 9.68 *I**: 71.7 % *Đ*: 1.09	Conv: 72.7 % M_n: 14.3 M_W: 15.0 *I**: 52.7 % *Đ*: 1.05	Conv: 40.8 % M_n: 6.34 M_W: 7.47 *I**: 65.9 % *Đ*: 1.18	Conv: 83.9 % M_n: 9.86 M_W: 10.6 *I**: 87.2 % *Đ*: 1.07	Conv: 62.4 % M_n: 10.9 M_W: 11.3 *I**: 59.6 % *Đ*: 1.04
9 μ = 26.75	Conv: < 10 %	Conv: 14.0 % M_n: 6.61 M_W: 10.9 *I**: 21.7 % *Đ*: 1.65	Conv: 13.3 % M_n: 7.03 M_W: 7.96 *I**: 19.4 % *Đ*: 1.13	Conv: 64.0 % M_n: 10.7 M_W: 11.8 *I**: 61.3 % *Đ*: 1.10	Conv: 39.4 % M_n: 7.55 M_W: 7.93 *I**: 55.4 % *Đ*: 1.05

Figure 39. Polymerization data from O-ATRP using the 9 different PCs (vertical, μ = dipole moment of the ^{3}PC*) in solvents with various $E_T(30)$, horizontal. All polymerizations were conducted for 8 h, 1.00 mL solvent, 1.00 mL MMA (9.35 mmol, 1000 eq), 16.4 µL EBP (93.5 µmol, 10 eq), and 3.12-6.26 mg (9.35 µmol, 1 eq) depending on the PC used.

Table 7. Polymerization results of the O-ATRP of MMA using CT PCs in Ethyl Acetate.[a]

Trial	PC	Initiator	Conv. (%)[b]	M_n (kDa)[c]	M_W (kDa)[c]	$Đ$ (M_W/ M_n)[c]	I^* (%)[d]
10	5	M2BP	84.2	9.12	9.75	1.07	93.9
11	6	DBMM	69.3	8.44	8.72	1.03	84.2
12	6	M2BP	68.3	9.60	9.91	1.03	72.3
13	7	DBMM	77.8	8.57	9.57	1.12	93.0
14	7	M2BP	74.2	7.64	9.11	1.19	98.7
15	8	DBMM	77.2	9.47	9.79	1.03	83.6
16	8	M2BP	85.6	10.1	10.7	1.06	86.2
17	9	DBMM	76.9	9.44	10.0	1.06	83.6
18	9	M2BP	83.5	8.27	9.50	1.15	102.6

[a]Polymerizations were performed with 1.00 mL MMA (9.35 mmol, 1000 eq), 16.4 μL EBP (93.5 μmol, 10 eq), 4.00-5.00 mg of PC (9.35 μmol, 1 eq), 1.00 mL ethyl acetate, and irradiated by white LEDs for 20 h. Polymerization stoichiometry: [MMA]:[I]:[PC] 1000:10:1. [b]% Conversion from ^{1}H NMR. [c]Measured using GPC-MALS. [d]Initiator efficiency (I^*) calculated from theoretically calculated M_n/experimentally measured M_n

3.3.2 Catalyst Synthesis

Syntheses for catalysts **1**,**2**,**5**,**6**,**7** were previously described in Section 2.7.3.

Synthesis of catalysts **8** and **9**, plus Supporting Information for the work described in Section 3.3.1 can be found in Ryan, M.D. *et al. J. Polym. Sci. A* **2017**, *55* (18), 3017-3027.

*5,10-di-p-fluorophenyl-5,10-dihydrophenazine (**3**):*

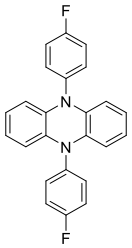

An oven-dried vacuum tube was charged with 5,10-dihydrophenazine (1.00 g, 5.50mmol, 1.00 eq.), *t*-BuONa (2.11 g, 22.0 mmol, 4.00 eq.), RuPhos (103 mg, 0.22 mmol, 0.04

eq.), RuPhos precatalyst (180 mg, 0.22 mmol, 0.04 eq.), 4-bromofluorobenzene (3.85 g, 22.0 mmol, 4.00 eq), and 11 mL dioxane. This flask was sealed under nitrogen and heated at 110 ˚C for 12 h. After cooling to room temperature, 200 mL CH_2Cl_2 and 200 mL H_2O was added to the reaction flask, causing the product to precipitate. Filtration and washing with cold CH_2Cl_2 afforded the title compound as a light yellow powder (677 mg, 1.82 mmol, 33%). ^{1}H NMR (300 MHz, C_6D_6) δ 7.02 – 6.83 (m, 4H), 6.83 – 6.67 (m, 4H), 6.45 – 6.15 (m, 4H), 5.83 – 5.57 (m, 4H); ^{13}C NMR (75 MHz, C_6D_6) δ 162.3 (d, $^1J_{C\text{-}F}$ = 245 Hz), 137.0, 136.3 (d, $^4J_{C\text{-}F}$ = 3 Hz), 133.4, (d, $^3J_{C\text{-}F}$ = 8 Hz), 121.6, 118.4 (d, $^2J_{C\text{-}F}$ = 23 Hz), 113.1; ^{19}F NMR (282 MHz, C_6D_6) δ -112.84; HRMS (ESI): calcd. For $C_{24}H_{16}F_2N_2^+$ [M$^+$]: 370.1271. Found 370.1294.

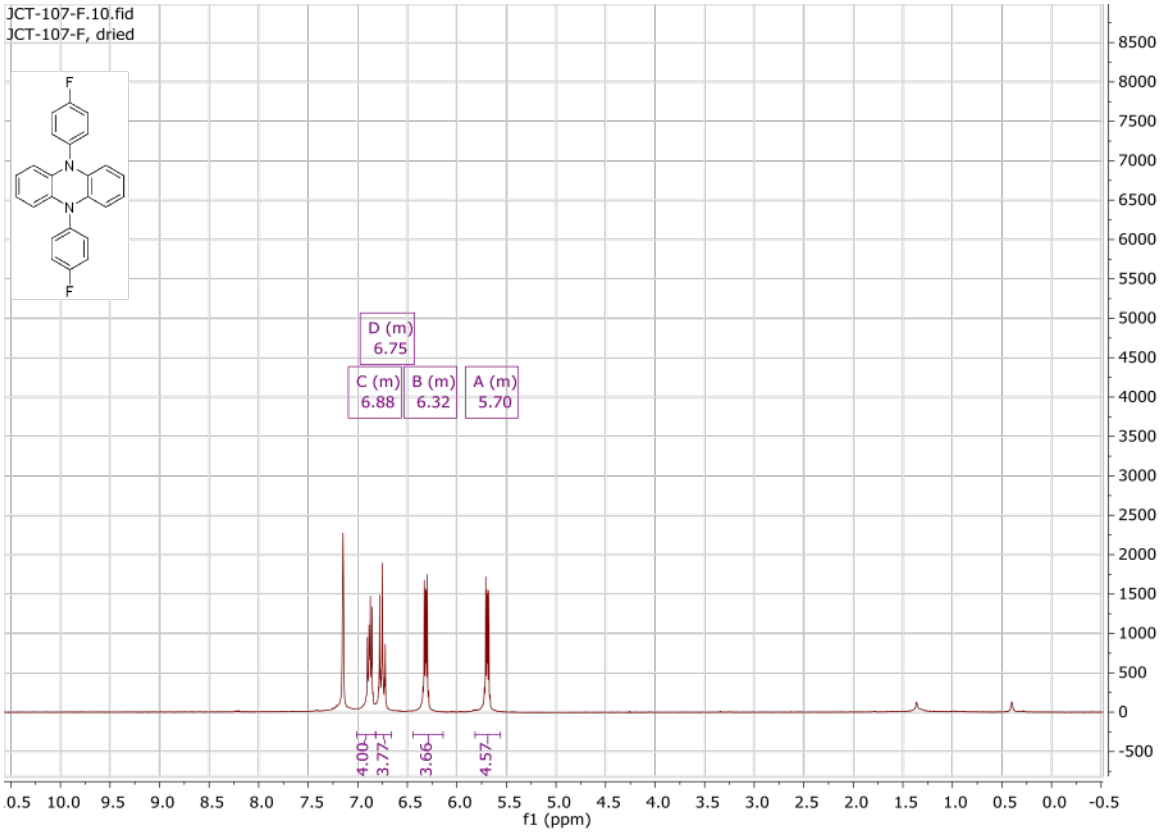

Figure 40. ^{1}H NMR of PC **3**.

*5,10-di-(p-diphenylaminophenyl)-5,10-dihydrophenazine (**4**):*

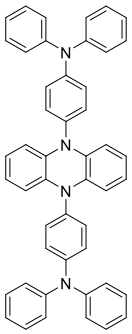

An oven-dried vacuum tube was charged with 5,10-dihydrophenazine (728 mg, 4.00 mmol, 1.00 eq.), *t*-BuONa (1.54 g, 16.0 mmol, 4.00 eq.), RuPhos (75 mg, 0.16 mmol, 0.04 eq.), RuPhos precatalyst (131 mg, 0.16 mmol, 0.04 eq.), 4-bromotriphenylamine (5.16 g, 16.0 mmol, 4.00 eq), and 8 mL dioxane. This flask was sealed under nitrogen and heated at 110 ˚C for 12 h. After cooling to room temperature, 200 mL CH_2Cl_2 and 200 mL H_2O was added to the reaction flask, causing the product to precipitate. Filtration and washing with cold CH_2Cl_2 afforded the title compound as a light yellow powder (544 mg, 0.81 mmol, 20%). ^{1}H NMR (300 MHz, C_6D_6) δ 7.13 – 6.98 (m, 24H), 6.91 – 6.79 (m, 4H), 6.37 (dd, *J* = 5.9, 3.4 Hz, 4H), 6.04 (dd, *J* = 5.8, 3.4 Hz, 4H); ^{13}C NMR (75 MHz, C_6D_6) δ 148.0, 147.9, 137.5, 134.1, 132.3, 129.8, 125.4, 125.3, 123.7, 121.5, 113.1. HRMS (ESI): calcd. For $C_{48}H_{36}N_4^+$ [M^+]: 668.2934. Found 668.2933.

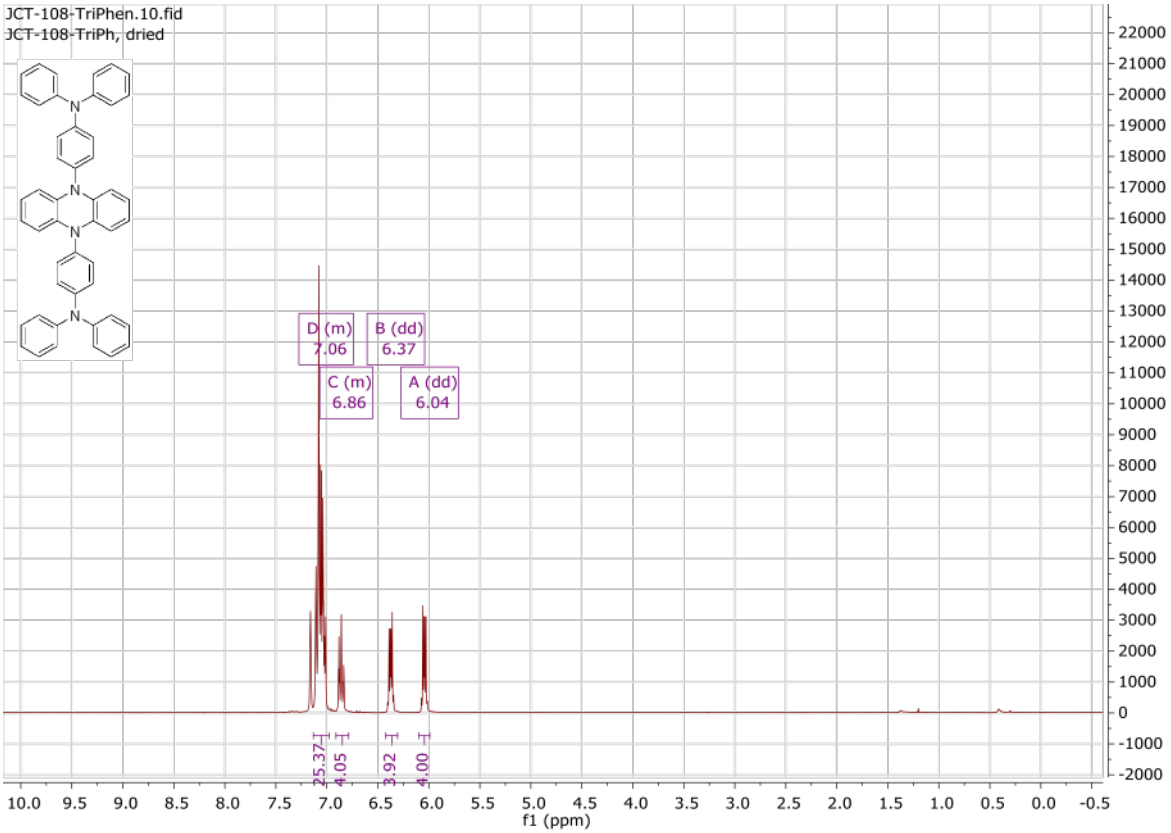

Figure 41. ^{1}H NMR of PC **4**.

3.4 O-ATRP of Butyl Acrylate

Butyl acrylate (BA) can be a difficult monomer to polymerize with control due to its high rate of polymerization propagation (k_p) as compared to the methacrylate monomers which have so far been successfully polymerized by O-ATRP. It would add value to O-ATRP as a methodology if it were able to be used for the controlled polymerization of BA, however initial results using DMAc as the standard solvent were not promising (*vide infra*). The

studies described in Section 3.3 gave hope, however, that the use of a solvent of lower polarity may improve BA polymerization outcomes.

A 20 mL scintillation vial with a non-metal lined cap was charged with a small stirbar and PC **7** (Figure 37) (4.4 mg, 9.35 μmol, 1 eq), and transferred to a nitrogen-atmosphere glovebox. Solvent (DMAc or THF, 1.00 mL), BA (1.33 mL, 9.35 mmol, 1000 eq), and EBP (16.4 μL, 93.5 μmol, 10 eq) were added sequentially *via* pipette for solvent and monomer, while initiator was added by a 25 μL Hamilton syringe. The vial was sealed and placed into a beaker fitted with white LEDs and stirred. At the specified times, 0.1mL aliquots were removed *via* syringe and injected into a sealed vial containing 0.7 mL of $CDCl_3$ with 250 ppm butylated hydroxytoluene (BHT) additive. This sample was analyzed by ^1H NMR for % conversion, and then dried under reduced pressure to remove solvent and volatiles. This dried sample was re-dissolved in spectral grade THF for analysis of M_W, M_n, and $Đ$ by GPC coupled with MALS.

Table 8. Results of O-ATRP of BA Using DMAc and THF as the Solvent

Experiment	Monomer	Initiator	Solvent	Time	Conversion	*Đ*	*I**
1	BA	EBP	DMA	6	95.1	1.72	100.1
2	BA	EBP	THF	8	93.5	1.42	62.4

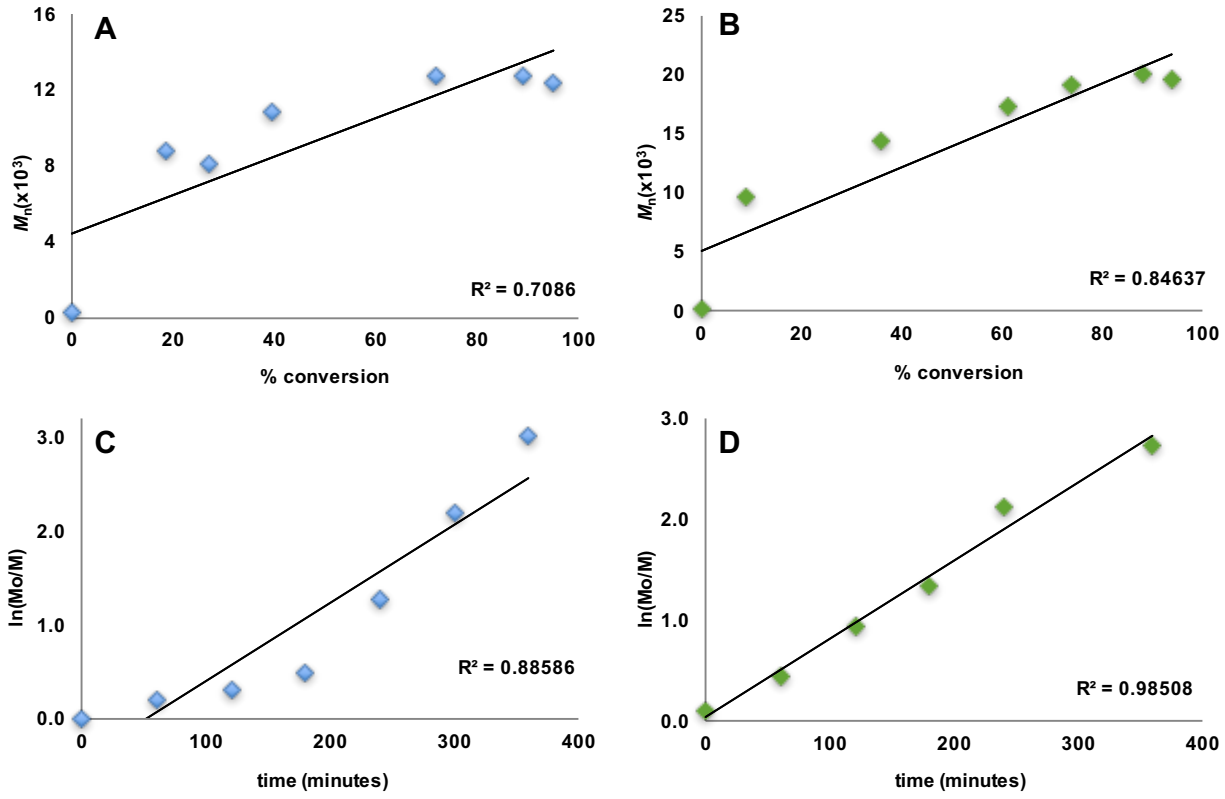

Figure 42. Plots of M_n *vs.* conversion for O-ATRP of BA run in DMAc (**A**) and THF (**B**). Plots of ln(M_o/M) *vs.* time for O-ATRP of BA run in DMAc (**C**) and THF (**D**).

The results of such experiments indicate that the use of THF as the solvent for O-ATRP of BA does improve some polymerization outcomes compared to DMAc as the solvent (Table 8 and Figure 42). Both types of kinetic plots become significantly more linear (indicating that the polymerization behaves more like a CRP is expected to) and an apparent induction period has disappeared when THF is used as the solvent. Additionally, *Đ* drops from 1.72 to 1.42. However, *I** was observed to decrease when THF was used as a solvent. The reason for this observation is not apparent.

To lend more support for the control offered by THF as a solvent for O-ATRP, chain extension experiments were performed in order to confirm the re-installation of the Br end groups to the polymer chains. A sample of PBA formed according to the above procedure for

O-ATRP of BA in THF and precipitated into methanol 3 times (M_n = 9.7 kDa, $Đ$ = 1.18). The sample (145 mg, 0.015 mmol, 10 eq.) was added to a 20 mL vial along with stirbar and PC **7** (0.70 mg, 0.0015 mmol, 1 eq.). The vial was transferred to a nitrogen-atmosphere glovebox where THF (1 mL) and BA or MMA (3.0 mmol, 2000 eq.) were added *via* pipette. The vial was then placed in a beaker illuminated with white LED lights and stirred. After 12 hours, the vial was removed from the glovebox and the reaction contents were precipitated into methanol. The collected polymer was then analyzed by GPC (Figure 43). It was found that chain extension occurred efficiently from a PBA macroinitiator for both types of monomer used in the second block.

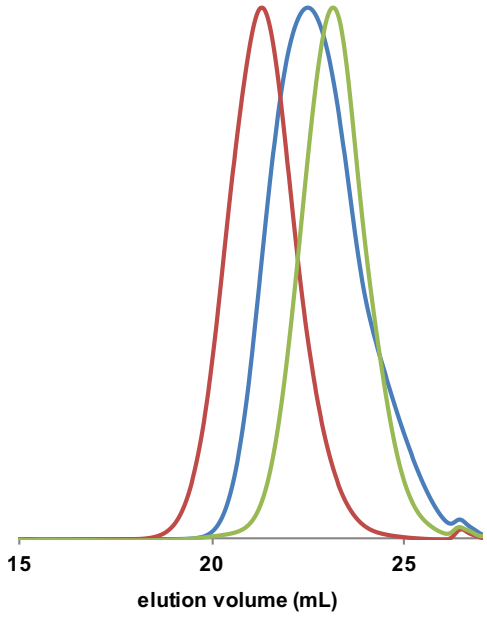

Figure 43. GPC traces for chain extension from a PBA macroinitiator (green trace) to create PBA-*b*-PBA (blue trace) and PBA-*b*-PMMA (red trace).

3.5 Quantum Yield Measurements

As mentioned at the end of Section 3.1, a high triplet quantum yield (QY) is a desirable feature of a potential PC for O-ATRP. With this in mind, the fluorescence QY of several *N,N*-diaryl dihydrophenazine PCs were measured. Because fluorescence QY is related to radiative decay pathways, which are nonproductive for electron transfer reactions, a high fluorescence QY would be an indicator of low triplet QY and therefore poor performance as a photoredox catalyst. Fluorescence QY can be measured by comparison to a fluorescence standard with known QY according to the following equation:

$$QY = QY_{std}\frac{I}{I_{std}}\frac{A_{std}}{A}\frac{n^2}{n_{std}^2}$$

where I is the integrated fluorescence intensity, *n* is the refractive index of the solvent in which the measurements were taken, A is the absorption, and the subscript std indicates values for the fluorescence standard with known QY.[46]

Such measurements were performed for PCs **1** – **9** (Figure 37) using either coumarin 480 or coumarin 540A as the standard, depending on which standard has λ_{max} of emission closer to the observed λ_{max} of emission for that particular PC. Absorption spectroscopy was performed on an Agilent spectrophotometer using DMAc as the solvent. Emission spectroscopy was performed on a SLM 8000C spectrofluorimeter using DMAc as the solvent. Samples were sparged with argon for 15 minutes prior to analysis on the spectrofluorimeter. It was found that the only non-CT PCs had measurable QYs (Table 9), and all of the CT PCs were found to have QY of fluorescence <1%. These measurements are in line with the expectation that CT PCs would have high rates of ISC to the photoredox-active triplet state (i.e. high triplet QY) and therefore low rates of radiative decay (i.e. low fluorescence QY).

Table 9. Fluorescence Quantum Yields of PCs **1** – **9**.

non-Charge Transfer		Charge Transfer	
Catalyst	QY	Catalyst	QY
PC 1	68%	PC **5**	<1%
PC 2	36%	PC **6**	<1%
PC 3	19%	PC **7**	<1%
PC 4	not measured	PC **8**	<1%
		PC **9**	<1%

3.6 Perspectives on Catalyst Design and Performance[**]

3.6.1 Introduction

As of the writing of this section, five major classes of organic PCs including polycyclic aromatic hydrocarbons, phenothiazines, phenazines, phenoxazines, and carbazoles, have been explored for use in O-ATRP (Figure 52). While this section does not provide a comprehensive review of the field of O-ATRP, it strives to highlight the unique photophysical and chemical properties that make certain organic molecules suitable for O-ATRP and recognize the broad scope of applications for which these PCs have been previously used. The following sections will include, for each catalyst type, discussion of the historic uses of these PCs, their key photophysical features, and their performance as O-ATRP catalysts, followed by a comparison of PCs, with a focus on those containing phenothiazine, dihydrophenazine, and phenoxazine core structures.

[**] This section is extracted from Theriot, J.C. *et al. Macromol. Rapid Commun*. **2017**, 1700040. See *Contributor Attributions* for additional information.

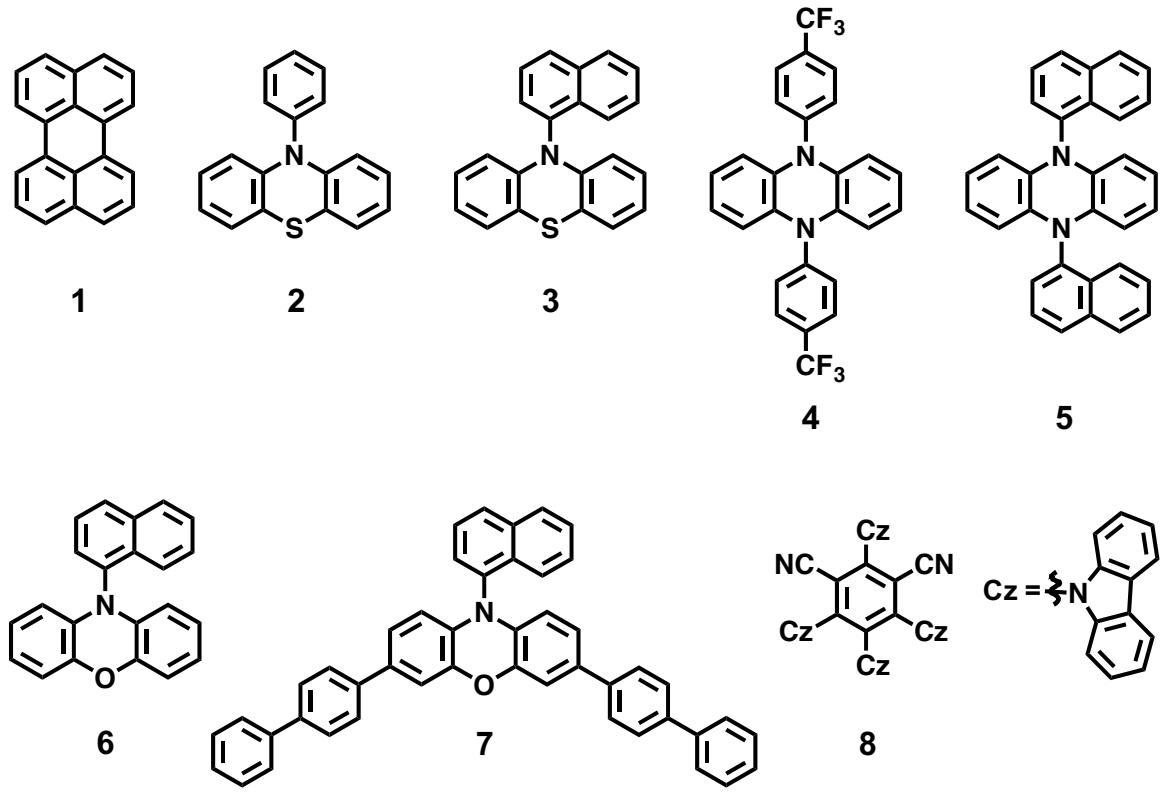

Figure 44. Structures of photocatalysts 1 – 8. PC 1 = perylene; PC 2 = 10-phenyl-phenothiazine; PC 3 = 1-naphthalene-10-phenothiazine; PC 4 = 5,10-di(4-trifluoromethylphenyl)-5,10-dihydrophenazine; PC 5 = 5,10-di(1-naphthyl)-5,10-dihydrophenazine; PC 6 = 1-naphthalene-10-phenoxazine; PC 7 = 3,7-di(4-biphenyl) 1-naphthalene-10-phenoxazine; PC 8 = 1,2,3,5-tetrakis(carbazol-9-yl)-4,6-dicyanobenzene (4CzIPN).

3.6.2 Classes of O-ATRP Catalysts

Polycyclic Aromatic Hydrocarbons

Polycyclic aromatic hydrocarbons (PAHs) consist of multiple fused aromatic rings composed of only carbon and hydrogen. PAHs are known as a terrestrial carcinogen that results primarily from incomplete combustion reactions,[47] and PAHs are also abundant in space.[48,49] Although the properties of PAHs vary significantly with MW, PAHs are typically excellent light absorbers that exhibit strong fluorescence. PAHs have received much

attention in the field of organic electronics (OEs) and organic photovoltaics (OPVs) for their ability to effectively manipulate photonic energy.[50–53] Additionally, perylene (PC 1, Figure 44) and related PAHs have been investigated as photosensitizers and photoinitiators for cationic and free radical polymerizations.[54–57] Perylene derivatives have tunable absorptions throughout the visible and IR regions, with typically high molar extinction coefficients ($\varepsilon > 10^4\ M^{-1}cm^{-1}$).[58] Perylene derivatives have been recognized as strong excited state reductants relative to other organic dyes,[59] and perylene itself has $E^0(PC^{\bullet+}/PC^*) = -1.87$ V vs. SCE from the S_1 state and $E^0(PC^{\bullet+}/PC^*) = -0.58$ V vs. SCE from the T_1 state.[60–62]

PC 1 was investigated early on as a potential PC for the first demonstration of organocatalyzed ATRP to proceed through the oxidative quenching pathway using visible light.[26,27] Using methyl methacrylate (MMA) and butyl acrylate (BA) as demonstrative monomers, polymers with moderately low $Đ$ (a measure of the broadness of the MW distribution), typically 1.3 – 1.8, were synthesized under white light irradiation. Matrix-assisted laser desorption ionization – time of flight (MALDI-TOF) mass spectrometry and chain extension experiments confirmed re-installation of the bromide end group, however it was not quantitative. Temporal control allowed the polymerization to be completely halted with the removal of light, and resumed with re-introduction of light. However, the system exhibited low initiator efficiencies (I^*, the theoretical MW divided by the observed MW). In addition to perylene, PAHs anthracene and pyrene were investigated as PCs for O-ATRP under 350 nm irradiation.[63] In addition to styrene and *tert*-butyl acrylate, MMA was polymerized to low conversion (< 30%) with $Đ$ typically 1.4 – 1.5. However, as with the perylene system, I^* was consistently low.

Phenothiazines

Phenothiazine derivatives have been investigated in medical and biological applications since the 1880s.[64–66] For example, methylene blue is a popular histologic stain used in biological research that changes color due to electron transfer reactions involving the phenothiazine core structure.[67,68] Due to their redox-active nature, phenothiazines have been applied in dye-sensitized solar cells,[69,70] organic light-emitting diodes (OLEDs),[71] and battery electrode applications.[72,73] Recently, phenothiazine's ability to act as a photoreductant has been exploited in catalysis for applications such as dehalogenation[74] and C–C bond formation on aryl halide substrates.[75] Phenothiazine can be relatively easily oxidized to form a radical cation, whose salt is stable enough to be isolated and studied.[76,77] Phenothiazines were also applied in cationic polymerization,[78] RAFT polymerization,[79] and the synthesis of conjugated polymers with donor-acceptor architecture.[80]

Phenothiazine's use in photophysical applications made it an excellent candidate for O-ATRP PCs. 10-phenyl phenothiazine (PC 2, Figure 44) was found to have $E^0(PC^{\bullet+}/PC^*)$ of –1.97 V vs. SCE in DMAc.[42] PC 2, along with other phenothiazine derivatives, was employed in the O-ATRP polymerization of MMA under 380 nm irradiation to give polymers of low dispersity ($Đ$ = 1.18 to 1.32) and high initiator efficiency (I^* = 90% to 116%).[28] Preservation of chain-end functionality was confirmed by successful chain extensions and copolymerizations, as well as MALDI-TOF analysis. Since its first demonstration, PC 2 has also been used to polymerize acrylonitrile[29] and biomass-based monomers[81] via O-ATRP. A mechanistic study of O-ATRP catalyzed by PC 2, PC 3, and other phenothiazines was performed.[42] In that study, the short-lived singlet state was proposed to be responsible for

ET from phenothiazine PCs, while later work suggested the longer-lived triplet state was the electronic state responsible for O-ATRP initiation.[82]

Phenazines

Phenazine derivatives are well-known natural products, first recognized as colorful secondary metabolites produced by *Pseudomonas*.[30,83] In nature, phenazine metabolites produced from bacteria serve many purposes ranging from protection against competitive microorganisms to influencing structural organization in bacterial populations. Synthetic and naturally-derived phenazines have demonstrated antibiotic, antitumor, antimalarial, and antiparasitic activity.[31,84] In the field of OEs, researchers have capitalized on the electron rich nature of the phenazine core to make hole injection materials and donor-acceptor molecules with CT character.[85–87] Phenazine-containing emissive materials demonstrate tunable emission profiles and were successfully incorporated into OLEDs.[33,34,88] Radical cations of phenazine are exceptionally stable and have been explored as components in ferromagnetic organic materials.[36,89,90] In catalysis, phenazines were employed as components in photoinitiating systems for cationic polymerization.[91]

Guided by density functional theory (DFT) predictions, several substituted diaryl dihydrophenazines were investigated for use in O-ATRP due to their strong excited state reduction potentials, with predicted $E^0(PC^{\bullet+}/PC^*)$ ranging from -2.06 to -2.36 V vs. SCE, absorption stretching into the visible regime.[40] Initial polymerization results indicated that catalysts with electron-withdrawing groups on the aryl substituent, in particular PC 4 (Figure 44), gave superior results for the polymerization of MMA under white light irradiation ($Đ$ = 1.17), albeit with low I^* of 66%. Further computational investigation

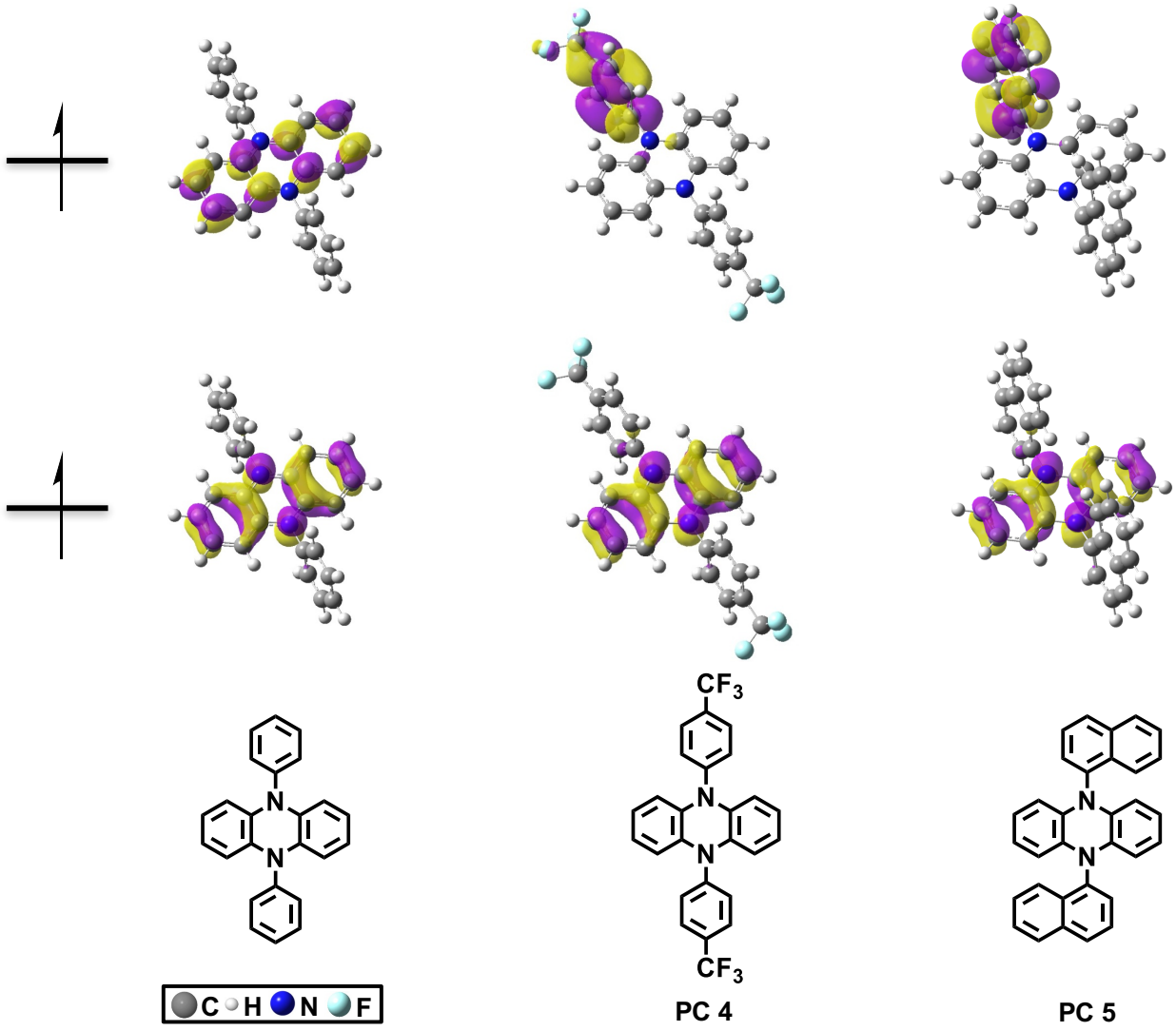

Figure 45. PCs 4 and 5 display spatially-separated SOMOs in the DFT-predicted triplet excited state, whereas diphenyl dihydrophenazine (left) does not. Figure adapted from Theriot, J.C. *et al*. *Science* **2016**, *352*, 1082.

revealed that, unlike dihydrophenazines with electron-donating or neutral substituents on the aryl group, those with electron-withdrawing substituents possessed spatially-separated singly-occupied molecular orbitals (SOMOs) in the triplet excited state (Figure 45), indicating intramolecular charge transfer (CT) (see Section 3.6.3). Based on this observation, more substituted dihydrophenazine catalysts with computationally-predicted spatially-

separated SOMOs were synthesized and tested, and PC 5 (Figure 44) was found to polymerize MMA to low dispersities ($Đ < 1.3$) with near-quantitative initiator efficiency. High end-group fidelity was confirmed by copolymerizations and MALDI-TOF analysis. This contribution placed diaryl dihydrophenazines as the first example of visible light O-ATRP catalysts capable of producing results on par with conventional ATRP.

Phenoxazines

The phenoxazine core structure has been found in several naturally occurring, biologically active compounds isolated from bacteria.[92] In medicine, phenoxazine derivatives have been investigated as antitumor agents,[93–96] antifungal agents,[97] antimalarial drugs,[98] and for gene therapy.[99] Due to their strong emission in the visible light regime, derivatives containing the phenoxazine core structure have also been investigated for biological imaging applications[100] and biosensor applications.[101] Within the chemical and materials science fields, phenoxazine derivatives have been employed as donors in small molecule, donor-acceptor species for OLEDs,[102] dyes for dye-sensitized solar cells,[103,104] and investigated for other OPV applications[105] due to the electron rich nature of the phenoxazine core and stability of the phenoxazine radical cation.[106] In addition, phenoxazine-based polymers have been used as p-channel semiconductors in organic field transistors.[107]

Several *N*-aryl substituted phenoxazines were synthesized for use as PCs and found to have predicted $E^0(PC^{\bullet+}/PC^*)$ ranging from -1.9 V to -2.1 V vs. SCE.[44] It was found that those bearing naphthyl substituents, such as PC 6 (Figure 44) were able to synthesize PMMA under 365 nm irradiation in a controlled fashion as evidenced by a linear growth of polymer MW with increasing conversion, low $Đ$ (1.07 to 1.38), and high I^* (typically 80% to 100%).

Interestingly, the trend observed with diaryl dihydrophenazines, that PCs exhibiting computationally-predicted spatially separated SOMOs in the triplet excited state, a hallmark of CT, performed better in O-ATRP compared to PCs that did not exhibit this feature, was also seen with the phenoxazine PCs (see Section 3.6.3). Encouraged by these results, it was sought to retain the catalytic power of the phenoxazine structure while pushing absorption into the visible regime. Synthetic modification of the phenoxazine core with biphenyl substituents at the 3 and 7 positions yielded a new catalyst (PC 7, Figure 44) with an absorption profile redshifted by 65 nm (λ_{max} = 323 nm for PC 6, λ_{max} = 388 nm for PC 7) and a dramatically

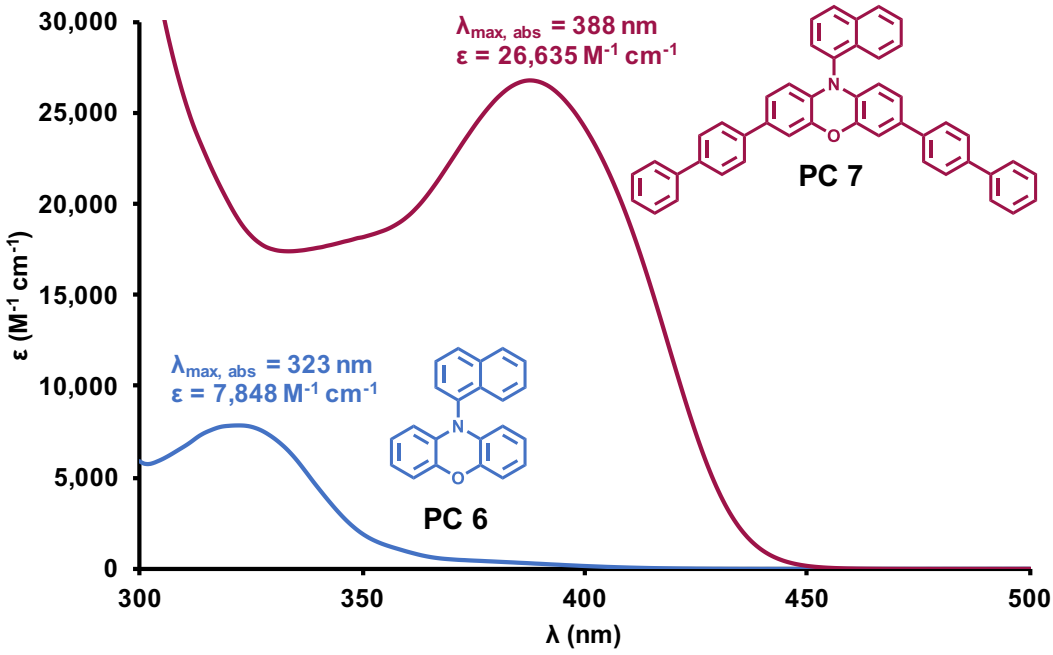

Figure 46. Change in absorption spectra upon substitution of PC 6 with biphenyl groups to yield PC 7. Adapted from Pearson, R.M. *et al. J. Am. Chem. Soc*. **2016**, *138*, 11399.

increased molar absorptivity (ε = 7,848 $M^{-1}cm^{-1}$ for PC 6, ε = 26,635 $M^{-1}cm^{-1}$ for PC 7) (Figure 46). Polymerization of MMA by PC 7 irradiated with white light resulted in polymers with quantitative I^* and low $Đ$ (1.13 to 1.31).

Carbazoles

Various carbazole-based derivatives[108] and alkaloids have been synthesized[109,110] to study their effects and functions in biological systems.[111] As an example, the antibiotic properties of murrayanine, a naturally occurring carbazole-derived alkaloid were first described in 1965.[112] The electron-rich carbazole moiety, when paired with an electron poor substituent, forms a donor-acceptor pair that exhibits CT character.[113] Carbazole's ability to form CT complexes has been exploited in various applications, including OEs,[114] OPVs,[115,116] and OLEDs.[117] However, in 2012, carbazole derivatives attracted significant attention when the donor-acceptor pair of carbazolyl dicyanobenzene (4CzIPN, PC 8) was shown to exhibit thermally activated delayed fluorescence for efficient OLED application.[118,119] Additionally, PC 8 was recently applied in small molecule synthesis for the formation of C-C bonds via dual photoredox / nickel catalysis.[120]

The use of PC 8 [$E^0(PC^{\bullet+}/PC^*)$ = -1.04 V vs. SCE] [118,121] as a catalyst for O-ATRP was recently described.[122] PC 8 has absorption features into the visible spectrum and thus polymerization was able to be carried out under blue light irradiation. PC 8 mediated the polymerization of MMA with exceptionally low ppm-level catalyst loading, but typically broad molecular weight distributions ($Đ \geq 1.50$). Photocontrol was demonstrated with on-off irradiation experiments, and chain ends were confirmed through MALDI-TOF and chain extension experiments, though it was estimated 11% of chains were "dead" or terminated.

Two other carbazole derivatives, 9-phenylcarbazole and 4,4′-bis(N-carbazolyl)biphenyl, were also employed as O-ATRP catalysts, producing polymers with high dispersity ($Đ \geq 1.80$). These catalysts were also found to exhibit irreversible CV curves, an indication that the radical cations were not stable in the polymerization solvent.[42,121]

3.6.3 Discussion

The available photophysical data for each of the highlighted PCs 1 – 8 are summarized in Table 10. Returning to the overall list of design principles (see Section 3.1), a general comparison can be made between the 5 classes of PCs. In terms of the first principle – a strong photon absorption in the visible regime – perylene is the strongest visible light absorber among the catalysts, with λ_{max} = 436 nm and ε_{max} = 38,500 $M^{-1}cm^{-1}$. The remaining catalysts all have absorption maxima in the UV. However, it is worth noting that PCs 4, 5, 7, and 8, despite having λ_{max} values < 400nm, have absorption profiles that extend into the visible region which has enabled them to conduct O-ATRP using white LED light (PCs 4, 5, and 7) or blue LED light (PC 8). Importantly, it has been shown in the case of phenoxazines that synthetic modification can be employed to drastically alter absorption properties without necessarily affecting catalytic behavior (see Section 3.4).

Principles 2 and 3 state the need for efficient ISC to the triplet excited state and sufficiently long excited state lifetime. Available singlet and triplet lifetimes are listed in Table 10. Singlet lifetimes typically are short (in the nanoseconds) and most likely decay to the ground state before a successful bimolecular encounter with the desired substrate can occur. Some exceptions do exist. For example, phenothiazine was shown to perform ET from its S_1 state to chloroalkanes because these two species associate into a complex and are

Table 10. Summary of Properties of Photocatalysts **1** – **8**.

PC	λ_{max} [nm]	ε_{max} [$M^{-1}cm^{-1}$]	τ	$E^0(PC^{\bullet+}/PC^*)$ [V vs. SCE]	$E^0(PC^{\bullet+}/PC)$ [V vs. SCE]	Rev. CV?
PC 1	436	38500	5.5 ns [a)] 5000 μs [b)]	-1.87 [a)], -0.58 [b)]	0.98	Y
PC 2	320	3200	4.5 ns [a)], 420 ns [b)]	-1.97 [a), e)], -2.1 [a), f)]	0.82 [e)], 0.68 [f)]	Y
PC 3	317	3163	7.6 ns [a)]	-2.23 [a)]	0.83	Y
PC 4	367	4700	21 ns [a), c)] 1.20 s [b), c)]	-1.80 [g)] (-2.17) [h), i)]	0.29 (0.21) [h), i)]	Y
PC 5	366	5500	-	-1.64 [g)] (-2.04) [h), i)]	0.23 (0.10) [h), i)]	Y
PC 6	323	7848	3.2 ns [a), d)] 2.31 s [b), d)]	-1.67 [g)] (-1.84) [h)]	0.70 (0.55) [h)]	Y
PC 7	388	26635	-	-1.80 [g)] (-1.70) [h), j)]	0.65 (0.42) [h), j)]	Y
PC 8	375	19000	17.8 ns [a)]	-1.06 [g)]	1.50	N

[a)]Singlet state; [b)]Triplet state; [c)]Determined for dihydrophenazine derivative of 5,10-diphenyl-5,10-dihydrophenazine. Singlet lifetime was determined at 298 K and triplet lifetime was determined at 77 K, both in 3-methylpentane; [d)]Determined for phenoxazine derivative of 10-phenyl phenoxazine. Singlet lifetime was determined at 298 K in cyclohexane and triplet lifetime was determined at 77 K in 3-methylpentane; [e)]Determined in Pan, X. *et al*. *J. Am. Chem. Soc.* **2016**, *138*, 2411 in DMA; [f)]Determined in Treat, N. J. *et al. J. Am. Chem. Soc*. **2014**, *136*, 16096 in MeCN. [g)]Determined from a broad and featureless emission peak that was attributed as emssion from the charge transfer state. Charge transfer singlet and triplet states are close to isoenergetic such that singlet and triplet excited state reduction potentials are similar in values. [h)]Available DFT predicted values are enclosed in parenthesis. [i)]Reported values here were computed at the improved M06/6-311+G(d,p)//M06/6-31+G(d,p) level of theory. Previously reported values in Theriot, J.C. *et al. Science* **2016**, *352*, 1082 were computed at the M06/6-31+G(d,p) level of theory.m[j)]Reported values here were computed at the improved M06/6-311+G(d,p)//M06/6-31+G(d,p) level of theory. Previously reported values in Pearson *et al. J. Am. Chem. Soc.* **2016**, *138*, 11399 were computed at the M06/6-311+G(d,p)//M06/Lanl2dz level of theory.

therefore in close proximity prior to the ET reaction.[123] However, reactivity from the triplet state is typically proposed for photoredox catalysis due to its much longer lifetime (in the microseconds or more) because the triplet's transition to the singlet ground state is a spin-

forbidden process. Triplet lifetimes and triplet quantum yield for some related phenothiazines, dihydrophenazines and phenoxazines have been reported. For example, the triplet lifetime of 10-phenyl phenothiazine (PC 2) was determined to be ~ 420 ns in acetonitrile,[124] while the related 10-methyl phenothiazine has a triplet lifetime and quantum yield of 40 μs and 60% in DMA, respectively.[82] Similarly, 5,10-diphenyl-5,10-dihydrophenazine's triplet is long-lived (1.20 s) and its quantum yield is at least 26% in 3-methylpentane at 77 K. Moreover, 10-phenyl phenoxazine was determined to have a long triplet lifetime of 2.3 s and a triplet quantum yield of at least 94% in 3-methylpentane at 77K.[125] Future work should include measurement of triplet lifetimes and quantum yields of the remaining PCs featured in Figure 44 in order to provide important photophysical information pertinent to O-ATRP.

After the successful generation of the active exited state, the remainder of the catalytic cycle consists of electron transfer reactions to activate and deactivate the alkyl halide bond (~ - 0.8 V vs. SCE). Principles 4 and 5 are related to the thermodynamics of activation and deactivation, respectively. Table 10 lists $E^0(PC^{\bullet+}/PC^*)$ and $E^0(PC^{\bullet+}/PC)$ of PCs 1 – 8; available DFT predicted values are enclosed in the parenthesis. PC 1's singlet excited state is much more reducing than its corresponding triplet excited state with $E^0(PC^{\bullet+}/PC^*)$ values of -1.87 V and -0.58 V vs. SCE, respectively. PC 2 and 3's singlet excited state has reported $E^0(PC^{\bullet+}/PC^*)$ values of ~ -2V vs. SCE. PC 4, 5, 6, 7 and 8's $E^0(PC^{\bullet+}/PC^*)$ values were estimated from emission containing a broad and featureless peak, which suggests emission from a CT state. Singlet and triplet CT states are close to isoenergetic (<0.2 eV), thus the obtained $E^0(PC^{\bullet+}/PC^*)$ values from these emission data can represent both the singlet and triplet

excited state reduction potential.[118,126] PC 4, 5, 6, and 7 have $E^0(PC^{\bullet+}/PC^*)$ values of ~ -2 V while PC 8 has $E^0(PC^{\bullet+}/PC^*)$ = -1.06 V vs. SCE.

Generally, PCs employed in O-ATRP (Figure 44 and Table 10) are more reducing than is thermodynamically necessary for activation. It is expected, however, that some amount of overpotential will be necessary to overcome ET activation barriers (e.g. to overcome energetic costs for structural reorganization in the donor and / or acceptor), which makes a more negative $E^0(PC^{\bullet+}/PC^*)$ desirable.[127] With respect to O-ATRP deactivation, all PCs in Table 10 have sufficiently oxidizing radical cations to deactivate the growing polymer chains, where their $E^0(PC^{\bullet+}/PC)$ values are more positive than ~ - 0.8 V vs. SCE. Dihydrophenazine-derived radical cations are the most stable (~ 0.2 V vs. SCE for PC 4 and 5), followed by phenoxazines (~ 0.7 V vs SCE for PC 6 and 7), phenothiazines (~ 0.8 V vs. SCE for PC 2 and 3), perylene (0.98 V vs. SCE for PC 1), and 4CzIPN (1.50 V vs. SCE for PC 8). Dihydrophenazines, phenoxazines, and phenothiazines' radical cations are sufficiently stable that they exhibit reversible cyclic voltammograms, and many can be isolated (see Section 3.6.2). The radical cations should be sufficiently stable that they should not degrade prior to deactivation by the propagating radical. On the contrary, they also should not be too stable that the rate of deactivation is too slow. In another extreme, the radical cation of 4CzIPN is so reactive that it does not exhibit a reversible cyclic voltammogram.

The O-ATRP PCs that have demonstrated the most success thus far are derivatives of phenothiazine, phenazine, and phenoxazine core structures, due to their balance of strong excited state reduction potentials with stable and sufficiently oxidizing radical cations. However, their catalytic outcomes are not equivalent, which indicates there is more to be learned about catalyst design from a closer examination of this series. The most striking

difference between these three groups is the proposed ability of phenazines and phenoxazines, upon excitation, to more efficiently enter an intramolecular CT state, where the tricyclic core behaves as the electron donor and the *N*-aryl substituent behaves as the acceptor. The existence of the role CT plays in O-ATRP was first evidenced by computationally-observed spatially-separated SOMOs in PCs 4 – 6, among others (see

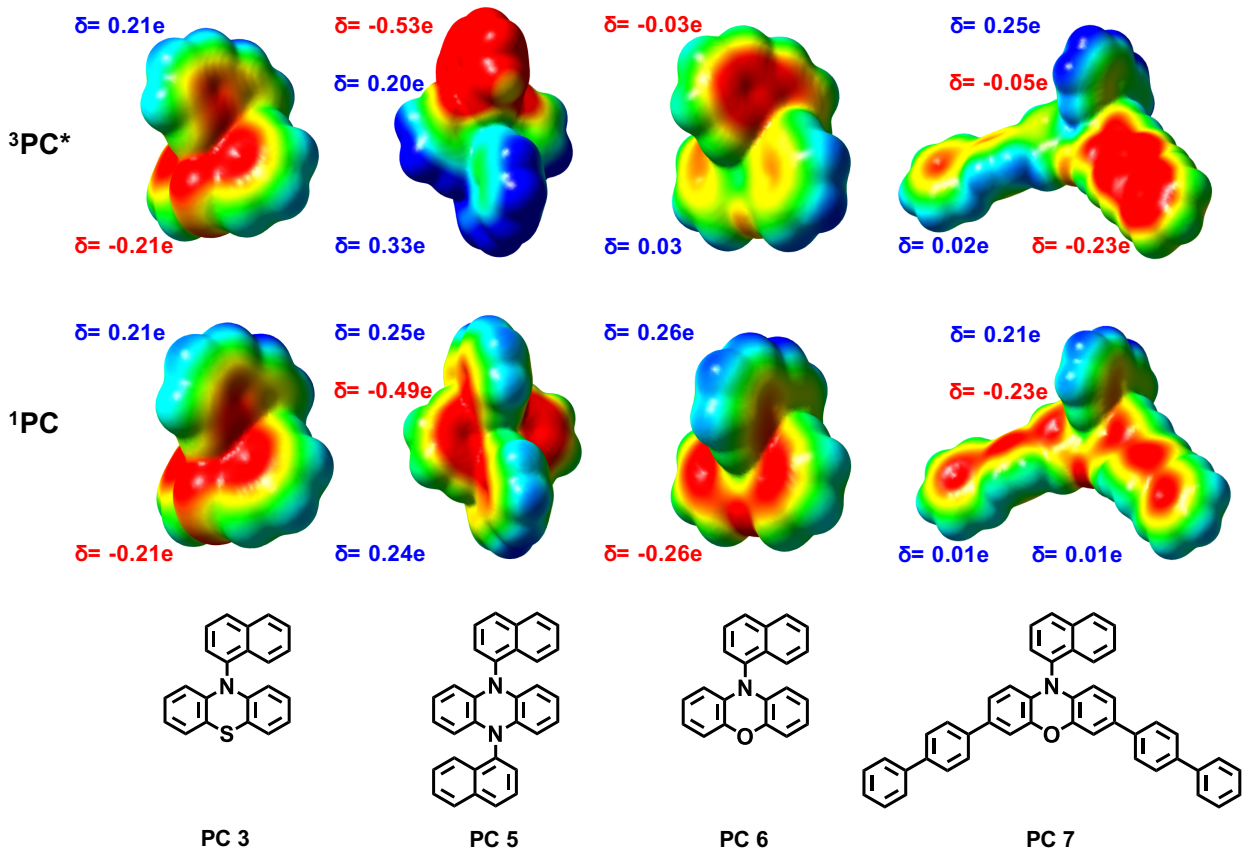

Figure 47. DFT-predicted electrostatic potential mapped electron density indicates intramolecular CT as the photocatalysts transition from the ground state ^{1}PC to the triplet state ^{3}PC*, in naphthyl-substituted dihydrophenazine and phenoxazines, but not phenothiazine. High electron density region is indicated by "red" color while low electron density region is indicated by "blue" color. Partial charges (δ) in the unit of electron (e) of the N-aryl substituent, catalyst core, and core-substituent are indicated. All PC 3, 5, 6, 7 were optimized at the unrestricted M06/6-31+G(d,p) level of theory. Adapted from Lim, C.-H. *et al. J. Am. Chem. Soc.* **2017**, *139*, 348 and Pearson *et al. J. Am. Chem. Soc.* **2016**, *138*, 11399.

Section 3.6.2). Further, electrostatic potential mapped electron density shows high localization of negative charge on the *N*-aryl substituent in the excited state, along with the observation of strong emission solvatochromism, provides additional support for the formation of CT states in dihydrophenazine catalysts (Figure 47).[128]

Direct comparison of the crystal structures of isoelectronic PCs 3 and 6 reveals that the core of PC 3 is bent into a boat shape whereas the core of PC 6 is planar (Figure 48).[44] The bent geometry of phenothiazine was attributed to the larger van der Waals radius of sulfur (1.80 Å) relative to oxygen (1.52 Å). Previous work posited that the bent core structure reduces electronic coupling between the core and the *N*-aryl substituent, which reduces the extent of CT in phenothiazine in comparison to phenoxazine.[129] To date, CT is empirically determined to be a major contributing factor to the successful polymerization results seen with phenazine and phenoxazine catalysts. While further investigation of the exact role of CT in O-ATRP is warranted, it is interesting to note that CT in these organic PCs is reminiscent to the photoredox-active metal-to-ligand charge transfer (MLCT) state observed for Ir and Ru polypyridyl PCs.[130–132]

Another factor to consider is the structural reorganization cost of the PCs during the photoredox O-ATRP cycle. Computations predict phenazines and phenoxazines (PCs 4 – 7) adopt close to planar geometries in their triplet, radical cation, and singlet ground states; as a result, these PCs have small structural reorganization energy and thus small kinetic barriers to electron transfer during the activation and deactivation steps. In contrast, phenothiazine is bent in the triplet and singlet ground states, while it is planar in the radical cation state. This represents more significant structural reorganization and thus kinetic cost during electron transfer events in the O-ATRP cycle. The effect that this additional energetic

toll has on the PC performance for phenothiazine PCs versus phenoxazine and phenazine PCs is unclear but it is hypothesized that this contributed to the poorer control over molecular weight distribution observed for phenothiazine PCs 2 and 3.

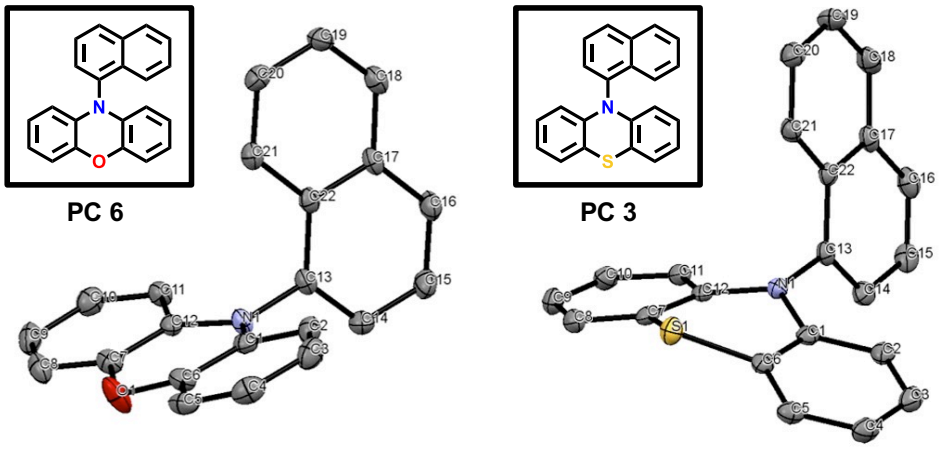

Figure 48. Crystal structures of PCs 3 and 6 show that PC 6 has a planar core whereas PC 3 has a bent core. Adapted from Pearson *et al. J. Am. Chem. Soc.* **2016**, *138*, 11399.

What arises from this deeper comparison of PCs, then, are additional design principles for O-ATRP PCs that are not as evidently presented by the mechanism as the first five. First is the ability to form CT states (see earlier Discussion). Second is a consistent geometry in the PC's ground state, excited state, and radical cation, as it limits the reorganization energy necessary for changing redox state of the PC during an O-ATRP catalytic cycle. While future mechanistic studies will undoubtedly uncover more design principles, these two (in addition to the five presented earlier) represent the current level of understanding in O-ATRP PC development, while the modular design of derivatives that allow for the tuning of properties of the PC and their continued study will undoubtedly refine these principles and reveal new insight.

3.6.4 Future Outlook

Despite its status as a relatively new methodology, O-ATRP is already establishing itself as a robust method for the metal-free production of specialty polymers. For example, PC 2 has been used for metal-free surface-initiated ATRP to functionalize silicon[133] and nanodiamond surfaces.[134] However, in order for O-ATRP to continue to expand its utility, some significant challenges remain to be addressed. Foremost among these is the need for increased mechanistic understanding. Factors such as the importance of CT and PC geometry make it clear that the success of O-ATRP is more detailed than simply matching reduction potentials. As more is learned into the intricacies of the mechanism, for example the kinetics of activation and mechanism of deactivation, additional design principles will be revealed, evolving PCs for more efficient catalysis. It will also be important to extend the application of O-ATRP to a broader monomer scope. Successful controlled polymerization of monomers including various (meth)acrylates and acrylonitrile has already been reported for O-ATRP. However, an increased monomer scope as well as expansion to additional classes of monomers, in particular unconjugated monomers such as vinyl acetate, is desirable.[16] Additionally, the ability to produce high MW polymers by O-ATRP must be demonstrated. Only phenazine PCs 4 and 5 have been shown to synthesize PMMA much larger than 20 kDa in a controlled manner.[40] Finally, the ability to use O-ATRP to synthesize more advanced copolymeric architectures beyond linear diblocks, such as multiblock copolymers, dendrimers, and graft copolymers.

CHAPTER 4

DEACTIVATION AND TERMINATION IN O-ATRP

4.1 Introduction

Atom transfer radical polymerization (ATRP) is a type of controlled radical polymerization which produces well-defined polymers by employing a metal catalyst to reversibly activate and deactivate a propagating carbon-centered radical.[10,135] Recently, organocatalyzed ATRP (O-ATRP) has emerged as a variant of ATRP which uses an organic photoredox catalyst (PC) to mediate the activation and deactivation steps of the ATRP mechanism.[26,28,40] Since the introduction of O-ATRP, continued efforts have focused on improved polymerization outcomes,[29,43,63,122] catalyst design,[44,128,136] and application to materials development.[81,134] Although mechanistic elucidation has been pursued, much remains to be learned about the mechanism of O-ATRP.[82,137] In particular, the nature of the deactivating species is yet to be confirmed and potential termination pathways within O-ATRP remain undefined.

In traditional copper catalyzed ATRP (Figure 49A), a Cu(I) catalyst reduces an alkyl halide in the activation step to yield the oxidized Cu(II) catalyst and a carbon-centered radical which can participate in polymerization propagation. Deactivation regenerates the Cu(I) catalyst and a produces the dormant halogen-capped species. In the proposed mechanism of O-ATRP (Figure 49B), activation occurs when the photoexcited PC directly

reduces an alkyl bromide initiator to give the oxidized, radical cation form of the PC, a bromide anion, and a carbon-centered radical which can propagate. Deactivation is proposed to occur through the reaction of the ion-paired radical cation PC and bromide with the propagating radical.

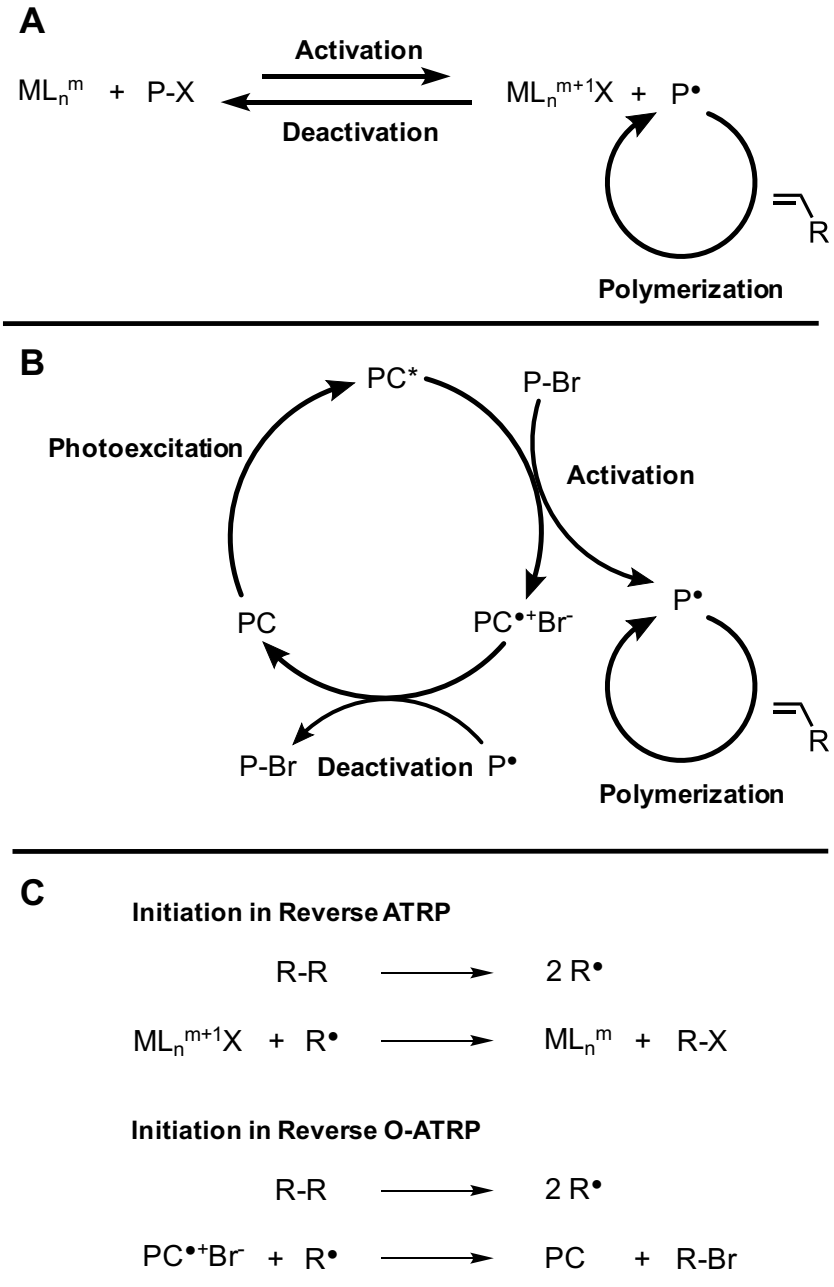

Figure 49. (A) General mechanism of ATRP. **(B)** Proposed mechanism of O-ATRP. **(C)** Comparison of initiation mechanism in reverse ATRP (top) and reverse O-ATRP (bottom)

Of the several types of organic PCs that have been shown to mediate O-ATRP, our group has particular interest in *N,N*-diaryl dihydrophenazines and *N*-aryl phenoxazines.[138] To probe deactivation in O-ATRP, we sought to synthesize, characterize, and employ in polymerization reactions the radical cation bromide of *N,N*-di(4-trifluoromethyl phenyl) dihydrophenazine PC **1**. We posited that dihydrophenazine-based PCs are well-suited to produce such radical cation salts due to their rather low oxidation potentials (0.29 V *vs.* the saturated calomel electrode [SCE] for **1**).[40] Further, isolable radical cations of *N,N*-dialkyl dihydrophenazines in the form of charge-transfer salts have been explored for their use in organic electronics.[139] However, radical cations of *N,N*-diaryl dihydrophenazines have, to the best of our knowledge, only been prepared and studied electrochemically.[140]

4.2 Radical Cation Synthesis and Characterization

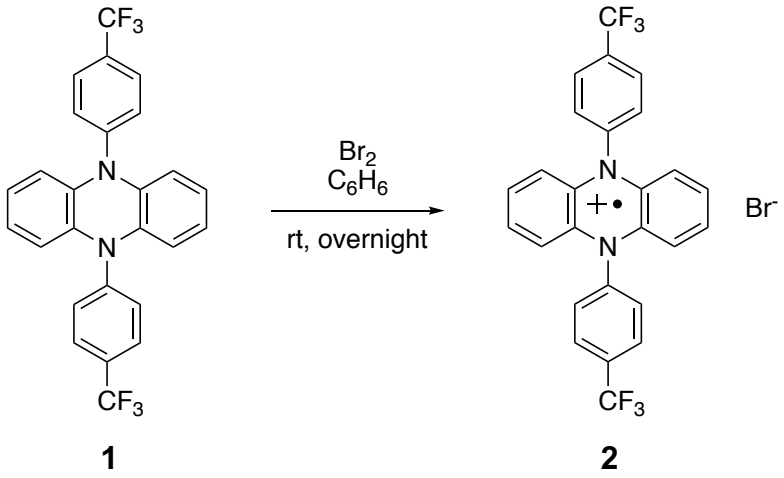

1 **2**

Figure 50. Scheme of the synthesis of radical cation bromide salt **2** from neutral species **1**.

5,10-di(4-trifluoromethylphenyl)-5,10-dihydrophenazine (PC **1**, Figure 50) (1.00 g, 2.13 mmol, 1.00 eq.) was added to an oven-dried round bottom flask fitted with stirbar. To this flask was added 400 mL benzene and liquid bromine (403 mg, 2.55 mmol, 1.20 eq.). A dark precipitate was observed to form almost immediately. The flask was sealed, vented, and left to stir overnight. The precipitate was collected *via* vacuum filtration and rinsed with approximately 50 mL of benzene three consecutive times to afford an army green powder (1.12 g). Elemental analysis indicated this product was primarily a tribromide. To obtain the bromide salt, this powder was then dissolved in stirring methanol, heated at 60 °C for 15 minutes, filtered, and placed in a freezer. After three days, the solution was filtered to obtain 377 mg dark green crystals of **2** (Figure 50). Elem. Anal: calc'd for $C_{26}H_{16}F_6N_2Br$: C, 56.75; H, 2.93; N, 5.09. Found: C, 56.74; H, 2.86; N, 5.05. HRMS (ESI+): calc'd for $M^{\bullet+}$ $C_{26}H_{16}F_6N_2$, 470.1218; found 470.1218. UV/Vis: λ_{max} 481 nm (DMAc) (See Figures 51 and 52 for

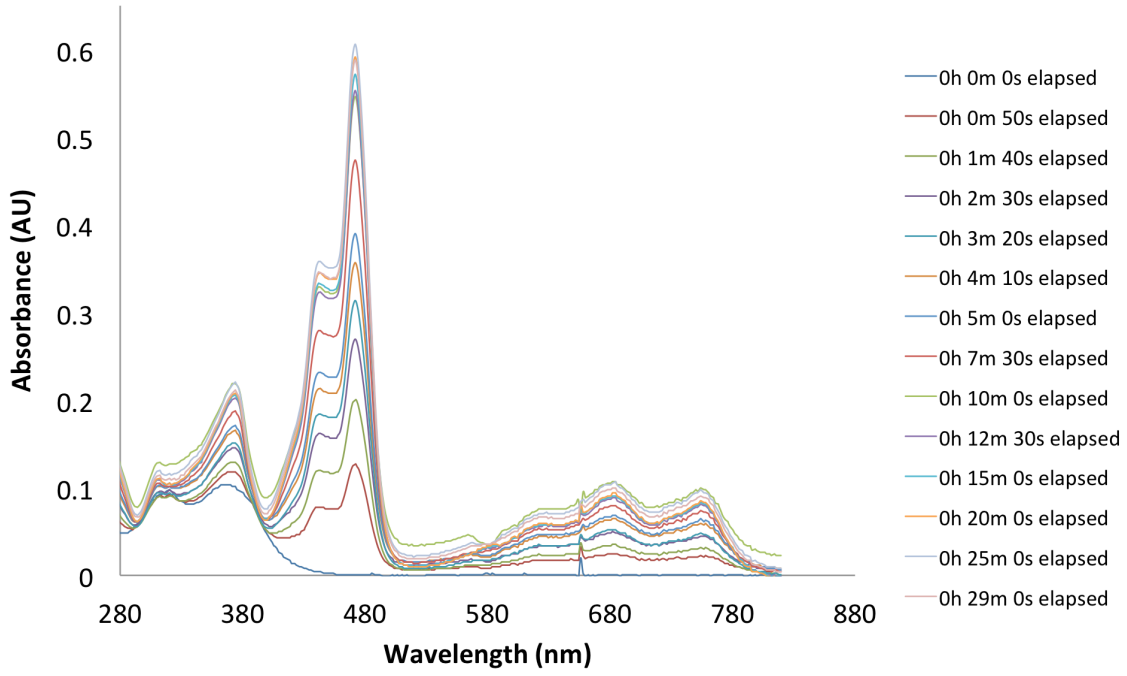

Figure 51. Spectroelectrochemical analysis of **1** in MeCN at an applied potential of 0.25 V.

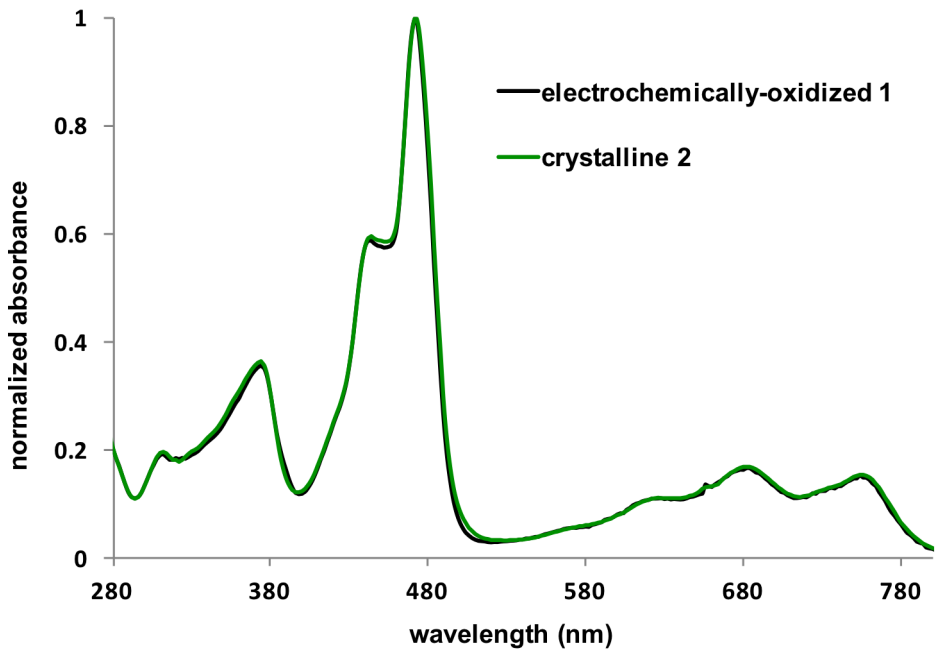

Figure 52. Overlay of the absorbance spectra collected from the final time point from Figure 51 and of crystalline **2** in MeCN.

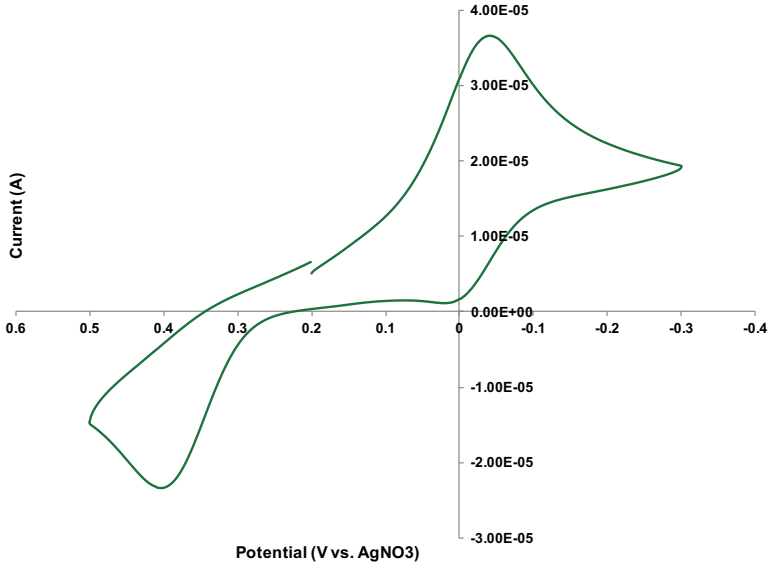

Figure 53. Cyclic voltammogram of **2** as a tribromide salt in MeCN.

additional spectral data). E^0 = 0.28 V *vs*. SCE (Figure 53). Product **2** was found to be water-soluble and, in the solid state, able to be handled and stored in air over a period of several months.

Single-crystal X-ray diffraction (SCXRD) data were acquired for both species **1** and **2** (Figure 54). It has been previously suggested that an advantage for *N,N*-diaryl dihydrophenazines as O-ATRP catalysts is the near-planar nature of the ground state PC.[44] Computations predicted that, for this class of PCs, the singlet and triplet ground states as well as the radical cation all adopt a nearly-planar geometry within the tricyclic core. Having similar geometries reduces the reorganization energy, and therefore kinetic barrier, of the electron-transfer steps within O-ATRP, which we hypothesize favors improved polymerization outcomes.[136]

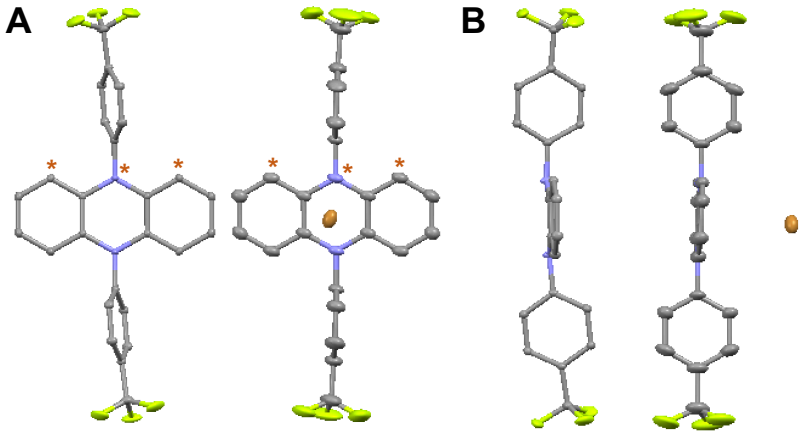

Figure 54. (**A**) Crystal structures of the tricyclic core-facing view of **1** (left) and **2** (right). Asterisks indicate atoms used for core planarity measurements. (**B**) Crystal structures of the side-facing view of **1** (left) and **2** (right).

The geometric similarity of the ground state PC **1** and the radical cation **2** is evidenced by the SCXRD data. The core of the neutral catalyst **1** deviates from planarity by 9.3° (determined by a C-N-C angle of 170.7°, atoms as indicated in Figure 54A), whereas the core of radical cation bromide salt **2** is, as expected, effectively planar (as determined by a C-N-C angle of 179.0°). This change in geometry is smaller than that needed for an *N*-aryl phenoxazine (analogous C-N-C 11.1° off-planar) or an *N*-aryl phenothiazine (analogous C-N-C 26.6° off-planar).[44]

4.3 Reverse O-ATRP

In copper-catalyzed ATRP, a reverse-initiation polymerization begins with the oxidized form of the catalyst and a free radical initiator, such as azobisisobutryronitrile (AIBN), instead of an alkyl halide initiator (Figure 49C, top).[141,142] As radicals are generated by decomposition of the radical initiator, they are deactivated by Cu(II), to yield Cu(I) and a halide-capped radical, which can then participate in the traditional ATRP catalytic cycle. To investigate the proposed role of the PC radical cation bromide as the deactivating species in O-ATRP, the ability of **2** to participate in an analogous reverse-initiation O-ATRP (Figure 49C, bottom) was investigated.

To perform reverse-initiation O-ATRP, a solution of methyl methacrylate (MMA), AIBN, and **2** in dimethylacetamide (DMAc) was heated at 110 °C for 15 minutes to allow for rapid decomposition of the AIBN, and then irradiated with visible light for 18h. The results of a set of such experiments show that reverse-initiation O-ATRP produces poly(methyl methacrylate) (PMMA) of low dispersity ($Đ$) of 1.30, indicating a controlled polymerization (Table 11). When the AIBN concentration is increased such that there are more equivalents

of radicals produced than equivalents of **2** present, $Đ$ increases to 1.70. Additionally, no polymerization is observed in the absence of light and no control is observed when the neutral catalyst **1** is used instead of the deactivator. Finally, control is also observed for a reverse O-ATRP system which omits AIBN and instead relies on spontaneous generation of MMA radicals from the reaction conditions. Because **2** is still able to deactivate such radicals to produce a controlled polymerization, this experiment represents an initiator-free version of O-ATRP.

Table 11. Results of Reverse O-ATRP Experiments.

Entry	PC	[MMA]:[AIBN]:[PC][a]	Conv. (%)[b]	M_w (kDa)[c]	$Đ$[c,d]
1	**2**	100:0.5:1	48	23.2	1.30
2	**2**	100:1:1	75	15.7	1.70
3	none	100:0.5:0	64	39.2	2.38
4	none	MMA only	25	857	1.68
5[e]	**2**	100:0.5:1	0	-	-
6	**1**	100:0.5:1	59	45.4	3.30
7	**2**	100:0:1	33	34.7	1.32

[a] Relative to 1.87 mmol MMA. Run in 0.20 mL DMAc. [b] Measured using ^{1}H NMR. [c] Measured using light scattering. [d] M_w / M_n. [e] No light exposure.

Taken together, these results show that **2** is capable of mediating a controlled radical polymerization in a reverse fashion, a substantiation of its role as the deactivating species in O-ATRP. To further support this claim, a chain extension experiment was performed using a PMMA macroinitiator synthesized using reverse O-ATRP (Figure 55). The macroinitiator was employed in a normal-initiation O-ATRP experiment using **1** as the PC. A high proportion of the macroinitiator extended, indicating the successful installation of bromide end-groups onto polymers synthesized *via* reverse O-ATRP (Figure 56).

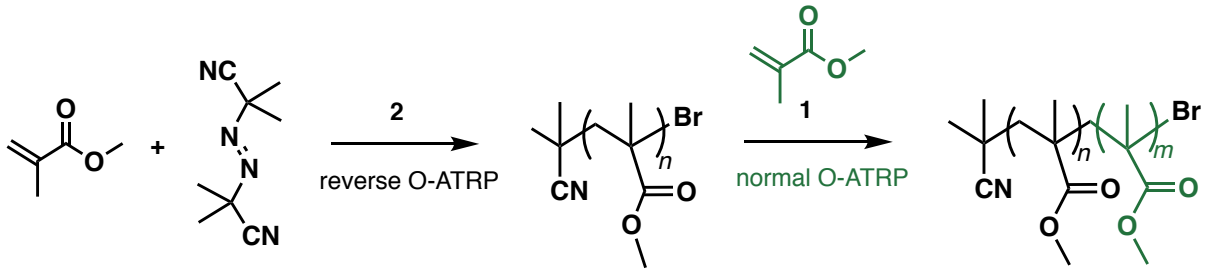

Figure 55. Scheme depicting chain extension from a macroinitiator prepared *via* reverse O-ATRP.

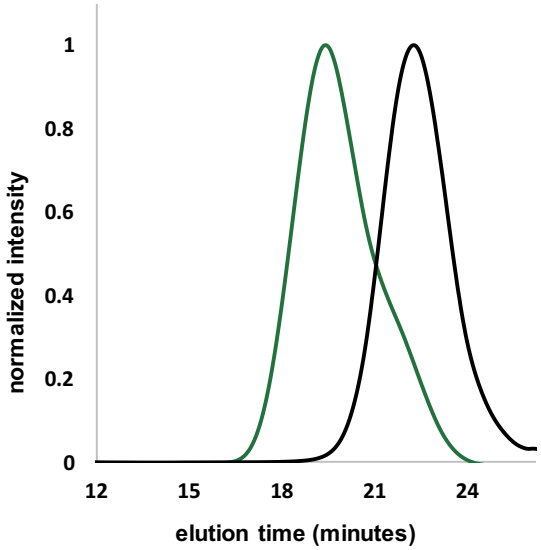

Figure 56. GPC traces of the macroinitiator (black) and chain-extended polymer (green).

4.4 O-ATRP with Supplemental Deactivator

In ATRP, control is dependent upon the ability to rapidly deactivate growing radical chains. However, in a normal-initiation ATRP, deactivator is not initially present and is instead generated through the activation process. As such, it has been shown that the addition of supplemental Cu(II) to a normal-initiation ATRP improves control over the polymerization.[143] With this phenomenon in mind, we added supplemental deactivator in the form of **2** to normal-initiation O-ATRP experiments (Table 12). Addition of up to 0.1

equivalents of **2** improved the linearity of number-average MW growth *vs*. conversion and reduced the observed *Đ* at earlier stages of the polymerizations (Figure 57). The use of greater amounts of deactivator, ranging from 0.2 to 3.0 equivalents, did not continue to improve polymerization results. Instead, a slight rise in *Đ* from 1.25 to 1.30 and a sharp decrease in initiator efficiencies (*I**) from approximately 80% to 43% are observed.

Table 12. Results of O-ATRP Experiments Using **2** as Supplemental Deactivator.

Entry	[MMA]:[I]:[1]:[2][a]	Time (h)	Conv. (%)[b]	M_w (kDa)[c]	*Đ*[c,d]	*I**[e]
1	1000:10:1:0	7	93	15.2	1.25	78
2	1000:10:1:0.1	6	96	15.7	1.24	77
3	1000:10:1:0.2	7	94	14.4	1.25	83
4	1000:10:1:0.4	8	95	15.3	1.27	80
5	1000:10:1:0.6	8	94	17.0	1.27	71
6	1000:10:1:1	8	92	18.0	1.28	67
7	1000:10:1:2	10	94	24.5	1.30	51
8	1000:10:1:3	10	93	28.5	1.30	43

[a] I = initiator, MBriB. Ratios relative to 9.35 mmol MMA. Run in 1.00 mL DMAc. [b] Measured using ^{1}H NMR. [c] Measured using light scattering. [d] M_w / M_n. [e] ($M_{n,\,theo.}$ /$M_{n,\,GPC}$).

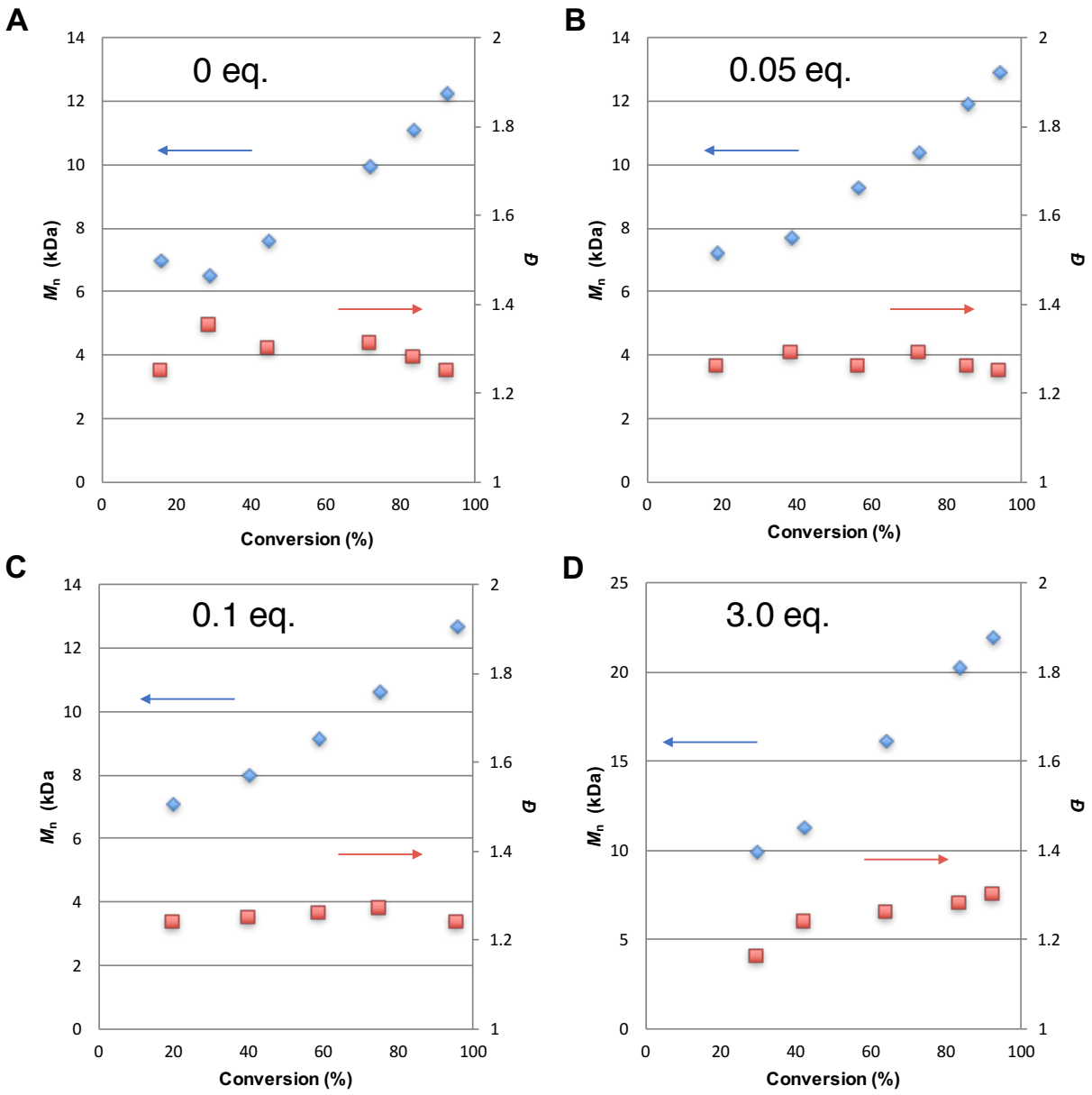

Figure 57. Traces of M_n and *Đ vs.* conversion for selected polymerizations using supplemental deactivator. (**A**) 0 eq., (**B**) 0.05 eq., (**C**) 0.1 eq., (**D**) 3.0 eq. Blue diamonds: M_n *vs.* conversion. Red squares: *Đ vs.* conversion.

4.5 Radical Addition to Catalyst

The sharp decrease in *I** as increasing equivalents of PC (be it **1** or **2** – see Table 14) are added to the polymerization suggests reactivity between the catalyst and the initiator. To further investigate this possibility, a series of mass spectrometry (MS) experiments were performed. PC **1** and alkyl halide initiator (either methyl bromoisobutyrate [MBriB] or ethyl α-bromophenylacetate [EBP]) were combined in DMAc and irradiated with visible light for 2 hours. The volatiles were removed and the residue was analyzed using electrospray ionization MS (ESI-MS) (Figures 62 and 63). In this analysis, **1** was not observed and instead, masses corresponding to structures **3** (for the MBriB experiment) and **4** (for the EBP experiment) were observed (Figure 58).

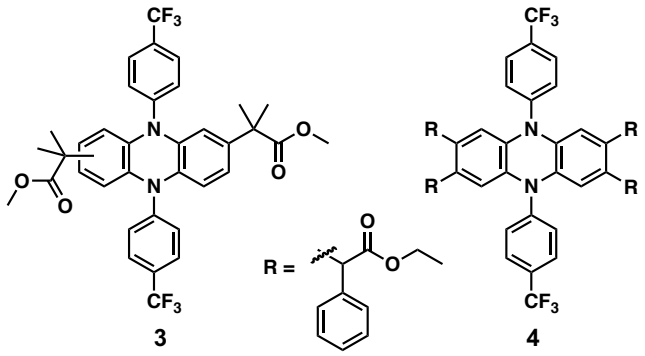

Figure 58. Structures **3** and **4**.

These results indicate that initiator fragment addition to catalyst is a potential termination pathway in O-ATRP, and may contribute to the non-ideal *I** regularly seen when **1** is employed in O-ATRP. A similar experiment was performed, this time including MMA (Figure 64). An aliquot was taken after 20 minutes and similarly analyzed by ESI-MS (Figure 65). This experiment revealed that PMMA oligomers can also add to the catalyst, suggesting

that radical addition to catalyst, whether in the form of initiator fragments or oligomers, is a termination pathway in O-ATRP.

Such radical additions to catalysts have been seen elsewhere in photoredox catalysis, in the form of alkylation of the ligands of *fac*-Ir(ppy)$_3$ PC.[144] To investigate whether this termination pathway can be eliminated by blocking reactive sites on the PC, **3** and **4** were synthesized (see Section 4.6) and employed as catalysts in O-ATRP using their respective initiators (MBriB for **3** and EBP for **4**). Significantly, the use of these substituted catalysts results in polymerizations with $I^* > 90\%$ (Table 13). These data suggest that the termination pathway of radical addition to catalyst which consumed initiator and therefore lowered I^*, has been effectively suppressed by the use of substituted PCs.

Table 13. O-ATRP results using substituted catalysts **3** and **4**.

Entry	PC	Initiator	Time (h)	Conv. (%)[a]	M_w (kDa)[b]	$Đ$ (M_w/M_n)[b]	I^* ($M_{n,\,theo.}/M_{n,\,GPC}$)
1	1	MBriB	7	92	15.2	1.25	77
2	3	MBriB	6	93	14.3	1.33	91
3	1	EBP	8	98	17.9	1.17	64
4	4	EBP	7	92	12.4	1.24	94

Ratios relative to 9.35 mmol MMA. Run in 1.00 mL DMAc. [a]Measured using ^{1}H NMR. [b]Measured using light scattering.

In conclusion, the deactivation mechanism of O-ATRP has been explored, establishing the radical cation bromide salt of the PC to be the deactivator in O-ATRP. Additionally, the use of supplemental deactivator in normal-initiation O-ATRP was found to give minor improvements to control in the early stages of polymerization. These experiments provided insight into reactions occurring between the initiator and PC. Further investigation of these reactions showed that radical addition to PC, in the form of both initiator addition and

oligomer addition, is a termination pathway in O-ATRP. Finally, it was shown that the use of core-substituted catalysts effectively blocks these radical addition termination pathways, resulting in high *I** for the polymerization.

4.6 Supporting Information

Materials and Methods

Reagents used in this research were purchased from *Sigma-Aldrich*. Chemicals used in polymerizations were purified in the following manner: methyl methacrylate (MMA) and dimethylacetamide (DMAc) were dried over CaH_2, vacuum distilled, and degassed by three consecutive freeze-pump-thaw cycles before storage and use in the nitrogen glovebox. Initiators (methyl bromoisobutyrate [MBriB] and ethyl alpha-bromophenylacetate [EBP]) were vacuum distilled and degassed by three consecutive freeze-pump-thaw cycles before storage and use in the nitrogen glovebox. MBriB, EBP, azobisisobutyronitrile (AIBN), and MMA were stored at -34 ^{o}C in the glovebox freezer and allowed to warm to room temperature before use in polymerizations. All other reagents were used as received.

The photoreactors were assembled with a 400 mL beaker wrapped in aluminum foil and lined on the inside with a coil of white LEDs (16-inch strip, double density white LEDs).[40] See "Polymerization Procedures" for additional information on specific methods used for each polymerization type.

^{1}H, ^{13}C, and ^{19}F NMR spectroscopy were obtained using a Bruker 300MHz spectrometer, or a Varian INOVA 400 MHz or 500 MHz spectrometer, as reported. Chemical shifts were referenced to an internal solvent resonance as parts-per-million (ppm) relative to tetramethylsilane (TMS). Polymer molecular weights were obtained *via* gel permeation

chromatography (GPC) coupled with multi-angle light scattering (MALS), using an Agilent HPLC fitted with one guard column and three PLgel 5 μm MIXED-C gel permeation columns, a Wyatt Technology TrEX differential refractometer, and a Wyatt Technology miniDAWN TREOS light scattering detector, using THF as the eluent at a flow rate of 1.0mL/min. Electrospray ionization mass spectrometry (ESI-MS) was performed on a Waters Synapt G2 HDMS Qtof with MeCN as the solvent at the University of Colorado Boulder's Central Analytical Mass Spectrometry Facility. Ultraviolet-visible spectroscopy was performed on an Aglient spectrophotometer or a Varian Cary 5000 UV-VIS-NIR spectrophotometer. Cyclic voltammetry and spectroelectrochemical experiments were performed using a CH Instruments electrochemical analyzer with a $Ag/AgNO_3$ (0.01 M in MeCN) reference electrode using MeCN as the solvent and $TBAPF_6$ (0.1 M in MeCN) as the electrolyte. Elemental analysis data were acquired by Robertson Microlit Laboratories. Single crystal X-ray diffraction (SCXRD) data were acquired at the Colorado State University Central Instrumentation Facility. See "X-Ray Diffraction Experiments" for more information.

Synthesis and Characterization

*Synthetic Procedure for **3** (2,7-di(methylisobutyrate-yl)-5,10-di(4-trifluoromethylphenyl)-5,10-dihydrophenazine)*

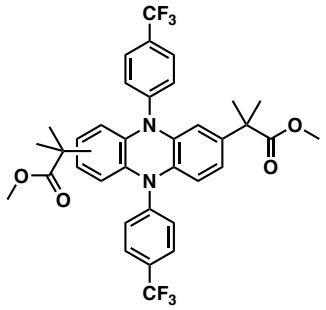

A 100 mL round bottom flask was charged with a small stirbar and **1** (200 mg, 0.425 mmol, 1.00 eq.), and transferred into an N_2 glovebox. MBriB (231 mg, 1.28 mmol, 3.00 eq.), and solvent (40.0 mL DMF) were added to the flask sequentially *via* pipette. The flask was sealed and placed into a beaker on a stirplate and irradiated with white LED light for 18 h. The resulting solution was then removed from the glovebox and dried under reduced pressure to reveal a yellow solid. This solid was dissolved in minimal DCM and hexanes were added until a precipitate formed. This precipitate was collected *via* vacuum filtration and dried under reduced pressure to afford a light yellow powder (201 mg, 71%). ^{1}H NMR (C6D6, 400 MHz): δ 7.38 (d, 4H), 7.01 (d, 4H), 6.43 (d, 2H), 5.99 (d, 2H), 5.66 (d, 2H), 3.22 (s, 6H), 1.31 (s, 12H). ^{13}C NMR (C6D6, 300 MHz): δ 176.24, 144.36, 139.21, 136.25, 135.00, 131.24, 130.28, 127.92, 119.23, 114.15, 113.67, 112.74, 111.98, 51.54, 45.97, 26.40. HRMS (ESI+): calc'd for for M^+ $C_{36}H_{32}F_6N_2O_4$, 670.2266; found 670.2287.

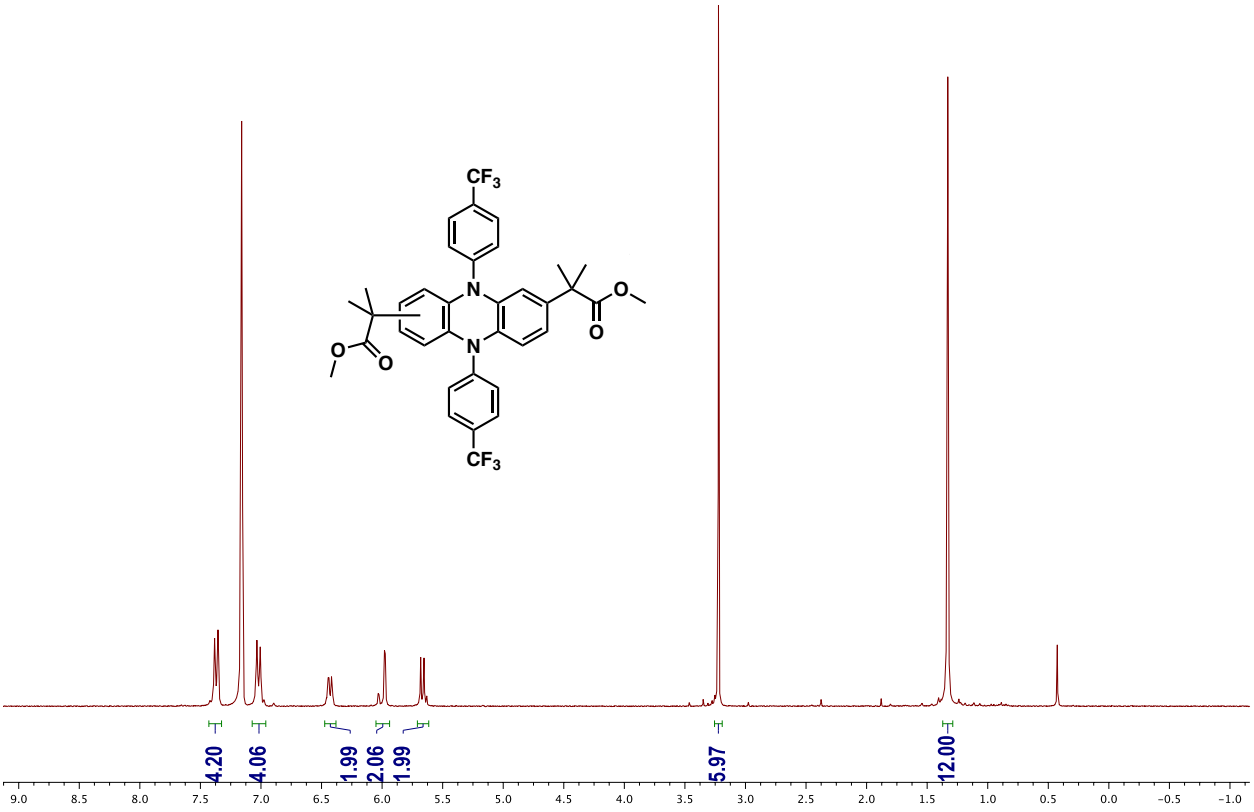

Figure 59. ^{1}H NMR spectrum of **3**.

*Synthetic procedure for **4***

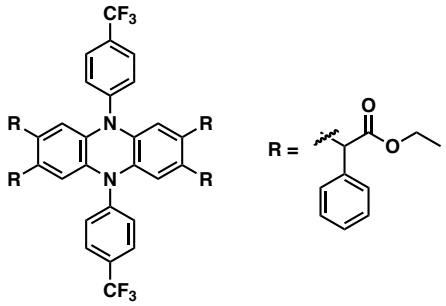

A 100mL round bottom flask was charged with a small stirbar and **1**, (200 mg, 0.425 mmol, 1.00 eq.), and transferred into an N_2 glovebox. EBP (516 mg, 2.13 mmol, 5.00 eq.), and solvent (40.0 mL DMF) were added to the flask sequentially *via* pipette. The flask was sealed

and placed into a beaker on a stirplate and irradiated with white LED light for 18h. The resulting solution was then removed from the glovebox and dried on a rotovap to reveal a red-brown viscous liquid. This liquid was dissolved in a minimal amount of a 50% DCM / 50% hexanes mixture placed in the freezer for 24h. A yellow microcrystalline material was collected and dried under reduced pressure to afford 11 mg yellow powder (<5 %). ^{1}H NMR (C6D6, 400 MHz): δ 7.22 (d, 4H), 7.08 (d, 8H), 7.03-6.93 (m, 12H), 6.84 (d, 4H), 5.93 (s, 4H), 5.24 (s, 4H), 3.93-3.71 (m, 8H), 0.79 (t, 12H). HRMS (ESI+): calc'd for M^{+} $C_{66}H_{56}F_6N_2O_8$, 1118.3940; found 1118.3920.

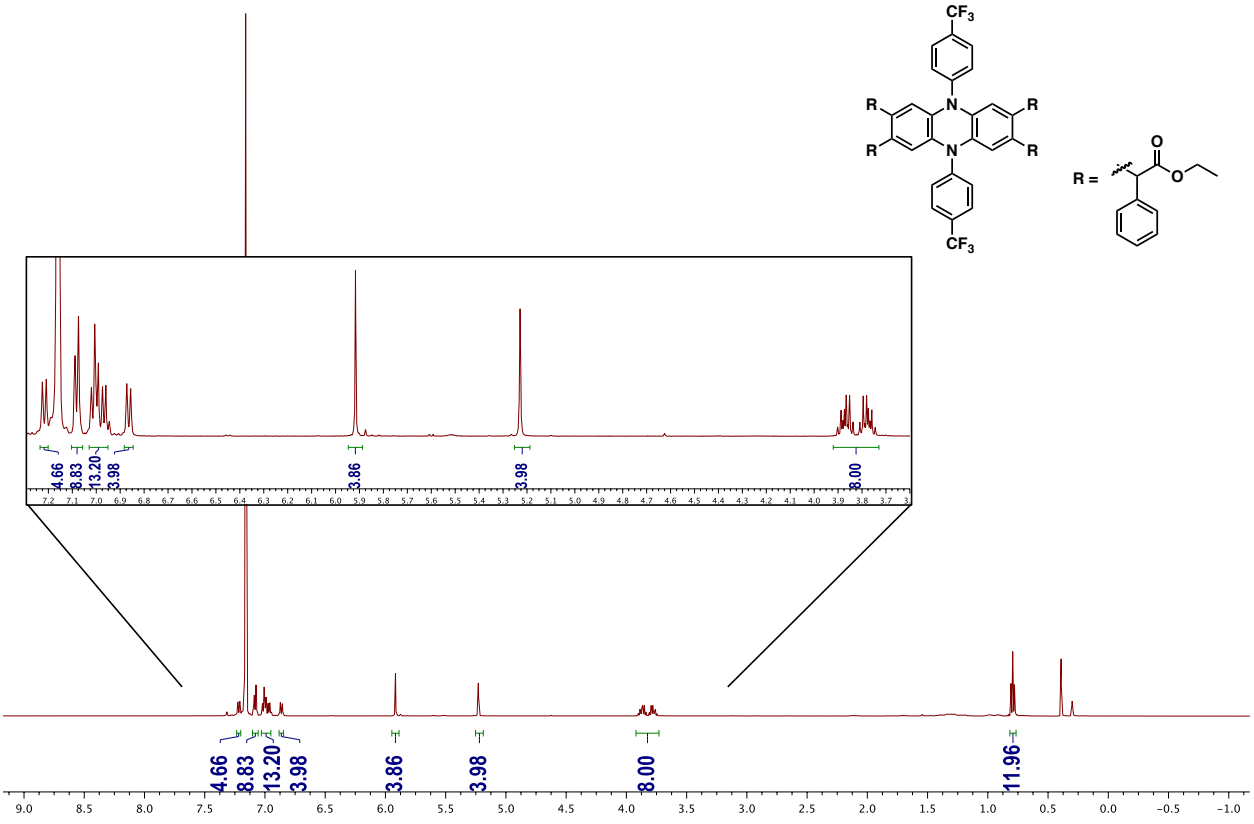

Figure 60. ^{1}H NMR spectrum of **4**.

Polymerization Procedures

General Procedure for Reverse O-ATRP (Table 11)

A 20 mL glass vial with a non-metal lined cap was charged with a small stirbar and the indicated number of equivalents of **2** and transferred to a nitrogen-atmosphere glovebox. Solvent (DMAc, 0.200 mL) monomer (MMA, 0.200 mL, 1.87 mmol, 100 eq.) and initiator (AIBN, number of equivalents as indicated) were then added to the vial. The vial was sealed under the nitrogen environment and brought out of the glovebox and additionally sealed with plastic laboratory film. The polymerization mixture at this time was a clear liquid, of varying shades of dark green in color (depending on the amount of **2** used). The vial was placed in a dark oven chamber and heated at 110 °C for 15 minutes. Within this timespan, the reaction mixture underwent noticeable color change from the dark green to a light yellow. The vial was then set to stir in a photoreactor inside a hood for 18 hours. The product was analyzed by dissolving a portion into $CDCl_3$ with 250 ppm butylated hydroxytoluene (BHT) to quench any further reaction and subjecting to ^1H NMR to measure conversion. The sample was then dried and re-dissolved in THF for analysis of molecular weights (MWs) by gel permeation chromatography coupled with multi-angle light scattering (GPC).

General Procedure for Normal-Initiation O-ATRP (Including O-ATRP with Supplemental Deactivator [Table 12] and O-ATRP with Substituted Catalysts [Table 13])

A 20 mL vial was charged with a small stirbar and 4.4 mg (0.00935 mmol, 1 eq.) **1** and the indicated number of equivalents of **2** and transferred into a nitrogen-atmosphere glovebox. Solvent (DMAc, 1.0 mL) monomer (MMA, 1.0 mL, 9.35 mmol, 1000 eq.) and initiator (EBP or MBriB as indicated, 0.0935 mmol, 10 eq.) were then added to the vial

sequentially *via* pipette. The vial was then sealed and placed inside a photoreactor on a stir plate. The reaction was then analyzed at the indicated time point by removing a 0.1 mL aliquot *via* syringe and injecting into a vial containing 0.7 mL $CDCl_3$ with 250 ppm BHT. This aliquot was then analyzed by ^1H NMR for conversion, dried, and re-dissolved in THF for analysis of MWs by GPC.

Procedure for Chain Extension from a Reverse O-ATRP Macroinitiator

A sample of polymer was prepared according to the above reverse O-ATRP polymerization procedure using 0.400 mL MMA (3.74 mmol, 100 eq.), 3.05 mg AIBN (0.019 mmol, 0.50 eq.), and 20.3 mg **2** (0.037 mmol, 1.00 eq.) in 0.400 mL DMAc. The polymerization was performed for 10 hours, and then the reaction mixture was added dropwise to rapidly stirring 50% MeOH / 50% water solution to precipitate out the polymer product, which was collected by vacuum filtration. The polymer was then re-dissolved in a minimal amount of THF and subjected to the same precipitation process two more times. This "macroinitiator" was analyzed by GPC and found to have M_n = 16.6 kDa, $Đ$ = 1.40 (Figure 56, black trace). 127 mg (0.008 mmol, 10 eq.) of this macroinitiator was then added to a 20 mL vial fitted with a stirbar and brought into a nitrogen atmosphere glovebox. To this was added 0.5 mL (4.7 mmol, 6000 eq.) MMA, 1.0 mL DMAc, and 0.4 mg (0.0008 mmol, 1 eq.) **1.** The vial was then sealed and placed inside a photoreactor on a stir plate. After 22 hours, the vial was removed from the glovebox and the reaction mixture was diluted with 1.00 mL THF. This mixture was added dropwise to rapidly stirring 50% MeOH / 50% water solution to precipitate out the product polymer. This product was then collected by vacuum filtration and analyzed by GPC (M_n = 105 kDa, $Đ$ = 1.74) (Figure 56, green trace).

Additional Polymerization Results

Chain-End Analysis of a Polymer formed from Reverse O-ATRP

A sample of polymer was prepared according to the above reverse O-ATRP polymerization procedure using 0.400 mL MMA (3.74 mmol, 100 eq.), 3.05 mg AIBN (0.019 mmol, 0.50 eq.), and 20.3 mg **2** (0.037 mmol, 1.00 eq.) in 0.400 mL DMAc. The polymerization was performed for 10 hours, and then the reaction mixture was added dropwise to rapidly stirring 50% MeOH / 50% water solution to precipitate out the product polymer, which was collected by vacuum filtration. This sample was analyzed by MALDI-TOF (Figure 61). A plot of m/z vs. number of repeat units gave a slope equal to the mass of MMA and a y-intercept equal to the mass of isobutyronitrile plus Na (used in preparation of the sample). The Br chain-end group is not observed, which has been reported to be cleavable during MALDI-TOF analysis of polymers formed *via* ATRP and O-ATRP.[26,145]

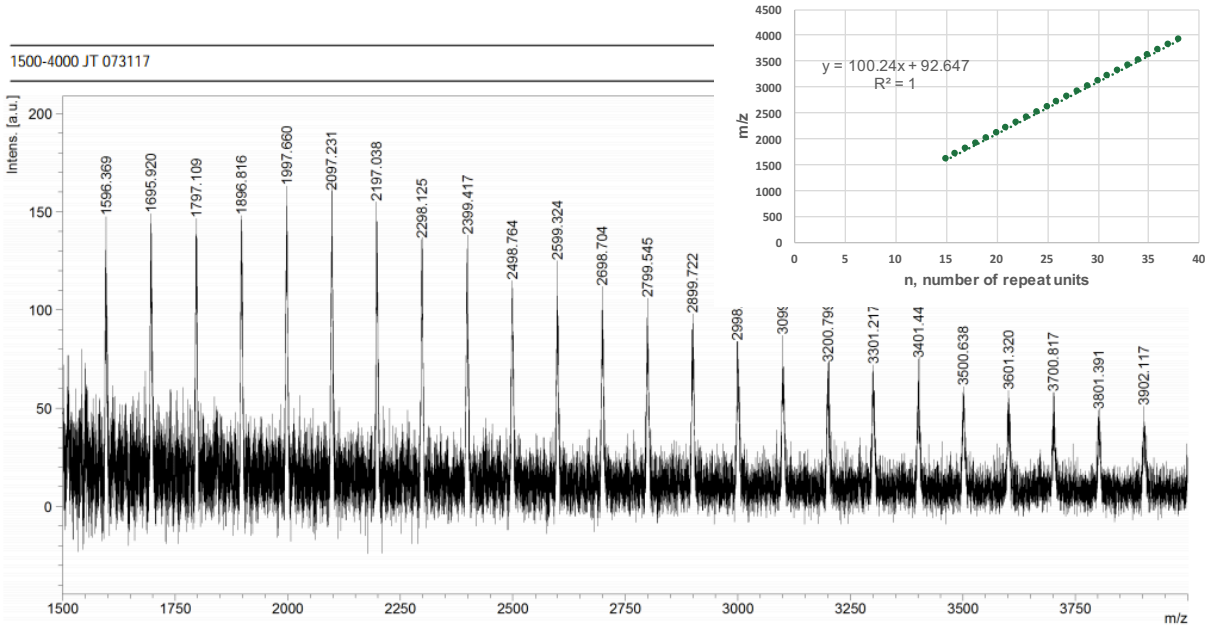

Figure 61. MALDI-TOF mass spectrum of a PMMA sample prepared using reverse O-ATRP. (Inset) Plot of m/z vs. number of repeat units showing a slope equal to the mass of MMA and a y-intercept equal to the mass of isobutyronitrile plus Na.

Results with Additional Neutral Catalyst

Polymerizations with additional neutral catalyst were performed according to the general polymerization procedure for normal-initiation O-ATRP.

Table 14. O-ATRP results using various amounts of **1**.

Entry	[MMA]:[MBriB]:[**1**]	Time (h)	Conv. (%)[a]	M_w (kDa)[b]	$Đ$ (M_w/M_n)[b]	I^* ($M_{n,\,theo.}/M_{n,\,GPC}$)
1	1000:10:1	7	92	15.2	1.25	77
2	1000:10:1.5	6	88	13.5	1.26	83
3	1000:10:2	6	90	13.5	1.29	88
4	1000:10:3	6	88	19.4	1.33	61

Ratios relative to 9.35 mmol MMA. Run in 1.00 mL DMAc. [a]Measured using ^{1}H NMR. [b]Measured using light scattering.

Mass Spectrometry Experiments

Initiator Addition to Catalyst

A 20 mL vial was charged with 5 mg (0.01 mmol, 1.00 eq.) **1** and a stirbar and brought into a nitrogen atmosphere glovebox. To this vial was added 1.00 mL DMAc and 10.0 eq. initiator (MMA or EBP, as indicated). The vial was then sealed and placed in a photoreactor on a stirplate. After 2 hours, the vial was removed from the glovebox and the volatiles were removed under reduced pressure. The sample was then analyzed by ESI-MS.

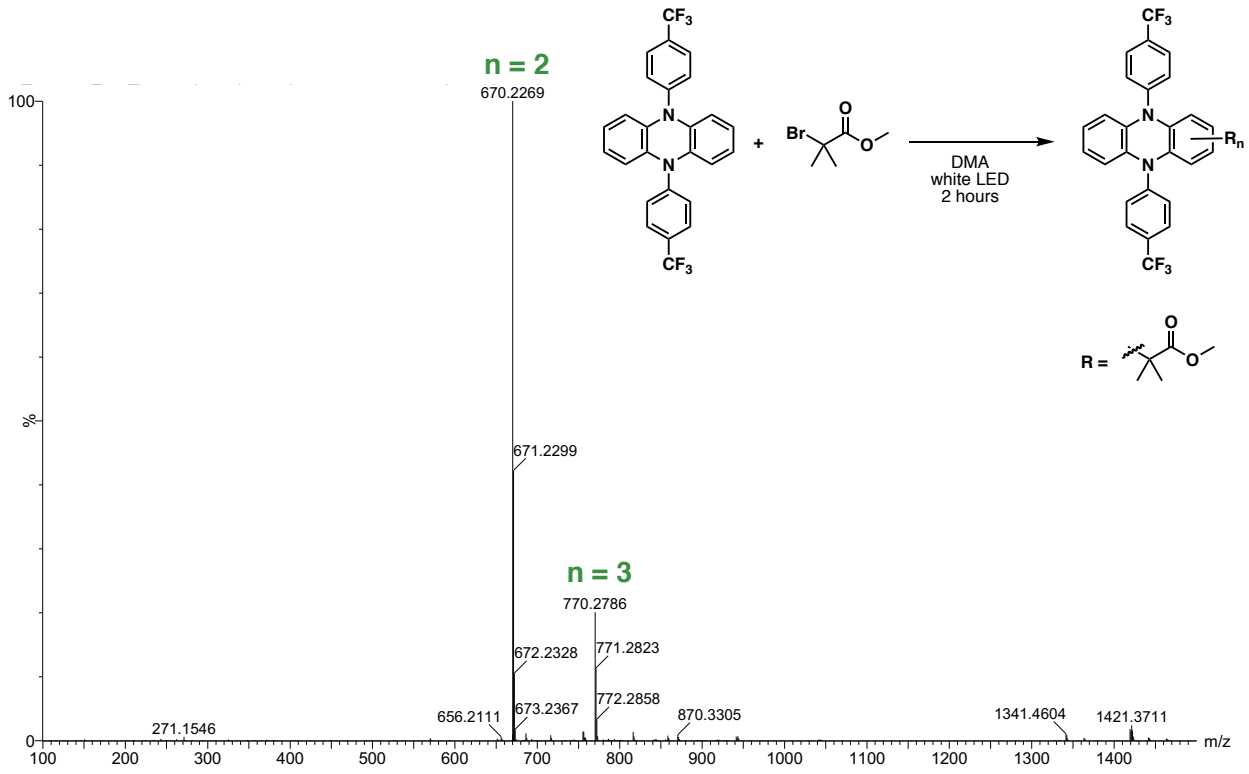

Figure 62. ESI-MS of residue from above experiment using MBriB.

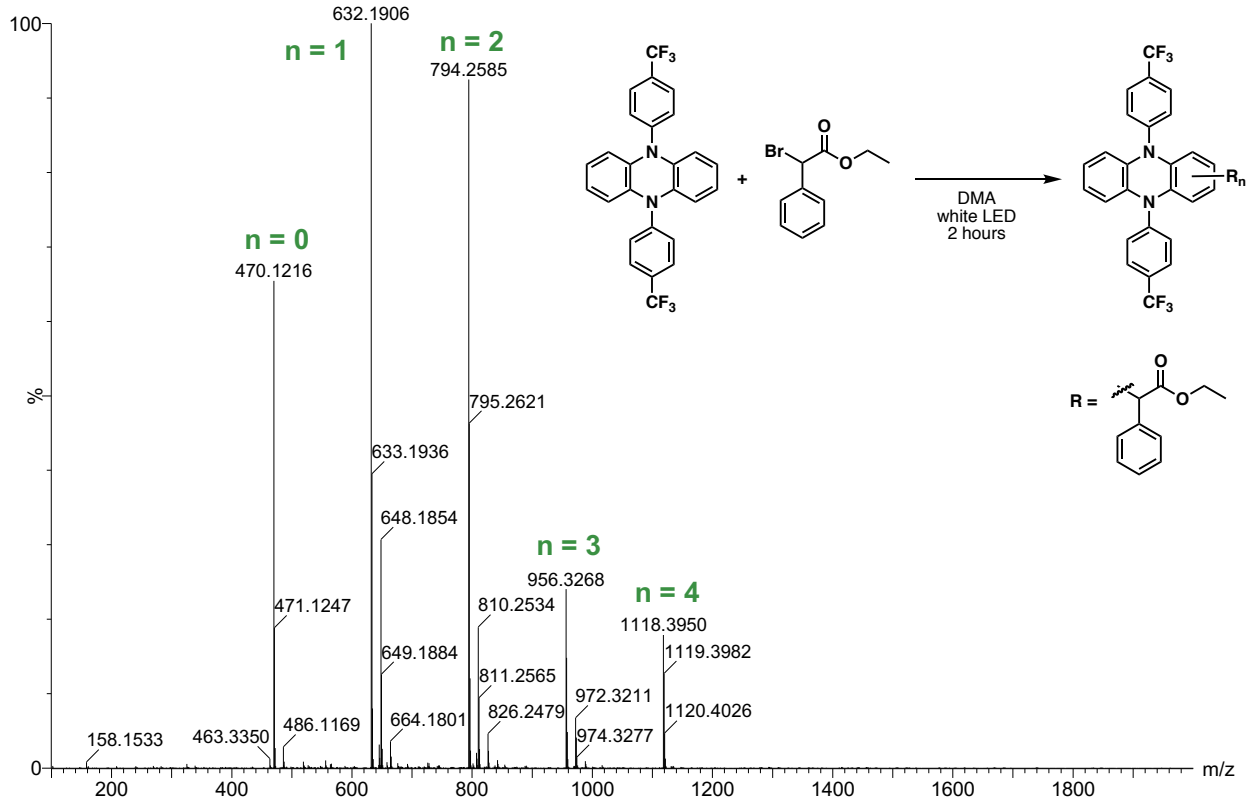

Figure 63. ESI-MS of residue from above experiment using EBP.

Oligomer Addition to Catalyst

A 20 mL vial was charged with 5 mg (0.01 mmol, 1.00 eq.) **1** and a stirbar and brought into a nitrogen atmosphere glovebox. To this vial was added 1.00 mL DMAc, 25.8 mg (0.106 mmol, 10.0 eq.) EBP, and 1.06 g MMA (10.6 mmol, 1000 eq.). The vial was then sealed and placed in a photoreactor on a stirplate. After 20 minutes, the vial was removed from the glovebox and the volatiles were removed under reduced pressure. The sample was then analyzed by ESI-MS.

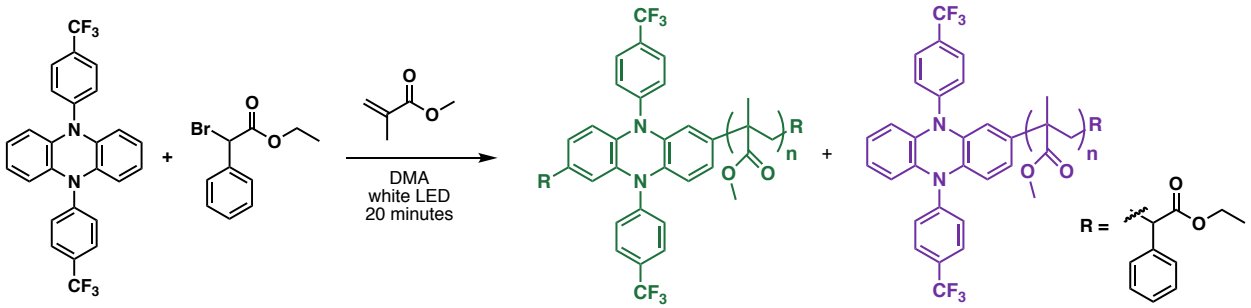

Figure 64. Scheme describing the above oligomerization experiment.

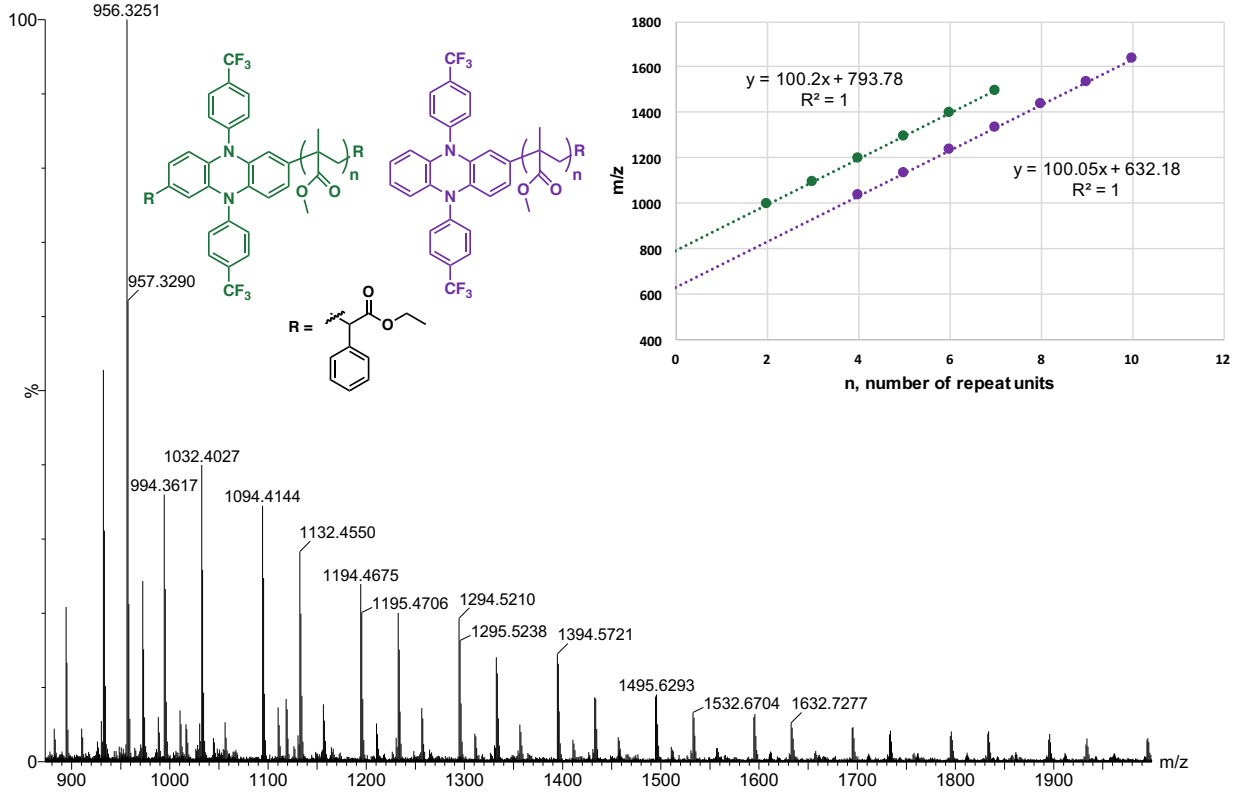

Figure 65. ESI-MS of above oligomerization experiment.

X-Ray Diffraction Data

Single crystals were coated with Paratone-N oil and mounted under a cold stream of dinitrogen gas. Single crystal X-ray diffraction data were acquired on a Bruker Kappa APEX II CCD diffractometer with Mo Kα radiation (λ = 0.71073 Å) and a graphite monochromator.

Initial lattice parameters were obtained from a least-squares analysis of more than 100 reflections; these parameters were later refined against all data. None of the crystals showed significant decay during data collection. Data were integrated and corrected for Lorentz and polarization effects using Bruker APEX3 software, and semiempirical absorption corrections were applied using SCALE (Sheldrick, G. M. *SADABS – a program for area detector absorption corrections*). Space group assignments were based on systematic absences, E statistics, and successful refinement of the structures. Structures were solved using Direct Methods and were refined with the aid of successive Fourier difference maps against all data using the SHELXTL 6.14 software package (Sheldrick, G, M. *SHELXTL*, v. 6.12; Bruker AXS: Madison, WI, 1999). Thermal parameters for all non-hydrogen atoms were refined anisotropically. All hydrogen atoms were assigned to ideal positions and refined using a riding model with an isotropic thermal parameter 1.2 times that of the attached carbon atom (1.5 times for methyl hydrogens).

In the structure of **2**, a methanol solvate molecule (about six per molecule) was found in Fourier difference maps to be disordered over two sites; the site occupancy ratio refined to 51:49. After numerous attempts to model the remaining disorder failed to improve agreement factors, SQUEEZE (Spek, A. L. *J. Appl. Crystallogr.* 2003, *36*, 7.) was used to remove the remaining disordered components. According to the SQUEEZE output, approximately 6 methanol solvate molecules are present per molecule in the void space and were removed. The chemical data presented for **2** in Table 1-5 do not include the components removed by SQUEEZE.

5,10-di(4-trifluoromethylphenyl)-5,10-dihydrophenazine (1)

Crystal data and structure refinement for 1.

Identification code	1	
Empirical formula	C26 H16 F6 N2	
Formula weight	470.41	
Temperature	100(2) K	
Wavelength	0.71073 Å	
Crystal system	Monoclinic	
Space group	C2/c	
Unit cell dimensions	a = 12.7938(15) Å	a= 90°.
	b = 9.3272(15) Å	b= 105.024(11)°.
	c = 17.600(2) Å	g = 90°.
Volume	2028.4(5) $Å^3$	
Z	4	
Density (calculated)	1.540 Mg/m^3	
Absorption coefficient	0.130 mm^{-1}	
F(000)	960	
Crystal size	0.663 x 0.237 x 0.174 mm^3	
Theta range for data collection	2.396 to 32.583°.	
Index ranges	-19<=h<=19, -14<=k<=14, -26<=l<=26	
Reflections collected	44391	
Independent reflections	3692 [R(int) = 0.0648]	
Completeness to theta = 25.242°	100.0 %	
Absorption correction	Semi-empirical from equivalents	
Max. and min. transmission	0.7465 and 0.6477	
Refinement method	Full-matrix least-squares on F^2	
Data / restraints / parameters	3692 / 0 / 154	
Goodness-of-fit on F^2	1.013	
Final R indices [I>2sigma(I)]	R1 = 0.0450, wR2 = 0.1190	
R indices (all data)	R1 = 0.0596, wR2 = 0.1304	
Extinction coefficient	n/a	
Largest diff. peak and hole	0.546 and -0.288 $e.Å^{-3}$	

Atomic coordinates (x 10^4) and equivalent isotropic displacement parameters ($Å^2$x 10^3) for 1. U(eq) is defined as one third of the trace of the orthogonalized U^{ij} tensor.

	x	y	z	U(eq)
C(1)	1784(1)	9228(1)	1829(1)	12(1)
C(2)	2430(1)	10428(1)	1830(1)	14(1)
C(3)	3365(1)	10317(1)	1564(1)	14(1)
C(4)	3627(1)	9004(1)	1288(1)	13(1)
C(5)	2962(1)	7811(1)	1260(1)	15(1)
C(6)	2039(1)	7922(1)	1534(1)	14(1)
C(7)	4654(1)	8816(1)	1039(1)	19(1)
C(8)	1067(1)	9215(1)	2986(1)	10(1)
C(9)	2112(1)	9104(1)	3471(1)	12(1)
C(10)	2297(1)	9022(1)	4288(1)	14(1)
C(11)	1429(1)	9055(1)	4621(1)	16(1)
C(12)	376(1)	9152(1)	4141(1)	14(1)
C(13)	181(1)	9223(1)	3326(1)	11(1)
F(1)	5361(1)	7977(1)	1541(1)	41(1)
F(2)	5163(1)	10050(1)	996(1)	34(1)
F(3)	4491(1)	8188(1)	336(1)	41(1)
N(1)	875(1)	9340(1)	2162(1)	14(1)

Bond lengths [Å] and angles [°] for 1.

C(1)-C(2)	1.3902(15)
C(1)-C(6)	1.3951(15)
C(1)-N(1)	1.4358(13)
C(2)-C(3)	1.3964(14)
C(3)-C(4)	1.3907(15)
C(4)-C(5)	1.3934(15)
C(4)-C(7)	1.4993(15)
C(5)-C(6)	1.3915(14)
C(7)-F(2)	1.3339(14)
C(7)-F(3)	1.3351(15)
C(7)-F(1)	1.3402(15)
C(8)-C(9)	1.3915(14)
C(8)-N(1)	1.4115(13)
C(8)-C(13)	1.4118(13)
C(9)-C(10)	1.3967(14)
C(10)-C(11)	1.3845(15)
C(11)-C(12)	1.3958(15)
C(12)-C(13)	1.3924(14)
C(13)-N(1)#1	1.4044(13)
N(1)-C(13)#1	1.4044(13)

C(2)-C(1)-C(6)	120.48(9)
C(2)-C(1)-N(1)	119.02(9)
C(6)-C(1)-N(1)	120.47(9)
C(1)-C(2)-C(3)	120.02(10)
C(4)-C(3)-C(2)	119.15(10)
C(3)-C(4)-C(5)	121.06(9)
C(3)-C(4)-C(7)	120.91(9)
C(5)-C(4)-C(7)	118.00(9)
C(6)-C(5)-C(4)	119.52(10)
C(5)-C(6)-C(1)	119.71(10)
F(2)-C(7)-F(3)	106.73(10)
F(2)-C(7)-F(1)	106.61(10)
F(3)-C(7)-F(1)	105.71(11)

F(2)-C(7)-C(4)	113.16(10)
F(3)-C(7)-C(4)	112.57(10)
F(1)-C(7)-C(4)	111.56(10)
C(9)-C(8)-N(1)	121.36(9)
C(9)-C(8)-C(13)	119.31(9)
N(1)-C(8)-C(13)	119.32(8)
C(8)-C(9)-C(10)	121.00(9)
C(11)-C(10)-C(9)	119.63(9)
C(10)-C(11)-C(12)	119.97(9)
C(13)-C(12)-C(11)	120.89(10)
C(12)-C(13)-N(1)#1	121.29(9)
C(12)-C(13)-C(8)	119.18(9)
N(1)#1-C(13)-C(8)	119.51(8)
C(13)#1-N(1)-C(8)	120.31(8)
C(13)#1-N(1)-C(1)	119.90(8)
C(8)-N(1)-C(1)	117.99(8)

Symmetry transformations used to generate equivalent atoms:

#1 -x,y,-z+1/2

Anisotropic displacement parameters ($Å^2 x\ 10^3$) for 1. The anisotropic displacement factor exponent takes the form: $-2p^2[\ h^2\ a^{*2}U^{11} + ... + 2\ h\ k\ a^*\ b^*\ U^{12}\ ]$

	U^{11}	U^{22}	U^{33}	U^{23}	U^{13}	U^{12}
C(1)	9(1)	17(1)	10(1)	1(1)	3(1)	-1(1)
C(2)	13(1)	14(1)	14(1)	-1(1)	5(1)	0(1)
C(3)	13(1)	13(1)	16(1)	0(1)	5(1)	-2(1)
C(4)	11(1)	14(1)	14(1)	1(1)	5(1)	0(1)
C(5)	15(1)	12(1)	19(1)	-1(1)	8(1)	-1(1)
C(6)	14(1)	14(1)	17(1)	0(1)	6(1)	-2(1)
C(7)	15(1)	18(1)	27(1)	1(1)	11(1)	0(1)
C(8)	10(1)	11(1)	9(1)	0(1)	2(1)	0(1)
C(9)	10(1)	13(1)	12(1)	0(1)	2(1)	0(1)
C(10)	12(1)	17(1)	13(1)	1(1)	1(1)	2(1)
C(11)	15(1)	22(1)	10(1)	1(1)	2(1)	2(1)
C(12)	13(1)	20(1)	10(1)	0(1)	4(1)	1(1)
C(13)	9(1)	13(1)	10(1)	0(1)	2(1)	0(1)
F(1)	18(1)	48(1)	62(1)	23(1)	17(1)	15(1)
F(2)	27(1)	24(1)	63(1)	-2(1)	31(1)	-7(1)
F(3)	36(1)	57(1)	41(1)	-22(1)	28(1)	-9(1)
N(1)	9(1)	25(1)	9(1)	0(1)	3(1)	0(1)

Hydrogen coordinates (x 10^4) and isotropic displacement parameters ($Å^2$x 10^3)
for 1.

	x	y	z	U(eq)
H(2)	2235	11323	2011	16
H(3)	3816	11129	1572	16
H(5)	3138	6927	1054	18
H(6)	1584	7113	1522	17
H(9)	2709	9083	3243	14
H(10)	3015	8944	4612	17
H(11)	1550	9012	5176	19
H(12)	-217	9171	4373	17

5,10-di(4-trifluoromethylphenyl)-5,10-dihydrophenazine radical cation bromide salt (2)

Crystal data and structure refinement for 2		
Identification code	2	
Empirical formula	C26 H16 Br F6 N2	
Formula weight	550.32	
Temperature	100(2) K	
Wavelength	0.71073 Å	
Crystal system	Monoclinic	
Space group	C2/c	
Unit cell dimensions	a = 28.097(6) Å	a= 90°.
	b = 8.1730(16) Å	b= 112.448(7)°.
	c = 12.602(3) Å	g = 90°.
Volume	2674.7(9) $Å^3$	
Z	4	
Density (calculated)	1.367 Mg/m^3	
Absorption coefficient	1.594 mm^{-1}	
F(000)	1100	
Crystal size	0.552 x 0.407 x 0.303 mm^3	
Theta range for data collection	2.613 to 26.371°.	

Index ranges	-34<=h<=34, -10<=k<=10, -15<=l<=15
Reflections collected	43887
Independent reflections	2740 [R(int) = 0.0333]
Completeness to theta = 25.242°	100.0 %
Absorption correction	Semi-empirical from equivalents
Max. and min. transmission	0.7461 and 0.6585
Refinement method	Full-matrix least-squares on F^2
Data / restraints / parameters	2740 / 0 / 159
Goodness-of-fit on F^2	1.076
Final R indices [I>2sigma(I)]	R1 = 0.0426, wR2 = 0.1040
R indices (all data)	R1 = 0.0468, wR2 = 0.1065
Extinction coefficient	n/a
Largest diff. peak and hole	0.730 and -0.512 e.$Å^{-3}$

Atomic coordinates (x 10^4) and equivalent isotropic displacement parameters ($Å^2$x 10^3) for 2. U(eq) is defined as one third of the trace of the orthogonalized U^{ij} tensor.

	x	y	z	U(eq)
Br(1)	5000	3313(1)	7500	38(1)
N(1)	5481(1)	5652(3)	5606(2)	27(1)
C(1)	5049(1)	6554(3)	5512(2)	27(1)
C(2)	5090(1)	8108(3)	6007(2)	31(1)
C(3)	4655(1)	8979(4)	5903(2)	34(1)
C(4)	4165(1)	8293(4)	5295(2)	37(1)
C(5)	4117(1)	6772(4)	4799(2)	34(1)
C(6)	5445(1)	4131(3)	5109(2)	27(1)
C(7)	5988(1)	6323(3)	6278(2)	31(1)
C(8)	6254(1)	7142(4)	5716(3)	41(1)
C(9)	6749(1)	7715(4)	6362(3)	48(1)
C(10)	6958(1)	7453(4)	7531(3)	47(1)
C(11)	6682(1)	6662(4)	8089(3)	47(1)
C(12)	6187(1)	6085(4)	7453(2)	38(1)
C(13)	7500(1)	8029(5)	8237(4)	63(1)
F(1)	7745(1)	8593(4)	7595(3)	103(1)
F(2)	7791(1)	6807(3)	8863(2)	80(1)
F(3)	7517(1)	9182(3)	8991(3)	96(1)

Bond lengths [Å] and angles [°] for 2.

N(1)-C(6)	1.379(3)
N(1)-C(1)	1.385(3)
N(1)-C(7)	1.457(3)
C(1)-C(2)	1.400(4)
C(1)-C(6)#1	1.424(3)
C(2)-C(3)	1.377(4)
C(2)-H(2)	0.9500
C(3)-C(4)	1.410(4)
C(3)-H(3)	0.9500
C(4)-C(5)	1.375(4)
C(4)-H(4)	0.9500
C(5)-C(6)#1	1.400(4)
C(5)-H(5)	0.9500
C(7)-C(12)	1.382(4)
C(7)-C(8)	1.383(4)
C(8)-C(9)	1.397(4)
C(8)-H(8)	0.9500
C(9)-C(10)	1.378(5)
C(9)-H(9)	0.9500
C(10)-C(11)	1.389(5)
C(10)-C(13)	1.516(4)
C(11)-C(12)	1.396(4)
C(11)-H(11)	0.9500
C(12)-H(12)	0.9500
C(13)-F(3)	1.326(5)
C(13)-F(1)	1.330(5)
C(13)-F(2)	1.340(4)

C(6)-N(1)-C(1)	122.1(2)
C(6)-N(1)-C(7)	119.3(2)
C(1)-N(1)-C(7)	118.6(2)
N(1)-C(1)-C(2)	121.6(2)
N(1)-C(1)-C(6)#1	118.5(2)
C(2)-C(1)-C(6)#1	119.9(2)

C(3)-C(2)-C(1)	120.5(2)
C(3)-C(2)-H(2)	119.7
C(1)-C(2)-H(2)	119.7
C(2)-C(3)-C(4)	119.5(3)
C(2)-C(3)-H(3)	120.2
C(4)-C(3)-H(3)	120.2
C(5)-C(4)-C(3)	120.8(3)
C(5)-C(4)-H(4)	119.6
C(3)-C(4)-H(4)	119.6
C(4)-C(5)-C(6)#1	120.5(2)
C(4)-C(5)-H(5)	119.7
C(6)#1-C(5)-H(5)	119.7
C(12)-C(7)-C(8)	122.7(2)
C(12)-C(7)-N(1)	118.4(2)
C(8)-C(7)-N(1)	118.9(2)
C(7)-C(8)-C(9)	118.4(3)
C(7)-C(8)-H(8)	120.8
C(9)-C(8)-H(8)	120.8
C(10)-C(9)-C(8)	119.6(3)
C(10)-C(9)-H(9)	120.2
C(8)-C(9)-H(9)	120.2
C(9)-C(10)-C(11)	121.4(3)
C(9)-C(10)-C(13)	120.1(3)
C(11)-C(10)-C(13)	118.5(3)
C(10)-C(11)-C(12)	119.5(3)
C(10)-C(11)-H(11)	120.2
C(12)-C(11)-H(11)	120.2
C(7)-C(12)-C(11)	118.3(3)
C(7)-C(12)-H(12)	120.8
C(11)-C(12)-H(12)	120.8
F(3)-C(13)-F(1)	107.7(3)
F(3)-C(13)-F(2)	105.1(3)
F(1)-C(13)-F(2)	106.0(3)
F(3)-C(13)-C(10)	113.2(3)
F(1)-C(13)-C(10)	112.8(3)
F(2)-C(13)-C(10)	111.4(3)

Symmetry transformations used to generate equivalent atoms:

#1 -x+1,-y+1,-z+1

Anisotropic displacement parameters ($Å^2 x\ 10^3$) for 2. The anisotropic displacement factor exponent takes the form: $-2p^2[\ h^2\ a^{*2}U^{11} + ... + 2\ h\ k\ a^*\ b^*\ U^{12}\ ]$

	U^{11}	U^{22}	U^{33}	U^{23}	U^{13}	U^{12}
Br(1)	57(1)	29(1)	34(1)	0	24(1)	0
N(1)	15(1)	38(1)	25(1)	3(1)	3(1)	-5(1)
C(1)	18(1)	38(1)	22(1)	6(1)	4(1)	-2(1)
C(2)	21(1)	40(2)	27(1)	4(1)	4(1)	-7(1)
C(3)	28(1)	40(1)	32(1)	2(1)	9(1)	-2(1)
C(4)	23(1)	47(2)	37(1)	1(1)	8(1)	3(1)
C(5)	20(1)	46(2)	32(1)	0(1)	4(1)	-3(1)
C(6)	19(1)	37(1)	22(1)	5(1)	4(1)	-2(1)
C(7)	13(1)	38(1)	34(1)	-2(1)	2(1)	-4(1)
C(8)	28(1)	51(2)	42(2)	2(1)	11(1)	-9(1)
C(9)	27(1)	55(2)	64(2)	-3(2)	18(1)	-15(1)
C(10)	21(1)	52(2)	58(2)	-9(2)	3(1)	-7(1)
C(11)	28(1)	63(2)	38(2)	-2(2)	-2(1)	-5(1)
C(12)	22(1)	51(2)	34(1)	1(1)	4(1)	-5(1)
C(13)	24(2)	67(2)	80(3)	0(2)	0(2)	-8(2)
F(1)	34(1)	139(3)	117(2)	18(2)	6(1)	-41(1)
F(2)	23(1)	75(2)	109(2)	0(1)	-11(1)	-6(1)
F(3)	44(1)	82(2)	121(2)	-43(2)	-15(1)	-12(1)

Hydrogen coordinates (x 10^4) and isotropic displacement parameters ($Å^2$x 10^3)
for 2.

	x	y	z	U(eq)
H(2)	5421	8566	6417	37
H(3)	4684	10034	6238	41
H(4)	3865	8890	5228	44
H(5)	3784	6330	4390	41
H(8)	6104	7310	4909	49
H(9)	6940	8282	5999	58
H(11)	6829	6515	8898	57
H(12)	5992	5542	7818	45

CHAPTER 5

PHENAZINE CATALYSIS FOR PET-RAFT

5.1 Introduction

The use of photoredox catalysis[37,130,146–148] has allowed for the introduction of light-controlled photoredox-mediated variants of many controlled radical polymerizations (CRPs), including two of the most well-known CRPs, reversible addition-fragmentation chain transfer (RAFT) polymerization[149–153] and atom transfer radical polymerization (ATRP).[20,21,23–25] Initial development of these photoredox-catalyzed variants involved the use of a transition metal based photocatalyst (PC), such as tris(bipyridine)ruthenium(II) chloride [$Ru(bpy)_3$] or tris(2-phenylpyradinato-C^2,N)iridium(III) [*fac*-$Ir(ppy)_3$]. However, in order to eliminate the potential for metal contamination in the polymeric product, organic PCs have been sought to replace these transition metal photocatalysts.[16] In the case of photoinduced electron / energy transfer RAFT (PET-RAFT) polymerization, organic molecules such as eosin Y and pheophorbide A have been reported to efficiently mediate the polymerization of methacrylates and acrylates[154–156] and a phenothiazine derivative has been reported for the polymerization of acrylates and acrylamides.[79]

In the case of photoredox-mediated ATRP, a number of PC types have been employed in organocatalyzed ATRP (O-ATRP).[26,28,136] Among these, *N*,*N*-diaryl dihydrophenazines have emerged as highly promising PCs for O-ATRP due in part to their strong reducing power in

their triplet excited state [$E^0(^2PC^{\bullet+}/^3PC^*)$ < -2.0 V *vs.* SCE] and their ability to access an intramolecular charge transfer (CT) excited state upon photoexcitation with visible light. This intramolecular CT state is characterized by the transfer of the excited electron from the phenazine core to the *N*-aryl substituent, and the ability to access an intramolecular CT state has been shown to be a crucial aspect of efficient O-ATRP by these catalysts.[40,43,128] Given the similarity of the role of the PC as a electron-transfer agent in both PET-RAFT and O-ATRP (Figure 66), we hypothesized that the same physical properties which make *N*,*N*-diaryl dihydrophenazines successful PCs for O-ATRP would also extend to the PET-RAFT process.

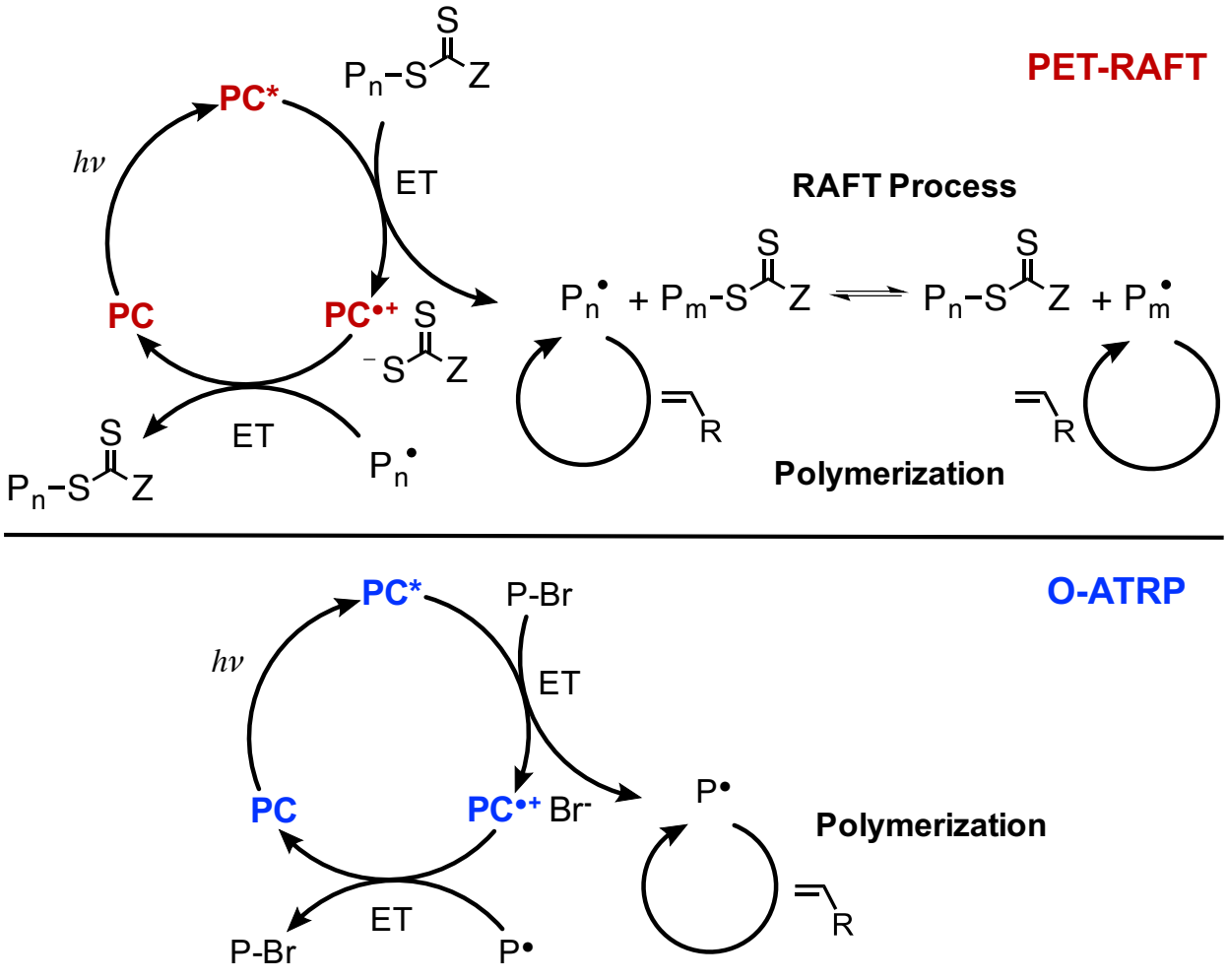

Figure 66. Proposed mechanisms of PET-RAFT (top) and O-ATRP (bottom), highlighting the similar role of the PC in each.

5.2 N,N-Diaryl Dihydrophenazines as PCs for PET-RAFT

To begin, we sought to address whether or not *N*,*N*-diaryl dihydrophenazines are generally capable of serving as PCs for PET-RAFT. Two representative PCs, one exhibiting CT (PC **1**, Table 17) and one without CT (PC 4, Table 17) were tested in the PET-RAFT polymerization of a number of different monomers using 460 nm blue LED as the light source (Table 15). PC **1** proved to be an efficient catalyst for the PET-RAFT of methyl acrylate (MA), methyl methacrylate (MMA), vinyl acetate (VAc), and *N*,*N*-dimethyl acrylamide (DMA). All of the polymers produced were of low dispersity (*Đ*, determined by GPC), and experimental and theoretical molecular weights (MWs) were in relatively good agreement. Notably, this is the first reported PET-RAFT polymerization of VAc by an organic PC. In contrast, PC **4** showed low or no conversion for all of the tested monomers.

Table 15. PET-RAFT Polymerizations of Various Monomers using PCs **1** and **4** as Catalyst.

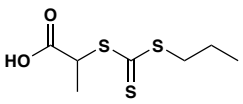

BTPA

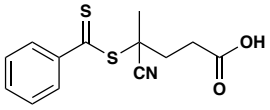

CPADB

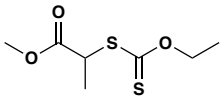

xanthate

Monomer	RAFT Agent	Time (h)	PC 1 *(CT catalyst)*				PC 4 *(non-CT catalyst)*			
			Conv. (%)[a]	$M_{n,th}$ (kDa)	M_n (kDa)[b]	$Đ$ (M_w/M_n)[c]	Conv. (%)[a]	$M_{n,th}$ (kDa)	M_n (kDa)[b]	$Đ$ (M_w/M_n)[c]
MA	BTPA	6	79	13.8	13.9	1.06	6	1.29	2.30	1.44
MMA	CPADB	24	40	8.28	9.02	1.06	<1	-	-	-
VAc	xanthate	20	33	5.93	8.62	1.12	<1	-	-	-
DMA	BTPA	4	44	9.04	11.4	1.06	11	2.41	2.90	1.18

[a]Determined *via* ^{1}H NMR spectroscopy. [b]Determined *via* GPC. [c]Determined *via* GPC. For all entries, [monomer]:[RAFT agent]:[PC] = 200:1:0.01 based on 0.5 mL monomer; run in 0.5 mL DMSO; 460 nm blue LED.

For the polymerization of MA with PC **1**, control experiments were performed in which each of the polymerization components were removed, which resulted in no conversion in the absence of light, or low conversion when PC was removed, indicating the potential for self-initiation of the RAFT agent under polymerization conditions (Table 16).[157–159] The absence of RAFT agent results in an uncontrolled polymerization, as demonstrated by high MW and *Đ.* To lend support to a PET-RAFT mechanism, ^{1}H NMR and MALDI-TOF analysis of a sample of PMA confirmed the presence of BTPA end groups (Figures 67 and 68). Additionally, a sample of PMA was employed as a macroinitiator and efficiently chain extended in the presence of MA to yield PMA-*b*-PMA polymer, which is demonstrated by the shift in MW distribution after chain extension. (Figure 69).

Table 16. Control Experiments for the PET-RAFT of MA.

			DMSO	DMF	DMAc	EtOAc	THF	dioxane
Trial 1	*no PC*	Conv. (%)	28.6	16	13	0	0	21.3
		Đ	1.14	1.22	1.21	-	-	1.19
Trial 2	*no PC*	Conv. (%)	28.6	0	30.5	12.2	28.6	39.7
		Đ	1.09	-	1.14	1.24	1.17	1.11
Trial 3	*no BTPA*	Conv. (%)	> 99	x	x	x	x	x
		Đ	2.84					
Trial 4	*no PC*	Conv. (%)	0	x	x	x	x	x
	no BTPA	*Đ*	-					

Standard conditions [MA]:[BTPA]:[PC **1**] = 200:1:0; 0.5 mL MA; 0.5 mL indicated solvent; 460 nm LED; 6 hours irradiation (Trials 1 and 2) or 18 hours irradiation (Trials 3 and 4).

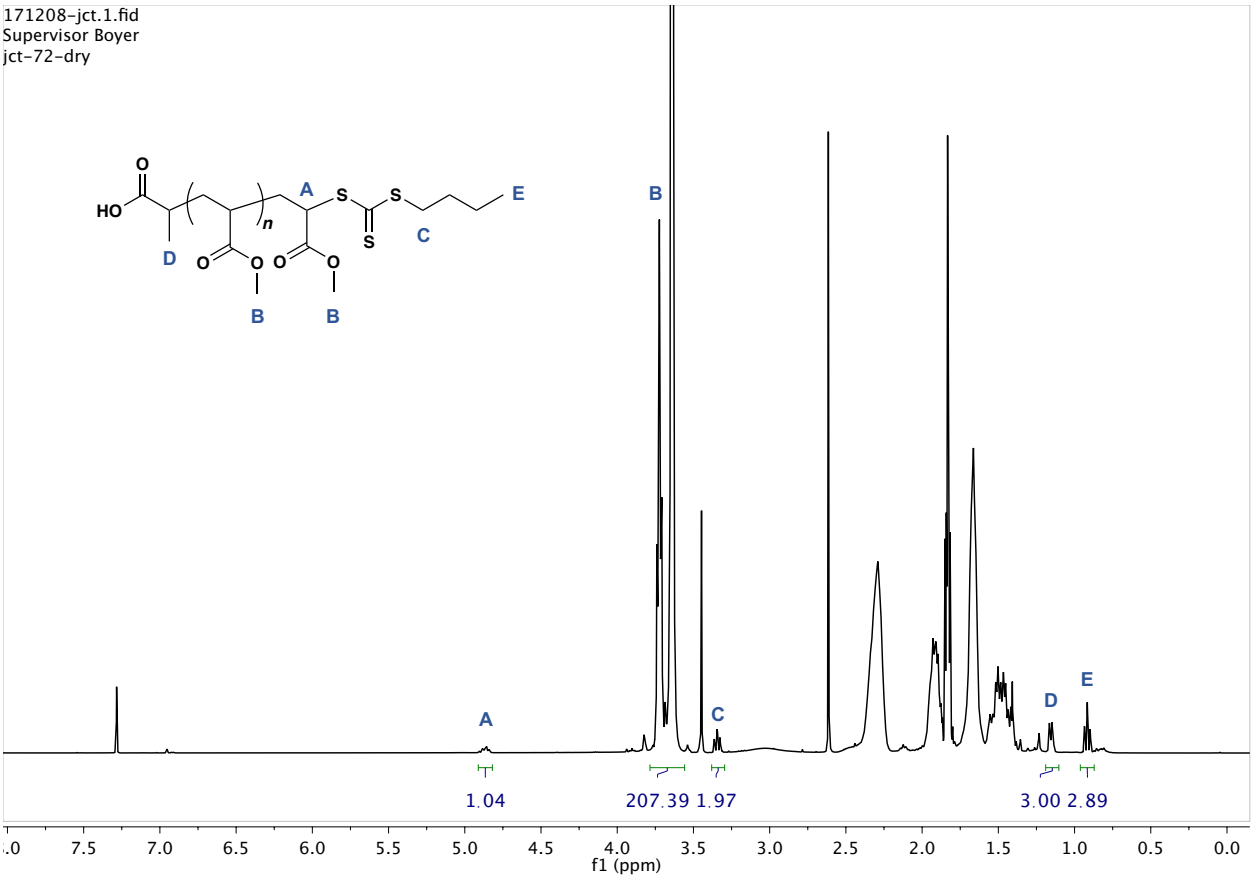

Figure 67. ^{1}H NMR analysis of JCT-72 showing the BTPA end groups.

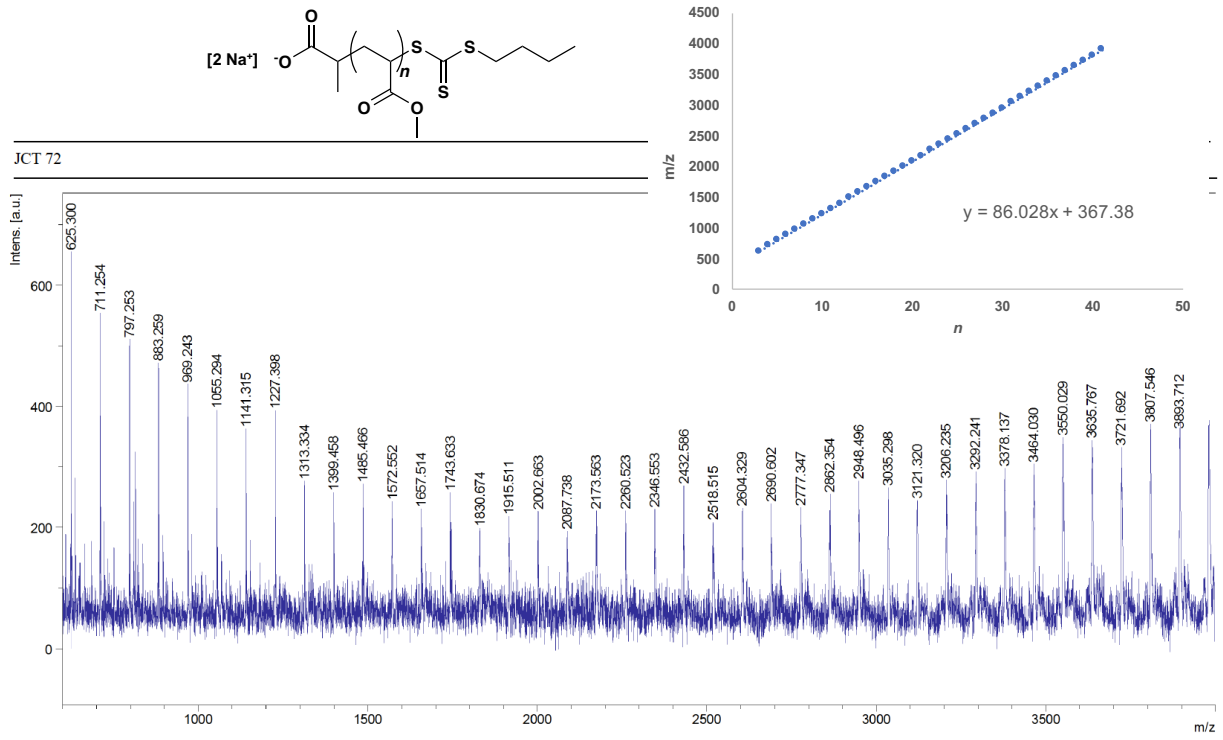

Figure 68. MALDI-TOF mass spectrum of JCT-72. (Inset) Linear regression of peaks in the spectrum, showing a y-intercept with a mass equivalent to the ionized BTPA end group with 2 units of Na^+.

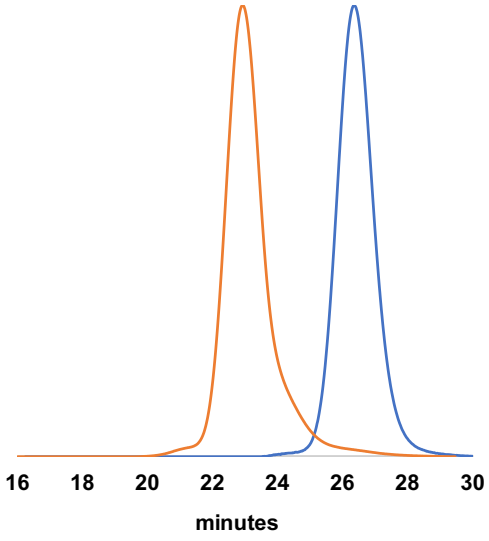

Figure 69: GPC traces for **JCT-72** before chain extension (blue trace) and after chain-extension (red trace).

5.3 Intramolecular Charge Transfer and PET-RAFT

Table 17. PET-RAFT Polymerizations of MA Using PCs **1** – **6** in Solvents of Varying Polarity.

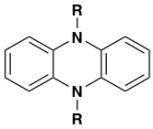	DMSO	DMF	DMAc	EtOAc	THF	dioxane
Charge Transfer Catalysts						
PC 1, R = 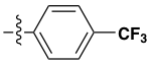	conv.[a] = 78.9% M_n[b] = 13.9 $Đ$[c] = 1.06	conv. = 68.8% M_n = 12.5 $Đ$ = 1.07	conv. = 85.4% M_n = 15.1 $Đ$ = 1.07	conv. = 80.0% M_n = 13.6 $Đ$ = 1.08	conv. = 90.7 % M_n = 13.8 $Đ$ = 1.16	conv. = 90.8% M_n = 18.4 $Đ$ = 1.06
PC 2, R = 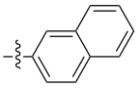	conv. = 87.2 % M_n = 17.3 $Đ$ = 1.08	conv. = 93.3% M_n = 19.1 $Đ$ = 1.06	conv. = 97.8% M_n = 19.7 $Đ$ = 1.08	conv. = 92.1% M_n = 17.5 $Đ$ = 1.11	conv. = 97.0% M_n = 15.2 $Đ$ = 1.20	conv. = >99% M_n = 21.0 $Đ$ = 1.12
PC 3, R = 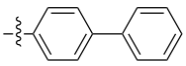	conv. = 76.4% M_n = 15.9 $Đ$ = 1.07	conv. = 70.7% M_n = 13.4 $Đ$ = 1.07	conv. = 86.0% M_n = 17.0 $Đ$ = 1.06	conv. = 29.1% M_n = 7.4 $Đ$ = 1.16	conv. = 76.4% M_n = 13.4 $Đ$ = 1.07	conv. = 91.5% M_n = 19.4 $Đ$ = 1.08
Non-Charge Transfer Catalysts						
PC 4, R = 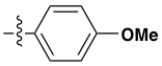	conv. = 5.6% M_n = 2.3 $Đ$ = 1.44	conv. = 0%	conv. = 16.7% M_n = 3.7 $Đ$ = 1.25	conv. = 0%	conv. = 0%	conv. = 0%
PC 5, R = 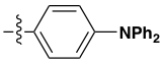	conv. = 8.3% M_n = 2.6 $Đ$ = 1.35	conv. = 0%	conv. = 29.6% M_n = 7.1 $Đ$ = 1.15	conv. = 0%	conv. = 10.7% M_n = 2.7 $Đ$ = 1.32	conv. = 0%
PC 6, R = 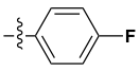	conv. = 49.2% M_n = 10.7 $Đ$ = 1.05	conv. = 0%	conv. = 17.3% M_n = 5.6 $Đ$ = 1.17	conv. = 0%	conv. = 24.8% M_n = 5.4 $Đ$ = 1.20	conv. = 31.0% M_n = 8.2 $Đ$ = 1.15

[a]Determined *via* ^{1}H NMR spectroscopy. [b]kDa, determined *via* GPC. [c]M_w/M_n, determined *via* GPC. For all runs, [MA]:[BTPA]:[PC] = 200:1:0.01, based on 0.5 mL MA; run in 0.5 mL of the indicated solvent (11 M); λ = 460 nm blue LED; irradiation time 6 h. Green denotes conv. > 50%; Yellow denotes 50% > conv. > 20%; Red denotes conv. < 20%.

In order to further investigate the behavior of these PCs as PET-RAFT catalysts, 6 *N*,*N*-diaryl dihydrophenazine PCs (3 with CT and 3 without CT) were employed in the PET-RAFT polymerization of MA in 6 different solvents (DMSO, DMF, DMAc, EtOAc, THF, and dioxane)

under 460 nm blue LED light (Table 17). PCs **1** – **3** are capable of mediating the PET-RAFT of MA to high monomer conversion with low *Đ* and good agreement between theoretical and experimental MWs in solvents with a wide range of polarities. However, PCs **4** – **6** gave low or no monomer conversion within 6 hours in all of the solvents tested.

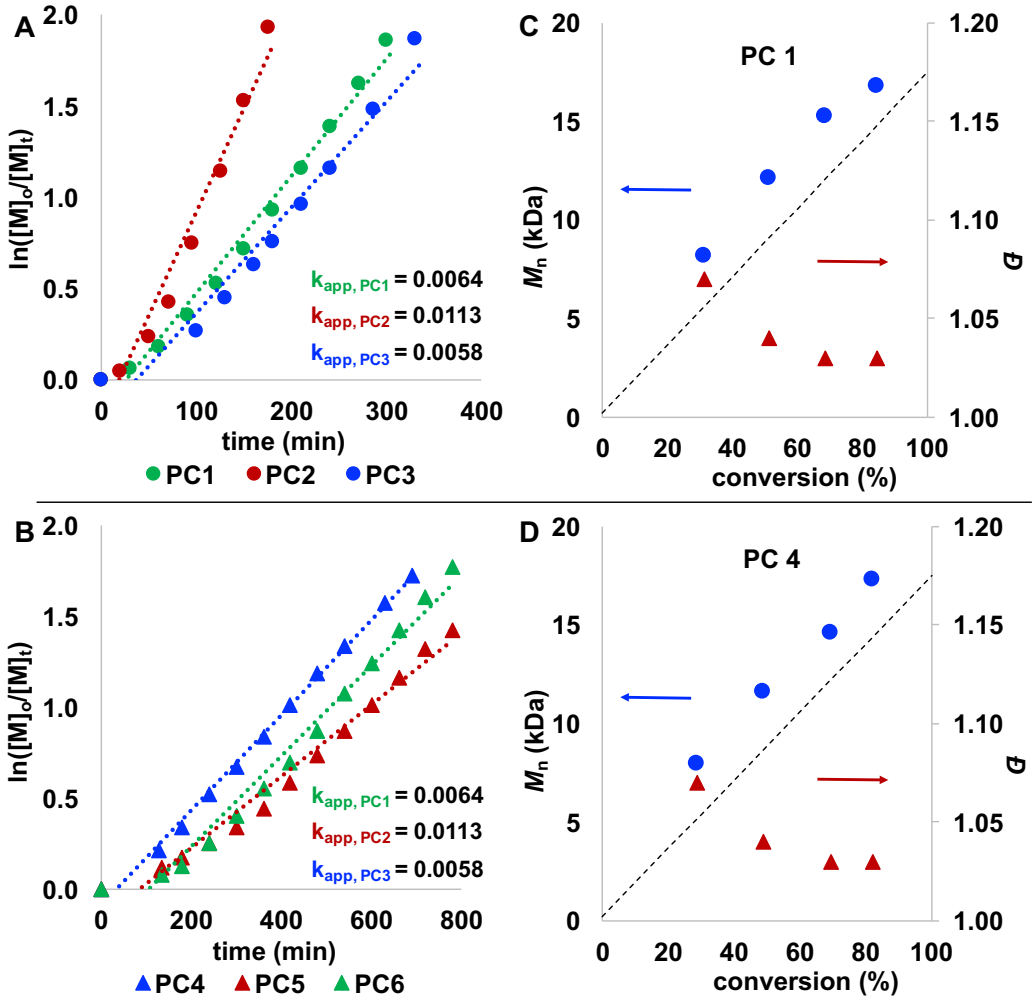

Figure 70. First-order kinetic analysis of the PET-RAFT polymerization of MA in DMSO using PCs **1** – **3 (A)** and PCs **4** – **6 (B)**. Evolution of M_n and *Đ* versus conversion using PC **1 (C)** and PC **4 (D)**.

The PET-RAFT polymerization of MA in DMSO using each of the 6 PCs was also monitored over time (Figure 70, see Section 5.5 for additional details). These data show that polymerizations using non-CT PCs as the catalyst present very low polymerization rates compared to those using CT PCs (k_{app} of PCs **4** – **6** is approximately three times slower than k_{app} of PCs **1** – **3**). Regardless of the CT nature of the PC, the polymerizations showed first order kinetics with respect to monomer concentration, a linear growth of M_n with respect to conversion and decrease in $Đ$ with increasing monomer conversion (Figures 70 and 71). These data indicate that both types of PCs are able to participate in the PET-RAFT process. However, we hypothesize that the presence of intramolecular CT in the excited state allows PCs **1** – **3** to more efficiently participate in the electron transfer step needed to activate the RAFT agent. Similar to our previous observations regarding the behavior of these PCs in O-ATRP, the presence of intramolecular CT, and the resulting localization of the excited electron on the *N*-aryl substituent of the PC, may minimize the potential for unproductive back electron transfer, resulting more efficient activation and overall faster PET-RAFT polymerizations. One key difference between the two polymerization types, however, is that to produce polymers with low $Đ$ O-ATRP requires a higher PC concentration, typically 500 ppm, whereas PET-RAFT of MMA requires a significantly lower PC concentration (typically 10 ppm) (Table 16).

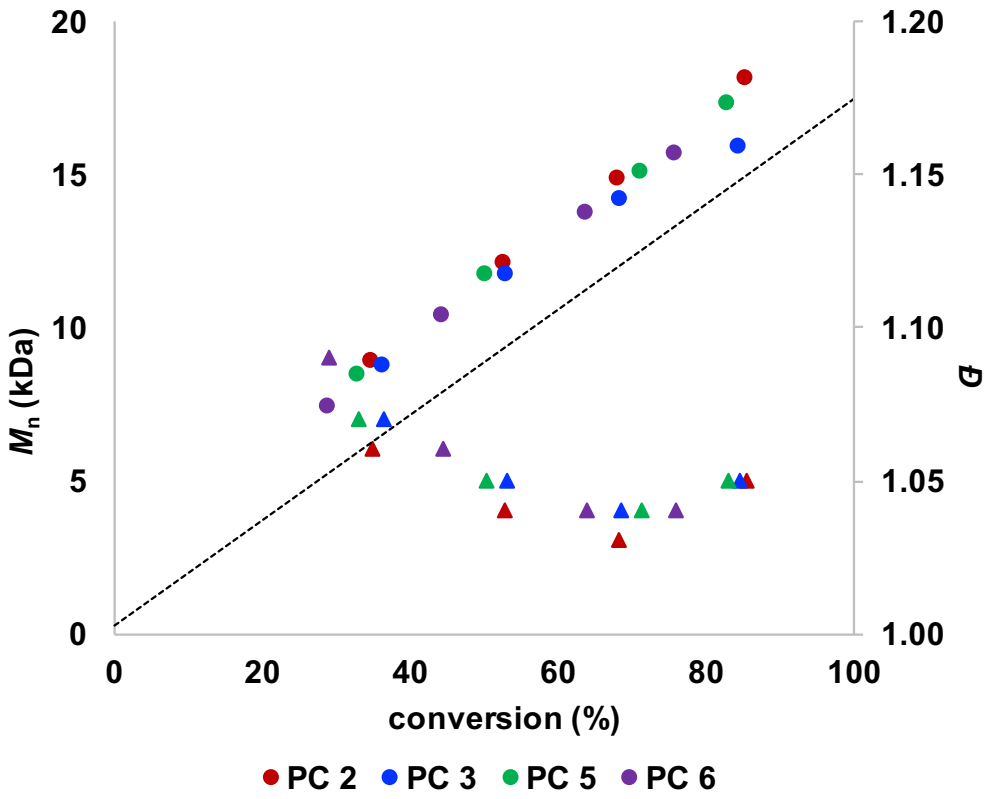

Figure 71. Plots of M_n and Đ *vs.* conversion for the polymerization of MA in DMSO by PCs **1**, **2**, **5**, and **6**. Dashed line = theoretical M_n growth.

Table 18. Effect of Photocatalyst Concentration on the Polymerization of MA in DMSO.

Time	PC 1 Amount	Conv. (%)	M_n (kDa)	M_w (kDa)	*Đ*	*I**
6 hours	500 ppm	91	17.5	18.3	1.04	91
	250 ppm	89	16.6	17.4	1.05	94
	100 ppm	90	16.1	16.7	1.03	98
	50 ppm	86	15.3	16.0	1.05	98
4 hours	100 ppm	77	13.5	13.9	1.03	100
	50 ppm	72	11.7	12.2	1.04	108
	25 ppm	66	10.9	11.3	1.04	107
	10 ppm	42	7.3	7.8	1.07	101

5.4 Sequential PET-RAFT / O-ATRP

With this information in hand, we sought to exploit the ability of PC **1** to efficiently catalyze both PET-RAFT and O-ATRP at different PC concentrations to devise an orthogonal copolymerization in which one PC is used to perform both types of CRPs in sequence. We began by synthesizing a dual initiator, EtBriB-BTPA, which contains a PET-RAFT initiating trithiocarbonate moiety and an O-ATRP initiating alkyl bromide moiety (Figure 72A).

In the first stage of the copolymerization, MA was polymerized *via* PET-RAFT using PC **1** as the catalyst at 50 ppm. ^{1}H NMR of the PMA product indicates that the polymerization was controlled by the trithiocarbonate moiety of EtBriB-BTPA and the alkyl bromide moiety was left unreacted as demonstrated by the presence of a methyl signal at 1.8 ppm (Figure 72B and 79). Subsequently, to form the second block, MMA was added and the PC was increased to 500 ppm. The PMMA block is expected to selectively polymerize *via* O-ATRP as the BTPA moiety cannot polymerize methacrylates.[160] GPC analysis revealed a shift in the retention time after chain extension, supporting the synthesis of PMA-*b*-PMMA (Figure 72C).

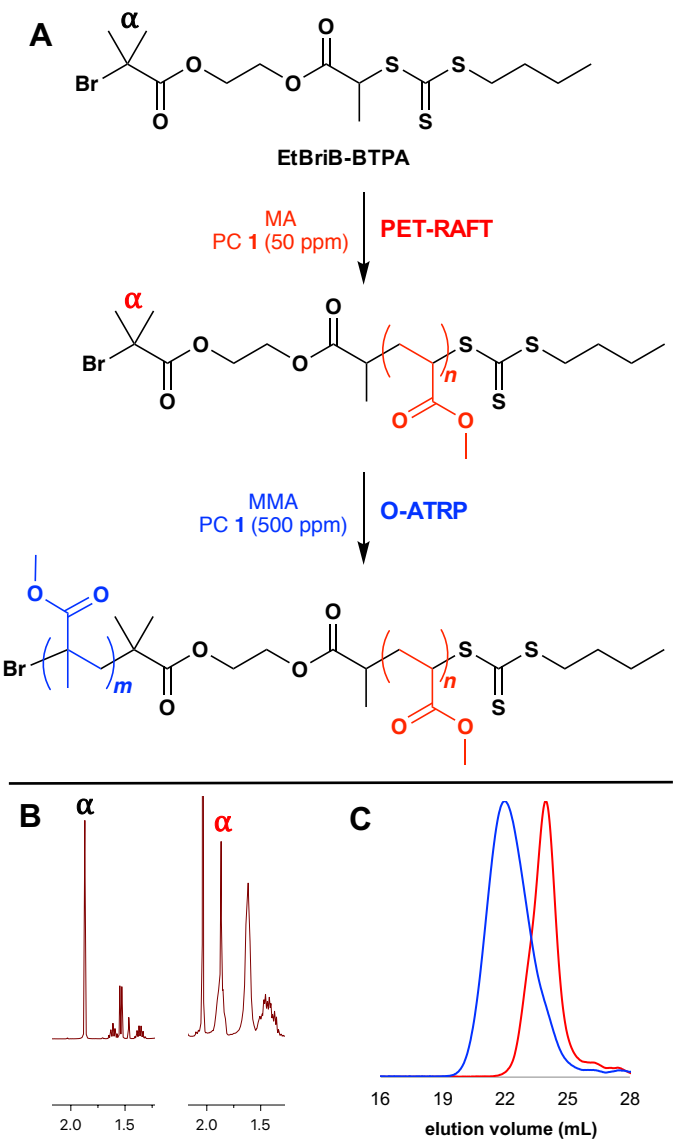

Figure 72. (A) Scheme of sequential PET-RAFT / O-ATRP copolymerization. **(B)** ^{1}H NMR spectra showing the indicated protons before (left) and after (right) the polymerization of MA **(C)** GPC traces of PMA block (red) and PMA-*b*-PMMA copolymer (blue).

In conclusion, *N,N*-diaryl dihydrophenazines, previously employed as PCs for O-ATRP, were investigated for their ability to serve as photocatalysts for PET-RAFT polymerization. It was found that those PCs which possess an excited state with intramolecular CT character are able to efficiently polymerize a number of classes of

monomers, including the first report of a PET-RAFT polymerization of VAc by an organic PC. Additionally, it was found that all of the CT PCs tested resulted in efficient polymerization of MA in solvents with a wide range of polarities. Kinetic analysis indicated that non-CT PCs are also capable of mediating the PET-RAFT of MA. However, these polymerizations are slow compared to those which use a CT PC, likely due to less efficient activation. Finally, the ability of this one class of PCs to mediate two different controlled radical polymerizations was exploited to form a PMA-*b*-PMMA copolymer using both PET-RAFT and O-ATRP in sequence.

5.5 Supporting Information

Materials and Methods

Methyl acrylate (MA), methyl methacrylate (MMA), vinyl acetate (VAc), and *N*,*N*-dimethyl acrylamide were all purchased from Sigma-Aldrich. Prior to use in polymerizations, monomers were de-inhibited by passing through a column of basic alumina (Ajax Chemical). Dimethyl sulfoxide (DMSO), *N*,*N*-dimethyl formamide (DMF), *N*,*N*-dimethyl acetamide (DMAc), ethyl acetate (EtoAc), tetrahydrofuran (THF), and dioxane (Ajax Chemical) were all used as received. 2-(*n*-butyltrithiocarbonate)-propionic acid (BTPA) and methyl 2-[(ethoxycarbonothioyl)sulfanyl]propanoate (xanthate) were synthesized according to literature procedure. PCs **1** – **6** were synthesized according to a previously published method (See Sections 2.7.3 and 3.3.3).

All photopolymerizations were carried out in one of two types of reaction vessels. Batch PET-RAFT polymerizations were performed in a photoreactor comprised of a crystallizing dish lined with 460 nm blue LEDs (Figure 73). Reactions were placed at a distance of 6 cm from the LEDs. Polymerization mixtures used for kinetic analyses were

illuminated by a blue LED light bulb (RS Component PACK LAMP RGB LED bulb, 5 W) at a distance of 6 cm..[155]

Figure 73. Picture of the 460 nm blue LED photoreactor.

Gel permeation chromatography (GPC) was performed using DMAc as the eluent on a Shimadzu system which includes an auto-injector, a Phenomenex 5.0 μm bead size guard column (50 x 7.5 mm), four Phenomenex 5.0 μm bead size columns (10^5, 10^4, 10^3, and 10^2 Å), and a differential refractive index detector. MW determination was performed by calibration with PMMA standards. Nuclear magnetic resonance (NMR) spectroscopy was carried out on a Bruker Avance III 300 MHz instrument using $CDCl_3$ as the solvent. Chemical shifts are referenced to the internal solvent resonance as parts-per-million (ppm) relative to tetramethylsilane (TMS). Fourier-transform near-infrared (FT-NIR) spectroscopy was performed on a Bruker IFS 66/S Fourier Transform spectrometer equipped with a tungsten

halogen lamp, a CaF_2 beam splitter, and a liquid nitrogen cooled InSb detector. Electrospray ionization mass spectrometry (ESI-MS) data were collected by the Central Instrumentation Facility at Colorado State University using an Agilent 1200 Series HPLC coupled to an Agilent 6220 time-of-flight mass spectrometer using flow injection analysis. A dual ESI ion source was used in positive ionization mode. Matrix assisted laser desorption ionization time of flight (MALDI-TOF) mass spectrometry data were collected by the Proteomics and Metabolomics Facility at Colorado State University using a Bruker Microflex-LRF mass spectrometer in positive ion reflector mode and 25 kV accelerating voltage. 1 μL of 1% NaI was spotted on the target and allowed to fully dry. 1 μL of sample was mixed with 1 μL of HABA [2-(4-hydroxyphenylazol) benzoic acid] (25 mg/mL in THF). This mixture was spotted on top of the NaI layer and allowed to air dry prior to analysis.

Polymerization Procedures

General Procedure for all PET-RAFT Polymerizations

A 5 mL glass vial is charged with PC (0.27 μmol, 0.01 eq [50 ppm relative to monomer]), RAFT agent (0.027 mmol, 1 eq.), monomer (5.4 mmol, 200 eq.), and 0.5 mL solvent. This stoichiometry was used in all experiments unless otherwise indicated. The vial is then sealed with a rubber septum, copper wire, and laboratory film and sparged with N_2 for 30 minutes. The vial is then placed in a 460 nm blue LED photoreactor (Figure 73). After the indicated amount of reaction time, the vial is removed from the photoreactor and samples of the reaction mixture are removed *via* syringe for analysis.

Kinetic Analysis

To perform kinetic analysis of a PET-RAFT polymerization, a stock reaction mixture is prepared in the same manner as above. Then, 0.7 mL of the reaction mixture is transferred to a 1 cm x 2 mm quartz cuvette suitable for FT-NIR. The cuvette is then sealed with a rubber septum and laboratory film and sparged with N_2 for 20 minutes. The cuvette is then placed into the blue LED bulb photoreactor (see General Methods). At the indicated time intervals, the cuvette is removed from the photoreactor and transferred to an FT-NIR spectrometer for analysis. After the scan is complete, the cuvette is returned to the photoreactor. Monomer conversion is determined by measurement of the decrease in the FT-NIR peak area from 6220 – 6120 cm^{-1}. Molecular weight determination is performed by removing the cuvette from the photoreactor, and removing an aliquot of reaction mixture *via* syringe under positive N_2 pressure. The cuvette is then returned to the photoreactor and the aliquot is then analyzed *via* GPC.

End-Group Analysis

End-group analysis was performed for a sample of PMA produced via the general PET-RAFT procedure using [MA]:[BTPA]:[PC **1**] in 100:1:0.01 ratio based on 1 mL MA and run in 1 mL DMSO. After 8 hours illumination in the blue LED photoreactor, the product PMA was precipitated into a mixture of 1:1 MeOH:H_2O and recovered via centrifugation and decanting off the supernatant. The recovered PMA was dried and then re-dissolved in a minimal amount of DMSO and re-precipitated. This procedure was repeated 3 more times. The purified PMA (JCT-72) was then analyzed via GPC and found to have M_w = 9.22 kDa, M_n

= 8.84 kDa, Đ = 1.04. Analysis of the ^{1}H NMR spectrum (Figure 67) shows the end-group fidelity (ratio of A to D/3) is close to 1.

In order to further confirm the presence of the BTPA end group, JCT-72 was used as a macroRAFT agent for a chain extension experiment. To JCT-72 (100 mg, 0.0113 mmol, 1 eq.) was added MA (291 mg, 3.39 mmol, 300 eq.), PC **1** (0.053 mg, 0.113 umol, 0.01 eq.) and 0.5 mL DMSO. This reaction mixture was polymerized according to the general PET-RAFT procedure for 8 hours. After 8 hours, a sample was removed from the reaction mixture for analysis *via* GPC and found to have M_w = 28.4 kDa, M_n = 26.5 kDa, $Đ$ = 1.07.

Additional Kinetic Results

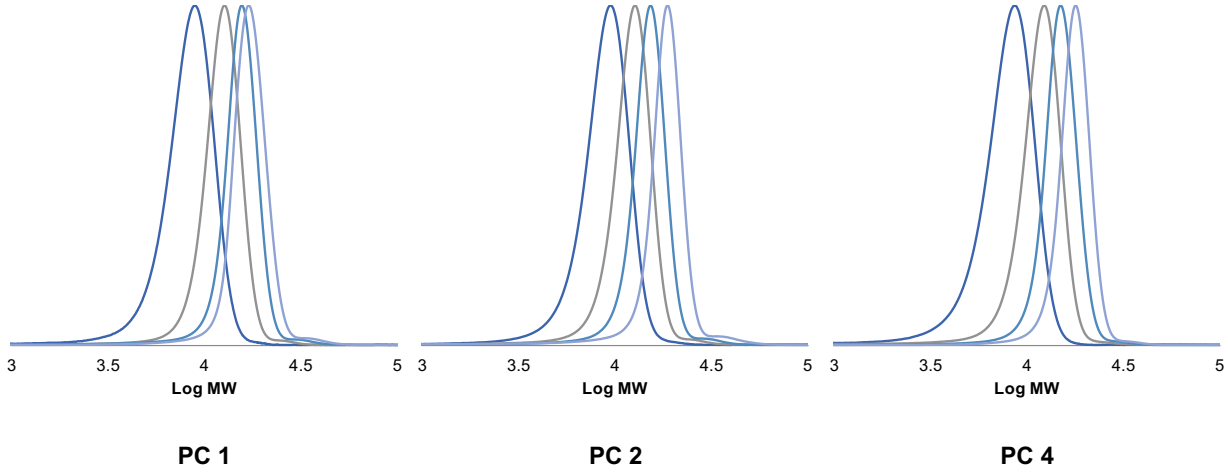

Figure 74. Evolution of molecular weight distribution for the polymerization of MA in DMSO by PCs **1**, **2**, and **4**.

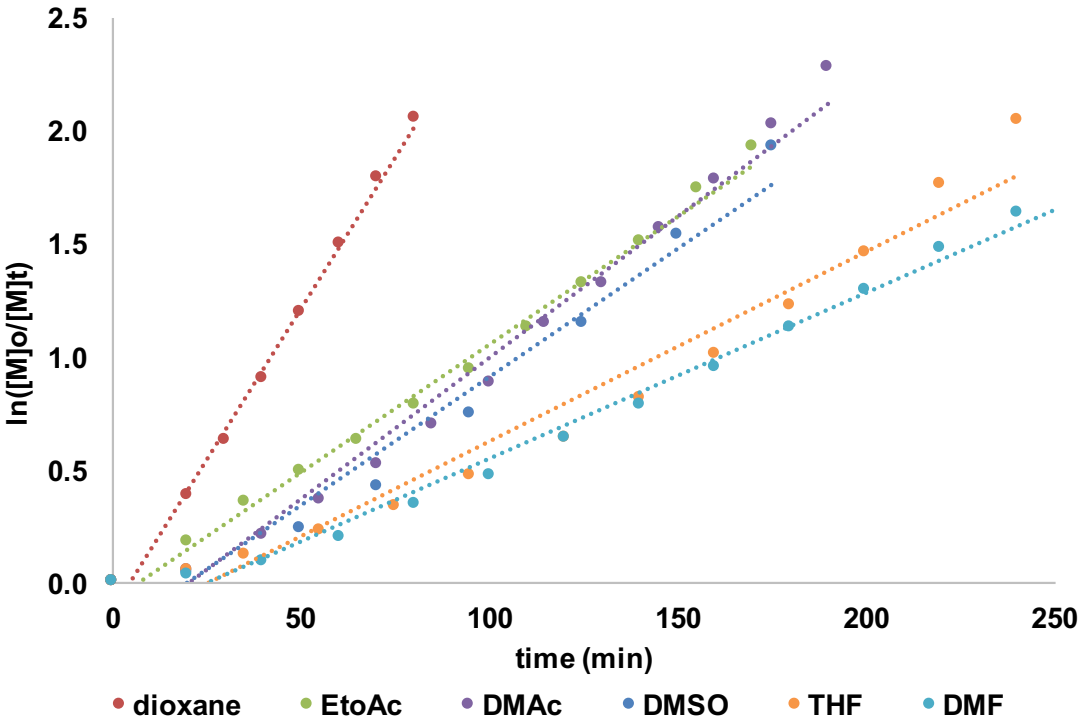

Figure 75. First-order kinetic plots for polymerizations from Table 17 which used PC **2** as the catalyst.

Synthesis and Characterization of EtBriB-BTPA

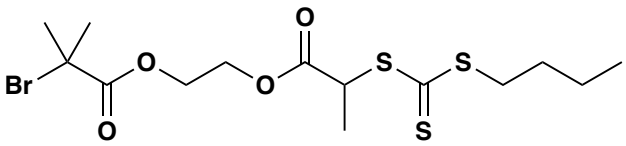

The synthesis of EtBriB-BTPA was adapted from a literature procedure.[156] To a round-bottom flask fitted with a stir bar was added BTPA (100 mg, 0.42 mmol, 1.0 eq.), hydroxyethyl bromoisobutyrate (133 mg, 0.63 mmol, 1.5 eq.), DCC (130 mg, 0.63 mmol, 1.5 eq.), DMAP (2.6 mg, 0.02 mmol, 0.05 eq.), and approximately 3 mL CH_2Cl_2. The flask was left stirring overnight in the dark. The resulting reaction mixture was dried under reduced pressure and purified on a silica gel column (CH_2Cl_2). The product was collected as a viscous

yellow liquid (137 mg, 76%). ^{1}H NMR (400 MHz, $CDCl_3$): δ 4.85 (1H, q), 4.40 (4H, s), 3.36 (2H, t), 1.94 (6H, s), 1.69 (2H, quintet), 1.61 (3H, d), 1.44 (2H, sextet), 0.94 (3H, t). ^{13}C NMR (101 MHz), $CDCl_3$): δ 222.05, 171.41, 170.99, 63.44, 62.96, 55.45, 47.74, 37.08, 30.76, 29.96, 22.06, 16.83, 13.68. HRMS (ESI+): calc'd for $(M+H)^+$ $C_{14}H_{24}BrO_4S_3$ 432.9993, found 432.9990.

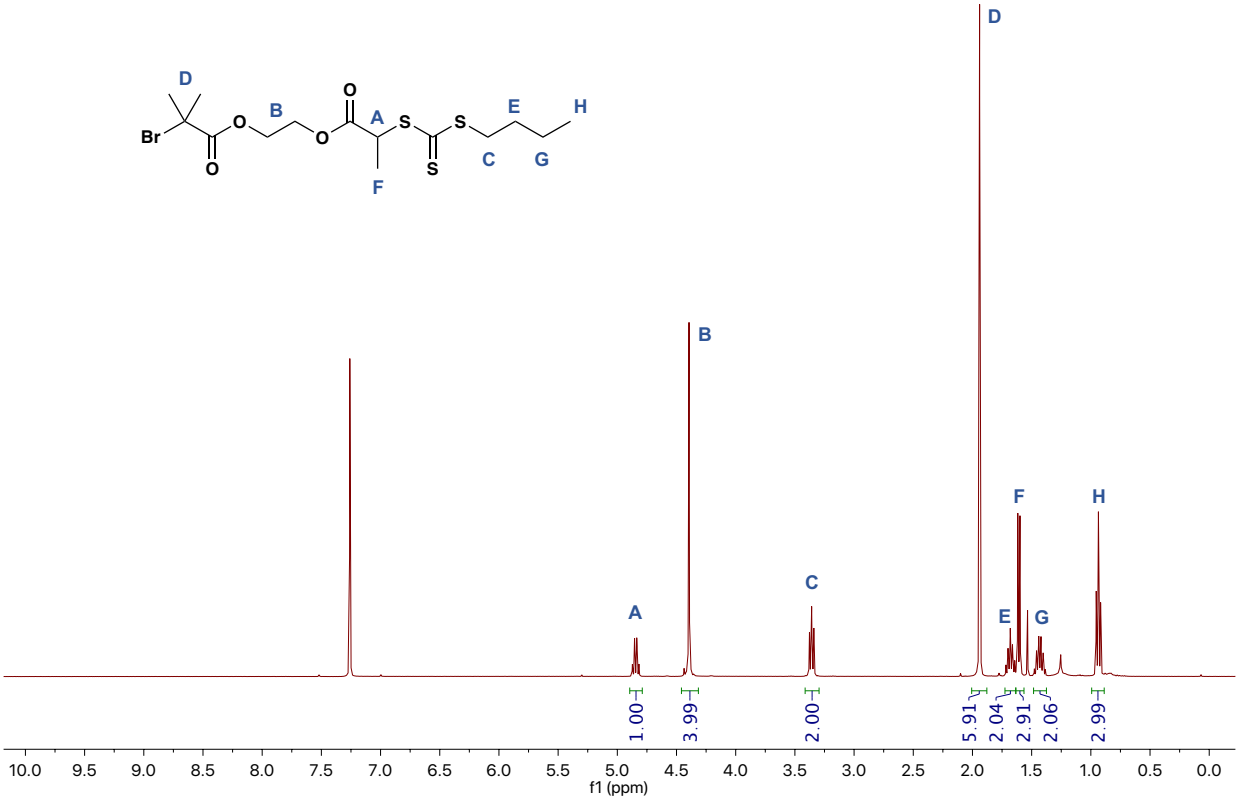

Figure 76. ^{1}H NMR spectrum of EtBriB-BTPA.

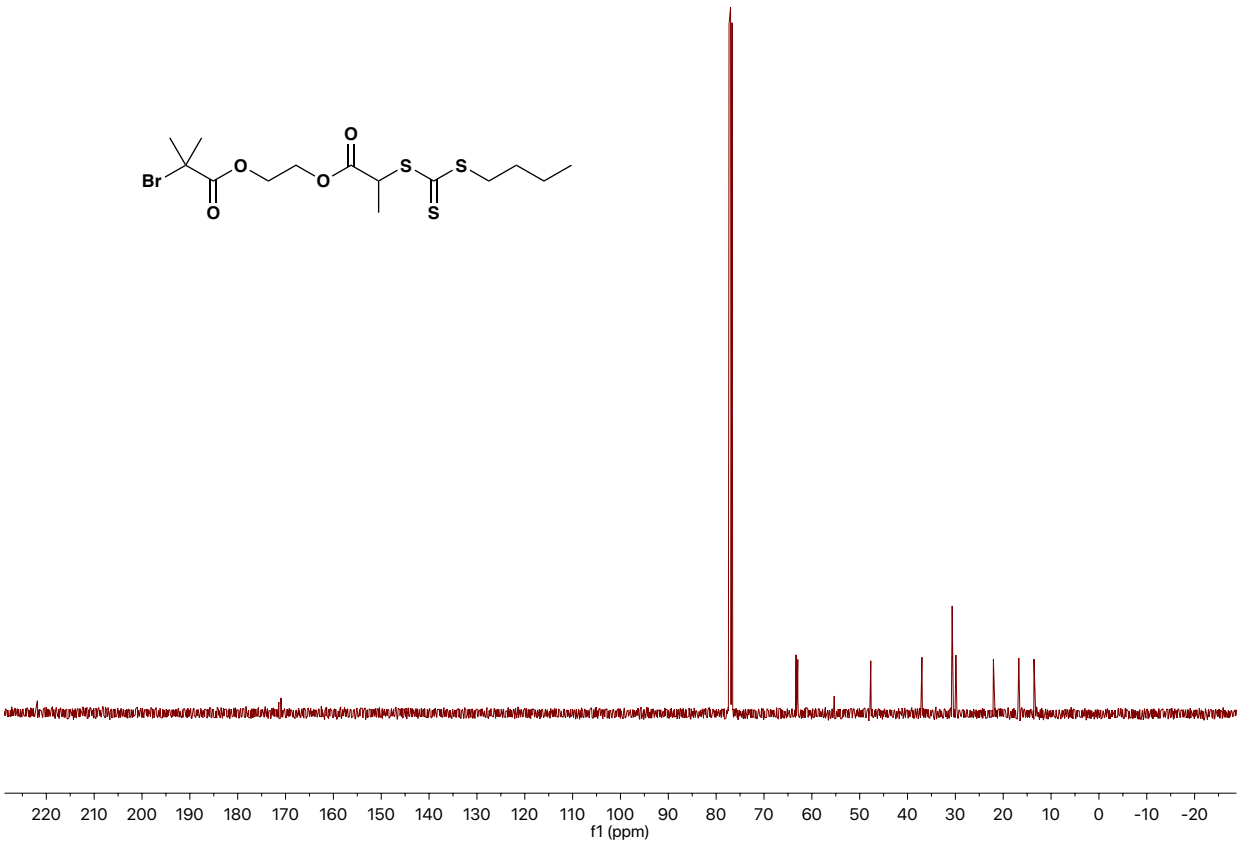

Figure 77. ^{13}C NMR spectrum of EtBriB-BTPA.

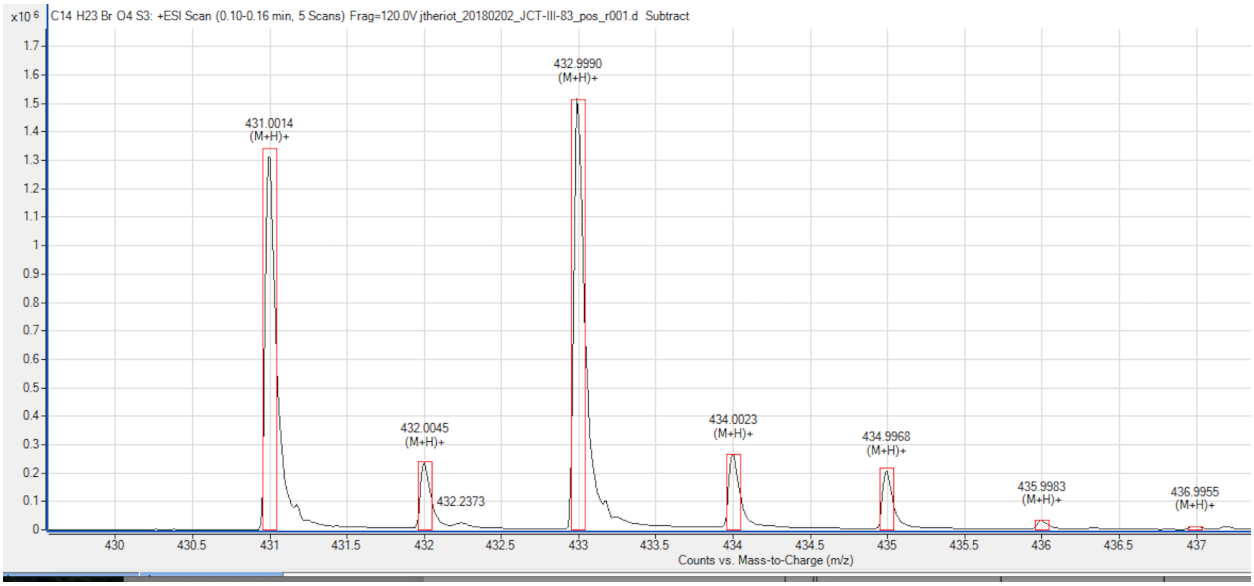

Figure 78. ESI-MS of EtBriB-BTPA. Red boxes indicate the theoretical isotopic pattern for $(M+H)^+$.

Sequential PET-RAFT / O-ATRP

Materials and Methods

Polymerization reagents (MA, MMA, and DMAc) were dried over CaH_2, vacuum distilled, and degassed by three consecutive freeze-pump-thaw cycles before storage and use in the nitrogen glovebox. MA, MMA, and a stock solution of PC **3** were stored at -34 °C in the glovebox freezer and allowed to warm to room temperature before use in polymerizations. All other reagents were used as received.

The photoreactors were assembled with a 400 mL beaker wrapped in aluminum foil and lined on the inside with a coil of white LEDs (16-inch strip, double density white LEDs).[40]

^{1}H NMR spectroscopy was obtained using a Bruker 400MHz spectrometer. Chemical shifts were referenced to an internal solvent resonance as parts-per-million (ppm) relative to tetramethylsilane (TMS). Polymer molecular weights were obtained *via* gel permeation chromatography (GPC) coupled with multi-angle light scattering (MALS), using an Agilent HPLC fitted with one guard column and three PLgel 5 μm MIXED-C gel permeation columns, a Wyatt Technology TrEX differential refractometer, and a Wyatt Technology miniDAWN TREOS light scattering detector, using THF as the eluent at a flow rate of 1.0mL/min.

Detailed Procedure

Stage 1: PET-RAFT of MA

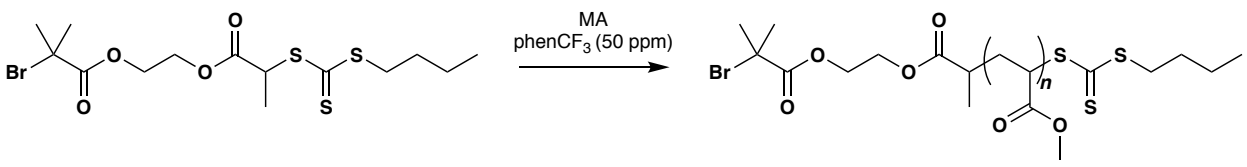

A 20 mL glass vial was charged with a stirbar and **BTPA-EtBriB** (23.27 mg, 0.054 mmol, 1 eq.) and transferred to a nitrogen atmosphere glovebox. To the vial was then added PC **1** (0.253 mg, 0.54 μmol, 0.01 eq.) as a stock solution in DMAc, MA (232 mg, 2.7 mmol, 50 eq.), and 0.5 mL DMAc. The vial was then closed with a screw cap and placed in a white LED photoreactor. After irradiation by white LEDs for 10 hours, a sample weighing 182 mg was removed from the reaction mixture and analyzed by ^{1}H NMR to determine conversion. This NMR analysis indicated 68.2% conversion of MA, indicating a theoretical DP of 34, or a MW_{theo} of 3350 Da. This sample was then dried under reduced pressure to remove any residual MA and facilitate end-group analysis. The ^{1}H NMR spectrum of this sample is shown in Figure 79. At least 3 signals corresponding to the BTPA end group (A, D, and F) are observable and integrable. An additional 2 signals which correspond to the EtBriB portion of the end-group (see Figure 76) are observable but not integrable due to overlap with other features. The observed MW based on the integration of the side-chains versus the end-groups is 3610 Da, which agrees well with the above-calculated theoretical MW. This same sample was then re-dried and analyzed *via* GPC (Figure 72C). The observed $M_{n,GPC}$ was 4640 Da ($Đ$ = 1.12).

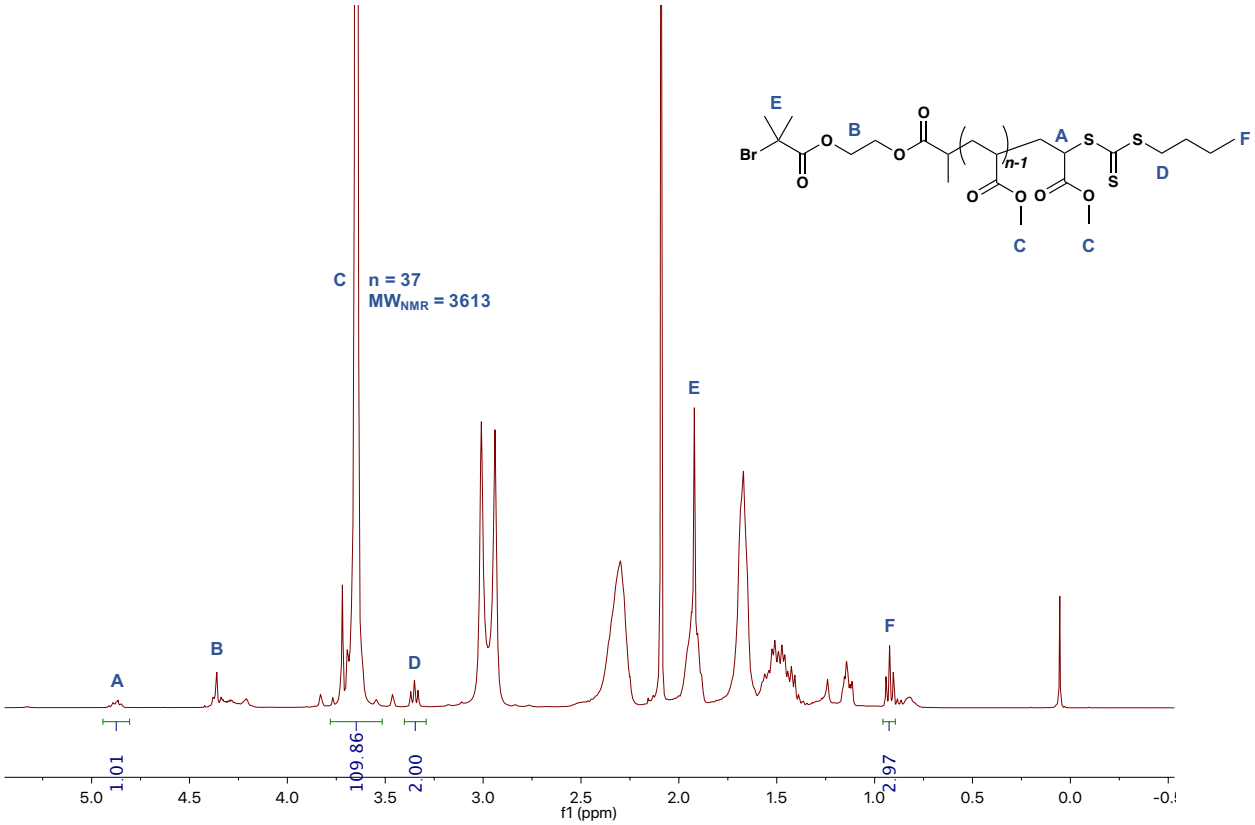

Figure 79. ^{1}H NMR of a dried sample of the PMA formed in the above reaction, showing the **EtBriB-BTPA** end groups.

Stage 2: O-ATRP of MMA

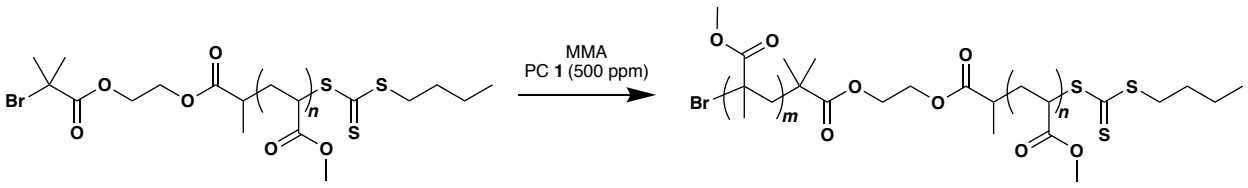

The reaction vial was removed from the glovebox and dried under reduced pressure to remove any residual MA. The vial was then returned to the glovebox where MMA (200 mg, 2.0 mmol, 50 eq. [adjusted for the amount of sample removed for analysis in Stage 1]), PC **1** (1.88 mg, 4.0 µmol, 0.1 eq.), and 0.5 mL DMAc were added to the reaction mixture. The vial

was then placed in a white LED photoreactor. After 8 hours, a sample was removed from the reaction mixture and analyzed by ^{1}H NMR to determine conversion. This NMR analysis indicated 89.0% conversion of MMA, indicating a theoretical DP_{MMA} of 45, or a MW_{theo} of 7850 Da for the MMA block. This sample was then dried under reduced pressure to remove any residual MMA and another ^{1}H NMR spectrum was taken (Figure 80). However, the end groups were not clearly visible, as the block copolymer has many broad peaks in the ^{1}H NMR spectrum. The same sample was then analyzed by GPC and found to have a symmetric, unimodal MW distribution (Figure 72C).

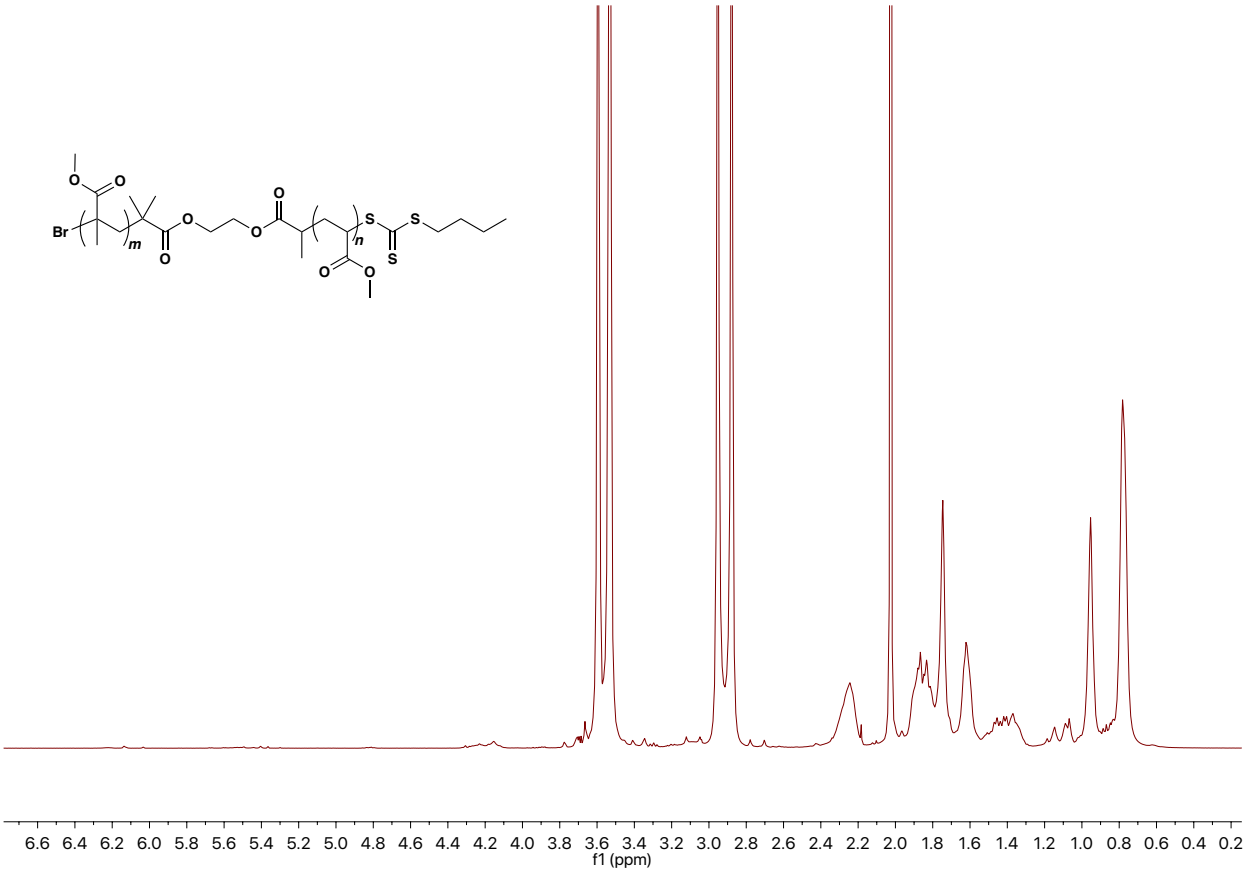

Figure 80. ^{1}H NMR of the PMA-*b*-PMMA copolymer.

CHAPTER 6

SUMMARY AND FUTURE OUTLOOK

6.1 Summary

At the outset of this work, the primary objective was to identify an organic photoredox catalyst that would enable the realization of O-ATRP as a metal-free alternative to traditional metal-catalyzed ATRP. Initial inspiration for such an organic PC came from transition-metal based PCs such as *fac*-Ir(ppy)$_3$ which had already been shown to mediate a photoredox ATRP. An ideal organic PC would behave in a similar fashion, that is, it would absorb in the visible wavelength regime, operate through an oxidative quenching cycle, and possess an excited state reduction potential sufficiently strong to reduce an alkyl bromide to initiate O-ATRP. The introduction of *N,N*-diaryl dihydrophenazines as PCs for O-ATRP allowed for the fulfillment of that primary objective by producing a variety of homopolymers and block copolymers in a controlled fashion with tunable MWs and low $Đ$ without the use of a metal catalyst.

Following that initial discovery, a great deal remained to be learned about dihydrophenazine-mediated O-ATRP. Upon closer investigation of what made these PCs so successful at mediating O-ATRP, it was found that they were even more similar to their transition metal PC precursors than had been initially predicted. Much like the metal-to-ligand charge transfer (MLCT) behavior observed in the excited states of Ir and Ru PCs that

has been suggested to be responsible for their exceptionally efficient electron transfer reactivity, the best-performing dihydrophenazine PCs display intramolecular CT in their excited states. Although work is ongoing to fully understand the similarities and differences between MLCT and the intramolecular CT observed in these organic PCs, the presence of the CT state allowed for manipulation of the energetics of O-ATRP through modulation of solvent polarity. Although initial development of O-ATRP had taken place in high-polarity solvents such as DMAc and DMF, it was found that the use of lower-polarity solvents such as THF and EtoAc gave access to improved and highly consistent polymerization outcomes for both methacrylate and acrylate monomers.

Without efficient deactivation, O-ATRP would be no more than a photoinduced free radical polymerization. However, the deactivation step is inherently more difficult to probe than either photoexcitation or activation, because it relies on a radical cation bromide which is produced in small quantities during the photocatalytic process. Access to a bench-stable radical cation bromide salt of the *N,N*-di(4-trifluoromethylphenyl) dihydrophenazine catalyst allowed for study of the deactivation mechanism through a reverse-initiation O-ATRP experiment, in which the PC enters the O-ATRP catalytic cycle at the deactivation step. This reverse-initiation O-ATRP showed signs of controlled polymerization, substantiating the role of the radical cation bromide form of the PC as deactivator. Follow-up experiments using the deactivator as a supplement to normal-initiation O-ATRP were intended to improve control in the early stages of polymerization, but instead gave evidence for the existence of a termination pathway in which radicals add to the PC. This discovery helped to address the issues with initiator efficiency seen in the early development of O-ATRP and allowed for a more complete mechanistic understanding of the process.

Finally, *N*,*N*-diaryl dihydrophenazines were introduced as catalysts for another type of photoinduced controlled radical polymerization, PET-RAFT. PET-RAFT also employs a PC to activate and deactivate a carbon-centered radical. However, it is mechanistically distinct from O-ATRP because the RAFT process, which is responsible for control over the polymerization, is decoupled from the photocatalytic cycle. This distinction enabled a more straightforward investigation of the impact of intramolecular CT on activation. Indeed, it was found that the presence of CT had a measurable impact on overall rates for PET-RAFT polymerization. Additionally, the use of dihydrophenazines as PCs enabled the first reported PET-RAFT polymerization of VAc with an organic PC. A sequential PET-RAFT / O-ATRP for the one-pot synthesis of a block copolymer demonstrated the potential of this class of PCs to have widespread impact throughout polymer chemistry.

6.2 Future Outlook

As with all scientific endeavors, there remains room for improvement with respect to the work described herein. As a polymerization methodology, O-ATRP would benefit from reduction of the amount of PC required[122] as well as increased oxygen tolerance,[16] both of which would make O-ATRP more appealing as an industrial-scale process. In terms of mechanistic studies, there are two areas which have proven to be the source of some debate within the academic community. First is the question of whether the singlet or triplet excited state of these PCs is responsible for electron transfer in the activation step. Some discussion of this question was given in Section 3.1, but new results and interpretations continue to be released.[82,161,162] Second is the modeling of the deactivation step as a bimolecular or termolecular reaction, which was also discussed in Section 3.1.[162] Finally, the toxicity of these

PCs is not known and will need to be investigated before polymers made from O-ATRP can be fully introduced into biomedical applications.

It is likely that many of the above-mentioned issues will be addressed not with the dihydrophenazine PCs that were the subject of this work, but instead with the next-generation O-ATRP PCs that have been developed within our group. Shortly after the initial introduction of *N,N*-diaryl dihydrophenazines as PCs for O-ATRP, *N*-aryl phenoxazines were announced as excellent PCs for O-ATRP under UV light, and with some synthetic modification, visible light.[44] Since then, phenoxazine PCs have been the subject of an in-depth investigation into the manipulation of intramolecular CT states[163] and continue to be employed in ongoing photophysical and mechanistic studies related to O-ATRP. *N*-aryl phenoxazines have also enabled the expansion of O-ATRP research into more applied areas, such as continuous flow polymerization[164] and the synthesis of complex polymeric architectures.[165] The utility of *N*-aryl phenoxazines as photoredox catalysts has also been expanded beyond O-ATRP into small molecule transformations.[138]

Although the growth of O-ATRP within the four years since it was introduced is nothing short of impressive, there remain new avenues to explore. O-ATRP itself would benefit from an expanded monomer scope to include vinyl acetate, styrene, and better control over acrylates. Each class of monomer will have different requirements, but continued catalyst development will enable fine-tuning of PC properties to match the needs of a given monomer class. Additional mechanistic studies are needed, especially those which use PC radical cation salts as a tool to identify catalyst design principles which specifically improve deactivation. *N,N*-diaryl dihydrophenazines are also fascinating molecules in their own right, demonstrating exceptionally strong visible solvatochomism which could be used

to develop new micropolarity sensors. Since their introduction as O-ATRP PCs, dihydrophenazines have also been used for small-molecule transformations employing dual organic / copper photoredox catalysis.[166] The broad utility scope of these PCs, ranging from O-ATRP to PET-RAFT and now to dual photoredox catalysis, means they will be excellent candidates for new tandem and cascade catalytic reactions not previously considered possible.

REFERENCES

(1) Matyjaszewski, K.; Davis, T. P. *Handbook of Radical Polymerization*; John Wiley & Sons, 2003.

(2) Braunecker, W. A.; Matyjaszewski, K. Controlled/Living Radical Polymerization: Features, Developments, and Perspectives. *Prog. Polym. Sci.* **2007**, *32* (1), 93–146.

(3) Bates, F. S.; Hillmyer, M. A.; Lodge, T. P.; Bates, C. M.; Delaney, K. T.; Fredrickson, G. H. Multiblock Polymers: Panacea or Pandora's Box? *Science* **2012**, *336* (6080), 434.

(4) Hawker, C. J.; Bosman, A. W.; Harth, E. New Polymer Synthesis by Nitroxide Mediated Living Radical Polymerizations. *Chem. Rev.* **2001**, *101* (12), 3661–3688.

(5) Nicolas, J.; Guillaneuf, Y.; Lefay, C.; Bertin, D.; Gigmes, D.; Charleux, B. Nitroxide-Mediated Polymerization. *Prog. Polym. Sci.* **2013**, *38* (1), 63–235.

(6) Moad, G.; Chong, Y. K.; Postma, A.; Rizzardo, E.; Thang, S. H. Advances in RAFT Polymerization: The Synthesis of Polymers with Defined End-Groups. *Polymer* **2005**, *46* (19), 8458–8468.

(7) Moad, G.; Rizzardo, E.; Thang, S. H. Radical Addition–fragmentation Chemistry in Polymer Synthesis. *Polymer* **2008**, *49* (5), 1079–1131.

(8) Matyjaszewski, K.; Xia, J. Atom Transfer Radical Polymerization. *Chem. Rev.* **2001**, *101* (9), 2921–2990.

(9) Coessens, V.; Pintauer, T.; Matyjaszewski, K. Functional Polymers by Atom Transfer Radical Polymerization. *Prog. Polym. Sci.* **2001**, *26* (3), 337–377.

(10) Ouchi, M.; Terashima, T.; Sawamoto, M. Transition Metal-Catalyzed Living Radical Polymerization: Toward Perfection in Catalysis and Precision Polymer Synthesis. *Chem. Rev.* **2009**, *109* (11), 4963–5050.

(11) Boyer, C.; Corrigan, N. A.; Jung, K.; Nguyen, D.; Nguyen, T.-K.; Adnan, N. N. M.; Oliver, S.; Shanmugam, S.; Yeow, J. Copper-Mediated Living Radical Polymerization (Atom Transfer Radical Polymerization and Copper(0) Mediated Polymerization): From Fundamentals to Bioapplications. *Chem. Rev.* **2016**, *116* (4), 1803–1949.

(12) Tasdelen, M. A.; Uygun, M.; Yagci, Y. Photoinduced Controlled Radical Polymerization. *Macromol. Rapid Commun.* **2011**, *32* (1), 58–62.

(13) Tasdelen, M. A.; Ciftci, M.; Yagci, Y. Visible Light-Induced Atom Transfer Radical Polymerization. *Macromol. Chem. Phys.* **2012**, *213* (13), 1391–1396.

(14) Konkolewicz, D.; Schröder, K.; Buback, J.; Bernhard, S.; Matyjaszewski, K. Visible Light and Sunlight Photoinduced ATRP with Ppm of Cu Catalyst. *ACS Macro Lett.* **2012**, *1* (10), 1219–1223.

(15) Pintauer, T.; Matyjaszewski, K. Atom Transfer Radical Addition and Polymerization Reactions Catalyzed by Ppm Amounts of Copper Complexes. *Chem. Soc. Rev.* **2008**, *37* (6), 1087.

(16) Shanmugam, S.; Boyer, C. Organic Photocatalysts for Cleaner Polymer Synthesis. *Science* **2016**, *352* (6289), 1053.

(17) Goto, A.; Wakada, T.; Fukuda, T.; Tsujii, Y. A Systematic Kinetic Study in Reversible Chain Transfer Catalyzed Polymerizations (RTCPs) with Germanium, Tin, Phosphorus, and Nitrogen Catalysts. *Macromol. Chem. Phys.* **2010**, *211* (5), 594–600.

(18) Goto, A.; Ohtsuki, A.; Ohfuji, H.; Tanishima, M.; Kaji, H. Reversible Generation of a Carbon-Centered Radical from Alkyl Iodide Using Organic Salts and Their Application as Organic Catalysts in Living Radical Polymerization. *J. Am. Chem. Soc.* **2013**, *135* (30), 11131–11139.

(19) Goto, A.; Suzuki, T.; Ohfuji, H.; Tanishima, M.; Fukuda, T.; Tsujii, Y.; Kaji, H. Reversible Complexation Mediated Living Radical Polymerization (RCMP) Using Organic Catalysts. *Macromolecules* **2011**, *44* (22), 8709–8715.

(20) Zhang, G.; Song, I. Y.; Ahn, K. H.; Park, T.; Choi, W. Free Radical Polymerization Initiated and Controlled by Visible Light Photocatalysis at Ambient Temperature. *Macromolecules* **2011**, *44* (19), 7594–7599.

(21) Liu, X.; Zhang, L.; Cheng, Z.; Zhu, X. Metal-Free Photoinduced Electron Transfer–atom Transfer Radical Polymerization (PET–ATRP) via a Visible Light Organic Photocatalyst. *Polym. Chem.* **2016**, *7* (3), 689–700.

(22) Furst, L.; Matsuura, B. S.; Narayanam, J. M. R.; Tucker, J. W.; Stephenson, C. R. J. Visible Light-Mediated Intermolecular C−H Functionalization of Electron-Rich Heterocycles with Malonates. *Org. Lett.* **2010**, *12* (13), 3104–3107.

(23) Fors, B. P.; Hawker, C. J. Control of a Living Radical Polymerization of Methacrylates by Light. *Angew. Chem. Int. Ed.* **2012**, *51* (35), 8850–8853.

(24) Ma, W.; Chen, H.; Ma, Y.; Zhao, C.; Yang, W. Visible-Light-Induced Controlled Polymerization of Hydrophilic Monomers with Ir(Ppy)3 as a Photoredox Catalyst in Anisole. *Macromol. Chem. Phys.* **2014**, *215* (10), 1012–1021.

(25) Treat, N. J.; Fors, B. P.; Kramer, J. W.; Christianson, M.; Chiu, C.-Y.; Read de Alaniz, J.; Hawker, C. J. Controlled Radical Polymerization of Acrylates Regulated by Visible Light. *ACS Macro Lett.* **2014**, *3* (6), 580–584.

(26) Miyake, G. M.; Theriot, J. C. Perylene as an Organic Photocatalyst for the Radical Polymerization of Functionalized Vinyl Monomers through Oxidative Quenching with Alkyl Bromides and Visible Light. *Macromolecules* **2014**, *47* (23), 8255–8261.

(27) Theriot, J. C.; Ryan, M. D.; French, T. A.; Pearson, R. M.; Miyake, G. M. Atom Transfer Radical Polymerization of Functionalized Vinyl Monomers Using Perylene as a Visible Light Photocatalyst. *J. Vis. Exp.* **2016**, No. 110.

(28) Treat, N. J.; Sprafke, H.; Kramer, J. W.; Clark, P. G.; Barton, B. E.; Read de Alaniz, J.; Fors, B. P.; Hawker, C. J. Metal-Free Atom Transfer Radical Polymerization. *J. Am. Chem. Soc.* **2014**, *136* (45), 16096–16101.

(29) Pan, X.; Lamson, M.; Yan, J.; Matyjaszewski, K. Photoinduced Metal-Free Atom Transfer Radical Polymerization of Acrylonitrile. *ACS Macro Lett.* **2015**, *4* (2), 192–196.

(30) Dietrich, L. E.; Teal, T. K.; Price-Whelan, A.; Newman, D. K. Redox-Active Antibiotics Control Gene Expression and Community Behavior in Divergent Bacteria. *Science* **2008**, *321* (5893), 1203–1206.

(31) Laursen, J. B.; Nielsen, J. Phenazine Natural Products: Biosynthesis, Synthetic Analogues, and Biological Activity. *Chem. Rev.* **2004**, *104* (3), 1663–1686.

(32) Zhang, Z.; Wu, Y.-S.; Tang, K.-C.; Chen, C.-L.; Ho, J.-W.; Su, J.; Tian, H.; Chou, P.-T. Excited-State Conformational/Electronic Responses of Saddle-Shaped *N* , *N* ′-Disubstituted-Dihydrodibenzo[*a* , *c*]Phenazines: Wide-Tuning Emission from Red to Deep Blue and White Light Combination. *J. Am. Chem. Soc.* **2015**, *137* (26), 8509–8520.

(33) Zheng, Z.; Dong, Q.; Gou, L.; Su, J.-H.; Huang, J. Novel Hole Transport Materials Based on N,N′-Disubstituted-Dihydrophenazine Derivatives for Electroluminescent Diodes. *J Mater Chem C* **2014**, *2* (46), 9858–9865.

(34) Okamoto, T.; Terada, E.; Kozaki, M.; Uchida, M.; Kikukawa, S.; Okada, K. Facile Synthesis of 5,10-Diaryl-5,10-Dihydrophenazines and Application to EL Devices. *Org. Lett.* **2003**, *5* (3), 373–376.

(35) Terada, E.; Okamoto, T.; Kozaki, M.; Masaki, M. E.; Shiomi, D.; Sato, K.; Takui, T.; Okada, K. Exchange Interaction of 5,5‘-(*m* - and *p* -Phenylene)Bis(10-Phenyl-5,10-Dihydrophenazine) Dications and Related Analogues. *J. Org. Chem.* **2005**, *70* (24), 10073–10081.

(36) Hiraoka, S.; Okamoto, T.; Kozaki, M.; Shiomi, D.; Sato, K.; Takui, T.; Okada, K. A Stable Radical-Substituted Radical Cation with Strongly Ferromagnetic Interaction: Nitronyl Nitroxide-Substituted 5,10-Diphenyl-5,10-Dihydrophenazine Radical Cation. *J. Am. Chem. Soc.* **2004**, *126* (1), 58–59.

(37) Prier, C. K.; Rankic, D. A.; MacMillan, D. W. C. Visible Light Photoredox Catalysis with Transition Metal Complexes: Applications in Organic Synthesis. *Chem. Rev.* **2013**, *113* (7), 5322–5363.

(38) Arias-Rotondo, D. M.; McCusker, J. K. The Photophysics of Photoredox Catalysis: A Roadmap for Catalyst Design. *Chem. Soc. Rev.* **2016**, *45* (21), 5803–5820.

(39) Frick, E.; Anastasaki, A.; Haddleton, D. M.; Barner-Kowollik, C. Enlightening the Mechanism of Copper Mediated PhotoRDRP via High-Resolution Mass Spectrometry. *J. Am. Chem. Soc.* **2015**, *137* (21), 6889–6896.

(40) Theriot, J. C.; Lim, C.-H.; Yang, H.; Ryan, M. D.; Musgrave, C. B.; Miyake, G. M. Organocatalyzed Atom Transfer Radical Polymerization Driven by Visible Light. *Science* **2016**, *352* (6289), 1082.

(41) Romero, N. A.; Nicewicz, D. A. Organic Photoredox Catalysis. *Chem. Rev.* **2016**, *116* (17), 10075–10166.

(42) Pan, X.; Fang, C.; Fantin, M.; Malhotra, N.; So, W. Y.; Peteanu, L. A.; Isse, A. A.; Gennaro, A.; Liu, P.; Matyjaszewski, K. Mechanism of Photoinduced Metal-Free Atom Transfer Radical Polymerization: Experimental and Computational Studies. *J. Am. Chem. Soc.* **2016**, *138* (7), 2411–2425.

(43) Ryan, M. D.; Theriot, J. C.; Lim, C.-H.; Yang, H.; G. Lockwood, A.; Garrison, N. G.; Lincoln, S. R.; Musgrave, C. B.; Miyake, G. M. Solvent Effects on the Intramolecular Charge Transfer Character of *N* , *N* -Diaryl Dihydrophenazine Catalysts for Organocatalyzed Atom Transfer Radical Polymerization. *J. Polym. Sci. Part Polym. Chem.* **2017**, *55* (18), 3017–3027.

(44) Pearson, R. M.; Lim, C.-H.; McCarthy, B. G.; Musgrave, C. B.; Miyake, G. M. Organocatalyzed Atom Transfer Radical Polymerization Using *N* -Aryl Phenoxazines as Photoredox Catalysts. *J. Am. Chem. Soc.* **2016**, *138* (35), 11399–11407.

(45) Verhoeven, J. W. Sigma-Coupled Charge-Transfer Probes of the Fluoroprobe and Fluorotrope Type. In *Topics in Fluorescence Spectroscopy*; Springer, 2005; pp 249–284.

(46) Lakowicz, J. R. *Principles of Fluorescence Spectroscopy*, 3rd ed.; Springer: New York, 2006.

(47) Kim, K.-H.; Jahan, S. A.; Kabir, E.; Brown, R. J. C. A Review of Airborne Polycyclic Aromatic Hydrocarbons (PAHs) and Their Human Health Effects. *Environ. Int.* **2013**, *60*, 71–80.

(48) Tielens, A. G. G. M. Interstellar Polycyclic Aromatic Hydrocarbon Molecules. *Annu. Rev. Astron. Astrophys.* **2008**, *46* (1), 289–337.

(49) Henning, T.; Salama, F. Carbon in the Universe. *Science* **1998**, *282* (5397), 2204.

(50) Herrmann, A.; Müllen, K. From Industrial Colorants to Single Photon Sources and Biolabels: The Fascination and Function of Rylene Dyes. *Chem. Lett.* **2006**, *35* (9), 978–985.

(51) Nagao, Y. Synthesis and Properties of Perylene Pigments. *Prog. Org. Coat.* **1997**, *31* (1–2), 43–49.

(52) Halls, J. J. M.; Friend, R. H. The Photovoltaic Effect in a Poly(p-Phenylenevinylene)/Perylene Heterojunction. *Synth. Met.* **1997**, *85* (1–3), 1307–1308.

(53) Zhan, X.; Facchetti, A.; Barlow, S.; Marks, T. J.; Ratner, M. A.; Wasielewski, M. R.; Marder, S. R. Rylene and Related Diimides for Organic Electronics. *Adv. Mater.* **2011**, *23* (2), 268–284.

(54) Denizligil, S.; Resul, R.; Yagci, Y.; Mc Ardle, C.; Fouassier, J.-P. Photosensitized Cationic Polymerization Using Allyl Sulfonium Salt. *Macromol. Chem. Phys.* **1996**, *197* (4), 1233–1240.

(55) Lalevée, J.; Telitel, S.; Xiao, P.; Lepeltier, M.; Dumur, F.; Morlet-Savary, F.; Gigmes, D.; Fouassier, J.-P. Metal and Metal-Free Photocatalysts: Mechanistic Approach and Application as Photoinitiators of Photopolymerization. *Beilstein J. Org. Chem.* **2014**, *10*, 863–876.

(56) Telitel, S.; Dumur, F.; Faury, T.; Graff, B.; Tehfe, M.-A.; Gigmes, D.; Fouassier, J.-P.; Lalevée, J. New Core-Pyrene π Structure Organophotocatalysts Usable as Highly Efficient Photoinitiators. *Beilstein J. Org. Chem.* **2013**, *9*, 877–890.

(57) Tehfe, M.-A.; Lalevée, J.; Morlet-Savary, F.; Graff, B.; Blanchard, N.; Fouassier, J.-P. Tunable Organophotocatalysts for Polymerization Reactions Under Visible Lights. *Macromolecules* **2012**, *45* (4), 1746–1752.

(58) Avlasevich, Y.; Li, C.; Müllen, K. Synthesis and Applications of Core-Enlarged Perylene Dyes. *J. Mater. Chem.* **2010**, *20* (19), 3814.

(59) Huang, C.; Barlow, S.; Marder, S. R. Perylene-3,4,9,10-Tetracarboxylic Acid Diimides: Synthesis, Physical Properties, and Use in Organic Electronics. *J. Org. Chem.* **2011**, *76* (8), 2386–2407.

(60) Bachman, J. C.; Kavian, R.; Graham, D. J.; Kim, D. Y.; Noda, S.; Nocera, D. G.; Shao-Horn, Y.; Lee, S. W. Electrochemical Polymerization of Pyrene Derivatives on Functionalized Carbon Nanotubes for Pseudocapacitive Electrodes. *Nat. Commun.* **2015**, *6* (1).

(61) Singh-Rachford, T. N.; Castellano, F. N. Triplet Sensitized Red-to-Blue Photon Upconversion. *J. Phys. Chem. Lett.* **2010**, *1* (1), 195–200.

(62) Parac, M.; Grimme, S. A TDDFT Study of the Lowest Excitation Energies of Polycyclic Aromatic Hydrocarbons. *Chem. Phys.* **2003**, *292* (1), 11–21.

(63) Allushi, A.; Jockusch, S.; Yilmaz, G.; Yagci, Y. Photoinitiated Metal-Free Controlled/Living Radical Polymerization Using Polynuclear Aromatic Hydrocarbons. *Macromolecules* **2016**, *49* (20), 7785–7792.

(64) Gilman, H.; Moore, L. O. The Preparation of Some 10-Substituted Phenoxazines [1]. *J. Am. Chem. Soc.* **1957**, *79* (13), 3485–3487.

(65) Gilman, H.; Shirley, D. A. Some Derivatives of Phenothiazine. *J. Am. Chem. Soc.* **1944**, *66* (6), 888–893.

(66) Massie, S. P. The Chemistry of Phenothiazine. *Chem. Rev.* **1954**, *54* (5), 797–833.

(67) Aguirre-Soto, A.; Lim, C.-H.; Hwang, A. T.; Musgrave, C. B.; Stansbury, J. W. Visible-Light Organic Photocatalysis for Latent Radical-Initiated Polymerization via $2e^-/1H^+$ Transfers: Initiation with Parallels to Photosynthesis. *J. Am. Chem. Soc.* **2014**, *136* (20), 7418–7427.

(68) Pitre, S. P.; McTiernan, C. D.; Ismaili, H.; Scaiano, J. C. Metal-Free Photocatalytic Radical Trifluoromethylation Utilizing Methylene Blue and Visible Light Irradiation. *ACS Catal.* **2014**, *4* (8), 2530–2535.

(69) Tian, H.; Yang, X.; Chen, R.; Pan, Y.; Li, L.; Hagfeldt, A.; Sun, L. Phenothiazine Derivatives for Efficient Organic Dye-Sensitized Solar Cells. *Chem. Commun.* **2007**, No. 36, 3741.

(70) Wu, W.; Yang, J.; Hua, J.; Tang, J.; Zhang, L.; Long, Y.; Tian, H. Efficient and Stable Dye-Sensitized Solar Cells Based on Phenothiazine Sensitizers with Thiophene Units. *J. Mater. Chem.* **2010**, *20* (9), 1772.

(71) Yao, L.; Pan, Y.; Tang, X.; Bai, Q.; Shen, F.; Li, F.; Lu, P.; Yang, B.; Ma, Y. Tailoring Excited-State Properties and Electroluminescence Performance of Donor–Acceptor Molecules through Tuning the Energy Level of the Charge-Transfer State. *J. Phys. Chem. C* **2015**, *119* (31), 17800–17808.

(72) Godet-Bar, T.; Leprêtre, J.-C.; Le Bacq, O.; Sanchez, J.-Y.; Deronzier, A.; Pasturel, A. Electrochemical and Ab Initio Investigations to Design a New Phenothiazine Based Organic Redox Polymeric Material for Metal-Ion Battery Cathodes. *Phys Chem Chem Phys* **2015**, *17* (38), 25283–25296.

(73) Golriz, A. A.; Suga, T.; Nishide, H.; Berger, R.; Gutmann, J. S. Phenothiazine-Functionalized Redox Polymers for a New Cathode-Active Material. *RSC Adv.* **2015**, *5* (29), 22947–22950.

(74) Discekici, E. H.; Treat, N. J.; Poelma, S. O.; Mattson, K. M.; Hudson, Z. M.; Luo, Y.; Hawker, C. J.; de Alaniz, J. R. A Highly Reducing Metal-Free Photoredox Catalyst: Design and Application in Radical Dehalogenations. *Chem. Commun.* **2015**, *51* (58), 11705–11708.

(75) Poelma, S. O.; Burnett, G. L.; Discekici, E. H.; Mattson, K. M.; Treat, N. J.; Luo, Y.; Hudson, Z. M.; Shankel, S. L.; Clark, P. G.; Kramer, J. W.; et al. Chemoselective Radical Dehalogenation and C–C Bond Formation on Aryl Halide Substrates Using Organic Photoredox Catalysts. *J. Org. Chem.* **2016**, *81* (16), 7155–7160.

(76) Dwivedi, P. C.; Rao, K. G.; Bhat, S. N.; Rao, C. N. R. Spectroscopic Studies of Electron Donor Properties and Radical Cations of Phenothiazine Derivatives. *Spectrochim. Acta Part Mol. Spectrosc.* **1975**, *31* (2), 129–135.

(77) Iida, Y. The Cation Radical Salts of Phenothiazine and Related Compounds. *Bull. Chem. Soc. Jpn.* **1971**, *44* (3), 663–667.

(78) Gomurashvili, Z.; Crivello, J. V. Phenothiazine Photosensitizers for Onium Salt Photoinitiated Cationic Polymerization. *J. Polym. Sci. Part Polym. Chem.* **2001**, *39* (8), 1187–1197.

(79) Chen, M.; MacLeod, M. J.; Johnson, J. A. Visible-Light-Controlled Living Radical Polymerization from a Trithiocarbonate Iniferter Mediated by an Organic Photoredox Catalyst. *ACS Macro Lett.* **2015**, *4* (5), 566–569.

(80) Jenekhe, S. A.; Lu, L.; Alam, M. M. New Conjugated Polymers with Donor−Acceptor Architectures: Synthesis and Photophysics of Carbazole−Quinoline and Phenothiazine−Quinoline Copolymers and Oligomers Exhibiting Large Intramolecular Charge Transfer. *Macromolecules* **2001**, *34* (21), 7315–7324.

(81) Wang, J.; Yuan, L.; Wang, Z.; Rahman, M. A.; Huang, Y.; Zhu, T.; Wang, R.; Cheng, J.; Wang, C.; Chu, F.; et al. Photoinduced Metal-Free Atom Transfer Radical Polymerization of Biomass-Based Monomers. *Macromolecules* **2016**, *49* (20), 7709–7717.

(82) Jockusch, S.; Yagci, Y. The Active Role of Excited States of Phenothiazines in Photoinduced Metal Free Atom Transfer Radical Polymerization: Singlet or Triplet Excited States? *Polym. Chem.* **2016**, *7* (39), 6039–6043.

(83) Price-Whelan, A.; Dietrich, L. E. P.; Newman, D. K. Rethinking "secondary" Metabolism: Physiological Roles for Phenazine Antibiotics. *Nat. Chem. Biol.* **2006**, *2* (2), 71–78.

(84) Mavrodi, D. V.; Blankenfeldt, W.; Thomashow, L. S. Phenazine Compounds in Fluorescent Pseudomonas Spp. Biosynthesis and Regulation. *Annu Rev Phytopathol* **2006**, *44*, 417–445.

(85) Xie, Y.; Fujimoto, T.; Dalgleish, S.; Shuku, Y.; Matsushita, M. M.; Awaga, K. Synthesis, Optical Properties and Charge Transport Characteristics of a Series of Novel Thiophene-Fused Phenazine Derivatives. *J. Mater. Chem. C* **2013**, *1* (21), 3467.

(86) Li, Y.; Fu, Y.; Tong, H.; Xie, Z.; Wang, L. Effect of Side-Chain Positions on Morphology and Photovoltaic Properties of Phenazine-Based Donor-Acceptor Copolymers. *J. Polym. Sci. Part Polym. Chem.* **2013**, *51* (13), 2910–2918.

(87) Fan, Q.; Liu, Y.; Xiao, M.; Tan, H.; Wang, Y.; Su, W.; Yu, D.; Yang, R.; Zhu, W. Donor–acceptor Copolymers Based on Benzo[1,2- B :4,5- b ′]Dithiophene and Pyrene-Fused Phenazine for High-Performance Polymer Solar Cells. *Org. Electron.* **2014**, *15* (11), 3375–3383.

(88) Lee, J.; Shizu, K.; Tanaka, H.; Nakanotani, H.; Yasuda, T.; Kaji, H.; Adachi, C. Controlled Emission Colors and Singlet–triplet Energy Gaps of Dihydrophenazine-Based Thermally Activated Delayed Fluorescence Emitters. *J. Mater. Chem. C* **2015**, *3* (10), 2175–2181.

(89) Masuda, Y.; Kuratsu, M.; Suzuki, S.; Kozaki, M.; Shiomi, D.; Sato, K.; Takui, T.; Okada, K. Preparation and Magnetic Properties of Verdazyl-Substituted Dihydrophenazine Radical Cation Tetrachloroferrate Salts. *Polyhedron* **2009**, *28* (9–10), 1950–1954.

(90) Gordienko, L. L.; Chukhlantseva, A. G. Cation Radicals of Dihydrophenazine and Its Derivatives. *Theor. Exp. Chem.* **1972**, *5* (6), 616–618.

(91) Tehfe, M.-A.; Dumur, F.; Xiao, P.; Zhang, J.; Graff, B.; Morlet-Savary, F.; Gigmes, D.; Fouassier, J.-P.; Lalevée, J. Photoinitiators Based on a Phenazine Scaffold: High Performance Systems upon near-UV or Visible LED (385, 395 and 405 Nm) Irradiations. *Polymer* **2014**, *55* (10), 2285–2293.

(92) Waksman, S. A.; Katz, E.; Vining, L. C. NOMENCLATURE OF THE ACTINOMYCINS. *Proc. Natl. Acad. Sci. U. S. A.* **1958**, *44* (6), 602–612.

(93) Ren, J.; Liu, D.; Tian, L.; Wei, Y.; Proksch, P.; Zeng, J.; Lin, W. Venezuelines A–G, New Phenoxazine-Based Alkaloids and Aminophenols from Streptomyces Venezuelae and the Regulation of Gene Target Nur77. *Bioorg. Med. Chem. Lett.* **2013**, *23* (1), 301–304.

(94) Tomoda, A.; Arai, S.; Ishida, R.; Shimamoto, T.; Ohyashiki, K. An Improved Method for the Rapid Preparation of 2-Amino-4,4a-Dihydro-4a,7-Dimethyl-3H-Phenoxazine-3-One, a Novel Antitumor Agent. *Bioorg. Med. Chem. Lett.* **2001**, *11* (8), 1057–1058.

(95) Kato, S.; Shirato, K.; Imaizumi, K.; Toyota, H.; Mizuguchi, J.; Odawara, M.; Che, X.-F.; Akiyama, S.; Abe, A.; Tomoda, A. Anticancer Effects of Phenoxazine Derivatives Combined with Tumor Necrosis Factor-Related Apoptosis-Inducing Ligand on Pancreatic Cancer Cell Lines, KLM-1 and MIA-PaCa-2. *Oncol. Rep.* **2006**, *15* (4), 843–848.

(96) Koishibu-Koizumi, J.; Akazawa, M.; Iwamoto, T.; Taskasaki, M.; Mizuno, F.; Kobayashi, R.; Abe, A.; Tomoda, A.; Hamatake, M.; Ishida, R. Antitumor Activity of a Phenoxazine Compound, 2-Amino-4,4α-Dihydro-4α,7-Dimethyl-3H-Phenoxazine-3-One against Human B Cell and T Cell Lymphoblastoid Cell Lines: Induction of Mixed Types of Cell Death, Apoptosis, and Necrosis. *J. Cancer Res. Clin. Oncol.* **2002**, *128* (7), 363–368.

(97) Frade, V. H. J.; Sousa, M. J.; Moura, J. C. V. P.; Gonçalves, M. S. T. Synthesis, Characterisation and Antimicrobial Activity of New Benzo[a]Phenoxazine Based Fluorophores. *Tetrahedron Lett.* **2007**, *48* (47), 8347–8352.

(98) Ge, J.-F.; Arai, C.; Yang, M.; Bakar Md., A.; Lu, J.; Ismail, N. S. M.; Wittlin, S.; Kaiser, M.; Brun, R.; Charman, S. A.; et al. Discovery of Novel Benzo[*a*]Phenoxazine SSJ-183 as a Drug Candidate for Malaria. *ACS Med. Chem. Lett.* **2010**, *1* (7), 360–364.

(99) Flanagan, W. M.; Wagner, R. W.; Grant, D.; Lin, K.-Y.; Matteucci, M. D. Cellular Penetration and Antisense Activity by a Phenoxazine-Substituted Heptanucleotide. *Nat. Biotechnol.* **1999**, *17* (1), 48–52.

(100) Sun, R.; Liu, W.; Xu, Y.-J.; Lu, J.-M.; Ge, J.-F.; Ihara, M. A Cyanobenzo[a]Phenoxazine-Based near Infrared Lysosome-Tracker for in Cellulo Imaging. *Chem. Commun.* **2013**, *49* (91), 10709.

(101) Sherman, D. B.; Pitner, J. B.; Ambroise, A.; Thomas, K. J. Synthesis of Thiol-Reactive, Long-Wavelength Fluorescent Phenoxazine Derivatives for Biosensor Applications. *Bioconjug. Chem.* **2006**, *17* (2), 387–392.

(102) Okamoto, T.; Kozaki, M.; Doe, M.; Uchida, M.; Wang, G.; Okada, K. 1,4-Benzoxazino[2,3-*b*]Phenoxazine and Its Sulfur Analogues: Synthesis, Properties, and Application to Organic Light-Emitting Diodes. *Chem. Mater.* **2005**, *17* (22), 5504–5511.

(103) Tian, H.; Yang, X.; Cong, J.; Chen, R.; Liu, J.; Hao, Y.; Hagfeldt, A.; Sun, L. Tuning of Phenoxazine Chromophores for Efficient Organic Dye-Sensitized Solar Cells. *Chem. Commun.* **2009**, No. 41, 6288.

(104) Karlsson, K. M.; Jiang, X.; Eriksson, S. K.; Gabrielsson, E.; Rensmo, H.; Hagfeldt, A.; Sun, L. Phenoxazine Dyes for Dye-Sensitized Solar Cells: Relationship Between Molecular Structure and Electron Lifetime. *Chem. - Eur. J.* **2011**, *17* (23), 6415–6424.

(105) Cheng, M.; Yang, X.; Chen, C.; Tan, Q.; Sun, L. Molecular Engineering of Small Molecules Donor Materials Based on Phenoxazine Core Unit for Solution-Processed Organic Solar Cells. *J Mater Chem A* **2014**, *2* (27), 10465–10469.

(106) Gegiou, D.; Huber, J. R.; Weiss, K. Photochemistry of Phenoxazine. Flash-Photolytic Study. *J. Am. Chem. Soc.* **1970**, *92* (17), 5058–5062.

(107) Zhu, Y.; Babel, A.; Jenekhe, S. A. Phenoxazine-Based Conjugated Polymers: A New Class of Organic Semiconductors for Field-Effect Transistors. *Macromolecules* **2005**, *38* (19), 7983–7991.

(108) Joule, J. A. Recent Advances in the Chemistry of 9H-Carbazoles. In *Advances in Heterocyclic Chemistry*; Elsevier, 1984; Vol. 35, pp 83–198.

(109) Knolker, H.-J. Transition Metal Complexes in Organic Synthesis, Part 70&#. Synthesis of Biologically Active Carbazole Alkaloids Using Organometallic Chemistry. *Curr. Org. Synth.* **2004**, *1* (4), 309–331.

(110) Youn, S. W.; Bihn, J. H.; Kim, B. S. Pd-Catalyzed Intramolecular Oxidative C–H Amination: Synthesis of Carbazoles. *Org. Lett.* **2011**, *13* (14), 3738–3741.

(111) Schmidt, A. W.; Reddy, K. R.; Knölker, H.-J. Occurrence, Biogenesis, and Synthesis of Biologically Active Carbazole Alkaloids. *Chem. Rev.* **2012**, *112* (6), 3193–3328.

(112) Chakraborty, D. P.; Barman, B. K.; Bose, P. K. On the Constitution of Murrayanine, a Carbazole Derivative Isolated from Murraya Koenigii Spreng. *Tetrahedron* **1965**, *21* (2), 681–685.

(113) Kapturkiewicz, A.; Herbich, J.; Karpiuk, J.; Nowacki, J. Intramolecular Radiative and Radiationless Charge Recombination Processes in Donor−Acceptor Carbazole Derivatives. *J. Phys. Chem. A* **1997**, *101* (12), 2332–2344.

(114) Wu, Y.; Li, Y.; Gardner, S.; Ong, B. S. Indolo[3,2- *b*]Carbazole-Based Thin-Film Transistors with High Mobility and Stability. *J. Am. Chem. Soc.* **2005**, *127* (2), 614–618.

(115) Blouin, N.; Michaud, A.; Gendron, D.; Wakim, S.; Blair, E.; Neagu-Plesu, R.; Belletête, M.; Durocher, G.; Tao, Y.; Leclerc, M. Toward a Rational Design of Poly(2,7-Carbazole) Derivatives for Solar Cells. *J. Am. Chem. Soc.* **2008**, *130* (2), 732–742.

(116) Li, J.; Dierschke, F.; Wu, J.; Grimsdale, A. C.; Müllen, K. Poly(2,7-Carbazole) and Perylene Tetracarboxydiimide: A Promising Donor/Acceptor Pair for Polymer Solar Cells. *J Mater Chem* **2006**, *16* (1), 96–100.

(117) Brunner, K.; van Dijken, A.; Börner, H.; Bastiaansen, J. J. A. M.; Kiggen, N. M. M.; Langeveld, B. M. W. Carbazole Compounds as Host Materials for Triplet Emitters in Organic Light-Emitting Diodes: Tuning the HOMO Level without Influencing the Triplet Energy in Small Molecules. *J. Am. Chem. Soc.* **2004**, *126* (19), 6035–6042.

(118) Uoyama, H.; Goushi, K.; Shizu, K.; Nomura, H.; Adachi, C. Highly Efficient Organic Light-Emitting Diodes from Delayed Fluorescence. *Nature* **2012**, *492* (7428), 234–238.

(119) Zhang, Q.; Li, B.; Huang, S.; Nomura, H.; Tanaka, H.; Adachi, C. Efficient Blue Organic Light-Emitting Diodes Employing Thermally Activated Delayed Fluorescence. *Nat. Photonics* **2014**, *8* (4), 326–332.

(120) Luo, J.; Zhang, J. Donor–Acceptor Fluorophores for Visible-Light-Promoted Organic Synthesis: Photoredox/Ni Dual Catalytic C(Sp^3)–C(Sp^2) Cross-Coupling. *ACS Catal.* **2016**, *6* (2), 873–877.

(121) Ishimatsu, R.; Matsunami, S.; Kasahara, T.; Mizuno, J.; Edura, T.; Adachi, C.; Nakano, K.; Imato, T. Electrogenerated Chemiluminescence of Donor-Acceptor Molecules with Thermally Activated Delayed Fluorescence. *Angew. Chem. Int. Ed.* **2014**, *53* (27), 6993–6996.

(122) Huang, Z.; Gu, Y.; Liu, X.; Zhang, L.; Cheng, Z.; Zhu, X. Metal-Free Atom Transfer Radical Polymerization of Methyl Methacrylate with Ppm Level of Organic Photocatalyst. *Macromol. Rapid Commun.* **2017**, *38* (10), 1600461.

(123) Nath, S.; Pal, H.; Palit, D. K.; Sapre, A. V.; Mittal, J. P. Steady-State and Time-Resolved Studies on Photoinduced Interaction of Phenothiazine and 10-Methylphenothiazine with Chloroalkanes. *J. Phys. Chem. A* **1998**, *102* (29), 5822–5830.

(124) Guo, Q.-X.; Liang, Z.-X.; Liu, B.; Yao, S.-D.; Liu, Y.-C. A Study on the Laser Flash Photolysis of Phenothiazine and Its N-Alkyl Derivatives. *J. Photochem. Photobiol. Chem.* **1996**, *93* (1), 27–31.

(125) Huber, J. R.; Mantulin, W. W. Emission Properties of Aromatic Amines in Solution. Phenoxazine System. *J. Am. Chem. Soc.* **1972**, *94* (11), 3755–3760.

(126) Tao, Y.; Yuan, K.; Chen, T.; Xu, P.; Li, H.; Chen, R.; Zheng, C.; Zhang, L.; Huang, W. Thermally Activated Delayed Fluorescence Materials Towards the Breakthrough of Organoelectronics. *Adv. Mater.* **2014**, *26* (47), 7931–7958.

(127) Marcus, R. A. Electron Transfer Reactions in Chemistry. Theory and Experiment. *Rev. Mod. Phys.* **1993**, *65* (3), 599–610.

(128) Lim, C.-H.; Ryan, M. D.; McCarthy, B. G.; Theriot, J. C.; Sartor, S. M.; Damrauer, N. H.; Musgrave, C. B.; Miyake, G. M. Intramolecular Charge Transfer and Ion Pairing in *N,N* -Diaryl Dihydrophenazine Photoredox Catalysts for Efficient Organocatalyzed Atom Transfer Radical Polymerization. *J. Am. Chem. Soc.* **2017**, *139* (1), 348–355.

(129) Malińska, M.; Nowacki, J.; Kapturkiewicz, A.; Woźniak, K. Differences in Electron Densities of Phenoxazine and Phenothiazine Derivatives—charge Density Studies. *RSC Adv.* **2012**, *2* (10), 4318.

(130) Tucker, J. W.; Stephenson, C. R. J. Shining Light on Photoredox Catalysis: Theory and Synthetic Applications. *J. Org. Chem.* **2012**, *77* (4), 1617–1622.

(131) Flamigni, L.; Barbieri, A.; Sabatini, C.; Ventura, B.; Barigelletti, F. Photochemistry and Photophysics of Coordination Compounds: Iridium. In *Photochemistry and Photophysics of Coordination Compounds II*; Balzani, V., Campagna, S., Eds.; Springer Berlin Heidelberg: Berlin, Heidelberg, 2007; Vol. 281, pp 143–203.

(132) Juris, A.; Balzani, V.; Barigelletti, F.; Campagna, S.; Belser, P.; von Zelewsky, A. Ru(II) Polypyridine Complexes: Photophysics, Photochemistry, Eletrochemistry, and Chemiluminescence. *Coord. Chem. Rev.* **1988**, *84*, 85–277.

(133) Discekici, E. H.; Pester, C. W.; Treat, N. J.; Lawrence, J.; Mattson, K. M.; Narupai, B.; Toumayan, E. P.; Luo, Y.; McGrath, A. J.; Clark, P. G.; et al. Simple Benchtop Approach to Polymer Brush Nanostructures Using Visible-Light-Mediated Metal-Free Atom Transfer Radical Polymerization. *ACS Macro Lett.* **2016**, *5* (2), 258–262.

(134) Zeng, G.; Liu, M.; Shi, K.; Heng, C.; Mao, L.; Wan, Q.; Huang, H.; Deng, F.; Zhang, X.; Wei, Y. Surface Modification of Nanodiamond through Metal Free Atom Transfer Radical Polymerization. *Appl. Surf. Sci.* **2016**, *390*, 710–717.

(135) Matyjaszewski, K. Atom Transfer Radical Polymerization (ATRP): Current Status and Future Perspectives. *Macromolecules* **2012**, *45* (10), 4015–4039.

(136) Theriot, J. C.; McCarthy, B. G.; Lim, C.-H.; Miyake, G. M. Organocatalyzed Atom Transfer Radical Polymerization: Perspectives on Catalyst Design and Performance. *Macromol. Rapid Commun.* **2017**, *38* (13), 1700040.

(137) Fantin, M.; Isse, A. A.; Gennaro, A.; Matyjaszewski, K. Understanding the Fundamentals of Aqueous ATRP and Defining Conditions for Better Control. *Macromolecules* **2015**, *48* (19), 6862–6875.

(138) Du, Y.; Pearson, R. M.; Lim, C.-H.; Sartor, S. M.; Ryan, M. D.; Yang, H.; Damrauer, N. H.; Miyake, G. M. Strongly Reducing, Visible-Light Organic Photoredox Catalysts as Sustainable Alternatives to Precious Metals. *Chem. - Eur. J.* **2017**, *23* (46), 10962–10968.

(139) Soos, Z. G.; Keller, H. J.; Moroni, W.; Nöthe, D. Cation Radical Salts of Phenazine. *J. Am. Chem. Soc.* **1977**, *99* (15), 5040–5044.

(140) Cauquis, G.; Delhomme, H.; Serve, D. Les Caracteristiques Des Radicaux Cations de Quelques Diaryl-5, 10 Dihydro-5, 10 Phenazines et Des Tetraarylhydrazines Correspondantes. La Degradation de Ces Dernieres Par Les Acides. *Tetrahedron Lett.* **1971**, *12* (48), 4649–4652.

(141) Wang, J.-S.; Matyjaszewski, K. Controlled/" Living" Radical Polymerization. Halogen Atom Transfer Radical Polymerization Promoted by a Cu (I)/Cu (II) Redox Process. *Macromolecules* **1995**, *28* (23), 7901–7910.

(142) Xia, J.; Matyjaszewski, K. Controlled/"Living" Radical Polymerization. Homogeneous Reverse Atom Transfer Radical Polymerization Using AIBN as the Initiator. *Macromolecules* **1997**, *30* (25), 7692–7696.

(143) Tsarevsky, N. V.; Pintauer, T.; Matyjaszewski, K. Deactivation Efficiency and Degree of Control over Polymerization in ATRP in Protic Solvents. *Macromolecules* **2004**, *37* (26), 9768–9778.

(144) Devery III, J. J.; Douglas, J. J.; Nguyen, J. D.; Cole, K. P.; Flowers II, R. A.; Stephenson, C. R. J. Ligand Functionalization as a Deactivation Pathway in a Fac-Ir(Ppy) $_3$ -Mediated Radical Addition. *Chem. Sci.* **2015**, *6* (1), 537–541.

(145) Barner-Kowollik, C.; Davis, T. P.; Stenzel, M. H. Probing Mechanistic Features of Conventional, Catalytic and Living Free Radical Polymerizations Using Soft Ionization Mass Spectrometric Techniques. *Polymer* **2004**, *45* (23), 7791–7805.

(146) Shaw, M. H.; Twilton, J.; MacMillan, D. W. C. Photoredox Catalysis in Organic Chemistry. *J. Org. Chem.* **2016**, *81* (16), 6898–6926.

(147) Corrigan, N.; Shanmugam, S.; Xu, J.; Boyer, C. Photocatalysis in Organic and Polymer Synthesis. *Chem. Soc. Rev.* **2016**, *45* (22), 6165–6212.

(148) Yoon, T. P.; Ischay, M. A.; Du, J. Visible Light Photocatalysis as a Greener Approach to Photochemical Synthesis. *Nat. Chem.* **2010**, *2* (7), 527–532.

(149) Xu, J.; Jung, K.; Atme, A.; Shanmugam, S.; Boyer, C. A Robust and Versatile Photoinduced Living Polymerization of Conjugated and Unconjugated Monomers and Its Oxygen Tolerance. *J. Am. Chem. Soc.* **2014**, *136* (14), 5508–5519.

(150) Xu, J.; Jung, K.; Boyer, C. Oxygen Tolerance Study of Photoinduced Electron Transfer–Reversible Addition–Fragmentation Chain Transfer (PET-RAFT) Polymerization Mediated by Ru(Bpy) $_3$ Cl $_2$. *Macromolecules* **2014**, *47* (13), 4217–4229.

(151) Shanmugam, S.; Xu, J.; Boyer, C. Photoinduced Electron Transfer–Reversible Addition–Fragmentation Chain Transfer (PET-RAFT) Polymerization of Vinyl Acetate and *N* -Vinylpyrrolidinone: Kinetic and Oxygen Tolerance Study. *Macromolecules* **2014**, *47* (15), 4930–4942.

(152) Shanmugam, S.; Xu, J.; Boyer, C. Light-Regulated Polymerization under Near-Infrared/Far-Red Irradiation Catalyzed by Bacteriochlorophyll *A*. *Angew. Chem. Int. Ed.* **2016**, *55* (3), 1036–1040.

(153) Shanmugam, S.; Xu, J.; Boyer, C. Utilizing the Electron Transfer Mechanism of Chlorophyll a under Light for Controlled Radical Polymerization. *Chem. Sci.* **2015**, *6* (2), 1341–1349.

(154) Xu, J.; Shanmugam, S.; Duong, H. T.; Boyer, C. Organo-Photocatalysts for Photoinduced Electron Transfer-Reversible Addition–fragmentation Chain Transfer (PET-RAFT) Polymerization. *Polym. Chem.* **2015**, *6* (31), 5615–5624.

(155) Xu, J.; Shanmugam, S.; Boyer, C. Organic Electron Donor–Acceptor Photoredox Catalysts: Enhanced Catalytic Efficiency toward Controlled Radical Polymerization. *ACS Macro Lett.* **2015**, *4* (9), 926–932.

(156) Xu, J.; Shanmugam, S.; Fu, C.; Aguey-Zinsou, K.-F.; Boyer, C. Selective Photoactivation: From a Single Unit Monomer Insertion Reaction to Controlled Polymer Architectures. *J. Am. Chem. Soc.* **2016**, *138* (9), 3094–3106.

(157) McKenzie, T. G.; Costa, L. P. da M.; Fu, Q.; Dunstan, D. E.; Qiao, G. G. Investigation into the Photolytic Stability of RAFT Agents and the Implications for Photopolymerization Reactions. *Polym. Chem.* **2016**, *7* (25), 4246–4253.

(158) McKenzie, T. G.; Fu, Q.; Wong, E. H. H.; Dunstan, D. E.; Qiao, G. G. Visible Light Mediated Controlled Radical Polymerization in the Absence of Exogenous Radical Sources or Catalysts. *Macromolecules* **2015**, *48* (12), 3864–3872.

(159) Xu, J.; Shanmugam, S.; Corrigan, N. A.; Boyer, C. Catalyst-Free Visible Light-Induced RAFT Photopolymerization. In *Controlled Radical Polymerization: Mechanisms*; Matyjaszewski, K., Sumerlin, B. S., Tsarevsky, N. V., Chiefari, J., Eds.; American Chemical Society, Series Ed.; American Chemical Society: Washington, DC, 2015; Vol. 1187, pp 247–267.

(160) Keddie, D. J.; Moad, G.; Rizzardo, E.; Thang, S. H. RAFT Agent Design and Synthesis. *Macromolecules* **2012**, *45* (13), 5321–5342.

(161) Koyama, D.; Dale, H. J. A.; Orr-Ewing, A. J. Ultrafast Observation of a Photoredox Reaction Mechanism: Photoinitiation in Organocatalyzed Atom-Transfer Radical Polymerization. *J. Am. Chem. Soc.* **2018**, *140* (4), 1285–1293.

(162) Pan, X.; Tasdelen, M. A.; Laun, J.; Junkers, T.; Yagci, Y.; Matyjaszewski, K. Photomediated Controlled Radical Polymerization. *Prog. Polym. Sci.* **2016**, *62*, 73–125.

(163) McCarthy, B.; Pearson, R.; Lim, C.-H.; Sartor, S. M.; Damrauer, N. H.; Miyake, G. M. Structure-Property Relationships for Tailoring Phenoxazines as Reducing Photoredox Catalysts. *J. Am. Chem. Soc.* **2018**.

(164) Ramsey, B. L.; Pearson, R. M.; Beck, L. R.; Miyake, G. M. Photoinduced Organocatalyzed Atom Transfer Radical Polymerization Using Continuous Flow. *Macromolecules* **2017**, *50* (7), 2668–2674.

(165) Buss, B. L.; Beck, L. R.; Miyake, G. M. Synthesis of Star Polymers Using Organocatalyzed Atom Transfer Radical Polymerization through a Core-First Approach. *Polym. Chem.* **2018**.

(166) Tlahuext-Aca, A.; Candish, L.; Garza-Sanchez, R. A.; Glorius, F. Decarboxylative Olefination of Activated Aliphatic Acids Enabled by Dual Organophotoredox/Copper Catalysis. *ACS Catal.* **2018**, *8* (3), 1715–1719.